# REPORT DOCUMENTATION PAGE

*Form Approved OMB No. 0704-0188*



| 1. AGENCY USE ONLY (*Leave Blank*) | 2. REPORT DATE | 3. REPORT TYPE AND DATES COVERED |
|---|---|---|
| | Nov. 4, 1997 | Technical 5/16/92 - 8/15/97 |

**4. TITLE AND SUBTITLE**
Octant Analysis of the Reynolds Stresses in the Three-Dimensional Turbulent Boundary Layer of a Prolate Spheroid

**5. FUNDING NUMBERS**
N00014-91-J-1 732
N00014-94-1-0092

**6. AUTHOR(S)**
Michael M. Madden and Roger L. Simpson

**7. PERFORMING ORGANIZATION NAME(S) AND ADDRESS(ES)**
Aerospace and Ocean Engineering Department
Virginia Polytechnic Institute and State University
Blacksburg, VA 24061-0203

**8. PERFORMING ORGANIZATION REPORT NUMBER**
VPI-AOE-252

**9. SPONSORING/MONITORING AGENCY NAME(S) AND ADDRESS(ES)**
Office of Naval Research
800 N. Quincy St.
Arlington, VA 22217

**10. SPONSORING/MONITORING AGENCY REPORT NUMBER**



**11. SUPPLEMENTARY NOTES**

**12a. DISTRIBUTION/AVAILABILITY STATEMENT**
Approved for public releases, distribution unlimited

**12b. DISTRIBUTION CODE**

**13. ABSTRACT** The Reynolds stress contributions to each of the 8 octants of combinations of u, v, and w fluctuations were examined in local free-stream and local wall-collateral co-ordinates for a pressure-driven three-dimensional turbulent wall-bounded shear flow on the leeside ($x/L$=0.76-0.78, $\phi$=105°-130° from the windward side) of a 6:1 prolate spheroid at 10° angle of attack and Reynolds number $Re_L = 4.2 \times 10^{+6}$. The laser-Doppler velocimeter data of Chesnakas, Simpson, and Madden (1994) were used in this examination of the sweep/ejection concepts for a 3-D mean flow. As described and assessed here, a post-processing technique for fitting the data to the Spalding composite law-of-the-wall velocity profile was used to both reduce the measurement location uncertainty and estimate the wall shear stress. In the resulting flow model, ejections and sweeps produce w' with the same mechanism that produces u'; they transport fluid across a spanwise velocity gradient. Asymmetries that evolve between ejections and sweeps with spanwise fluctuations (w') of opposite sign cause non-zero u'w' and v'w' in the buffer layer. While the model results remain consistent with co-ordinate rotation, wall-collateral coordinates are simpler for octant analysis and are more closely aligned with the quasi-streamwise vortex structures than free-stream coordinates. The sweep and ejection octants maintain a nearly equal distribution of velocity events throughout the buffer and lower log layers. The model's results remain consistent with the four mechanisms revealed by the direct numerical simulation of Sendstad and Moin (1992).

**14. SUBJECT TERMS**
Three Dimensional Separation
Turbulence
Coherent Turbulent Structures
Laser-Doppler Velocimetry

**15. NUMBER OF PAGES**
210

**16. PRICE CODE**

| 17. SECURITY CLASSIFICATION OF REPORT | 18. SECURITY CLASSIFICATION OF THIS PAGE | 19. SECURITY CLASSIFICATION OF ABSTRACT | 20. LIMITATION OF ABSTRACT |
|---|---|---|---|
| Unclassified | Unclassified | Unclassified | None |

July 14, 1998

TO: DEFENSE TECHNICAL INFORMATION CENTER
ATTN: DTIC-FDAC
8725 JOHN KINGMAN ROAD
STE 0944
FT. BELVOIR, VA 22060-6218

FROM: DR. ROGER L. SIMPSON
AEROSPACE AND OCEAN ENGINEERING
VIRGINIA POLYTECHNIC INSTITUTE AND
STATE UNIVERSITY
BLACKSBURG, VA 24061

SUBJECT: GRANT REPORT

ENCLOSED ARE TWO COPIES OF THE FOLLOWING TECHNICAL REPORT THAT DESCRIBES WORK THAT WAS PERFORMED UNDER GRANT:

VPI-AOE-252 by Michael M. Madden and Roger L. Simpson
TITLE: Octant Analysis of the Reynolds Stresses in the Three-Dimensional Turbulent Boundary Layer of a Prolate Spheroid

GRANTS: N00014-91-1-1732 and N00014-94-0092.

# Table Of Contents

# Table Of Figures

# Table Of Tables

# Nomenclature

2DTBL .....Two-Dimensional Turbulent Boundary Layer

3DTBL .....Three-Dimenstional Turbulent Boundary Layer

$a_1$ .....Structural parameter

$\beta_i$ .....Weighted population percentage in octant i.

$\alpha_f$ .....Flow angle.

$\alpha_{fg}$ .....Flow gradient angle.

$\alpha_\sigma$ .....Intensity angle.

$\alpha_\tau$ .....Shear stress angle.

$\alpha_v$ .....Mean QSV direction.

$\alpha_{wc}$ .....Angle from free-stream to wall collateral coordinates.

$C_f$ .....Skin friction

$C_{f\text{-}0}$ .....Skin friction computed without wall refinement.

$C_{f\text{-}\Delta y}$ .....Skin friction computer with wall refinement.

$\delta$ .....Boundary layer height

$\Delta y$ .....The wall refinement

DNS .....Direct Numerical Simulation

FFT .....Fast Fourier Transform

LDV .....Laser Doppler Velocimeter

PSL .....Polystyrene latex

QSV .....Quasi-Streamwise Vortex

Re, $Re_L$ .....Reynolds number (length)

$Re_\theta$ .....Momentum thickness Reynolds number

S .....Flow structure parameter, $\tau/v'^2$

TBL .....Turbulent Boundary Layer

TKE .....Turbulent Kinetic Energy

u, v, w .....Instantaneous velocities (x, y, and z axes)

$u^+$, $v^+$, $w^+$ Mean velocities normalized by $u_\tau$

u', v', w' .....Velocity fluctuations (x, y, and z axes)

$u'^2$, $v'^2$, $w'^2$,
u'v', u'w', and
v'w' .....Reynolds stress tensor

$(u'^2)^+$, $(v'^2)^+$,
$(w'^2)^+$, $(u'v')^+$,
$(u'w')^+$, and
$(v'w')^+$ .....Reynolds stress tensor normalized by wall-shear-stress.

U, V, W .....Mean velocities

$U_e$ .....Boundary layer edge 'velocity'

$u_\tau$ .....Wall-shear-stress velocity

$\tau$ .....Shear stress magnitude in a plane tangential to the wall.

$\tau_i$ .....A Reynolds averaged stress in octant i.

$\omega_x$ .....Streamwise vorticity

$y^+$ .....Distance from the wall normalized by the wall-shear stress.

VPI .....Virginia Polytechnic Institute and State University.

# Chapter 1 Introduction

Three dimensional turbulent boundary layers (3DTBLs) demonstrate chaos. This apparently unpredictable behavior is paradoxically described by physical laws; the Navier-Stokes equations (momentum principle), the continuity equation (conservation of mass), and the energy equation (conservation of energy) embody these laws for fluid flow. Given the proper initial conditions, these equations can predict the activity of any 3DTBL. Unfortunately, their complexity prevents timely solutions using modern computers except for the simplest of flows. A simplification must be introduced if general solutions are to be made practical.

Any simplification must have physical significance. Observation of the flow's structure may provide a solid background for uncovering flow relationships that reduce the equations of motion. This paper will examine near-wall coherent structure behavior for a 3DTBL. Prior coherent structure research has focused mainly on 2DTBLs, particularly flow over a flat plate. Robinson (1991) provides a good overview of this research. Numerous experimental techniques have been developed for examining flow coherent structure; these methods can be divided into three categories: flow visualization, multi-probe measurements, and statistical analysis. Flow visualization involves the introduction of a visible marker into the fluid; popular markers are smoke, hydrogen bubbles, and dyes. Multi-probe hot-wire or hot film anemometers provide correlated velocity measurements over multiple points in a plane. Statistical analysis attempts to correlate single point velocity events with structural dynamics. Popular statistical techniques are quadrant analysis (Willmarth & Lu, 1972) and the variable-interval time average (VITA) method (Gupta, et. al., 1971).

Despite the amount of data collected, debate still continues over the structural model of the simple 2DTBL over a flat plate. The debate highlights the limitations of the experimental techniques. The two biggest limitations are observability of the flow field and correlation of velocity events with structural events. None of the techniques can accurately observe a large volume of flow. Although flow visualization methods observe markers as they travel in a volume; recording devices lose depth information and essentially map the flow structures onto a plane (Robinson, 1991; Fleming and Simpson, 1994). Limitations of these recording devices also restrict flow visualization experiments to low Reynolds number flows. A multi-sensor hot-wire anemometer interferes with the flow. The interference forces a minimum separation between probes; thus, the probes cannot observe structures whose length scales are smaller than a certain distance (Robinson, 1991). Many statistical analysis techniques concentrate on only one or two points in the flow field. However, they are also the most flexible in their applicability. Recent advances in Laser Doppler Velocimetry (LDV) techniques can provide data that penetrates the sublayer, even within high Reynolds number flows of engineering interest. Statistical analysis techniques are the only currently viable option for examining the structure of these flows.

Identifying the passage of a coherent structure is only the first step. Structural events must be mapped to flow quantity changes in order to complete the dynamic model of the flow. None of the techniques provides a perfect solution to this problem. The flow visualization techniques

provide good qualitative identification of coherent structures. Only bubble visualization can be used to extract quantitative results; even so, many factors limit the accuracy and type of the quantitative data that can be extracted. These factors include accuracy of recording optics, bubble deformation and dissolution, and differing histories for the flow and the bubbles. Multi-probe, hot-wire anemometers provide moderately accurate quantitative data. Identification of structural events is partly interpretive, based on the expected behavior of coherent structures either observed in flow visualization experiments or existing in a hypothesized structural model. Assuming the accuracy of the coherent structure model, the correlated muli-point measurements obtained from multi-probe anemometers allow a strong mapping between structural and quantitative events. The direction or temporal characteristics of coherent structures unveiled by multi-probe anemometers are difficult to determine since measurements are made only in a plane; thus, results remain open to some uncertainty. Statistical techniques rely entirely on a pre-existing structural model for identification of structural events. The direction and temporal characteristics of a coherent structure cannot be determined; this limits the scope of the results and leaves them open to wide interpretation. Using single point data in statistical analysis provides poor mapping between structural and quantitative events. Such a mapping relies on the assumption of dominance, i.e. coherent structures are the dominant producers of correlated velocity fluctuations. All other velocity fluctuations are random or weakly correlated. However, statistical analysis is the only option available for extracting structural results from highly accurate LDV measurements.

Direct numerical simulation (DNS) of fluid flow has recently become a viable tool for examining flow structure. It carries fewer limitations than the experimental methods. It provides observability of a large volume of fluid with simultaneous velocity measurements. However, current computing technology still restricts the flow to simple geometries at low Reynolds numbers. DNS also has its own problems. The amount of data supplied by DNS is orders of magnitude larger than that typically gathered from experimental techniques. New visualization and analysis techniques have been and continue to be developed for interpreting the data. The fidelity of these simulations also remains in doubt. These simulations have shown good correlation with known mean velocity and Reynolds stress measurements. However, the uncertainty surrounding structural experiments makes it difficult to determine whether simulated coherent structures match reality. Simulation of an experiment provides the simplest verification solution; unfortunately, such a simulation introduces complications such as mixed fluids (e.g. markers) or complex geometries (e.g. probes). Nevertheless, DNS studies have provided valuable input into the flow structure debate and have narrowed the possible structural models (Robinson, 1991).

Lack of consensus on the structure of 2DTBLs has not prevented structural experiments using 3DTBLs. These experiments generally concentrate on those aspects of TBL structure for which some agreement does exist, namely quasi-streamwise vortices, wall layer streaks, and the ejection/sweep process. Most experiments are constructed as initial two dimensional flows experiencing imposed three dimensionality downstream making comparisons between 3DTBLs and 2DTBLs simple. These experiments include the swept step and turning channel flows of Flack and Johnston (1993), a revisiting of the turning channel flow by Flack and Johnston (1995), and the wing body junction flow of Fleming and Simpson (1994). Chiang and Eaton (1993)

performed flow visualization on the fully developed 3DTBL of a rotating disk flow. Sendstad and Moin (1992) also produced a DNS study of a 2D channel flow experiencing a sudden spanwise pressure gradient.

Thus far, the use of statistical analysis techniques in examining 3DTBL structures have largely been ignored. The main obstacle in using statistical techniques to examine 3DTBL structures is coordinate system choice. Sendstad and Moin (1992) noted that results from octant analysis (a 3D extension of quadrant analysis) differed depending on the coordinate system chosen. Nevertheless, statistical analysis techniques have important benefits and can significantly contribute to the understanding of 3DTBL structures. They are the only techniques generally applicable to a wide range of flows, particularly high Reynolds number flows of engineering interest. They are the only techniques that can take advantage of the highly accurate data obtained from LDV devices. This paper takes a thorough look at one of these techniques, octant analysis. The paper examines application issues including coordinate system choice and compares the octant analysis results with other recent studies in 3DTBL structure.

This paper uses the LDV data of Chesnakas, Simpson, and Madden (1994); this data was taken on the leeward side of 6:1 prolate spheroid inclined at 10°. It is one of the few data sets that reaches down to the sublayer ($y^+ \sim 7$-11) in a high Reynolds number flow ($Re_L \sim 4.2 \times 10^6$). This was made possible by the novel construction of the LDV probe used in the experiment. The three component LDV probe, developed by Dr. Christopher Chesnakas (Chesnakas & Simpson, 1994), was placed inside a 6:1 prolate spheroid model. It examined the flow through a plexiglass window grafted onto the surface of the model. This setup nearly eliminates the relative motion that would exist between the model and the measurement volume if the probe were external to the model.

# Chapter 2 Facilities And Instruments

## 2.1 Stability Wind Tunnel

The LDV data examined in this paper was gathered in the Stability Wind Tunnel located at Virginia Polytechnic Institute and State University. The Stability Wind Tunnel is a continuous return, subsonic wind tunnel. A 600 HP fan, 4.27 m in diameter, provides a maximum speed of 80 m/s in the 1.8 x 1.8 m test section which is 25 m long; this fan was recently fitted with new blades. Downstream of the fan, an air exchange tower stabilizes the flow temperature to the local atmospheric temperature. The flow then passes through seven anti-turbulence screens in the settling chamber and a 9:1 contraction ratio nozzle. Together, they limit the turbulence level of the test section flow to 0.03% with another 0.03% due to unsteadiness. Vortex generators and a diffuser of 3° slope follow the test section. Streamlined turning vanes occupy the diagonal of every corner in the wind tunnel loop to reduce swirl. An airtight test and control room enclose the test section to minimize air exchange with the test section, since the total pressure in the test section equals atmospheric pressure.

## 2.2 6:1 Prolate Spheroid Model

The axis of the model is 1.37 m in length, and its maximum diameter is 0.229 m. Three hollow sections link to form the model whose shell consists of 6.3 mm of fiberglass bonded to an aluminum frame. The center piece contains supports for a sting. The forward and aft sections are identically constructed; interchangeable nose and tail pieces connect to their ends. The tail allows the sting to pass through the model and mate with the center section.

A 0.75 mm thick Plexiglas window occupies a 30 x 150 mm portion of the aft section to allow optical penetration of the LDV beams into the flow. This window, molded to the curvature of the model, is mounted flush with the model surface to within 0.1 mm. Wax, applied to the window's edges, smoothes away any steps between the model and window surfaces. At x/L = 0.2, an acrylic-post trip dots the circumference of the model. Each 1.2 mm diameter post stands 0.7 mm high at a spacing of 2.5 mm. The trip stabilizes the laminar/turbuletn transition location.

## 2.3 LDV Probe

The three component, fiber-optic LDV probe (Figure 69) was designed and constructed in the AOE department of Virginia Tech (Chesnakas and Simpson, 1994). The probe measures three simultaneous, orthogonal velocity components. The three correlated velocities allow direct calculation of the Reynolds stress tensor. The compact design places the transmitting and receiving optics inside the model. This design produces three advantages over external devices. The probe does not disturb the flow. The probe is physically close to the measurement volume; thus, the use of short focal length optics maximizes the signal-to-noise ratio. Since the probe is attached to the model frame, relative motion between the measurement volume and the model is negligible.

The probe head is mounted on a two component traverse that remotely positions the probe to a limit of $\pm$ 2.5cm along both the model axis and radius. A cable connected to the lead screw of a linear stage controls axial movement. A rotary-encoded servo-motor, which produces 20,157 encoder counts per centimeter, drives radial movement. Repeatability of radial position is $\pm$ 10μm. The probe and traverse assembly weighs 1.1 kg and occupies a volume of 21 x 11.7 x 8.25 cm. An etalon-tuned, argon-ion laser produces the light for the probe. A series of mirrors and prisms splits the laser light into five separate beams; three are green (514.5 nm) and two are blue (488 nm). Bragg shifting differentiates similarly colored beams. The green beams experience shifts of -27 MHz, 0 MHz (unshifted), and +40 MHz. One blue beam is shifted +40 MHz; the other remained unshifted. Single-mode, polarization-preserving fibers direct the beams to the probe.

The probe supports three sets of optics; two transmit and the third receives. The transmission assemblies, each with a lens of focal length of 88 mm, focus the 1.1 mm diameter, collimated beams to intersect a volume 55 μm in diameter. The resulting fringe spacing is 5 μm. The optics direct the beams through the model window at an angle of 45° and p-polarize the beams with respect to the window; this reduces reflections. Each of the transmission optics handles beams of a single color. The green beams measure two orthogonal velocity components. The blue beams detect the third orthogonal component (see section 4.2.2 Probe Coordinates). The 60 mm, f/2.4 receiving assembly collects back-scattered light at 45° to both of the transmission optics. This off-axis angle prevents the entrance of direct, beam reflections off the window.

A 62.5 μm gradient index fiber leads the light to two photomultiplier tubes. A dichroic filter separates the captured light into its green and blue components. Three Macrodyne FDP3100 frequency domain signal processors manipulate the photomultiplier output. These processors perform a fast Fourier transform (FFT) on each incoming Doppler burst to extract the peak frequency. The processors can communicate with each other to force coincidence criteria on all three signals; therefore, the Macrodynes automatically correlate the three velocity components. A DOSTek GPIB acquisition board, plugged into a 386SX/20 PC, collected the Macrodyne output; accompanying software recorded the data into a DOS file.

## 2.4 Seeding System

Dr. Christopher Chesnakas designed the seeding system. The seed consisted of polystyrene latex (PSL) spheres 0.7 μm in diameter. One part 6.5% wt. PSL solution was mixed with 280 parts ethanol. Two Spraying Systems Incorporated air-atomizing paint spray nozzles introduced this mixture to the tunnel just downstream of the anti-turbulence screens. The ethanol would quickly evaporate, leaving a cloud of PSL that expanded around the model to a height of about 10 cm.

## 2.5 Miscellaneous

A Pitot-static tube with a Datametric Model 1173 manometer measured the free-stream dynamic pressure. A Valdyne Model DB99 digital barometer indicated the static pressure in the test section. An Instrulab Model 1563 digital thermometer displayed the free-stream temperature.

# Chapter 3 Experimental Techniques

## 3.1 Model Geometry And Measurement Location

Before discussing the experimental techniques, the nomenclature used to describe the 6:1 prolate spheroid and the measurement locations must be established. The model used in this study is a 6:1 prolate spheroid (Figure 3.1). The rotation of an ellipse about its major axis creates the volume enclosed by a prolate spheroid. The 6:1 ratio designates that the major axis of this ellipse is six times longer than its minor axis. Throughout this paper, the 'major axis' (L) and the spheroid's 'axis' are synonymous. Any plane that intersects the model perpendicular to its axis reveals a circular cross section.

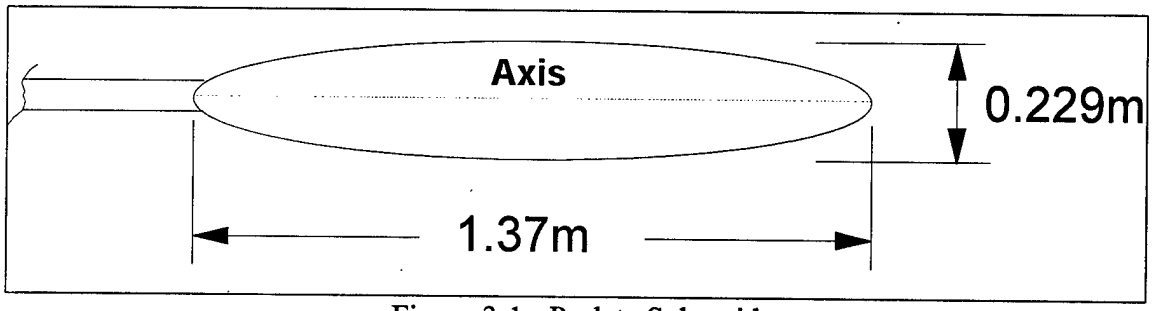


Figure 3-1: Prolate Spheroid

Three quantities define location of the measurement volume with respect to the model (Figure 3.2): the percentage axis position (x/L), its distance from the model surface (r or y), and an angle ($\phi$). A line, perpendicular to the axis, can connect with the center of the measurement volume. The distance between the line and the nose of the model is x. The volume hovers above the percentage of the axis, x/L. R (or y) is the distance, along this line, from the volume's center to the model surface. A plane containing the line and perpendicular to the axis cuts a circular cross section of the model. One radius points directly to the model's windward side. The angle that runs from the windward radius to the radius, which intersects the measurement volume, is $\phi$.

Throughout this paper, a shorthand notation is used to identify the radial and axial coordinates of the measurement location. This shorthand combines the radial location $\phi$ with a character representing the axial location. The valid characters are 'a' (x/L = 0.7722), 'b' (x/L = 0.7622), and 'c' (x/L = 0.7522). (The characters are allocated from the greater to smaller axial location because that was the order in which the data was collected.) Thus, the profile designation, 123b, identifies $\phi = 123°$ and x/L = 0.7622.

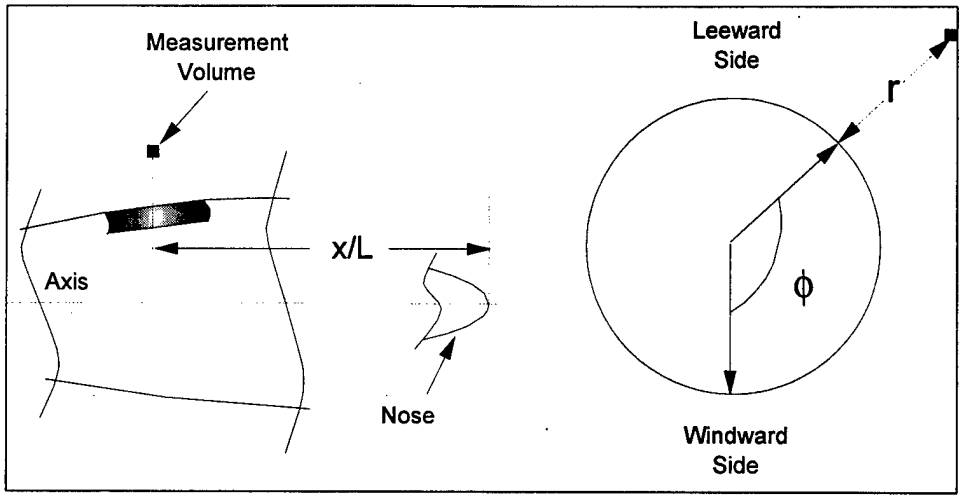

Figure 3-2: Measurement Location

## 3.2 Calibration

The edge of a rotating wheel of known diameter and angular velocity was placed before the LDV probe. The signal frequency produced by the scattered light allowed calibration of the fringe spacing to ±0.5%. This translates to an identical uncertainty in the velocity measurements. To calibrate the radial positioning of the traverse, the measurement volume was lowered until it touched the model window. The signal processing instruments could not determine this event; as the measurement volume gets closer to window, the glare off the model window from the five beams converges and floods the receiving optics. The small signal-to-noise ratio makes it difficult to recognize the Doppler burst that should occur when the measurement volume enters the window. Instead, the beam reflections were examined using a magnifying lens from an angle tangent to the window surface. When the reflections overlap, the measurement volume is coincident with the surface. The estimated uncertainty of this procedure is one third the diameter of the measurement volume, ±19 μm. The expansion (or contraction) of the model with temperature change also contributes to the position uncertainty. The tunnel has no controls for maintaining a predefined temperature. The ambient temperature in the tunnel behaves as the local atmospheric temperature outside the tunnel facility. It rises as much as 20°F from morning to mid-afternoon and drops an equivalent amount by nightfall. To minimize the impact of the model expansion and contraction, the radial position of the probe was re-calibrated under the following conditions: every morning, before measurements were made at $r < 0.04$cm, a 5° or greater change in temperature since the last calibration, and every time the model was rotated. Overall, the positioning error is large when compared with the distance of the lowest point (100 μm). Therefore, a scheme employing the Spalding continuous law of the wall velocity profile was derived to refine the position of the surface after taking data (section 5).

## 3.3 Test Conditions

All tests occurred at a 10° angle of attack and a Reynolds number of $4.2 \times 10^6$ (based on the model axis and the tunnel velocity). Three axial locations (x/L= 0.7522, 0.7622, and 0.7722) were examined. Surface oil flow visualization (Ahn, 1992) had shown that primary separation occurs at approximately 123°. Because of a desire to view the development and effects of separation, boundary layer profiles were taken at the circumferential positions shown in Table 3-1. Unfortunately, a later paper by Wetzel, Simpson, and Chesnakas (1997) would show that oil flow visualizations under-predict the separation location. That paper established a revised separation location of ~140°, beyond any of the locations measured in the experiment.

**Table 3-1: Measurement Locations**

| x/L | ϕ Location | | | | | | |
|---|---|---|---|---|---|---|---|
| | 105 | 110 | 115 | 120 | 123 | 125 | 130 |
| 0.77 | x | x | x | x | x | x | x |
| 0.76 | | | | x | x | x | |
| 0.75 | | | | x | x | x | |

Throughout this paper, the measurement locations are identified using an abbreviated scheme. The abbreviation consists of the ϕ location followed by a single character representing the x/L location. The valid characters are 'a' (x/L = 0.7722), 'b' (x/L = 0.7622), and 'c' (x/L = 0.7522). For example, profile 123a refers to the measurement location: ϕ = 123° and x/L = 0.7722.

Fourteen logarithmically spaced locations form each profile. They run from 0.01 cm to 2.5 cm; Table 3-2 lists these radial positions.

**Table 3-2: Radial Locations**

| R (cm) | Missing at Location(s) |
|---|---|
| 0.01 | |
| 0.02 | x/L= 0.7722 ϕ= 125° & 110° |
| 0.02 | |
| 0.03 | |
| 0.04 | |
| 0.08 | |
| 0.15 | |
| 0.25 | |
| 0.50 | |
| 1.00 | |
| 1.50 | |
| 2.00 | |
| 2.50 | x/L= 0.7722 ϕ= 130° |

A collection of 16,384 velocity vector (u, v, w) measurements were the goal for each point. However, problems arose at r = 0.01 cm and 0.015 cm. For some profiles, the data rate of the lowest points became very small (< ~100 measurements/second). At this rate, seed would accumulate on the model window; and laser reflection off these particles would enter the receiving

optics. The signal processing system would produce a continuous stream of zero velocity vectors. These erroneous values would later be removed from the data using a computer program; thus, the number of valid measurements would be reduced below 16,384. Occasionally, the seeding system would empty in the middle of a run. If the amount of data taken at that point was close to the goal (~11K or greater), then the data would not be retaken.

A summary of the data collection process follows. First, the probe would be remotely commanded to the next radial position. Then the tunnel velocity would be adjusted, according to the tunnel temperature and static pressure readings, so that the Reynolds number remained constant. The seeding system would be turned on. The downmix frequencies would be modified so that the initial signals fell into the middle of the Macrodyne processors' frequency range. (This was accomplished by either viewing the FFT's on the processor LCD displays as they were produced or by using the vendor-supplied software to construct dynamic histograms.) Next, the DOSTek board was commanded to collect the data and write it to a file. That file would immediately be run through a program written by the author called LDVS (LDV Statistics). The program generated velocity statistics (means, variances, etc.) and histograms. The histograms would be used to verify that no severe "clipping" had occurred (i.e., no important frequencies fell beyond the range of the processors because the downmixing frequencies were not maximally set). If clipping had occurred, the downmixing frequencies would be changed accordingly and the data would be retaken. For every three points (also, at r= 0.01cm, r= 0.015cm, and when the model was turned to the next $\phi$ location), the tunnel fan was turned off so that the model window could be cleaned; and the seed system was refilled.

# Chapter 4 The Flow Field

The prolate spheroid (section 3.1) is a simple geometry that produces a well-defined 3DTBL on its leeward side when inclined at a positive angle relative to the flow. Figure 68 illustrates the general flow characteristics. The flow separates from the leeside of the prolate spheroid at the point marked $S_1$. The separated flow rolls up into a strong primary vortex which induces a number of smaller secondary vortices. The flow reattaches at $R_2$ and $R_1$. The flow field is symmetrical about the x-z plane.

The prolate spheroid flow has been studied by a number of groups over the past two decades. Previous experiments at the DFVLR recorded surface flow, surface pressure, skin friction, mean velocity, and Reynolds stress tensor for a prolate spheroid at $Re_L$ = 7.7E+06: Meier and Kreplin (1980), Kreplin, Vollmers, and Meier (1982 and 1985) and Kreplin and Stager (1993). Similar data was recorded in a cooperative venture between Italian and Chinese researchers: Iuso, et. al. (1988). Barber and Simpson (1991) used hot-wire anemometry on an untripped model to obtain velocity-field and turbulence measurements along four cross sections (x/L = 0.6 - 0.9) containing the primary separation line. Ahn and Simpson (1992) used oil flow visualization to capture the cross-flow separation and examine the affect that Reynolds number and angle of attack have on it. Fu, Shekarriz, Katz, and Huang (1992) observed the affects that Reynolds number and boundary layer tripping had on the leeside flow field. Because of the prolate spheroid's rich set of accumulated data, AGARD (1990) used it as the primary test case for its evaluation of 3D computational models. Gee and Cummings (1992) expanded on this evaluation by testing Baldwin-Lomax and Johnston-King models with "3D extensions". The modified models produced better predictions of separation; but, they also emphasized the need for better experimental data, from which more refined assumptions can be extracted.

## *4.1 The LDV Data Set*

The LDV data set examined in this paper covers a small area near the separation point of a 6:1 prolate spheroid (x/L = 0.7522 - 0.7722, $\phi$ = 105° - 130°). This data was gathered in the fall of 1992. The data set was expanded the following year to include data at x/L = 0.4 and 0.6. Chesnakas, Simpson, and Madden (1994) produced a comprehensive catalogue of the LDV data's characteristics; this catalogue can also be found in the *Journal of Fluids Engineering* data bank. The measurement area was chosen based on the oil flow visualization results performed on the same model by Ahn, et. al (1992) and earlier hot-wire anemometer data taken by Barber, et. al (1991). These experiments identified the primary separation line within the area covered by the LDV data. However, later work by Wetzel, et. al. (1997) would show that the true separation location occurs further leeward, $\phi \approx 140°$ at x/L = 0.77.

The data has been the subject of numerous papers at VPI. An early paper by Chesnakas and Simpson (1994) showed good agreement between Barber's results and the LDV data presented here. Barber's hot-wire anemometer data described only the outer boundary layer due to physical limitations of the instrument; thus, his data could not be used to validate data taken at $y^+ < 100$.

Two other papers by Chesnakas and Simpson (1994b and 1996a) concentrated on the LDV device and the inner layer data obtained from it. Chesnakas and Simpson (1994a) used the LDV data to show that the structural parameter $a_1$ was related to Reynolds number, flow angle, and position. They also examined terms in the TKE equation and showed that commonly neglected production terms are significant for $y^+ > 100$. Chesnakas and Simpson (1996) further expanded the LDV data set to better observe data in the vicinity of the primary vortex. They discovered that fluid which lies between the primary vortex and separation sheet has low velocity and low turbulence. As mentioned earlier, Wetzel, et. al. (1997) used the LDV data in a survey of separation-identification techniques. The LDV data was among the data sets surveyed by Ciochetto and Simpson (1995) for similarities in v' related Reynolds averaged products.

## 4.2 Coordinate Systems

Before discussing the measured flow field, the coordinate systems used in the discussion must be established. Coordinate system choice is very important in analysis of 3DTBLs because the stress, gradient, and flow angles have differing directions. Five coordinate systems are used throughout this paper; they are tunnel coordinates, probe coordinates, body surface coordinates, free-stream coordinates, and wall-collateral coordinates. All these coordinate systems are orthogonal and follow the right hand rule. (See Figures 4.1-4.5 for graphic display of these axis systems.)

### 4.2.1 Tunnel Coordinates

The tunnel axis system serves as an inertial reference for the other coordinate systems described in this paper. The $X_T$ axis of the tunnel coordinate system points in the direction of the oncoming flow. The $Y_T$ axis juts upwards, perpendicular to the tunnel floor. The $Z_T$ axis completes the right handed system.

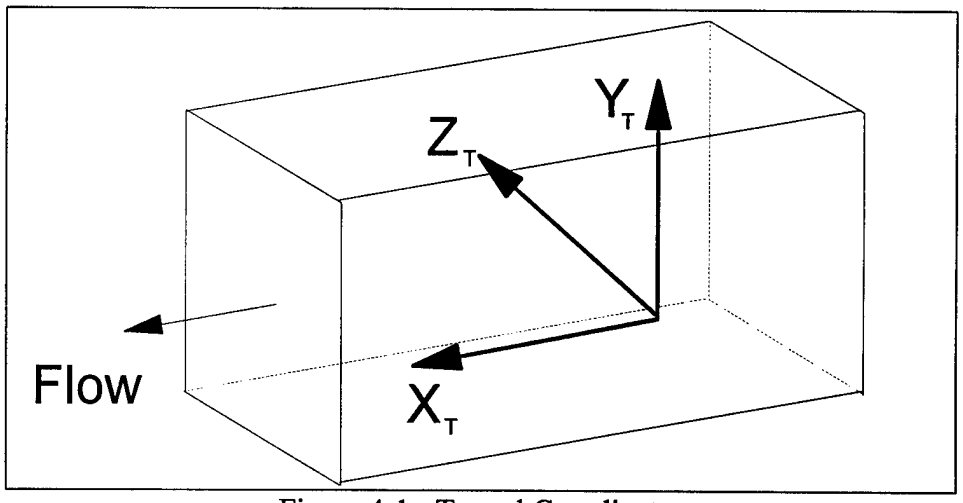


Figure 4-1: Tunnel Coordinates

### 4.2.2 Probe Coordinates

The LDV probe measures the flow velocity in three orthogonal directions. These directions define the probe coordinate system. Since the probe is mounted within the model, this axis system is fixed to the body. The $X_P$ axis and the model axis lie in the same plane, but the $X_P$ axis is rotated 45° away. It points into the oncoming flow. The $Y_P$ axis lies on this plane, rotated 135° from the axis. The $Z_P$ axis is tangent to the model circumference, directed opposite of increasing $\phi$. Later evaluation of the data showed a small V component near the wall at x/L= 0.7622 and 0.7522 in body surface coordinates. V should approach zero. Examination of the probe assembly revealed a screw that was not properly tightened; this compromised the rigidity of the mount. The added rotation required to bring V to zero was the same at each x/L station. Apparently, the $X_p$ axis is rotated 46° away from the model axis at x/L= 0.7622 and 46.6° away at x/L= 0.7522. This derived misalignment increases the uncertainty of quantities within the X-Y plane of the body-fixed coordinate systems presented here.

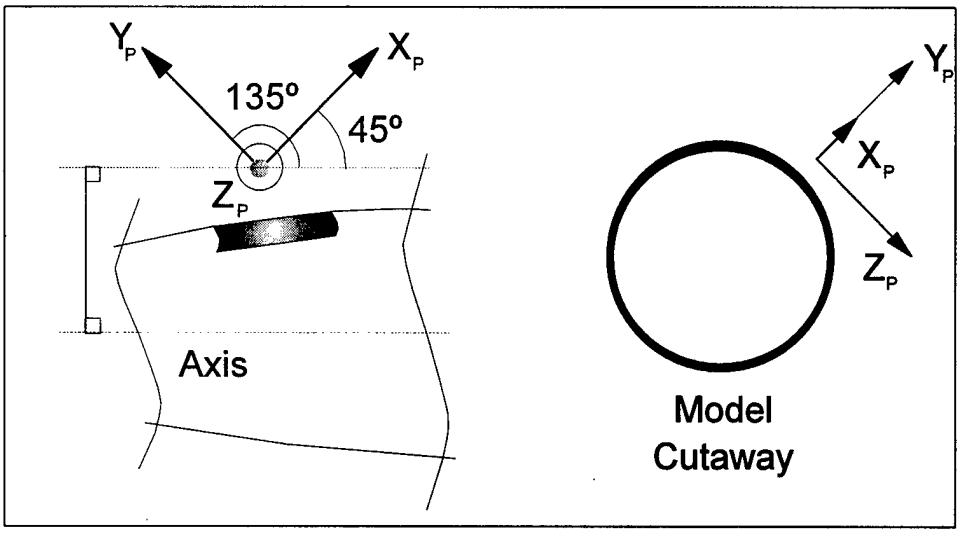


Figure 4-2: Probe Coordinates

### 4.2.3 Body-Surface Coordinates

This body-surface coordinate system aligns itself with the surface of the model. The $Z_{BS}$ axis runs tangent to the model circumference (in the opposite direction of the probe coordinate $Z_{BS}$ axis). The $Y_{BS}$ axis points perpendicular to model surface. The $X_{BS}$ axis follows the curvature of the model, in the direction of the tunnel flow.

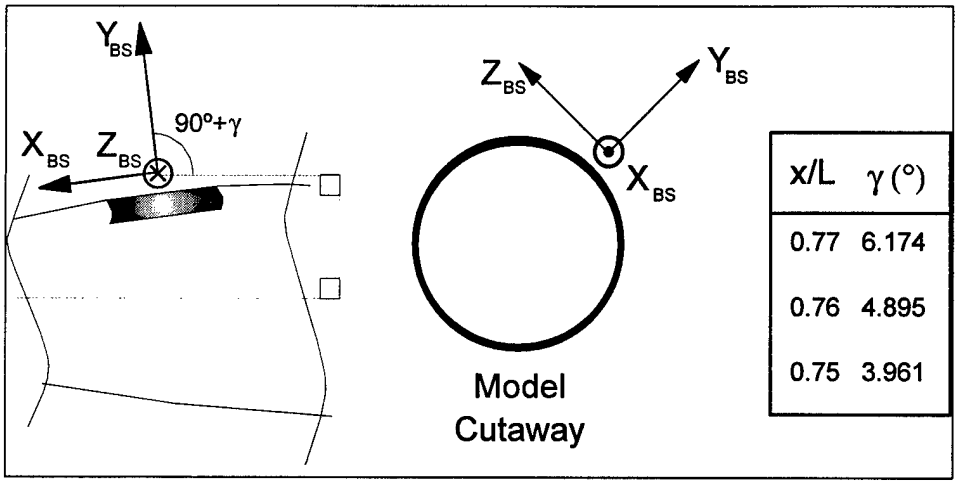


Figure 4-3: Body-Surface Coordinates

### 4.2.4 Free-Stream Coordinates

The free-stream coordinate system is obtained by rotating the body surface system about $Y_{BS}$. The $X_{FS}$ axis is positioned so that there is no mean spanwise velocity component (velocity along the $Z_{FS}$ axis) at the boundary layer edge. Therefore, the angle of rotation, $\theta_{FS}$, equals $\tan^{-1}(W_e/U_e)_{BS}$.

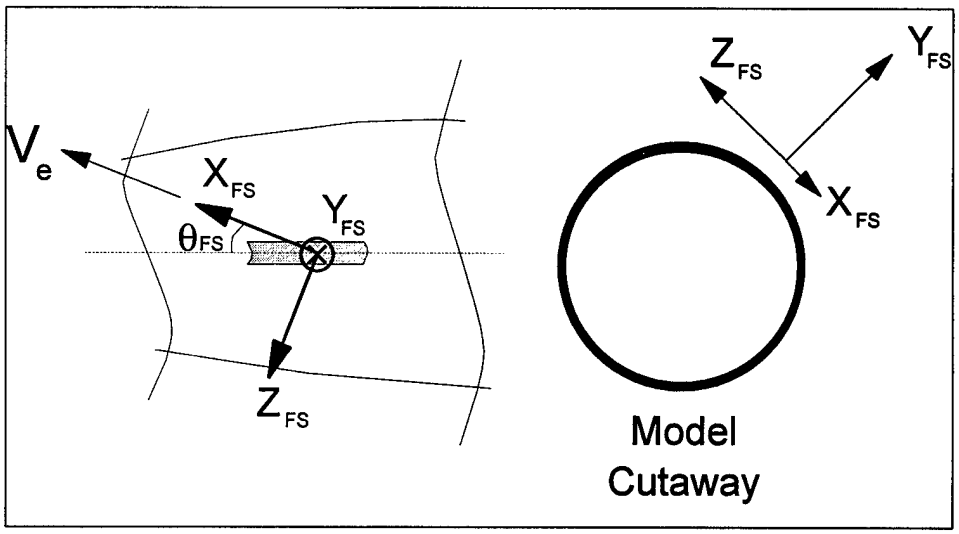


Figure 4-4: Free-stream Coordinates

### 4.2.5 Wall-Collateral Coordinates

In the viscous sublayer, the flow becomes collateral (i.e., mean 2D flow). Datum has been taken close enough to this region that it approximates a collateral flow (see section 4.4.1). This allows the use of the Spalding continuous law of the wall to estimate the skin friction coefficient (see sections 5 and D.6). The data shows that the flow angle, $\alpha_f$, does not appreciably change until the

fourth or fifth data point from the wall. Therefore, the third point from the wall is the reference from which to base this coordinate system. Like the free-stream axis system, the wall-collateral coordinate system is derived by rotating the body surface system about $Y_{BS}$. The rotation angle, $\theta_{QC}$, equals $\tan^{-1}(W_3/U_3)_{BS}$. This coordinate system is very close the normal stress coordinate system used by Olcmen (1991) in analysis of the wing-body junction flow. The normal stress coordinate system aligns its X axis in the direction of the local mean velocity at the y location were $u'^2$ is a maximum. For the profiles under study here, that location appears within the bottom three points. These coordinate systems are good references for the study of the flow characteristics in the buffer region and log layer.

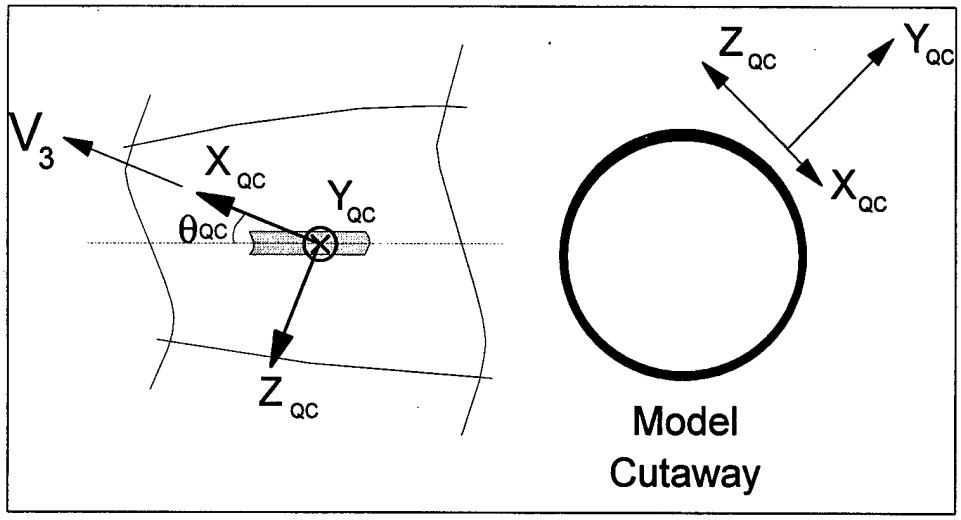


Figure 4-5: Wall-Collateral Coordinates

## 4.3 Boundary Layer Regions

In this discussion, the boundary layer will separated into four regions as defined by Kline (1992): the sublayer ($0 < y^+ < 7\text{-}10$), the buffer layer ($7\text{-}10 < y^+ < 30\text{-}40$), the log layer ($30\text{-}40 < y^+ < 100$), and the wake or outer layer ($y^+ > 100$). Collectively the first three regions are considered the inner layer. Much of this paper will focus on data in the buffer layer.

## 4.4 Characteristics Of The Measured Flow Field

Several methods were used to reduce the raw LDV data into time averaged quantities (mean flow, Reynolds stresses, and gradients) which were normalized using the skin friction. Velocity bias in statistical averages of the raw LDV data was corrected using an inverse-of-the-speed weighting factor proposed by McLaughlin and Tiederman (1973). Spatial bias, a.k.a. gradient broadening, was corrected using formulas created by Durst, Martinuzzi, Sender, and Thevin (1992). A Spalding law-of-the-wall equation was used not only to estimate the skin friction, but also to adjust the wall position which was calibrated using aided, human sight. A detailed justification of this post-processing technique is the subject of the next chapter. Velocity and Reynolds

stress gradients were computed using parabolic fits along five data points. The appendices contain more detailed information about reducing the LDV data set. In particular:

**Appendix A** describes the data reduction methods. It discusses corrections for velocity and spatial bias present in LDV measurements. It includes all of the techniques and formulas used to produce the information displayed in the figures.

**Appendix B** describes the uncertainty analysis. Uncertainties are reported for the position, mean flow, the Reynolds stress tensor, and gradients of the mean flow and Reynolds stress tensor.

### *4.4.1 General Characteristics*

The data set consists of thirteen closely spaced profiles. Thus, the boundary layer edge velocity changes little in strength and direction across profiles. The free-stream direction, with respect to body-surface coordinates, decreases with increasing $\phi$ and with decreasing axial location (x/L). At profile 105a, the free-stream direction is 16.7°; at profile 125c, the free-stream direction is 12.6°. The magnitude of the free-stream velocity ($U_e$) has no discernible pattern; its ratio with respect to the tunnel velocity ($U_\infty$) varies from 1.015 (at profile 123a) to 1.034 (at profile 125c). Other boundary layer characteristics experience larger changes across profiles. The boundary layer thickness (figure 66) increases with increasing $\phi$ and with increasing x/L. One exception is the values along x/L = 0.7622; they are larger than those at the other two axial locations given the same $\phi$ location. The boundary layer thickness ranges from 0.9 cm for 105a to 1.9 cm for 130a. The momentum thickness behaves similarly; its values range from 0.12 cm for 105a to 0.30 cm for 130a. The resulting momentum number Reynolds thickness ($Re_\theta$) varies from 3800 to 9400. The skin friction coefficient (figure 64) follows the opposite pattern. It generally decreases with increasing $\phi$ and with increasing x/L. Its value ranges from 0.0029 at 105a to 0.0016 at 130a.

Figures 1-12 present the mean velocity profiles in both wall-collateral coordinates (see section 4.2.5) and free-stream coordinates (see section 4.2.4). These profiles are normalized by the shear stress velocity. In both coordinates systems, the streamwise velocity profiles (U) monotonically increase to a peak value at the boundary layer edge. The streamwise profiles are very tightly packed for $y^+ < 600$; thus, they exhibit inner-layer self-similarity. The same is not true for the spanwise velocity profiles (W). In free-stream coordinates, the spanwise velocity contains a bulge, a common feature in pressure-driven 3DTBLs. The size and location of the bulge's peak varies considerably among the profiles. At 105a, the peak spanwise velocity is $w^+ = 1.1$ at $y^+ = 32$. At 130a, the peak spanwise velocity is $w^+ = 4.6$ at $y^+ = 125$. In wall-collateral coordinates, the spanwise velocity monotonically decreases to a peak negative value near the boundary layer edge. The magnitude of the peak varies from $w^+ = -2.5$ at 105a to $w^+ = -12$ at 130a. The wall-collateral profiles of spanwise velocity also exhibit a near-zero value for $y^+ < 50$. The flow region is collateral; i.e., the flow angle remains nearly the same value, zero. This is the reason for naming the coordinate system "wall-collateral". The Johnston Hodographs (Figures 43 and 44) further illustrate the collateral feature of the near-wall flow. A straight line, starting at the origin, nearly

connects the first four to six points on the hodograph profiles. The line represents a constant ratio of W to U; thus, it also represents a constant flow angle. The normal velocity profiles (V) lie about zero in the inner layer ($y^+ < 100$). In the outer layer, V monotonically increases to boundary layer edge (except for profile 105a, where there is a slight drop between points 9 and 10). Given that V and W are close to zero for $y^+ < 50$, the wall-collateral coordinate system is nearly aligned with streamline coordinates in this region. Thus, U approximates the mean-velocity streamline.

Figures 13-34 present the Reynolds stress profiles in both wall-collateral and free-stream coordinates. These profiles are normalized by the skin friction velocity. Under both coordinate systems, $u'^2$ peaks in the buffer layer. The peak values lie in a small range: 7.0 (at 105a) to 8.2 (at 123b) for wall-collateral coordinates and 7.0 (at 105a) to 7.8 (at 123b) for free-stream coordinates. $v'^2$, by contrast, peaks in the outer layer. The wider range of peak values run from 1.4 (at 105a) to 2.0 (at 130a). $w'^2$ also peaks in the outer layer although its peak is less pronounced than the other two normal stresses. The peak values run from 2.4 (at 105a) to 4.2 (at 125a) in wall-collateral coordinates and from 2.3 (at 105a) to 3.8 (at 125a) in free-stream coordinates. Thus, $u'^2$ is the dominant normal stress in the buffer layer where it can be up to four times larger than $w'^2$ and an order of magnitude larger than $v'^2$. In fact, the Reynolds normal stress is concentrated along a plane tangential to the wall in the buffer layer. As one moves into the log and outer layers, $u'^2$ decreases as $w'^2$ increases and $v'^2$ climbs dramatically. In the outer layer, $w'^2$ approaches (and sometimes surpasses) the strength of $u'^2$; $v'^2$ grows to slightly less than half the size of $u'^2$. In the outer-layer, the Reynolds normal stress, thus, becomes more uniform in space.

The Reynolds shear stresses are nearly an order of magnitude smaller than the normal stresses. The u'v' stress profiles do not have a clearly distinguishable peak; they appear to remain nearly flat for $30 < y^+ < 300$, dropping dramatically on either end. Most of the measurements lie between 0.8 and 1.1 in the "flat" region. The remain two shear stresses behave very differently between free-stream and wall-collateral coordinates. In wall-collateral coordinates, u'w' reaches a positive peak in the outer layer; then it gradually decreases until it crosses zero in the lower buffer layer. The peak value of u'w' ranges from 0.17 (at 105a) to 0.74 (at 130a). v'w' does the opposite. It decreases to a negative peak in the outer layer, then gradually decreases toward zero as one approaches the wall. Its peak value varies from 0.16 (at 105a) to 0.55 (at 130a). Throughout the boundary layer u'w' and v'w' are the same order of magnitude, and both are much smaller than u'v'. In free-stream coordinates, u'w' initially increases to a small positive peak in the outer layer then drops dramatically to a larger negative peak the lower buffer layer. The negative peak ranges in value from -0.38 (at 105a) to -2.0 (at 130a). v'w' behaves very differently. It begins with a positive value and quickly declines to a negative peak in the outer layer. For the majority of profiles, v'w' crosses zero again in the log layer; it achieves a positive peak in the buffer layer before decline toward zero at the wall. The positive and negative v'w' peaks are same order of magnitude; v'w' lies between -0.2 and 0.2. The free-stream u'w' becomes larger than u'v', $v'^2$, or $w'^2$ in the lower buffer layer; however, u'v' becomes the dominant shear stress in the log and outer layer.

Figures 35-60 present profiles for a variety of derived quantities: the structural parameter, the velocity defect, turbulent kinetic energy (TKE), Johnston Hodograph, shear stress angle difference, anisotropy constant, flow angle, shear stress angle, gradient angle, intensity angle, and flow structure parameter $S_1$ (see Appendix A). Many of these quantities have been analyzed in the papers cited in section 4.1. In particular, Chesnakas and Simpson (1994) discuss the $a_1$ parameter, Johnston hodographs, and TKE. Ciochetto and Simpson (1994) examined the $S_1$ parameter. These derived properties are presented here for completeness and because many are referenced in later chapters. Some of these quantities are analyzed in the next section for what they indicate about the three dimensionality of the flow.

### 4.4.2 Three-Dimensional Characteristics

The main measurements of three dimensionality are the maximum spanwise velocity and the maximum flow angle, both in free-stream coordinates. The Johnston Hodographs (Figures 43 and 44) provide the best illustration of the maximum spanwise velocity. The hodographs show that the spanwise velocity peak grows from ~4% $U_e$ at profile 105a to ~13% $U_e$ for profile 130a. The peaks occur between U/Ue of 0.45-0.5 which usually corresponds to a position in the log layer ($30 < y^+ < 100$). Figure 49-50 show the flow angle in wall-collateral coordinates. The flow angle peak grows from ~ -6° at 105a to ~ -19° at 130a. The gradient, shear, and intensity angle also provide an indication of the degree of three-dimensionality. In 2DTBLs, these three angles are all zero. Figures 51-56 display the values of these angles in wall-collateral coordinates. The gradient-angle peak ranges from ~ -14° at 105a to ~ -38° at 130a. The shear stress angle peak grows from ~ -10° at 105a to ~ -32° at 130a. The intensity angle peak increases from ~ -13° at 105a to ~ -40° at 130a. Of particular interest is the difference between the gradient and shear angles. This difference, illustrated by Figures 45 and 46, reflects the anisotropy of the flow; isotropic flow would have a difference of zero. 2DTBLs are isotropic; most 2DTBL closure models poorly predict 3DTBL flow features (e.g., separation) because they assume the flow is isotropic. In the outer layer, the gradient angle lags behind the shear stress angle; however, in the buffer layer, the opposite is true. Only in the log region does the difference, within uncertainty, come close to zero.

The anisotropy "constant" is a direct measure of the anisotropy of the flow. Figures 47 and 48 display the anisotropy constant. The flow is nearly isotropic for only a small portion of the boundary layer ($0.05 < y/\delta < 0.4$). Very close to the wall ($y/\delta < 0.04$) the anisotropy constant diverges rapidly. In fact, the lowest points in the profile frequently had to be extracted from the plots because they dwarf all other points. Tables 8-1 and 8-2 list the missing points. The anisotropy constant also diverges high in the outer layer ($y/\delta > 0.5$). The last indicator of three dimensionality is the $a_1$ structural parameter. For all 2DTBLs, $a_1$ reaches a level peak of 0.15. In 3DTBLs, the $a_1$ peak is smaller. In the current experiment, the $a_1$ peak (Figures 35-36) exists between 0.09 and 0.12. Overall, the 3D "indicators" verify that the flow field is populated with 3DTBLs of moderate crossflow.

# Chapter 5 The Wall Law Correction

In two dimensional turbulent boundary layers, the friction velocity is a correlation factor that collapses the velocity profiles. The resulting plot of the velocity profiles reveals a function dependent on radial distance from the wall alone. The best approximation to this function, from the wall to the free-stream, is the Spalding continuous wall law (eqn 5.2). Finding such a correlation for three dimensional turbulent boundary layers is much desired. Naturally, work has focused on finding 3DTBL wall laws based on the friction velocity. Olceman and Simpson (1992) provide a good overview of the proposed wall laws for 3DTBL's and tests them against a number of data sets. Their conclusion was that no law is adequate for all flows but that the Spalding wall law worked for a majority in a modified form (eqns 5.3 & 5.4). The work of Flack and Johnston (1993) and Moin, Shih, Driver, and Mansour (1990) corroborated this find.

$$C_f = \frac{\left|\vec{\tau}\right|}{\frac{1}{2}\rho U_e^2} \tag{6.8}$$

$$y^+ = u^+ + \frac{1}{E}\left[ e^{ku^+} - 1 - ku^+ - \frac{(ku^+)^2}{2!} - \frac{(ku^+)^3}{3!} \right] \tag{5.2}$$

$$y^+ = q^+ + \frac{1}{E}\left[ e^{kq^+} - 1 - kq^+ - \frac{(kq^+)^2}{2!} - \frac{(kq^+)^3}{3!} \right] \tag{5.3}$$

$$q^+ = \sqrt{(u^+)^2 + (w^+)^2} \tag{5.4}$$

The data for this experiment cannot be directly used to further validate the above results. No skin friction measurements were taken, and the lowest data point for each profile remained too far from the wall to obtain a direct calculation of the velocity gradient at the wall. Instead, the cited results are used as justification for applying the Spalding wall law to the data presented here. Originally, only the skin friction coefficient was to be extracted. However, observations, detailed in section 5.1, reveal that uncertainties in the position of the first data point required the application of an analytic adjustment. The Spalding wall law can be rearranged to produce the additional unknown, $\Delta y$, the 'wall refinement'. Section 5.2 discusses recent research, which further supports the idea that application of the Spalding Law to this flow is appropriate. The end result on the data, described in section 5.3, provides compelling reasons to keep this technique. Section 5.3 also elaborates the flaws with this approach, particularly those that apply to this data set. The implementation details of this technique are found in the Appendix B.6.

## *5.1 The Case For Wall Refinement*

The most difficult uncertainty to quantify is human error. Human error is the dominant uncertainty surrounding the position of the first data point from the wall. As explained in section 3.2,

the calibration the position of the measurement volume was done by observation with the aid of a magnifying lens. The estimated uncertainty, based on measurement volume size, was $\pm$ 19μm. However, simple analysis of the data reveals that it is much more.

Although no skin friction measurements were made during this experiment, a team of engineers at Göttingen made direct skin friction measurements on a 6:1 prolate spheroid at a Reynolds number of $7.2 \times 10^6$ (Kreplin, Vollmers, and Meier, 1985). Rough estimates of the skin friction coefficient for the LDV measurement locations were derived from the Göttingen data using linear interpolation. Figure 61 displays the interpolated $C_f$ values. The difference in Reynolds number between the two experiments should not translate to a large difference in $C_f$. Therefore, the interpolated $C_f$ values will be used to normalize velocity and radial distance in our initial investigation of the flow. One immediately finds inconsistencies between the velocity and the radial position at the first measurement point for many of the profiles. The first point falls into the range of $9 < y^+ < 12$; however, the velocity varies widely, $5 < q^+ < 11$. (Figure 65 demonstrates the erratic behavior of $U_l/U_e$; normalization by $u_\tau$ was not used to avoid increased uncertainty.) The $y^+$ values place the first point near the laminar sublayer (where $q^+ \approx y^+$). Here, $q^+$ should hover above nine and the tangential velocity should be well behaved. The wide range of $q^+$ values presents a different picture. Profile 125c displays the most striking disparity. At the first point, $y^+ \approx 9$ and $q^+ \approx 11$. The three neighboring profiles show that $q^+ \approx 8$ (123c), $q^+ \approx 7$ (125b), and $q^+ \approx 6.5$ (123b) at the same position. The most plausible explanation for this inconsistency is human error in calibrating the wall position.

## 5.2 Applying The Spalding Law

One characteristic of this flow that supports application of the Spalding law is the existence of a nearly collateral region in the inner layer ($y^+ < 100$). Figures 49 & 50 show the flow angle in wall-collateral coordinates; the flow angles are close to zero ($< \sim 1°$) for $y^+ < 50$. Degani, Smith, and Walker (1993) mathematically demonstrated that 3DTBLs will develop self-similar collateral regions as Reynolds number approaches infinity. However, for finite but large Reynolds numbers, pressure gradients can cause significant skewing of the flow. This flow does show some skewing for $y^+ < 50$, but the skewing is only slightly larger than the flow angle uncertainty. According to the results of Degani, et. al., this region of flow should approximately demonstrate self-similarity for all the LDV profiles.

The channel flow of Flack and Johnston (1993) further supports this position. They demonstrated the validity of the Spalding relation in the buffer layer ($y^+ < 50$) of this pressure driven 3D turbulent flow. The prolate spheroid flow under study is also a pressure driven 3D turbulent boundary layer; moreover, both flows examined data in which the maximum transverse velocity was less than 15% of $U_e$. Flack's and Johnston's conclusions should equally apply to this flow.

Both mathematical and experimental evidence show the inner layer of this flow should approximately follow a law of the wall relation. The Spalding equation was re-arranged to produce two

unknowns: the skin friction ($C_f$) and the wall refinement ($\Delta y$). The coefficients $k$ and $E$ were replaced with Cole's constants, 0.14 and 5 respectively (Stanford Conference, 1968). The method of least squares was applied using the data points in the wall-collateral region ($y^+ < 40$) in order to solve for $C_f$ and $\Delta y$.

## 5.3 Results Using Wall Refinement.

Figures 64 & 65 show the final results of applying wall refinement to the flow. Figure 64 displays $C_f$ for all the measurement locations. Figure 65 plots $\Delta y$ and $U_1/U_e$. To judge the success of this technique, the values of $\Delta y$ and $C_f$ are judged for realism. Then, the effect of the wall refinement on the plots of $a_1$ were examined and compared with the experimental results of Flack and Johnston (1993).

There is a clear relationship between $\Delta y$ and the erratic $U_1/U_e$ plots. The least-squares solution proportionally shifted the data with respect to the behavior of $U_1/U_e$. This behavior is expected; near the wall, $u^+ \approx y^+$ to leading order. Ten of the thirteen corrections are negative; i.e., the center of the measurement volume was above the plexiglass wall when the calibration was done. A very thin film of residue or spec of dust could blur the beam reflections coming off of the plexiglass window and cause the human operator to prematurely end the calibration. The method of calibration involved a moving the measurement volume towards the wall from the outside; thus, the likelihood for the measurement volume being above the wall would be greater. Thus, the tendency for the corrections to be negative is reasonable. The wall refinements fall within the estimated uncertainty ($\pm$ 19 $\mu$m) for seven of the thirteen profiles and within two-thirds of the measurement diameter (i.e., $\pm$ 37 $\mu$m) for all but two of the profiles. The remaining two corrections are larger than one measurement diameter. The eleven smallest corrections are within reason. The largest two corrections must be examined more closely.

If the wall refinement technique is sound, then the two profiles with largest corrections (130a and 125c) must show obvious physical inconsistencies. Profile 130a was the first constructed in the experiment. As such, it suffered from long delays between measurements of each point while bugs and experimental procedures were refined. Thus, model expansion due to rising temperatures introduced significant uncertainties in the creation of this profile. Furthermore, early mistakes forced the rerun of many points. The first point was among these. The wall position was re-calibrated for the second run of this point; this was executed hours after the measurement of the second point. Thus, the distance between these points suffers from large uncertainty. In fact, the velocity values of these first two points are closer in value than their distance suggests ($u^+ \cong 6$ vs. $u^+ \cong 7$ over a distance $y^+ \cong 5$). This profile contains larger uncertainties than all of the others; in the remainder of this paper, it is discussed cautiously. The other profile, 125c, is the exact opposite; its points were taken in rapid succession. However, the behavior of its means and Reynolds stresses only approximates those of its neighbors if the profile is shifted more than one measurement point to the right (+50 $\mu$m); the theoretical correction of +72 $\mu$m agrees.

The calculated values of $C_f$ provide the first clear evidence that the wall refinement method leads to more physically consistent results. $C_f$ was calculated from the Spalding law both with and without the wall refinement as an additional unknown. Figure 63 plots $C_{f\text{-}0}$, i.e. $C_f$ calculated without wall refinement. Figure 65 shows $C_{f\text{-}\Delta y}$, i.e. $C_f$ computed with wall refinement. Included on these plots are the direct skin friction measurements made by Wetzel (1997) on the same model at x/L = 0.75. The plot of $C_{f\text{-}\Delta y}$ is closer overall to Wetzel's data and maintains a similar moderate change between points. The plot of $C_{f\text{-}0}$ contains larger jumps between points than the plot of $C_{f\text{-}\Delta y}$; this is most evident at x/L=0.7522. However, the average of the values for $C_{f\text{-}0}$ at x/L=0.7522 is closer to Wetzel's data than the same three values for $C_{f\text{-}\Delta y}$. The large jumps in $C_{f\text{-}0}$ are also not consistent with the plot of $C_f$ interpolated from the Göttingen data set (Figure 62). Figure 63 compares $C_{f\text{-}0}$ and $C_{f\text{-}\Delta y}$ with the Göttingen data at x/L=0.7722. The plot shows that the $C_{f\text{-}\Delta y}$ is larger than $C_{f\text{-}0}$ except at 123a. $C_{f\text{-}\Delta y}$ is also much closer to the Göttingen values than $C_{f\text{-}0}$. With smoother plots and $C_f$ values that are closer, as a whole, to both Wetzel's data and the data from Göttingen, $C_{f\text{-}\Delta y}$ is a better set of $C_f$ values than $C_{f\text{-}0}$.

Plots of $a_1$ vs. $y^+$ (Figures 35-38) provide more physical evidence in support of wall refinement. Figures 35-36 were constructed using wall refinement (i.e., $C_{f\text{-}\Delta y}$ and $\Delta y$). Figures 37-38 were constructed without wall refinement (i.e., $C_{f\text{-}0}$ only). The $a_1$ curves constructed with wall refinement are more tightly bundled than the curves created without the refinement. Flack and Johnston (1993) demonstrated that plots of $a_1$ vs. $y^+$ collapsed for $y^+ < 50$. Thus, the plots which employed wall refinement agree more closely with this experiment than those where the refinement was not applied.

The fact that the evidence thus far favors the wall refinement technique is encouraging. The refinements were carried out in the final data reduction. Later findings discussed in the remainder of this paper will also lend some support for this technique. However, this method invites further investigation. It must be tested against direct skin friction measurements. And, the method must be applied to profiles with a greater density of points near the wall; the number of points, which were available for curve fit in this experiment, was barely sufficient.

# Chapter 6 Octant Analysis

With simultaneous measurements in three orthogonal directions, a unique opportunity exists to examine the characteristics of a high Reynolds number flow with octant analysis. Octant analysis was chosen over other statistical techniques because its mean two-dimensional flow cousin, quadrant analysis, is the most accurate technique for capturing the ejection event (Bogard and Tiederman, 1986). The technique also has the simplest application for the broad range of derived flow quantities. Statistical analysis techniques, including octant analysis, are used primarily to examine the near-wall structures. The majority of Reynolds stress production takes place in the near wall region of the boundary layer. Thus, an understanding of the near-wall dynamics provides the necessary background for discovering computational simplifications. The discussion will focus mainly on the near-wall region with some mention of outer layer dynamics.

This chapter takes an in-depth look at applying octant analysis to the LDV data. The chapter will define the octants and the decomposition of the Reynolds stress tensor. As stated in the introduction, statistical techniques require a structural model as the basis for interpreting the results. The structural model will be constructed through a review of recent 3DTBL structural experiments and the common elements of 2DTBL structural experiments. Then, application issues, including the choice of coordinates system, will be examined. The octant populations and decomposed Reynolds stress tensor are discussed next. The chapter ends with a detailed analysis of the results and a comparison with other 3DTBL coherent structure experiments.

## *6.1 Octant Definitions*

Octant analysis separates the measurements into octants of velocity space. Each octant represents a flow event: interactions, sweeps, or ejections. Table 6-1 presents the definition of each octant.

**Table 6-1: Octant Definitions**

| Octant # | Sign of | | | Event |
|---|---|---|---|---|
| | u' | v' | w' | |
| 1 | + | + | + | Interaction |
| 2 | - | + | + | Ejection |
| 3 | - | - | + | Interaction |
| 4 | + | - | + | Sweep |
| 5 | + | + | - | Interaction |
| 6 | - | + | - | Ejection |
| 7 | - | - | - | Interaction |
| 8 | + | - | - | Sweep |

The contributions to the Reynolds stress tensor from individual octants may deliver insight into the mechanics of the separating 3DTBL. Equations 6.1-6.6 demonstrate the results of breaking the Reynolds stress tensor into eight octants.

$$-\overline{u'^2} = \sum_{i=1}^{8} \beta_i \left(-\overline{u'^2}\right)_i \qquad -\overline{u'v'} = \sum_{i=1}^{8} \beta_i \left(-\overline{u'v'}\right)_i \qquad (6.1, 6.2)$$

$$-\overline{v'^2} = \sum_{i=1}^{8} \beta_i \left(-\overline{v'^2}\right)_i \qquad -\overline{u'w'} = \sum_{i=1}^{8} \beta_i \left(-\overline{u'w'}\right)_i \qquad (6.3, 6.4)$$

$$-\overline{w'^2} = \sum_{i=1}^{8} \beta_i \left(-\overline{w'^2}\right)_i \qquad -\overline{v'w'} = \sum_{i=1}^{8} \beta_i \left(-\overline{v'w'}\right)_i \qquad (6.5, 6.6)$$

$\beta_i$ is the weighted population percentage for the given octant. The inverse-of-the-speed weighting factor was used to obtain the velocity statistics (see Appendix A.2). If no weighting factor were used, then $\beta_i$ would simply be the number of measurements occupying "octant i" divided by the total number of measurements. Instead, $\beta_i$ is the sum of the weighting factor associated with the measurements populating "octant i" divided by the sum of the weighting factor associated with the total number of measurements. For example, if the sum of the inverse-of-the-speed weighting for all measurements at a given location were 50 (seconds/meter) and the sum for only those points occupying octant 4 were 20 (seconds/meter), then $\beta_4$ would be 0.4. Figures 104-107 display profiles of $\beta_i$ for each octant.

The product of $\beta_i$ and $\tau_i$ (a Reynolds averaged stress using measurements in "octant i") is the octant's contribution to $\tau$. Figures 78-103 graphically display the octant stress contributions for each measurement location. The figures group the octant profiles by stress (i.e. six graphs, one for each Reynolds stress, are present for each measurement location). The octant decomposition for each profile is presented in both wall-collateral and free-stream coordinates. Figures 118-127 plot $\tau_i$ for a subset of the profiles. These figures also group $\tau_i$ by stress and present it under both wall-collateral and free-stream coordinates.

## 6.2 Establishing The Structural Model

Interpretation of octant analysis requires the construction of a structural model. In this section, recent 3DTBL structural experiments are reviewed. They form the framework in which the results are discussed. These studies assume that the structural detail of 3DTBLs does not differ significantly from that of 2DTBLs as reviewed by Robinson (1991) and Kline (1992). A summary of these reviews follows.

The sublayer ($y^+ < 7$) is turbulent, not a steady laminar flow. This region of flow is dominated by unsteady regions of high and low speed velocity called "streaks". The majority of turbulent energy production occurs in the buffer layer ($7 < y^+ < 30$), which is characterized by ejections ($u' < 0, v' > 0$) and sweeps ($u' > 0, v' < 0$). Ejections are the sudden eruption of a low speed streak away from the wall. Sweeps are wallward injections of high speed fluid. Ejections and sweeps are frequently associated with quasi-streamwise vortices (QSVs). QSVs dominate the near-wall activity in the majority of proposed structural models in the literature (Robinson, 1991). Whether

all ejections and sweeps occur in the presence of QSVs is not clear. However, the fact that the majority (~ 80%) of observable sweep and ejection events occur in pairs leads credence to the notion that QSVs are present (Kline, 1992). Recent DNS studies have also demonstrated a strong relationship between sweep-ejection events and QSVs (Robinsion, 1991). Longevity of QSVs also remains a point of debate. Most of the 3DTBL experiments discussed in this section assume that QSVs have significant lifespans. Octant analysis cannot determine the longevity of a QSV; therefore, longevity is given only cursory attention. QSVs occur with either sign of rotation. In this discussion, two notations are used to categorize QSVs. QSVs are identified by the sign of their rotation, +QSV (positive rotation) or -QSV (negative rotation). Or, the notation introduced by Shizawa and Eaton (Eaton, 1995) is used; QSVs are labeled as either "case-1" or "case-2". QSVs termed "case-1" have the opposite sign of vorticity compared to the near-wall, mean streamwise vorticity. QSVs with the same sign are labeled "case-2".

A mixture of QSVs and transverse vortices populate the log and wake regions ($y^+ > 100$). Large entrainment eddies dominate the intermittent layer where the boundary layer mixes with the free-stream flow. These eddies are slowly-rotating, three-dimensional structures; they scale on $\delta$ in both the x and z directions. The interaction of the eddy and free-stream flow appears as a bulge. Valleys capturing high-speed, free-stream fluid exist between bulges; these valleys can span most of the boundary layer. The valleys potentially initiate the near-wall instability that causes the ejection/sweep process and the formation of QSVs. This completes a short summary of current 2DTBL structure knowledge. This section continues with a review of 3DTBL structure experiments.

Chiang and Eaton (1993) examined a rotating disk flow using LDV and flow visualization techniques. They concluded that case-1 and case-2 QSVs occur in equal numbers but that case-1 QSVs produce stronger ejections than their case-2 counterparts. This asymmetry contributes to the lower production of Reynolds shear stress in 3DTBLs. The reduced strength of QSV-induced ejections was attributed to interaction between the QSV and the crossflow. This interaction would deflect some ejections in the spanwise direction, reducing their height. The ejected fluid experiences a larger velocity difference the higher it rises, and greater velocity differences provide greater Reynolds shear stress production. Thus, deflection of the ejected fluid by the crossflow results in lower Reynolds stresses.

Flack and Johnston (1993) used flow visualization to uncover the near wall structure of a channel flow with a 30° bend. Like the Chiang and Eaton flow, QSVs of both signs appeared in equal numbers and an asymmetry in QSV ejection strength was present. However, the stronger ejections were caused by case-2 QSVs, the opposite of the Chiang and Eaton flow. Moreover, Flack and Johnston proposed a slightly different model for explaining the weakened ejections. The crossflow convects the QSVs from regions of high mean crossflow to regions of lower mean crossflow. This causes multiple-QSV interactions which limit the height of the ejection. Flack and Johnston (1993) also performed flow visualization in a channel with a sharp step that was swept back 45°. Bubbles were generated at $y^+ \sim 2$ and $y^+ \sim 37$. Their results were similar to those of the 30° bend flow. However, the QSV count showed a larger number of case-2 QSVs

than case-1. They propose that their QSV counting method could have been skewed in favor of the case-2 QSV.

Flack and Johnston (1995) revisited the 30° bend flow using hydrogen bubble visualization. Bubbles were generated at $y^+ = 2$ and $y^+ = 36$. They concluded that QSVs of both types occur with the same frequency and the same strength in both the 2DTBLs and 3DTBLs. However, the spacing between low-speed streaks was smaller in the 3DTBLs; and the low speed streaks showed greater stability in the 3DTBLs. This stability and the reduction in Reynolds stresses was attributed to a lower frequency of ejection events in the 3DTBLs compared with the 2DTBLs.

Fleming and Simpson (1994) performed flow visualization in the near-wall region of a wing-body junction. Their results were later refined with LDV data in a paper by Fleming, Simpson, and Shinpaugh (1995). The experiment focused on the behavior of the near-wall streaky structures in a 2DTBL upstream of the wing body junction and a 3DTBL downstream of the nose. They found that the inner region flow of the 3DTBL was more stable than that of the 2DTBL; the 3DTBL exhibited lower streak coalescence and division. This led them to conclude that high speed sweeps do not penetrate as deeply into the near wall region in 3DTBLs. The physical model, upon which these interpretations were based, was proposed by Simpson and Devenport (1990). Because the mean flow obtains a third degree of spatial freedom, the displacement mechanism is no longer constrained to produce ejections with symmetric spanwise strength (in the mean). The low-speed, near-wall fluid displaced in a sweep event develops a preference for spanwise motion under the influence of the transverse pressure gradient. Thus, less fluid ejects upward leading to lower Reynolds stresses.

Sendstad and Moin (1992) used direct numerical simulation (DNS) to examine the evolution of a 3DTBL. The 3DTBL evolved from a 2D channel flow experiencing a sudden spanwise pressure gradient. They identified four mechanisms that suppress the production of Reynolds stresses:

1) Fluid swept toward the wall by case-2 QSVs will not get as close to the wall as in a 2DTBL.
2) Ejections by case-1 QSVs generate lower velocity fluctuations because the fluid originates at further from the wall than in 2D flow.
3) The streamwise QSVs are tilted with respect to the near wall streaks. The resulting interaction causes the QSVs to eject high-speed fluid from the high speed streaks rather than low speed fluid from the wall. This mechanism primarily affects case-2 QSV ejections.
4) The spanwise mean flow retards near-wall penetration of high speed sweeps produced by case-1 QSVs.

The first two mechanisms appear shortly after the spanwise pressure gradient is imposed on the simulated flow. The last two develop and grow in influence as the flow evolves.

Differences exist among the 3DTBL experiments. Flack and Johnston (1993) conjecture that the difference between their results and those of Chiang and Eaton (1993) may be due to the

difference in the flow region examined. Chiang and Eaton introduced hydrogen bubbles at a height of $y^+ \sim 40$, the edge of the buffer region. Flack and Johnston introduced hydrogen bubbles at heights of $y^+ \sim 2$ (the sublayer) and $y^+ \sim 36$ (the buffer region). On the other hand, Chiang and Eaton suggest the difference may result from the nature of the flows. The Chiang and Eaton flow was three-dimensional from inception. The Flack and Johnston flow originated as a two-dimensional channel flow with three-dimensional effects imposed at the bend. The resultant flow exhibits "higher three-dimensionality" than the disk flow and may remain in an "adjustment phase". Chiang and Eaton reference the direct numerical simulation of Sendstad and Moin (1992) for support of their hypothesis. The DNS study showed that case-2 ejections are stronger during the initial period of the spanwise gradient imposition; however, case-1 ejections regain some importance as the flow evolves. However, Sendstad and Moin emphasize that the case-1 ejection remained more greatly weakened by the crossflow throughout the simulation. The flow of Fleming and Simpson (1994) did not discuss QSVs but focused mainly on the behavior of the low-speed streaks. Thus, no apparent discrepancy exists between this experiment and the others. In fact, Fleming and Simpson agree with the conclusion of Sendstad and Moin and Flack and Johnston (1995). The sublayer in 3DTBLs is more stable due to a reduction of ejection events.

The background for discussing the octant analysis has been established. The near wall LDV measurements will be examined for clues about the dynamics of ejections, sweeps, QSVs, and streaks; only minor attention will be paid to higher regions of the flow field. The differences in results of recent 3DTBL structural experiments provide specific points of interest for the discussion.

## 6.3 Application Issues

### 6.3.1 The Coordinate System Problem

Before examining the octant data for near-wall structure clues, it is important to discuss the choice of coordinate system reference. In 2DTBLs, coordinate choice is not an issue; the near wall and free-stream flow directions are equal. In 3DTBLs, the near-wall and free-stream flows have histories originating from two different directions. Thus, the wall shear stress vector is no longer aligned with the free-stream velocity vector. A choice of coordinate systems, in which to examine the flow, evolves; and the choice isn't restricted to just free-stream or wall-shear-stress coordinates. Four different angles are commonly used in the examination of 3DTBLs: flow angle ($\alpha_f$), gradient angle ($\alpha_g$), stress angle ($\alpha_\tau$), and intensity angle ($\alpha_i$). (Figures 49-56 show profiles of each angle in wall-collateral coordinates.) Neither of these angles is constant throughout the boundary layer. If one wishes to view the flow profile in a fixed set of coordinates based on one of these angles, one would have to choose the angle at a particular height.

Octant analysis shows different trends based on coordinate system choice (Sendstad and Moin, 1992). The most appropriate direction in which to examine the near wall structures is in a coordinate system whose x-axis roughly points in the "preferred" direction of the QSVs. The "preferred" direction shall be defined as the direction from which the average angular deviation of the QSVs' axis is at a minimum; in other words, the majority of QSVs are nearly streamwise in this

axis system. This direction will be denoted by the symbol, $\alpha_v$. As yet, no one has determined what this direction is or even if it exists. The studies cited in section 6.2 demonstrate that 3DTBLs are not radically different than 2DTBLs; this provides some assurance that $\alpha_v$ still does exist. Unfortunately, the data in this experiment cannot be used to directly determine this direction. Simultaneous measurements at multiple points in the flow field are required to define $\alpha_v$. Instead, this paper will start with the hypothesis that $\alpha_v$ does exist and that this direction is close to one of the flow property angles at some height in the flow. The next step is to narrow the coordinate-system candidates to a small list. As luck would have it, the list can be reduced to only two systems. The following paragraphs contain the pros and cons for each coordinate system and the rationale for reducing the list to two. Once the two candidate systems are identified, some interesting aspects of coordinate system choice are immediately apparent and discussed.

The free-stream coordinate system, based on $\alpha_f$ (Figures 49-50) at the edge of the boundary layer, has been the traditional context for describing flow structure because "three-dimensionality" is seen to grow from the wall outward. The free-stream coordinate system was used as the context of discussion for all of the flow visualization experiments cited above. Only the DNS study of Sendstad and Moin deviated from this trend; they used a fixed coordinate system aligned with the channel centerline during the initial period of 3D flow development. (At later times, they used a variety of axis systems to investigate the Reynolds stress behavior.) Even though the flow along the free-stream coordinate system has a different history than that of the near wall flow, it remains a valid coordinate system choice for discussing near-wall structures. The 2DTBL studies demonstrated that sweep motions influence the near wall dynamics. These sweep motions originate from various heights including the wake region, which is more closely aligned with the free-stream flow. (These are more likely to be "entrainment sweeps"; i.e. sweeps resulting from the entrainment of free-stream flow by the intermittent-layer eddies rather than QSVs.) Also, traditional use of free-stream coordinates provides a compelling reason to keep it for comparison purposes.

Ideally, one of our candidates would be the wall shear-stress coordinate system which represents the limit of $\alpha_f$ as one approaches the wall. However, no direct measurements of the wall shear-stress angle were made. Instead, it will be assumed that the $\alpha_f$ measurements near the wall are close in value to the wall shear-stress direction. The quasi-collateral nature of the flow provides the justification for this assumption. The resulting "wall-collateral" coordinate system replaces the wall shear-stress coordinate system in our deliberations. Wall-collateral coordinates perceive the flow in the direction of the mean tangential velocity component near the wall. If the dual history description of 3DTBLs is accurate, the near-wall coherent structures would exist in the vicinity of the near-wall mean velocity direction since they have a primary influence over the flow dynamics. Thus, the wall-collateral coordinate system has potential for alignment in the neighborhood of the QSV axes. Moreover, this coordinate system is a good contrast to the free-stream coordinate system. It will be our second choice. The angle between the wall-collateral and free-stream coordinate systems will be denoted by the symbol, $\alpha_{wc}$ (see Figures 51-52).

A coordinate system based on $\alpha_g$ holds potential because one of its components, $\frac{\partial \overline{W}}{\partial y}$, is the major contributor to the streamwise vorticity. This coordinate system represent the direction were the average streamwise vorticity is approximately zero; $\frac{\partial \overline{V}}{\partial z}$ would still contribute. As defined, QSVs are not true vortices; however, they do exist in a region of high vorticity although the converse is not necessarily true (Robinson, 1991). The flow visualization experiments of Chiang and Eaton and of Flack and Johnston both showed that near wall QSVs of both signs occurred equally in 3DTBLs. Since QSVs of opposite sign contain vorticity of opposing sign, the vicinity of minimum streamwise vorticity becomes a good candidate for $\alpha_v$. Nevertheless, the quasi-collateral nature of the current flow near the wall causes $\alpha_g$ to coincide with $\alpha_f$, within uncertainty. Figures 51-52 show that, near the wall, $\alpha_g$ is almost zero in wall-collateral coordinates. Therefore, a "gradient" coordinate system based on near-wall $\alpha_g$ and the wall-collateral coordinate system are nearly parallel and there is no need to treat the "gradient" coordinate system as a separate case.

Both $\alpha_\tau$ and $\alpha_i$ have merit in the discussion because they are based on the Reynolds stresses whose behavior is of primary interest in octant analysis. In a coordinate system aligned with $\alpha_\tau$, v'w' is zero. Using v'w' as the basis for a coordinate system is problematic near the wall. The uncertainty in v'w' is a large percentage of its near-wall values. The resulting uncertainty for $\alpha_\tau$ is, consequently, very large, ~6°; the scatter of $\alpha_\tau$ seen in figures 53-54 reflects the uncertainty. The lack of $\alpha_\tau$'s reliability makes it a poor choice on which to base a coordinate system. Therefore, it was not used in the analysis. In a coordinate system aligned with $\alpha_i$, u'w' is zero. In other words, the mean inviscid skewing in a plane parallel to the wall disappears. QSVs could show a preference for this direction if the inviscid skewing is significant compared to the viscous skewing. This cannot be directly tested using the present measurements. This coordinate system also maximizes the $u'^2$ stress. Ejections and sweeps are frequently the cause of large u' in the buffer layer; therefore, the direction of maximum $u'^2$ should also be near the average direction of the QSVs. Luckily, $\alpha_i$ and $\alpha_f$ almost coincide near the wall, within uncertainty; figures 55-56 demonstrate that, near the wall, $\alpha_i$ is close to zero. An "intensity" coordinate system is nearly parallel to the wall-collateral coordinate system; there is no need to treat the intensity coordinate system as a separate case.

Thus, the list of coordinate choices was narrowed to two, free-stream coordinates and wall-collateral coordinates. The free-stream coordinate system was chosen for its historic value and because sweeps can originate from the flow field it best describes. The wall-collateral coordinate system has the distinction of being parallel, within error, to two of the other coordinate system candidates and provides a good contrast to the free-stream system. Two important differences immediately emerge when examining the coordinate system choices.

The first difference is the shape of the spanwise velocity profile. In free-stream coordinates, the profile shows the characteristic near-wall bulge. In wall-collateral coordinates, the bulge disappears. Instead, the spanwise velocity decreases monotonically until it reaches a negative peak value in the outer layer. This profile has the same shape as the spanwise profile of Sendstad and

Moin's DNS experiment except that W is negative. Interestingly, both Chiang and Eaton (1993) and Flack and Johnston (1993) base some of their flow interpretation on the existence of the near wall bulge. Chiang and Eaton explain one observed ejection trajectory, which they named a "curl", in the context of a near wall bulge. A curl occurs when the fluid ejected by a case-1 QSV rises above the "bulge". The fluid now convects more slowly than the QSV below it and is soon forced back toward the wall by the downwash side of the QSV. Flack and Johnston state that the ejection events they uncovered were created by multiple QSV interaction. This interaction occurs because near-wall QSVs are convected further in the spanwise direction by the "bulge peak" than the QSVs above them. Flack and Johnston almost dismiss comparison with the DNS study because it does not have a bulge in its profile. The true issue could be coordinate system choice.

The other emerging difference is the sign of the near-wall mean streamwise vorticity, $\omega_x$:

$$\omega_x = \frac{\partial \overline{W}}{\partial y} - \frac{\partial \overline{V}}{\partial z} \tag{6.7}$$

In the present flow (as with most flows), the $\frac{\partial \overline{W}}{\partial y}$ is much larger than $\frac{\partial \overline{V}}{\partial z}$. Thus, $\frac{\partial \overline{W}}{\partial y}$ generally determines the sign of $\omega_x$. In free-stream coordinates, $\omega_x$ is positive below the spanwise velocity bulge and negative above it. In the wall-collateral coordinates, $\omega_x$ has a constant negative sign. The wall-collateral coordinate system, thus, simplifies the classification of QSVs. A case-1 QSV, as defined in section 6.2, would oppose $\omega_x$ throughout the boundary layer in wall-collateral coordinates. In free-stream coordinates, the case-1 QSV opposes $\omega_x$ close below the bulge, but has the same sign as $\omega_x$ above the bulge.

### 6.3.2 The Octant-QSV Mapping Problem

Now that the coordinate systems have been chosen, there is another issue to address, the mapping of octants to a QSV of a particular sign. Such a mapping is only meaningful if the height of the QSV is known. Below the QSV center, one mapping applies; above the QSV center, a different mapping applies. Numerous QSVs are created and convected during the typical measurement periods for data points in the current flow. The octant-QSV mapping for a flow region must be statistically significant to be useful; i.e., either the bottoms or the tops of the QSVs must dominate in a given region. Structural experiments for 2DTBLs demonstrate such a region near the wall. Flack and Johnston (1993) cite the work of Robinson when discussing the near-wall concentration of QSVs. According to Robinson, the centers of QSVs can be found in the range $10 < y^+ < 250$ with the largest number of QSV centers found near $y^+ \sim 30$. The average diameter of a QSV is $d^+ \sim 34$. For a 2DTBL, the sublayer and buffer region are dominated by the bottoms of QSVs.

Recent studies show that the same conclusion can be applied to 3DTBLs. Sendstad and Moin (1992) demonstrate that QSV induced events do not penetrate as deeply into the wall layer. This discovery was corroborated by Fleming and Simpson (1994) and Flack and Johnston (1995). Both experiments examined a flow with an initial 2DTBL which evolved into a 3DTBL. Both discovered that the near-wall streaky structures are more stable in the downstream 3DTBL compared to the upstream 2DTBL. However, Fleming and Simpson (1994) proposed that the

increased stability may be due to flow acceleration near the wall rather than a decrease in ejetion/sweep events. If the average size of a QSV has not change appreciably in 3DTBLs and the increased stability in 3DTBL streaky structures is due to decreased ejection/sweep events, then the region for a valid octant-QSV mapping is, at worst, equivalent to that of a 2DTBL; but it has potential to be taller. Flack and Johnston's (1995) flow visualization results further support the notion that the buffer layer is dominated by the bottoms of QSVs. They found that ejections of bubbles introduced at $y^+ = 2$ were caused by a single QSV. Ejections of bubbles introduced at $y^+ = 36$ still originated from a single QSV and only a minority exhibited trajectories attributed to multiple-QSV interaction. The average ejection height of hydrogen bubble emitted in the sublayer (at $y^+ = 2$) was $y^+ \sim 46$; the ejection height of bubble introduced at $y^+ = 36$ was $y^+ \sim 70$. Therefore, the bottoms of QSVs dominate for at least $y^+ < 50$. If the coordinate system that is aligned with the QSV axes in the buffer region is known, then one can successfully map the QSV events into particular octants. Figure 6-1 elaborates on Table 6-1 with this octant-QSV event mapping.

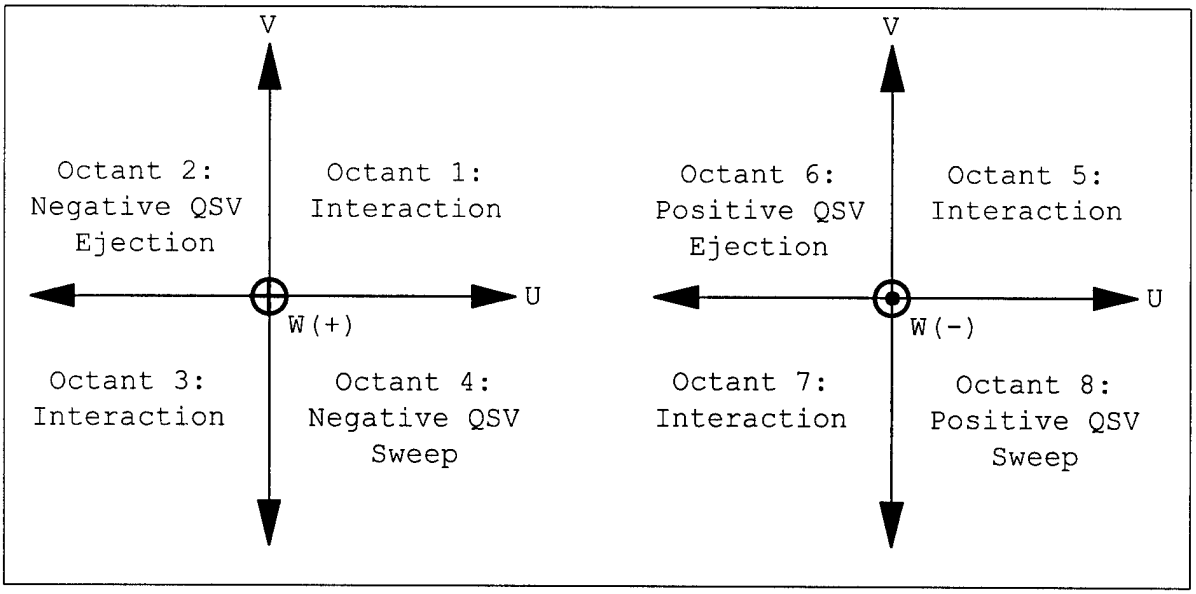


Figure 6-1. Octant-Vortex Mapping

Identifying the octant-QSV event mapping is only half the problem. Not all the data points that fall within an octant can be associated with a particular event. Thus, one must determine whether QSV events have a dominating influence over other, usually random, events that fall within their mapped octant. The 2DTBL studies of Bogart and Tiederman (1986), Luchik and Tiederman (1987) and Willmarth and Lu (1972) partly addressed this problem. Bogart and Tiederman (1986) compared the results of quadrant analysis with flow visualization. Quadrant-2 data ($u < 0$, $v > 0$) that fell outside of a certain threshold had high probabilities of being associated with an ejection event. The threshold $H$ is given by equation 6.8. Data points below $H \approx 1$ have a random probability of belonging to an ejection event. However, the analysis showed that even with a threshold of zero, only one third of the quadrant 2 data did not occur during a visual ejection event.

$$H = \frac{(uv)_2}{\sqrt{u'^2}\sqrt{v'^2}} \tag{6.8}$$

Unfortunately, these results only address the correlation of quadrant-two data with the ejection process. A similar study was not performed for sweeps. Furthermore, it is uncertain whether the threshold value equally applies to 3DTBLs. Also, Luchik and Tiederman (1987) demonstrated that applying thresholds to quadrant analysis captures less than 25% of the duration of each ejection event even though the technique accurately detects the event itself. Therefore, conditional averaging based on thresholds produces inaccurate stress contributions. Fortunately, Willmarth and Lu (1972) showed that the contribution to the Reynolds stress made by points under a threshold can be very small. The contribution of points under H = 0.5 was 1% of u'v'. Thus, these studies demonstrate that ejection events do dominate over other quadrant-two data. Therefore, no data will be excluded from the octant analysis for fear of losing important information or compromising comparisons between all octants. It will be assumed that contributions from structural events have a dominating influence over contributions from random events as demonstrated by Willmarth and Lu. Thus, the threshold technique for detecting bursts developed by Bogard and Tiederman (1986) will not be used; this exercise is left for future work.

### 6.3.3 Analyzing The Population Distribution

An often ignored but interesting set of data made available by octant analysis is population distribution of velocity events among octants. Before examining the octant population data, three major issues that affect interpretation of the results must be addressed. First, the validity of attributing octant population trends to coherent structures must be established. Second, the distribution of random events in velocity space must be explained. Third, uncertainties relating to coordinate rotation and population size are discussed.

QSVs dominate the Reynolds stress production in the near-wall flow. Section 6.3.2 established that trends in stress contributions from even octants can reasonably be attributed to actual ejection and sweep events. However, there is little experimental evidence that provides the same assurance for attributing octant population trends to these velocity events. The comparison study of Bogard and Tiederman (1986) does indirectly address this question. The study examined the correlation between visual ejections and anemometry measurements when a threshold of zero was applied to quadrant two; i.e., all of the quadrant-two data was included. Only one third of the data did not correlate with an ejection event. Thus, it appears that coherent structures, by their definition, would have a dominant influence on octant population values. All other motions would, by necessity, appear randomly.

Unfortunately, random motions may not populate octants evenly nor may they be represented by the same population percentage throughout a boundary layer. The octant coordinate system origin is directly based on the velocity distribution via the mean velocity; if one removed the coherent motions, the remaining random motions would produce a different mean velocity from which to base the coordinate system origin for the octant analysis. However, coherent motions have direction; thus, octants containing velocity events tied to coherent structures should see an

appreciable change in their population when the coordinate system axes rotate through a coherent structure. Thus, comparative examination of the free-stream and wall-collateral coordinate systems will uncover large population changes related to coherent structures that have a near streamwise or near transverse direction.

Uncertainties related to coordinate system and population size can also affect the distribution of points in the octants. The velocity distribution is vaguely egg-shaped. The major axis of this "egg" points near the direction of the U axis; the rounder "bottom" of the egg exists in the negative u' region. The minor axes of the "egg" point near the direction of the W and V axes. Points exist in a wider range along the U axis than along either the V or W axis. As one approaches the wall, the egg compresses along the V axis. Even if one assumes that points were distributed evenly within this egg, small rotations about the wall normal direction can lead to a net transfer of points between octants that share the U axis. As one approaches the wall, uncertainty in the wall normal direction can also lead to significant population contribution uncertainties as the distribution along the V axis flattens. Thus, the 0.5° uncertainty, which applies to both the wall normal coordinate systems ($\alpha_f$) and the wall normal direction, could lead to an absolute population uncertainty of $\pm$0.6% for any octant.

Sample size can also add uncertainty, particularly near the wall. As explained in section 3.2, data recording rates became low near the wall. The desired 16,384 data points was not always obtainable before the seed began to cover the plexiglass window and generate false, zero-velocity data. However, the number of points was always greater than four thousand. These numbers provide low statistical uncertainty for the mean flow quantities. However, it is not certain whether they are sufficient to examine coherent structures through their influence on octant populations. This examination has two requirements. A statistically significant number of coherent structures must pass through the measurement volume during the observation. Enough data points, which relate to these structures, must be collected so that this data can be discernible from random events; i.e., multiple measurements must be recorded for the duration of each structural event. Unfortunately, quantifying this uncertainty relies on two unknown quantities: the average duration of a structural event at a point and the average time between structural events. These values have been calculated for low-Reynolds-number 2DTBLs over a flat plate (Bogard and Tiederman, 1986); however, there are no equivalent experiments for high-Reynolds-number 3DTBLs. If the numbers do not drastically change for the high-Reynolds-number 3DTBL case, then even the smallest sample size and data rate in this experiment is more than sufficient. Thus, the uncertainty caused by sample size is negligibly small compared to the uncertainty due to coordinate rotation. (If this were not the case, then the sample size, though statistically significant, would fail to fully capture the velocity distribution and, thus, produce questionable Reynolds stress results overall.)

### 6.3.4 Application Limitations

The application issues discussed in the previous three subsections clearly demonstrate the limits of octant analysis in examining the near wall structure of 3DTBLs. Although much of the present work in 3DTBL structures heavily centers around the QSV model, there exists too many

unknowns to definitively connect velocity events in a particular octant with a QSV of a particular sign. The results and analysis that follow will focus purely on ejection and sweep events without regard to the coherent structures that cause them. Only when the discussion compares the results with the 3DTBL experiments surveyed in section 6.2 will the octant-QSV mapping be applied under the justifications established in this section. Nevertheless, Shizawa and Eaton's (1995) idea for classifying QSVs by how their sign of rotation compares with the mean, near-wall voritcity will be carried forward. Sweeps and ejections created by QSVs are associated with a w' that has the opposite sign of the QSV's rotation. Generalizing the classification to all ejection and sweep motions, the end result is very simple. Case-1 ejections and sweeps are associated with a w' that has the same sign as the mean, near-wall vorticity. Case-2 ejections and sweeps are associated with a w' that has the opposite sign of the mean, near-wall vorticity. The reason for adapting the classification is that some trends appear to be symmetric about the mean, near-wall vorticity.

## 6.4 Results

The following discussion contains a large number of references to the measurement profile locations. Identifying each location by its axis (x/L) and radial ($\phi$) coordinate can lead to cumbersome grammar. To make references to profile locations concise, the discussion uses the identification scheme defined in section 3.3.

Figures 78-103 contain plots of the octant contributions to the Reynolds stress grouped by stress; the stresses are normalized by the square of the free-stream velocity (not $U_\tau$). Figures 78-90 are in wall-collateral coordinates; Figures 91-103 are in free-stream coordinates. Figures 104-107 display the weighted octant populations ($\beta_i$). Figures 118-127 contain octant stress plots for a subset of the boundary layer profiles. The octant stress plots show the Reynolds averaged stress within a single octant rather than the contribution to the total. These plots provide a "population neutral" view of the velocity events occupying an octant. If octant 1 contained a small population with strong u' and octant 2 contained a larger population with equally strong u', then the octant contribution plots would show that octant 2 contributes more to $u'^2$ than octant 1; however, the octant stress plot would show that the value of $u'^2$, averaged within each octant, is equal.

Before discussing the octant contributions, it should be noted that profile 125a has an anomalous dip in $u'^2$ and u'v' at the third point. There appears to be no physical reason for the dip; the experimental data shows no signs of velocity clipping. However, the lab notes do reveal that the third and fourth point were measured immediately before the first and second. This leaves open the possibility of large positional errors in the first four points if the probe position was re-calibrated after measuring points three and four but before measuring points one and two. Unfortunately, there are no notes that indicate that this was the case. Thus, without any clear justification for removing it, this location is used in the discussion even though it skews the discussion of contribution peaks. It should also be noted that the profile at 125c does not penetrate below $y^+ = 16.68$. As will later become evident, this eliminates profile 125c from many discussions of the near-wall dynamics and statistics.

The next seven sections detail the population distribution and octant contribution to the six Reynolds stresses. Each section discusses:

1) The relative order of the octants by contribution size including the difference in size between ejection contributions (octants 2 and 8) and between sweep contributions (octants 4 and 6) of opposite sign w'.
2) The near-wall locations were sweep contributions overtake ejection contributions (Reynolds stresses only).
3) The location of the contribution peak for each octant (Reynolds stresses only).
4) The difference in contribution values between free-stream and wall-collateral coordinates (population, $u'^2$, $v'^2$, $w'^2$, and u'v' only).
5) The average near-wall difference in contribution between ejections and sweeps associated with same-sign w' ($w'^2$, u'w', and v'w' only).

The detailed analysis is a very dry read. The casual reader may skip these sections and proceed to the discussion in section 6.5 which highlights the most important trends that are revealed in the analysis.

### 6.4.1 Octant Population

Figures 104-107 display the weighted octant populations ($\beta_i$). $\beta_i$ of the interaction (odd) octants is generally smaller than the sweep and ejection octants. This is expected; the boundary layer is dominated by sweeps and ejections except possibly very close to the wall (Robinson, 1991). Under both coordinate systems, $\beta_i$ remains steadily close to 0.10 in the outer layer for all interaction octants. As one approaches the wall the behavior varies with each octant. Octant 1 maintains the nearly flat 10% level throughout the boundary layer. Octant 5 begins to decline in the buffer layer and approaches a value of 5% to 6% at the lowest measured points. Interestingly, octants 1 and 5 show little change between the coordinate systems. Octant 7 shows a slight decrease in the log layer, then quickly increases as one enters the buffer layer. This increase appears to grow with increasing $\phi$. The effect is more evident when viewed in free-stream coordinates than from wall-collateral coordinates. In wall-collateral coordinates, $\beta_i$ dips to ~7% at $y^+ \sim 20$; then, the points scatter during the recovery period to a range of 8% to 16%, barely approaching the level of the ejection/sweep octants. In free-stream coordinates, the dip in $\beta_i$ is smaller; it lowers only to ~8% at $y^+ \sim 20$. The population then steeply climbs to a range of ~10% - 20% at the lowest measured point. Many of the free-stream profiles show that the Octant 7 events become more numerous near the wall than either the +w' ejection or -w' sweep events (octants 2 and 8). Octant 3 also displays a significant variation between the coordinate systems. In wall-collateral coordinates, $\beta_i$ begins a slow decline in the log layer to ~6% at $y^+ \sim 20$; then it recovers a little to ~8.5% near the wall. In free-stream coordinates, the decline does not cease but levels out to ~5.5% near the wall.

The $\beta_i$ profiles of the ejection-sweep (even) octants clearly demonstrate how influential these events are in contributions to the Reynolds stresses. In free-stream coordinates, these octants have $\beta_i$ values between 10% and 27%. In wall-collateral coordinates, the range of $\beta_i$ is narrower, between 12% and 21%. In fact, the $\beta_i$ profiles of the even octants are almost flat in wall-collateral coordinates. Without the need to account for large variations in population percentage

along the profile, a more straight forward comparison of the Reynolds stress contributions from even octants can be made in wall-collateral coordinates. The other striking trend in the even octant populations is the cross coupling of the sweeps and ejections with w' of differing sign. The -w' ejection octant shares nearly the same population values and same trends as the +w' sweep octant. The same holds true for the -w' sweep and +w' ejection. This behavior is present in both coordinate systems; but it is more exaggerated in free-stream coordinates. In free-stream coordinates, $\beta_i$ for octants 2 (+w' ejection) and 8 (-w' sweep) range between 10% and 17% near the wall; $\beta_i$ for octants 4 (+w' sweep) and 6 (-w' ejection) lie between 16% and 27%. The percentage ratio of -w' to +w' ejection events ranges from 54/46 to 72/28 with a median of 66/34 at the bottom point. The ratio for sweeps (-w'/+w') is nearly the opposite, 47/53 to 34/67 with a median of 38/62. Both ratios widen with increasing $\alpha_{wc}$ and narrow as one moves away from the wall. At the sixth measurement point away from the wall ($y^+ \sim 70$), the range for both ratios is approximately 45/55 to 55/45 with a median of 50/50. In wall-collateral coordinates, $\beta_i$ for octants 2 and 8 hovers about 17.5; $\beta_i$ for octants 4 and 6 have a smaller value of about 0.15. Rotation to wall-collateral coordinates appears to have promoted octants 2 and 8 over octants 4 and 6. Moreover, the population difference has narrowed considerably. The percentage ratio of -w' to +w' ejection events ranges from 49/51 to 42/58 with a median of 46/54. The ratio for sweeps is a near mirror opposite, 59/41 to 52/48 with a median of 55/45. These ratios change very little within the inner layer. At the sixth measurement, the median for the ejection ratio moves very slightly to 45/55; the median for the sweep ratio remains unchanged at 55/45. Thus, the ratios maintain nearly the same value throughout the buffer and lower log layer ($y^+ < 70$).

Figures 108 and 109 take a closer look at the octant population differences between the two coordinate systems. These figures plot the population in free-stream coordinates subtracted by the population in wall-collateral coordinates. There are symmetries in the differences near the wall. Population differences can be coupled into mirror-image pairs: octant 1/octant 5, octant 2/octant 6 (ejections), octant 3/octant 7, and octant 4/octant 8 (sweeps). Referring to Figure 6-1, one will see that each of these pairs are neighbors along the U axis. Thus, the coordinate system rotation causes a much larger exchange of data across the U axis than across the W axis. This is not entirely surprising. As stated earlier, the velocity distribution is vaguely egg-shaped with the major axis near the U axis; thus, larger data exchanges should occur across the U axis. What is surprising is the magnitudes of the data transfers. The near-perfect symmetry of the differences demonstrates a negligible transfer of points across the W axis. No concentration of points exist near the W axis that are within the area crossed by the rotation; data points in this area are evenly distributed. Thus, velocity events in close proximity to the W axis correlate with random events or, at best, weakly correlate with a coherent structure. In short, there is no coherent structure that produces predominantly spanwise movements.

The data transfers across the U axis can become very large. The average size of the data transfer for each octant pair are: octants 1/5 (< 1%), octants 6/2 (< 9%), octants 7/3 (< 5%), and octants 4/8 (< 7%). The octant pairs are designated by the flow of data as one rotates from free-stream to wall-collateral coordinates; e.g., octant 1/5 means that data is exchanged from octant 1 into octant 5 as one rotates from free-stream to wall-collateral coordinates. For three of the octant pairs,

the data exchange across the U axis is a substantial percentage of the total population of both octants. The data transfers are much larger than those that would occur with randomly placed data. Thus, large concentrations of data points exist within the area swept by the coordinate rotation. Such concentrations are the footprints of coherent structures. Observing the direction in which the data transfers happen, one will see that the data transfers counter-clockwise; i.e., data moves from the left octant to the right octant for $u' < 0$ and from the right octant to the left octant for $u' > 0$. The consistent counter-clockwise direction of the transfer and the symmetry of the transfer both support the hypothesis that the coherent structures have a preferred direction, a streamwise direction. The size of the transfers reveal that all coherent structures may prefer nearly the same direction. This theory would be consistent with the structural model of Robinson (1991) in which the dynamics of streaks and QSVs are tightly coupled.

### 6.4.2 Octant Contributions To $\overline{u'^2}$

$u'^2$ (Figures 13 and 14) peaks in the buffer layer. The octant analysis reveals that contributions from ejections and sweeps are the primary source of the behavior. In free-stream coordinates, only the -w' ejection (octant 4) and +w' sweep (octant 6) contribute significantly. In wall-collateral coordinates, all the even octants significantly contribute. The octant contribution curves form two groups, although group membership differs between the coordinate systems. In free-stream coordinates, the groups are the octant 4/6 pair and then all other octants. In wall-collateral coordinates, the groups are even octants and then all interaction (odd) octants. Given the major differences between the coordinate systems, details of the contribution plots will be separated by coordinate system. The behavior of the $u'^2$ contributions will first be discussed in free-stream coordinates, then wall-collateral coordinates.

In free-stream coordinates, the $u'^2$ contributions of the octant 4/6 pair are greater than the octant 2/8 pair within the buffer layer. In the buffer layer, the gap between sweeps (octants 4 and 8) reaches a maximum of $(u'^2)^+_{4\text{-}8} \sim 1.8$ (profile 123b) with an average of 0.74 or 38% of the larger contributor. (The average includes the first four points in each profile.) The gap between ejections (octants 2 and 6) reaches a maximum of $(u'^2)^+_{2\text{-}6} \sim -2.1$ (profile 123b) with an average of -1.1 or 57%. The location, where the ejection and sweep contributions associated with the same-sign w' cross, also emphasizes the difference. The +w' sweep (octant 4) overcomes the +w' ejection (octant 2) over the range $19 < y^+ < 233$ with a median of 140. The -w' ejection (octant 6) becomes greater than the -w' sweep (octant 8) over the range $72 < y^+ < 125$ with a median of 92. (In profile 105a, the -w' sweep does retake the -w' ejection at $y^+ = 13.3$.) Furthermore, the contributions of the octant 2/8 pair diminish until they mingle with the contribution plots of interaction octants 1 and 7. Octant 7 overtakes octant 2 in nine of the thirteen profiles (110a-120a, 125a, 130a, 120b-125b, 120c, and 123c); this event occurs within $8 < y^+ < 23$ with a median location of 13.3. Octant 1 crosses octant 2 in eight profiles (110a-120a, 125a, 130a, 120b-125b, and 120c); this event occurs within $8 < y^+ < 25$ with a median location of 13.4. Within the context of the stronger (octant 4/6) and weaker (octant 2/8) ejection/sweep pairs, the sweep contribution does become the more dominant contributor as one approaches the wall. For the weaker pair, this holds true throughout the inner layer; the -w' sweep crosses the +w' ejection over the range $18 <$

$y^+ < 748$ with a median of 434. The stronger pair vies for dominance within the buffer layer. The +w' sweep overtakes the -w' ejection in eleven profiles (123a and 125a are the exceptions); the range is $10.8 < y^+ < 21.9$ with a median of 12.7.

Of the interaction octants, octants 1 and 5 dominate over octants 3 and 7 in the log layer. However, as one enters the buffer layer the octant 7 contribution increases dramatically. Octant 1 contributions rise steadily. The contributions from octants 3 and 5 remain almost flat, displaying an initial slow rise and then a slow decline. At the wall, octant 7 becomes the largest contributor among the interaction octants in nine profiles (110a-120a, 125a, 120b-125b, and 123c); octant 1 is close behind. The point, at which octant 7 overtakes octant 1, occurs in the range $8 < y^+ < 21$ with a median of 14.3. As discussed earlier, the contributions of octants 7 and 1 approach the octant 2/8 contributions near the wall as $\alpha_{wc}$ increases. Octant 5 follows in a distant third; octant 3 is the smallest contributor of all the octants.

The ejection octants peak (see Table 6-2) at different locations in the free-stream coordinate flow; moreover, the ejection contributions rapidly decline after reaching their peak. The -w' ejections reach a peak in range, $11 < y^+ < 21$ with an median of 16.7. The +w' ejections reach a peak further up and over much broader range, $18 < y^+ < 680$ with a median of 27.8. The +w' sweeps exhibit a peak outside of the first measurement location for less than half of the profiles, not enough to be considered a trend. The -w' sweeps peak beyond the first measurement location for all but three profiles (110a, 120c, and 125c). This peak typically occurs at the second or third measurement point: $11 < y^+ < 30$ with a median of 15. For profile 130a, the true peak occurs at $y^+ = 646$ although a local peak also exists at $y^+ = 30$.

| Table 6-2: Location Of Peak $u'^2$ Contribution. | | | | |
|---|---|---|---|---|
| Free-stream Coordinates | | | | |
| Octant | Location ($y^+$) | | | |
| | Average | Median | Low | High |
| 1 | 14.3 | 15.9 | 8.0 | 21.5 |
| 2 | 174.3 | 27.8 | 18.2 | 681.7 |
| 3 | 359.2 | 477.6 | 10.1 | 726.5 |
| 4 | 11.2 | 11.2 | 8.0 | 16.7 |
| 5 | 20.2 | 18.2 | 10.1 | 29.9 |
| 6 | 16.5 | 16.7 | 11.0 | 21.4 |
| 7 | 11.1 | 10.1 | 6.9 | 21.5 |
| 8 | 62.9 | 14.0 | 10.1 | 646.2 |
| Wall-Collateral Coordinates | | | | |
| Octant | Location ($y^+$) | | | |
| | Average | Median | Low | High |
| 1 | 12.9 | 11.5 | 6.9 | 21.5 |
| 2 | 16.7 | 16.8 | 11.0 | 21.4 |
| 3 | 88.2 | 11.3 | 6.9 | 477.6 |
| 4 | 11.7 | 11.8 | 8.0 | 16.7 |
| 5 | 19.4 | 18.1 | 9.1 | 29.9 |
| 6 | 17.7 | 17.5 | 11.0 | 25.9 |
| 7 | 10.8 | 9.6 | 6.9 | 21.5 |
| 8 | 11.2 | 11.4 | 8.0 | 16.7 |

In wall-collateral coordinates, all four ejection/sweep octants contribute significantly more to $u'^2$ than the interaction octants. The contributions from the interaction octants remain small except possibly very close to the wall. The ejection sweep octant pairs identified in the free-stream coordinate discussion reverse roles in wall-collateral coordinates. Octant 2/8 is the stronger pair; octant 4/6 is the weaker pair. However, the difference is much smaller than under free-stream coordinates. The gap between sweeps reaches a maximum of $(u'^2)^+_{4\text{-}8} \sim -0.5$ (profile 120a) with an average of -0.27 or 17% of the larger contributor. The gap between ejections reaches a maximum of $(u'^2)^+_{2\text{-}6} \sim 0.46$ (profile 105a) with an average of -0.14 or 10% of the larger contributor. In many profiles, the difference diminishes as one approaches the wall. The contributions from the ejection octants drop dramatically after they peak in the buffer region. In three profiles (115a, 125a, and 130a), the ejection contributions reach or dip below the contribution of octant 1, the largest contributor of the interaction octants. However, for the remaining profiles, the ejection contributions remain at least twice as large as octant 1. In all profiles that extend below $y^+$ of 10,

there exists a point where the contributions from both sweep octants surpass both ejection octants; this point did not exist under free-stream coordinates where the -w' ejection contribution remained larger than the -w' sweep contribution (except at 105a).

Unlike the free-stream coordinate plots, the location where a sweep octant overtakes the ejection octant associated with the same sign of w' do occur for both signs of w'. Moreover, this point exists within the buffer layer. The -w' sweep crosses the -w' ejection within the buffer layer in ten profiles. The exceptions include 110a and 120a, where the sweep is actually dominant throughout the buffer layer, and 125c, where the ejection is dominant throughout the boundary layer. The crossover occurs over the range $15 < y^+ < 33$ with a median of 20. The +w' sweep crosses the +w' ejection in eleven profiles. Profiles 123a and 125c are the exceptions; in both, the ejection remains dominant throughout the buffer layer. The crossover occurs in the range $11 < y^+ < 16$ with a median of 12.8. The +w' crossover location also represents a point where both sweep octants surpass both ejection octants. As in free-stream coordinates, the sweep octants become larger than the ejection octants in the context of the stronger (octant 2/8) and weaker (octant 4/6) pairs. However, this crossover always occurs within the buffer layer and the difference between the crossover points for stronger and weaker pairs is less than $y^+ \sim 5$ for a given profile. The location where the -w' sweeps contribute more than the +w' ejections is found in the range, $14 < y^+ < 28$ with a median of 16.4. (Only 125c does not contain this crossover.) The location where the +w' sweep contribution becomes larger than the -w' ejection contribution occurs in the range, $12 < y^+ < 23$ with a median of 14.4. (Only 123a and 125c do not contain this crossover).

Among the interaction octants, octant 1 remains dominant in a majority of the profiles under wall-collateral coordinates. Octant 5 maintains second place until $y^+ \sim 15$. At this point, the contribution of octant 5 slowly decreases while the contribution of octant 7 dramatically increases. The contribution in octant 7 quickly surpasses that of octant 5. At the point closest to the wall, octant 7 begins to approach or sometimes slightly surpass the contribution of octant 1. At $y^+ > 15$, octant 7 and octant 3 contribute nearly equally and these contributions are the smallest of all the octants. For $y^+ < 15$, octant 5 declines toward the contribution level of octant 3, which remains the smallest contributor of all the octants.

The locations of peak ejection contributions (Table 6-2) are found in a much smaller range than in free-stream coordinates. For a majority of profiles, the contribution peak occurs at the same point for both -w' and +w' ejection octants. Only at 120b and 125b do the peaks occur at different locations; even then they are neighboring measurement locations. These peaks occur in the range $11 < y^+ < 25$ with medians of ~17.4 (+w' ejection) and 18.8 (-w' ejection). The -w' sweeps have a peak in less than half the profiles and the +w' sweeps have a peak in seven out of the thirteen octants. Neither of these constitutes a trend worth exploring in depth. However, it is worth noting that the sweep peaks that exists beyond the first measurement point occur at a median of $y^+ \approx 12$.

Section 6.4.1 showed that data transfers between octants as one rotates from wall-collateral to free-stream coordinates. Coordinate rotation not only transfers points between the octants but it

also redefines the velocity components of all points. Thus, a transfer of points does not necessarily translate into a proportional $u'^2$ contribution transfer. Figures 110 & 111 show the difference in octant contributions between free-stream and wall-collateral coordinates (i.e., free-stream contribution - wall-collateral contribution). Octant contributions do increase or decrease in line with population changes. When comparing octants that exchange data (namely all octants except 1 and 5), the decreasing contributions in octants losing data (i.e. octants four, six, and seven) are greater than the increasing contributions in octants gaining data (i.e. octants two, three, and eight). In octants that lost data in the transfer, the coordinate rotation apparently also decreased the u' component of the remaining points. Octants one and five experienced very little change in octant population. Octant one also shows very little change in its contribution. Octant five, however, demonstrates a small but significant increase in its contribution.

### 6.4.3 Octant Contributions To $\overline{v'^2}$

$v'^2$ (Figures 17 & 18) peaks in the outer layer and quickly decreases as one approaches the wall. The octant analysis shows that the even octants are responsible for this behavior; they are the dominant contributors throughout the boundary layer. The odd octants form a closely grouped set of plots that produce a smaller contribution. Although $v'^2$ is invariant to coordinate rotation, the octant contributions retain coordinate system dependencies because their populations depend on coordinate system. Nevertheless, the near-wall behavior of the octant contributions between coordinate systems remains similar when reviewed from the perspective of the case-1/case-2 classification of ejections and sweeps (see section 6.3.4). In free-stream coordinates, the case-1 ejection and sweep are associated with +w' (octants 6 and 8); the case-2 ejection and sweep are associated with -w' (octants 2 and 4). In wall-collateral coordinates, the opposite is true.

Near the wall, the case-1 sweep provides a slightly higher contribution than the case-2 sweep. In opposition, the case-2 ejection contributes more than the case-1 ejection. The case-1 sweep is the largest contributor near the wall. In wall-collateral coordinates, the case-1 sweep dominates for $y^+ < 67$ at all locations. In free-stream coordinates, this event occurs in the range $17 < y^+ < 46$. The case-2 ejection and case-2 sweep vie for second largest contributor. In free-stream coordinates, the case-2 sweep delivers the second largest contribution at profiles 105a, 110a, and 115a; it is approximately equal to the case-2 ejection contribution at 120a. In wall-collateral coordinates, the contribution from the case-2 sweep and case-2 ejection converge in the buffer layer ($12 < y^+ < 25$) for all profiles. The case-1 ejection is the smallest contributor of the even octants in both coordinate systems. In wall-collateral coordinates, the octant 2/8 octant pair remains dominant throughout the boundary layer. In free-stream coordinates, the octant 4/6 pair becomes dominant but only near the wall. At some point, the octants 2/8 pair overtakes them and remains dominant throughout the outer layer. The point where the cross-over takes place generally increases as $\alpha_{wc}$ increases; it occurs over the range $17 < y^+ < 100$ with a median of 60.

Overall, the contribution differences among the sweep/ejection octants are very small for $y^+ < 30$. In free-stream coordinates, the average difference between sweep contributions is $(v'^2)^+_{4\text{-}8} = 0.025$ or 22% of the case-2 sweep. The average difference between ejection contributions is $(v'^2)^+_{2\text{-}6} =$

-0.029 or 30% of the case-1 ejection. In wall-collateral coordinates, $(v'^2)^+_{4\text{-}8} = -0.022$ or 24% of the case-2 sweep; $(v'^2)^+_{2\text{-}6} = 0.028$ or 22% of the case-1 ejection. The differences are significant but to a much smaller degree when the $v'^2$ uncertainty of ~ 8% is accounted for. Given this uncertainty, the magnitudes of $(v'^2)^+_{2\text{-}6}$ and $(v'^2)^+_{4\text{-}8}$ are approximately equivalent under both coordinate systems. Also, there is no significant change in the magnitude of either $(v'^2)^+_{2\text{-}6}$ or $(v'^2)^+_{4\text{-}8}$ with coordinate rotation.

Between the -w' sweep and ejection octants, contribution crossovers rarely take place near the buffer layer. In wall-collateral coordinates, the -w' sweep contribution dominates the -w' ejection contribution throughout most of the boundary layer ($y^+ < 620$) in all profiles. In free-stream coordinates, the -w' sweep becomes dominant in four of the profiles: 105a at $y^+ = 80$, 110a $y^+ = 563$, 120a at $y^+ = 7.8$, and 120b at $y^+ = 8.2$. However, for the remaining profiles, the -w' ejection dominates near the wall; it crosses -w' sweep over the range $27 < y^+ < 130$ with a median value of 74. The +w' sweep and ejection octants do experience crossovers under both coordinate systems. In free-stream coordinates, the +w' sweep overtakes the +w' ejection over the range $33 < y^+ < 147$ with a median of 78. In wall-collateral coordinates, the +w' sweep overtakes the +w' ejection in eleven of the profiles; 125a and 120b are the exceptions. The crossover point occurs over the range $7.3 < y^+ < 28$ with a median of 17. In free-stream coordinates, the majority of profiles do not contain a point near the wall where the contributions from both sweep octants surpass both ejection octants because the -w' sweep does not overtake the -w' ejection in those profiles. In wall-collateral coordinates this point exists in the majority of profiles. Since the -w' sweep dominates -w' ejection throughout most of the boundary layer and dominates all other octants near the wall, the location where both sweeps overcome both ejections is identical to the point where the +w' sweep overcomes the +w' ejection.

Of the interaction octants, only octant 1 stands out from the rest. It is the largest contributor of the interaction octants in the buffer region under both coordinate systems. For $y^+ < 10$, the contribution of octant one approaches the case-1 ejection contribution. Within uncertainty, octants three, five, and seven are equivalent near the wall; they are the smallest contributors.

The location of peak ejection and sweep contributions to $v'^2$ are given in Table 6-3. They move only slightly with coordinate rotation even though the contribution values change significantly. Only octants 1, 4, and 7 show a significant change in the median peak location. The peak contribution from sweeps and ejections occur mostly in the outer layer, $38 < y^+ < 680$.

| Table 6-3: Location Of Peak $v'^2$ Contribution. | | | | |
|---|---|---|---|---|
| Free-stream Coordinates | | | | |
| Octant | Location ($y^+$) | | | |
| | Average | Median | Low | High |
| 1 | 323.7 | 256.4 | 85.4 | 646.2 |
| 2 | 383.1 | 281.2 | 174.6 | 681.7 |
| 3 | 521.8 | 482.9 | 77.9 | 1,514.0 |
| 4 | 192.7 | 156.6 | 38.4 | 646.2 |
| 5 | 401.5 | 293.6 | 154.3 | 726.5 |
| 6 | 112.1 | 78.9 | 65.5 | 261.9 |
| 7 | 343.6 | 453.5 | 85.4 | 646.2 |
| 8 | 274.6 | 243.3 | 154.3 | 646.2 |
| Wall-Collateral Coordinates | | | | |
| Octant | Location ($y^+$) | | | |
| | Average | Median | Low | High |
| 1 | 359.6 | 453.5 | 85.4 | 646.2 |
| 2 | 338.1 | 248.5 | 154.3 | 681.7 |
| 3 | 535.5 | 482.9 | 174.6 | 1,514.0 |
| 4 | 259.3 | 237.5 | 70.3 | 681.7 |
| 5 | 339.0 | 250.9 | 147.8 | 681.7 |
| 6 | 179.0 | 85.4 | 65.5 | 646.2 |
| 7 | 324.0 | 256.4 | 85.4 | 646.2 |
| 8 | 233.3 | 240.2 | 134.2 | 427.8 |

Figures 112 & 113 show the difference in octant contributions between the free-stream and wall-collateral coordinate systems (i.e., free-stream contribution - wall-collateral contribution). Unlike the u' or w' values, v' values are not affected by coordinate rotation. Thus, the differences demonstrate a net transfer of v' between octants. Only the sweep and ejection octants experience a significant transfer of v' near the wall. The contribution difference among the interaction octants is minuscule in the buffer layer; only for $y^+ > 30$, do significant differences occur. Changes among the sweep and ejection octants, while more significant, also diminish as one approaches the wall; they are largest in the log and wake regions. In the near wall region, the ejection and sweep contribution changes have the same sign as the population exchanges. Thus, the data points transferred from the sweep or ejection octant to the other must contain larger v' events on average than the points originally occupying the recipient. The transferred data has a good probability of true association with a high v' event such as an ejection or sweep as opposed to a random event that

happens to populate an "ejection" or "sweep" octant. Since true sweep and ejection events are related to coherent structures (see section 6.2), this bolsters the conjecture (in section 6.4.1) that the size of the population exchanges indicate the presence of a coherent structure in the area swept by the rotation.

### 6.4.4 Octant Contributions To $\overline{w'^2}$

$w'^2$ (Figures 19-22) peaks in the outer layer ($y^+ > 300$). After peaking, it slowly declines until $y^+ \approx 50$; then it drops quickly to zero at the wall. Unlike the octant plots of $u'^2$ and $v'^2$, the behavior of $w'^2$ cannot be attributed to a small set of dominant octants. No clear separation of octant contribution profiles exist near the wall. The ejection/sweep octants mix with the interaction octants. However, generally the largest contributor remains an even octant and the smallest contributor is an interaction octant. Each coordinate system also has a distinct pair of "stronger" ejection/sweep contributors and "weakened" ejection/sweep contributors. They are identical pairs to those identified in the prior two sections (6.4.2 and 6.4.3); e.g., in wall-collateral coordinates, octants 4 and 6 are the "weakened" pair.

In both coordinate systems, the case-1 sweep is the largest contributor near the wall ($y^+ < 30$). Within the buffer layer, the case-2 ejection and octant 1 (interaction) vie for next largest contributor. In free-stream coordinates, octant 1 overtakes octant 6 (case-2 ejection) in eight profiles; the exceptions are 123a, 125b, 120c, 123c, and 125c. This events takes place over the range $9 < y^+ < 27$ with a median of 14.8. In wall-collateral coordinates, octant 1 overcomes octant 2 (case-2 ejection) in all but one profile, 125c. This occurs in the range $9 < y^+ < 29$ with a median of 15.1. Octant 1 dominates over the "weakened" ejection/sweep octants in the buffer region; as one moves away from the wall, the "weakened" ejection/sweep octants become larger contributors in the log layer. In free-stream coordinates, octant 1 crosses octant 8 (case-2 sweep) over the range $17 < y^+ < 61$ with a median of 42.6. In wall coordinates, octant 1 and octant 4 (case-2 sweep) cross in the range $17 < y^+ < 86$ with a median of 22.7; this occurs for all profiles except 125c. In both coordinates, the case-2 sweep and case-1 ejection are approximately equal in contribution near the wall; however, the case-2 sweep tends to be the larger of the two. Whether octant 7 or 5 follow in contribution size is coordinate system dependent. In free-stream coordinates, octant 7 quickly grows in size and overtakes octant 5 in many of the profiles; in wall-collateral coordinates, octant 5 remains dominant over octant 7 throughout the inner layer. Octant 3 remains the smallest contributor in both coordinate systems. In both coordinate systems, the octant 2/8 pair are the largest contributors in the outer layer. However, in free-stream coordinates, the octant 4/6 pair overtakes the octant 2/8 pair within the range, $20 < y^+ < 140$ with a median of 114.

The disparity in contributions between sweeps and between ejections varies for $w'^2$ under both coordinate systems. The following $w'^2$ contribution differences are averages based on the buffer layer points (first 4 points) of every profile. In free-stream coordinates, the average ejection "gap" is $(w'^2)^+_{2\text{-}6} = -0.22$ or 50% of the larger contributor; the average sweep "gap" is $(w'^2)^+_{4\text{-}8} = 0.25$ or 52% of the larger contributor. In wall-collateral coordinates, $(w'^2)^+_{2\text{-}6} = 0.056$ or 19% of the larger contributor; and $(w'^2)^+_{4\text{-}8} = -0.10$ or 28% of the larger contributor. Thus, $(w'^2)^+_{2\text{-}6}$ and

$(w'^2)^+_{4-8}$ are nearly equal in free-stream coordinates; however, in wall-collateral coordinates, the $(w'^2)^+_{4-8}$ (the sweep disparity) is nearly twice as large as $(w'^2)^+_{2-6}$ (the ejection disparity). Since this paper categorizes sweeps and ejections by the sign of w', examining the difference in $w'^2$ contribution between sweeps and ejections associated with the same sign of w' is of interest. In free-stream coordinates, the contribution difference between the -w' ejection and -w' sweep is $(w'^2)^+_{2-4}$ = 0.22 or 48% of the ejection contribution. The contribution difference between +w' ejection and +w' sweep is $(w'^2)^+_{6-8}$ = -0.26 or 61% of the sweep contribution. In wall-collateral coordinates, $(w'^2)^+_{2-4}$ = -0.12 or 33% of the sweep contribution; and $(w'^2)^+_{6-8}$ = 0.044 or 14% of the ejection contribution. These numbers reveal two trends. First, $(w'^2)^+_{2-4}$ and $(w'^2)^+_{6-8}$ are much larger in free-stream coordinates than in wall-collateral coordinates. Second, in free-stream coordinates, $(w'^2)^+_{6-8}$ is larger than $(w'^2)^+_{2-4}$; in wall-collateral coordinates, the opposite is true. In section 6.5, these trends are the foundation for creating a dynamic model based on the production of w'.

In both coordinate systems, the +w' ejection and -w' sweep generally peak in the outer layer (see Table 6-4); the peaks occur in the range, $44 < y^+ < 750$. In wall-collateral coordinates, the +w' sweep and -w' ejection contributions peak over a broader range of locations, $27 < y^+ < 750$. However, the -w' ejection and +w' sweep peak closer to the wall in free-stream coordinates. The +w' sweep contribution peaks in the range $11 < y^+ < 33$ with a median location of 17.5; only profile 123b does not exhibit this peak. The -w' ejection contribution peaks in the range $18 < y^+ < 44$ with a median of 27.6. All of the interaction octants peak in the outer layer ($30 < y^+ < 750$) with the exception of octant 1. Octant 1, under free-stream coordinates, peaks in the buffer region over the range $9 < y^+ < 32$ with a median of 19; however, octant 1 has no peak in profile 120a. In wall-collateral coordinates, octant 1 peaks over a much broader range, $20 < y^+ < 650$ but the median location of 37.6 remains in the log layer. In general, contributions from sweep and ejection octants with same-sign w' do not cross within the boundary layer. However, in free-stream coordinates, the -w' sweep does overtake the -w' ejection in eleven profiles (110a and 123c are the exception). These crossovers occur in the range $44 < y^+ < 180$ with a median of 112. In wall-collateral coordinates, the -w' octants only cross in five profiles (123a, 123b, 125b, 120c, and 125c); this is not sufficient to be identified as a trend.

| Table 6-4: Location Of Peak $w'^2$ Contribution. | | | | |
|---|---|---|---|---|
| Free-stream Coordinates | | | | |
| Octant | Location ($y^+$) | | | |
| | Average | Median | Low | High |
| 1 | 19.71 | 19.61 | 6.85 | 32.02 |
| 2 | 433.13 | 477.60 | 156.60 | 751.70 |
| 3 | 536.83 | 488.00 | 174.60 | 864.10 |
| 4 | 19.07 | 18.01 | 10.95 | 32.65 |
| 5 | 397.84 | 477.60 | 30.13 | 751.70 |
| 6 | 30.17 | 28.28 | 18.01 | 43.94 |
| 7 | 335.66 | 427.80 | 85.40 | 503.60 |
| 8 | 365.06 | 453.50 | 43.77 | 646.20 |
| Wall-Collateral Coordinates | | | | |
| Octant | Location ($y^+$) | | | |
| | Average | Median | Low | High |
| 1 | 230.8 | 37.6 | 19.6 | 646.2 |
| 2 | 426.3 | 477.6 | 85.4 | 751.7 |
| 3 | 535.7 | 511.4 | 174.6 | 751.7 |
| 4 | 204.4 | 42.2 | 26.6 | 751.7 |
| 5 | 378.8 | 477.6 | 30.1 | 751.7 |
| 6 | 195.2 | 71.9 | 38.4 | 751.7 |
| 7 | 320.7 | 427.8 | 77.6 | 488.0 |
| 8 | 346.7 | 281.2 | 43.8 | 646.2 |

Figures 114 & 115 show the octant contribution differences between the two coordinate systems (i.e., contribution in free-stream coordinates - contribution in wall-collateral coordinates). The contribution differences only weakly correlate with the population differences. The coordinate rotation has a greater influence on $w'^2$ contributions than does the actual data transfer between octants. Octant 1 shows a large decrease in $w'^2$ contribution as one rotates from free-stream to wall-collateral coordinates despite the fact that it experiences a negligible population loss. Octant five, which also undergoes a small population change, has a moderate gain in $w'^2$ contribution. Large data transfers occur from the -w' octants to the +w' octants. Nevertheless, the loss in the -w' ejection and +w' sweep contributions is ~50% larger than the gain in +w' ejection and -w' sweep contributions. A significant data transfer also takes place between octant 7 and octant 3. However, octant 7 experiences a large decrease in its $w'^2$ contribution and octant 3 achieves a very small gain.

### 6.4.5 Octant Contributions To $\overline{u'v'}$

u'v' (Figures 23-26) remains positive and slowly climbs to a peak in the range $30 < y^+ < 300$; then it quickly decreases toward zero at the wall. The octant analysis reveals that octant contributions fall into two groups. The even octants produce large positive u'v' contributions that account for the majority of the u'v' stress and its behavior. The interaction octants produce much smaller, negative u'v' contributions. However, in free-stream coordinates, the u'v' contribution from octant 1 becomes larger than the octant 2 contribution (+w' ejection) very close to the wall in three of the profiles: 115a, 120a, and 130a. Nevertheless, the octant 2 contribution remains larger than the octant 1 contribution in the remaining profiles. In wall-collateral coordinates, the gap between the even and interaction contributions is wider. Of the even octants, the case-2 ejection and case-1 sweep are the stronger contributors for $y^+ < 30$ in both coordinate systems; this repeats the pattern established in the last three Reynolds stresses (sections 6.4.2-6.4.4). (At 105a in free-stream coordinates, these octants do not actually become dominant until $y^+ \sim 20$; but the statement holds true for all other profiles) In wall-collateral coordinates, the "stronger" ejection/sweep pair (octants 2 and 8) remains the largest contributor throughout most of the boundary layer. In free-stream coordinates, the "weakened" ejection/sweep octants (2 and 8) eventually overtake the "stronger" ejection/sweep octants (4 and 6) as one enters the log layer; the crossover location occurs in the range $20 < y^+ < 110$ with a median of 64. This location increases with $\alpha_{wc}$.

The contribution differences between sweeps and between ejections is much larger in free-stream coordinates than in wall-collateral coordinates. The "gap" averages from the prolate spheroid flow were computed using the buffer layer measurements (first four points) of all the profiles. In free-stream coordinates, the average ejection "gap" is $(u'v')^+_{2\text{-}6} = -0.12$ or 41% of the larger contributor; the average sweep "gap" is $(u'v')^+_{4\text{-}8} = 0.10$ or 35% of the larger contributor. In wall-collateral coordinates, $(u'v')^+_{2\text{-}6} \sim 0.041$ or 17% of the larger contributor; $(u'v')^+_{4\text{-}8} \sim 0.062$ or 22% of the larger contributor.

Whether the sweep contributions grow larger than the contributions of their companion ejections as one approaches the wall is coordinate system dependent. In free-stream coordinates, the -w' sweep overtakes the -w' ejection in profiles 105a-120a. However, the crossing location grows closer to the wall as $\phi$ progress; it decreases from $y^+ = 18.2$ at 105a to $y^+ = 7.3$ at 120a. In the remaining profiles, the -w' ejection remains larger than the -w' sweep down to the lowest measurement point. The trend is different for the +w' contributions. The +w' sweep grows larger than the +w' ejection over a broad range of locations, $20 < y^+ < 198$ with a median of 104. In wall-collateral coordinates, the -w' sweep is larger than the -w' ejection throughout the inner layer in nine profiles. In the remaining four profiles (115a, 120b, 120c, and 125c), the -w' ejection momentarily climbs higher than the -w' sweep but the -w' sweep regains its dominance near the edge of the buffer layer ($y^+ \approx 28$). The +w' sweep overtakes the +w' ejection in the lower portion of the boundary layer (except for profile 125c). This occurs over the range $11.8 < y^+ < 15.8$ with a median of 13.5. As a consequence of these numbers, only the wall-collateral coordinate system has a location where both sweeps overtake both ejections; this location is identical to the location where the +w' sweep crosses the +w' ejection. Thus, wall-collateral coordinates better maintains

the near wall importance of sweep events found in 2DTBLs. However, when the sum of the sweep contributions (i.e., quadrant four) is compared to the sum of the ejection contributions (i.e., quadrant two), a location where the sweep contributions overtake the ejection contributions appears under both coordinate systems. Moreover, this location occurs over a nearly identical range of values, $16 < y^+ < 28$ with a median of 20.

There exist large disparities in the octant contributions between the two coordinate systems; yet, the coordinate systems agree on where the quadrant-2 sweep crosses the quadrant-4 ejection. Examining how the octant contributions change between free-stream and wall-collateral coordinates (Figures 116-117) provides some insight. Octants 2 and 8 experience a decrease in population (see section 6.4.1.) and in u'v' as one rotates from wall-collateral coordinates to free-stream coordinates. Octants 4 and 6 experience a nearly equal increase in population and u'v'. Thus, a net transfer of u'v' occurs. The quadrant crossing points remain constant for two reasons: 1) Transfers of large +u'v' events occur only between ejection octants and between sweep octants, i.e. within a quadrant. 2) v' remains constant over the coordinate rotation; and the rotation only reduces u' by 6%, worst case. Thus, the coordinate rotation has a small affect on the quadrant representation of u'v' events. The near invariance of the quadrant sweep-ejection crossover, with rotation to coordinate systems of interest, makes the location an undisputed feature of the flow. In fact, the previously quoted range of cross-over locations obscures the near constant location of this point in the prolate spheroid flow. If one removes the lowest and highest point in the range, the range becomes much narrower: $18.5 < y^+ < 21.5$.

The even octants have contribution peaks at different locations depending on coordinate system (see Table 6-5). In free-stream coordinates, the +w' sweep (case-2) exhibits a peak over the range $21 < y^+ < 79$ with a median of 49. The -w' ejection peaks over the range $26 < y^+ < 72$ with a median location of 30. The remaining ejection/sweep contributions peak much higher in the boundary layer. These peaks occur in the range $154 < y^+ < 682$. In wall-collateral coordinates, the +w' sweep peaks over a slightly larger range, $34 < y^+ < 143$ with a median of 71. The -w' ejection peaks in slightly higher range, $28 < y^+ < 72$ with a median of 35. The remaining octant peaks also remain outside of the valid octant mapping; but they do move closer to the wall, $32 < y^+ < 646$.

| Table 6-5: Location Of Peak u'v' Contribution. | | | | |
|---|---|---|---|---|
| Free-stream Coordinates | | | | |
| Octant | Location ($y^+$) | | | |
| | Average | Median | Low | High |
| 1 | 215.6 | 71.9 | 32.0 | 646.2 |
| 2 | 373.2 | 281.2 | 43.8 | 681.7 |
| 3 | 455.7 | 488.0 | 77.9 | 726.5 |
| 4 | 48.3 | 32.7 | 20.9 | 78.9 |
| 5 | 322.1 | 261.9 | 42.2 | 681.7 |
| 6 | 37.1 | 30.1 | 25.9 | 72.3 |
| 7 | 337.7 | 453.5 | 77.9 | 646.2 |
| 8 | 267.8 | 243.3 | 85.4 | 646.2 |
| Wall-Collateral Coordinates | | | | |
| Octant | Location ($y^+$) | | | |
| | Average | Median | Low | High |
| 1 | 213.0 | 71.9 | 32.0 | 646.2 |
| 2 | 217.5 | 240.2 | 31.9 | 503.6 |
| 3 | 455.7 | 488.0 | 77.9 | 726.5 |
| 4 | 67.3 | 71.9 | 31.9 | 142.6 |
| 5 | 246.2 | 225.5 | 42.2 | 646.2 |
| 6 | 48.7 | 35.9 | 28.3 | 85.4 |
| 7 | 343.6 | 453.5 | 85.4 | 646.2 |
| 8 | 222.3 | 236.7 | 70.3 | 646.2 |

### 6.4.6 Contributions To $\overline{u'w'}$

u'w' (Figures 27-30) initially climbs to a positive peak near the boundary layer edge; but for $y^+ <$ 300, continually declines. In free-stream coordinates, u'w' crosses zero outside of the log layer ($100 < y^+ < 300$). In wall-collateral coordinates, u'w' becomes negative below $y^+ \approx 15$. u'w' increases with maximum spanwise velocity; thus the u'w' profiles spread out rather than collect together in a tight range like u'v'. The octant contributions to u'w' show no obvious resemblance to their total. The plots generally separate into four pairs of octants. Two pairs are negative; two pairs are positive. The even octants pair as octants 4/6 and octants 2/8. The interaction octants pair as octants 1/5 and octants 3/7. The even octant pair is larger than the interaction octant pair on the same-sign of u'w'. In free-stream coordinates, the octant pairs generating negative u'w' (4/6 and 3/5) dominate over the ones generating positive u'w' (2/8 and 1/7) in the inner layer. In

wall-collateral coordinates, the even octant pair generating positive u'w' (2/8) dominates. However, the interaction octant pair generating negative u'w' (1/5) remains slightly dominant over the interaction octant pair generating positive u'w' (4/6).

The degree of even octant dominance is very different between the two coordinate systems. In free-stream coordinates, the +w' sweep (octant 4) is 49% larger than the -w' sweep (octant 8) on average in the buffer layer; $(u'w')^+_{4\text{-}8} = 0.35$ on average over the first four points of every profile. The, -w' ejection (octant 6) is larger than the +w' ejection (octant 2) by 61%; $(u'w')^+_{2\text{-}6} = -0.41$ on average. The large percentages result from the fact that the octant 4/6 pair diverges significantly as one enters the log layer and peaks within the buffer layer. At the same time, the octant 2/8 pair declines rapidly toward the interaction contributions. The level of divergence and decline appears to increase with $\alpha_{wc}$. This correlation is best demonstrated by the location where interaction octant 1 generates a larger contribution than the octant 2/8 pair. Octant 1 surpasses octant 2 in all profiles. The crossover location starts from $y^+ = 12$ at 105a and grows as large as $y^+ = 46$ at 130a; the median is 33. Octant 1 also surpasses octant 8 in eleven profiles; 105a and 125c are the exceptions. The crossover location starts from $y^+ = 13$ at 110a and grows to $y^+ = 39$ at 130a; the median is 27. Octant 7 also overcomes octant 2 in eleven profiles; 105a and 125c are again the exceptions. The crossover location covers the range, $11.7 < y^+ < 27$ with a median of 14.7.

In wall-collateral coordinates, the dominance of octant 2/8 is more subtle. The -w' sweep (octant 8) is 25% larger than the +w' sweep (octant 4) on average in the buffer layer; $(u'w')^+_{4\text{-}8} = -0.13$. The, +w' ejection (octant 2) is larger than the -w' ejection (octant 6) by 15%; $(u'w')^+_{2\text{-}6} = 0.06$. The octant 2/8 pair increases rapidly near the boundary layer edge. The remaining octant pairs increase moderately at the same location; of these, the octant 4/6 pair increases most. The octant contributions then stay nearly level until one enters the inner layer. Then, both even octant pairs increase slightly. Both -w' and +w' ejection contributions also drop sharply in the buffer layer. However, since the -w' ejection experienced a smaller increase in the outer layer; its rapid drop in the buffer layer keeps it below +w' ejection and eventually carries it below the contribution level of octant 1 in seven profiles (110a-120a, 125a, 130a, 120b, and 123b). The crossover locations range from $9 < y^+ < 26$.

Between coordinate systems, the relative strength of sweeps and their companion ejections differ slightly as one approaches the wall. In free-stream coordinates, the -w' ejection contributes more than the -w' sweep in the buffer layer for all profiles except at 105a. In the log region, the -w' sweep becomes larger and remains so near the boundary layer edge. The crossover occurs in the range $61 < y^+ < 129$ with a median of 97. The +w' sweep, however, overcomes the +w' ejection beyond the buffer layer and remains dominant down to the lowest measurement. This crossover occurs over the range $43 < y^+ < 186$ with a median of 127. In wall-collateral coordinates, the -w' sweep contributes more than the -w' ejection throughout the inner layer. The +w' sweep overcomes the +w' ejection within the buffer layer for all profiles except 130a. This event occurs over the range $11.7 < y^+ < 19.5$ with a median value of 14. As a consequence of these numbers, the free-stream coordinate system produces no location where both sweep contributions exceed their

companion ejections. However, this location does appear in wall-collateral coordinates; it is the same location where the +w' sweep and +w' ejection cross.

Between coordinate systems, the locations of peak ejection/sweep contributions vary little (see Table 6-6). In both coordinate systems, the -w' sweep and +w' ejection contributions peak across a broad range of locations, $13 < y^+ < 752$. The -w' ejection and +w' sweep peak within the buffer layer. In free-stream coordinates, the -w' ejection peaks over the range $11 < y^+ < 26$ with a median of 18. The +w' sweep peaks over the range $10 < y^+ < 18$ with a median of 12. In wall-collateral coordinates, the -w' ejection peaks over the range $18 < y^+ < 41$ with a median of 27. The +w' sweep peaks over the range $11 < y^+ < 22$ with a median of 17.

**Table 6-6: Location Of Peak u'w' Contribution.**

| Free-stream Coordinates | | | | |
|---|---|---|---|---|
| Octant | Location ($y^+$) | | | |
| | Average | Median | Low | High |
| 1 | 13.8 | 13.1 | 6.9 | 21.5 |
| 2 | 422.5 | 482.9 | 31.9 | 751.7 |
| 3 | 455.3 | 482.9 | 40.7 | 751.7 |
| 4 | 13.0 | 12.2 | 10.1 | 18.0 |
| 5 | 233.6 | 38.4 | 20.0 | 751.7 |
| 6 | 18.3 | 18.2 | 11.0 | 25.9 |
| 7 | 29.1 | 11.0 | 6.9 | 246.5 |
| 8 | 307.1 | 250.9 | 20.0 | 646.2 |
| Wall-Collateral Coordinates | | | | |
| Octant | Location ($y^+$) | | | |
| | Average | Median | Low | High |
| 1 | 13.82 | 13.08 | 6.85 | 21.50 |
| 2 | 262.55 | 236.70 | 18.15 | 681.70 |
| 3 | 453.28 | 482.90 | 40.68 | 751.70 |
| 4 | 16.12 | 16.73 | 10.95 | 21.50 |
| 5 | 21.43 | 19.98 | 14.34 | 29.94 |
| 6 | 26.61 | 26.61 | 18.01 | 40.68 |
| 7 | 167.78 | 43.77 | 8.01 | 477.60 |
| 8 | 120.66 | 19.98 | 11.63 | 477.60 |

### 6.4.7 Contributions To $\overline{v'w'}$

v'w' (Figures 31-34), like u'w', has very different behavior between the two coordinate systems. In free-stream coordinates, v'w' grows to a negative peak in the outer layer, it approaches zero as it enters the log layer. Then, for many profiles, it has a positive peak before approaching zero at the wall. In wall-collateral coordinates, v'w' has simpler behavior. It grows to a negative peak in the outer layer; then it gradually declines to zero near the wall. Like the u'w' octant decomposition, the octant contributions to v'w' show no obvious resemblance to their total. The plots generally separate into four pairs of octants. Two pairs are negative; two pairs are positive. The even octants pair as octants 4/6 and octants 2/8. The interaction octants pair as octants 1/7 and octants 3/5. The even octant pairs are larger than the interaction octant pair on the same sign of v'w'. In wall-collateral coordinates, the octant pairs generating negative v'w' (2/8 and 1/7) dominate over the ones generating positive v'w' (4/6 and 3/5) in the inner layer. In free-stream coordinates, the even octant pair generating positive v'w' (4/6) dominates in the inner layer. However, the interaction octant 1, generating negative v'w', remains slightly dominant over the other interaction octants.

The differences in the octant contributions between coordinate systems are most subtle for v'w'. As one rotates from free-stream coordinates to wall-collateral coordinates, the positive contributions from even octants decrease and the negative contributions from even octants increase with little change in the shape of the contribution profiles. However, the changes are large enough such that the larger contributing pair in the buffer layer changes from the octant 4/6 pair to the octant 2/8 pair. Also, octant 6 does moves slightly closer to octant 4; octant 8 migrates minutely away from octant 2. In free-stream coordinates, the disparity between the +w' sweep (octant 4) and the -w' sweep (octant 8) is 41% in the buffer layer on average; $(v'w')^+_{4\text{-}8} = 0.056$ averaged over the first four points of every profile. The disparity between the -w' ejection (octant 6) and the +w' ejection (octant 2) is 34%; $(v'w')^+_{2\text{-}6} = -0.051$. In wall-collateral coordinates, the -w' sweep is larger than the +w' sweep by 29%; $(v'w')^+_{4\text{-}8} = -0.038$. The +w' ejection is larger than the -w' ejection by 20%; $(v'w')^+_{2\text{-}6} = 0.019$. The interaction contributions demonstrate little change overall; this leads to the most notable difference between the two coordinates systems. Under free-stream coordinates, the octant 2/8 pair contributes less than octant 1 below a median location of $y^+ = 15$. The range of crossover locations is $12 < y^+ < 29$, including all profiles except 105a and 125c where octant 1 does not overcome the octant 2/8 pair. Under both coordinate systems, octant 1 occasionally surpasses the -w' ejection (octant 6). In free-stream coordinates, nearly half of the profiles (110a-120a, 125a, 130a, and 120b) display this trend; the crossover occurs very close to the wall ($y^+ \sim 10$). In wall-collateral coordinates, only profiles 115a, 120a, 125a, 130a, and 120b show this trend; the crossover also occurs very close to the wall though slightly higher than in free-stream coordinates ($y^+ \sim 15$). The strength of octant 1 is accentuated by the octant stress plots where the octant 1 v'w' stress surpasses the stress values of the +w' ejection and -w' sweep octants within the inner layer under both coordinate systems. Octant 5 also shows considerable strength; it intermixes with the stress profiles of the -w' ejection and +w' sweep under both coordinate systems. Thus, the octant stress profiles separate into two groups below the log layer: a strong group (even octants, octant 1, and octant 5) and a weak group (octants 3 and 7).

Near the wall, contribution magnitudes from ejections and sweeps associated with the same sign w' generally do not cross in the buffer layer. The +w' octants under free-stream coordinates provide the only instance of this event. The +w' sweep overtakes the +w' ejection over a wide range of locations, $31 < y^+ < 148$ with a median location of 75. For the -w' octants under free-stream coordinates, either the ejection or the sweep is the largest contributor throughout the buffer layer for a given profile. In profiles 105a and 110a (which have the smallest $\alpha_{wc}$), the -w' sweep is the larger contributor. In the remaining profiles, the -w' ejection is the larger contributor; it overtakes the -w' sweep near the log layer, $66 < y^+ < 130$ with a median of 102. Under wall-collateral coordinates, the -w' sweep contributes more than the -w' ejection through most of the boundary layer. Likewise, the +w' ejection contribution is larger the +w' sweep contribution for through of the boundary layer.

**Table 6-7: Location Of Peak v'w' Contribution.**

| Free-stream Coordinates | | | | |
|---|---|---|---|---|
| Octant | Location ($y^+$) | | | |
| | Average | Median | Low | High |
| 1 | 250.4 | 168.2 | 70.3 | 646.2 |
| 2 | 387.4 | 470.7 | 85.4 | 646.2 |
| 3 | 504.1 | 488.0 | 77.9 | 791.2 |
| 4 | 115.2 | 78.9 | 38.4 | 261.9 |
| 5 | 419.1 | 477.6 | 77.9 | 751.7 |
| 6 | 65.3 | 71.9 | 29.9 | 85.4 |
| 7 | 308.1 | 248.5 | 85.4 | 488.0 |
| 8 | 338.2 | 261.9 | 154.3 | 646.2 |
| **Wall-Collateral Coordinates** | | | | |
| Octant | Location ($y^+$) | | | |
| | Average | Median | Low | High |
| 1 | 351.5 | 453.5 | 85.4 | 646.2 |
| 2 | 376.4 | 281.2 | 85.4 | 681.7 |
| 3 | 485.5 | 488.0 | 77.6 | 912.5 |
| 4 | 228.4 | 237.5 | 38.4 | 681.7 |
| 5 | 401.9 | 477.6 | 43.8 | 681.7 |
| 6 | 168.9 | 77.9 | 38.4 | 681.7 |
| 7 | 316.1 | 261.9 | 85.4 | 485.4 |
| 8 | 293.1 | 246.5 | 154.3 | 646.2 |

The octant contributions tend to peak in the log or outer layer under both coordinate systems. In all cases, the peaks cover a broad range of values as show in Table 6-7. Between the coordinate systems, the median location of peak values change little for octants 3, 5, 7, and 8. The median of the octant 6 peaks increases slightly from ~72 to ~78 but masks a far greater change. The average location jumps from ~65 to ~170. Octant 1 experiences the greatest change in median peak location, from ~170 to ~450. With the exception of octants 6 and 7, the median peak of the even octants is close to 250 and the median peak of the interaction octants is in the neighborhood of 475 under wall-collateral coordinates. These peaks imply that the bulk of v'w' production occurs outside of the inner layer.

## 6.5 Discussion.

A number of octant trends are common to both free-stream and wall-collateral coordinate systems, particularly when they are viewed from the perspective of the case-1/case-2 classification of ejections and sweeps. As stated in section 6.2, Shizawa and Eaton (Eaton, 1995) introduced the idea of classifying QSVs by comparing the sign of their rotation with the streamwise component of the mean, near-wall vorticity ($\omega_{x,\,b.l.}$). Case-1 QSVs had a sign of rotation that opposed $\omega_{x,\,b.l.}$; case-2 QSVs had the same sign of rotation as $\omega_{x,\,b.l.}$. In this paper, we generalize the classification to ejections and sweeps. The ejections and sweeps caused by a QSV would be associated with w' whose sign is opposite that of the QSV's rotation. Thus, a case-1 ejection or sweep is associated with w' that has the same sign as $\omega_{x,\,b.l.}$. A case-2 ejection or sweep is associated with w' that has the opposite sign of $\omega_{x,\,b.l.}$. For the given flow, $\omega_{x,\,b.l.}$ is positive in free-stream coordinates and negative in wall-collateral coordinates. Thus, ejection and sweep octants swap classification as one rotates from the free-stream to wall-collateral coordinates. In free-stream coordinates, octants 2 and 4 (+w' ejection and sweep) are classified as case-1; octants 6 and 8 (-w' ejection and sweep) are classified as case-1. In wall-collateral coordinates, octants 6 and 8 are classified as case-1; octants 2 and 4 are classified as case-2.

When the case-1/case-2 classification is applied to the octant analysis we obtain the first three of the following trends that are coordinate system independent:

1) The case-2 ejections contribute more than the case-1 ejections to all six Reynolds stresses within the buffer and lower log layers (see table 6-8).
2) The case-1 sweeps contribute more than the case-2 sweeps to all six Reynolds stresses within the buffer and lower log layers (see table 6-8).
3) The case-2 ejection and case-1 sweep octants have a larger population of velocity events than either the case-2 sweep or case-1 ejection. In wall-collateral coordinates, the percentage ratio of case-2/case-1 ejection is 54/46 at the first point, averaged over all profiles; the percentage ratio of case-1/case-2 sweeps is 55/45. This ratio remains nearly constant for the first six points, $y^+ < 72$. In free-stream coordinates, the percentage ratio of case-2/case-1 ejections is 66/34; the percentage ratio of case-1/case-2 ejections is 62/38. However, at the sixth point in the profiles, both of these ratios narrow to an average of 50/50.

4) The sweep quadrant becomes a more important contributor to u'v' than the ejection quadrant below $y^+ \approx 20$.
5) Octant 1 produces significant contributions to $w'^2$, u'w', and v'w' in the lower log layer.
6) Octant 3 is the weakest contributor for any of the six Reynolds stresses.

Trends #4 and #5 will be discussed more in-depth in the comparison with other 3DTBL, coherent-structure experiments. Trend #6 is nothing more than a curiosity. Thus, the discussion will now focus on the first three trends. The three trends become the basis on which a simple dynamic model of the flow is built.

**Table 6-8 Contribution Differences**

| Reynolds Stress | Case-2 - Case-1 Ejection | | | | Case-1 - Case-2 Sweep | | | |
|---|---|---|---|---|---|---|---|---|
| | Free-stream Coordinates | | Wall-Collateral Coordinates | | Free-stream Coordinates | | Wall-Collateral Coordinates | |
| | Normalized | % | Normalized | % | Normalized | % | Normalized | % |
| $(u'^2)^+$ | 1.09 | 57.58 | 0.14 | 10.11 | 0.74 | 38.35 | 0.27 | 17.43 |
| $(v'^2)^+$ | 0.03 | 22.39 | 0.02 | 24.08 | 0.03 | 29.54 | 0.03 | 22.09 |
| $(w'^2)^+$ | 0.22 | 49.82 | 0.06 | 18.91 | 0.25 | 51.52 | 0.10 | 28.15 |
| $(u'v')^+$ | 0.12 | 40.86 | 0.04 | 17.44 | 0.10 | 34.68 | 0.06 | 22.00 |
| $(u'w')^+$ | 0.41 | 61.20 | 0.06 | 15.20 | 0.35 | 49.49 | 0.13 | 25.08 |
| $(v'w')^+$ | 0.05 | 34.16 | 0.02 | 19.55 | 0.06 | 41.27 | 0.04 | 29.03 |

- The differences are based on the magnitude of the contributions not their absolute values. The differences are also averaged over the first four points (buffer layer points) of all profiles.
- Values are normalized by $u_\tau^2$. Percentages represent the difference as a percentage of the larger contributor.

### *6.5.1 The Dynamic Model*

As shown in Table 6-8, the disparities in stress contributions for $w'^2$ are among the widest by percentage. Thus, the production of w' becomes the focus of our discussion. From a detailed examination of the w' asymmetry, a structural model will be formulated which not only explains the disparity in $w'^2$ but also provides a comprehensive explanation for the emergence of non-zero u'w' and v'w'. Recent experiments in 3DTBL structure (see section 6.2) show that the spanwise pressure gradient causes slight asymmetries in the spanwise trajectories of sweep and ejection events. Many of these experiments attribute the asymmetries to complex interactions between QSVs and the crossflow. However, these asymmetries can be explained in more simple terms by extending the ejection/sweep production of u' to three dimensions. The ejection/sweep process produces u' fluctuations because it moves fluid vertically through a high streamwise velocity gradient. In a 3DTBL, a spanwise profile evolves with its own gradient in the wall normal direction. Thus sweeps and ejections should also produce w' fluctuations using the same mechanism (see figure 70). The importance of the spanwise velocity gradient in the dynamic model is not surprising. Trends, which emerge from application of the case-1/case-2 classification, demonstrate a

symmetry about $\omega_{x,\,b.l.}$. Since $\frac{\partial \overline{W}}{\partial y}$ is the dominant term of $\omega_{x,\,b.l.}$, these trends are also symmetric about the spanwise velocity gradient. Thus, the spanwise velocity gradient must play an important role in the dynamics of this 3DTBL.

Characterizing the process in wall-collateral coordinates is simple because the spanwise profile monotonically decreases to the boundary layer edge. Ejections transport near-wall fluid where W is nearly zero upward to a region where W is negative; this results in +w'. Sweeps transport fluid from a region where W is largely negative down toward the wall where it approaches zero. This results in -w'. The same process in free-stream coordinates is slightly more complicated because the profile of W has a positive bulge in the log layer. Ejections originating near the wall transport fluid with near-zero spanwise velocity upward to a region where W is positive; this results in -w'. Sweeps originating in the vicinity of the bulge have the opposite affect. They push fluid with large positive W to the wall where W is near zero; this results +w'. Above the bulge the picture is more clouded; the effects of sweeps and ejections depend on their origination and destination. However, sufficiently far from the bulge ($y^+ > 150$-$300$), sweep-like and ejection-like motions should have the opposite effect to those near the wall. Sweep-like motions produce -w' and ejection-like motions produce +w'.

This production model of w' is complicated by the rotational nature of sweeps and ejections. In 2DTBLs, sweeps and ejections are frequently associated with QSVs (Robinson, 1991). The rotational motion of the QSV induces its own moderate w' (Sendstad and Moin, 1992). This rotationally-induced w' has a sign opposite to the rotational sign of the QSV; i.e., a +QSV produces -w' fluctuations (see Figure 71). u'w' and v'w' are zero in a 2DTBL because the QSVs of opposing sign appear in equal strength and equal numbers (though not necessarily in side-by-side pairs). When a spanwise velocity gradient evolves in the flow, the combination of rotationally-produced w' and translationally-produced w' results in asymmetrical production of w' events. Either the ejection or the sweep, induced by the same-sign QSV, will produce larger w' fluctuations than the other. In wall-collateral coordinates, the +QSV induced sweeps (-w' rotational, -w' translational) begin to generate larger w' than the +QSV induced ejections (-w' rotational, +w' translational). The -QSV induced ejections (+w' rotational, +w' translational) create larger w' than the -QSV induced sweep (+w' rotational, -w' translational). In free-stream coordinates, the opposite is true below the spanwise velocity bulge. Since the spanwise bulge occurs outside of the buffer layer at a median location of $y^+ \sim 72$, the spanwise velocity gradient can be characterized as positive throughout the buffer layer. The buffer layer asymmetry will be opposite that in wall-collateral coordinates. From the perspective of the case-1/case-2 classification of ejections and sweeps, the result is the same under both coordinate systems. The case-1 sweep produces larger w' than the case-1 ejection; likewise, the case-2 ejection generates larger w' than the case-2 sweep. This model does not describe what happens to the QSVs during the evolution of the spanwise gradient. The model only predicts the result on sweep and ejection contributions to w' after combining a spanwise velocity gradient with an initially 2DTBL. A generalization of this end effect to ejection and sweep motions is necessary because, as stated in section 6.3.4, the octant analysis cannot definitively map ejection and sweep motions to QSVs. Thus, only ejections and

sweeps classified as case-1 or case-2 will appear in this discussion. Also, throughout the remaining paper, the model just constructed will be called the w'-model.

The octant analysis of $w'^2$ in section 6.4.4 demonstrates the theoretical asymmetry predicted by the model. In free-stream coordinates, the contribution difference between the -w' ejection (case-2) and -w' sweep (case-2) is $(w'^2)^+ = 0.22$ or 48% of the larger contributor. The contribution difference between +w' ejection (case-1) and +w' sweep (case-1) is $(w'^2)^+ = -0.26$ or 61% of the larger contributor. In wall-collateral coordinates, the contribution difference between the -w' ejection (case-1) and -w' sweep (case-1) is $(w'^2)^+ = -0.12$ or 33% of the larger contributor. The contribution difference between the +w' ejection (case-2) and +w' sweep (case 2) is $(w'^2)^+ = 0.044$ or 14% of the larger contributor. The w'-model also indicates that, between the sweeps and between the ejections, one case will produce stronger w' than the other. Table 6-8 contains the size of these asymmetries. The octant analysis shows that the case-1 sweep has a larger $w'^2$ contribution that the case-2 sweep; the case-2 ejection has a larger contribution than the case-1 ejection.

A closer look at the dynamic model reveals that it can explain one subtle trend in the asymmetries. The asymmetry in $w'^2$ contribution between sweeps $[(w'^2)^+_{4\text{-}8}]$ is larger than the asymmetry between ejections $[(w'^2)^+_{2\text{-}6}]$. This trend also results from the spanwise profile. The mechanism will be illustrated in wall-collateral coordinates since it has a simple spanwise boundary layer that monotonically decreases to a steady value in the outer layer. A sweep-like motion can originate from as high as the edge of the boundary layer (though this is rare). The translationally-induced w' in higher originating sweep motions can potentially become larger than their rotationally-induced w'. There are two possible results. The higher-originating sweep motions are more likely to be captured by the -w' sweep octant despite what their original rotational motion is ("shifting") or the potential translationally-induced -w' can retard sweep motions with a rotationally-induced +w' ("retarded"). These motions would contribute significantly more to $w'^2$ since the spanwise velocity gradient increases rapidly in the log and outer layers. Thus, the case-2 sweep loses large w' events; and, if shifting occurs, the case-1 sweep is potentially gaining large w' events. A similar mechanism affects the ejections. However, the scale is much smaller due to the presence of the wall and due to the near-wall magnitude of the spanwise velocity gradient. The wall limits the origin of the ejections and, thus, the size of the translational w' contribution (see figure 72). Also, the spanwise velocity gradient remains very close to zero until one reaches the log layer. Thus, ejection events that are shifted or retarded would have contained smaller contributions to $w'^2$ than similarly affected sweep events. The spanwise velocity gradient will cause a greater weakening in case-1 sweep events than in case-2 ejection events. This causes $(w'^2)^+_{4\text{-}8}$ to be larger than $(w'^2)^+_{2\text{-}6}$.

The flow as viewed in free-stream coordinates maintains consistency with the above mechanism. However, the spanwise velocity profile is very different in free-stream coordinates, compared to wall-collateral coordinates. The spanwise velocity profile has a bulge in the log layer. The bulge brings the peak W closer to the wall and the peak is smaller than in wall-collateral coordinates. The bulge also increases the near-wall spanwise velocity gradient. This causes two modifications in $(w'^2)^+_{2\text{-}6}$ and $(w'^2)^+_{4\text{-}8}$. $(w'^2)^+_{2\text{-}6}$ and (w'2)+4-8 are closer in size than in wall-collateral coordinates. The bulge acts as a ceiling on the production of translational w' for the sweeps similar in

the way the wall acts as a limit on the translational w' created by ejections. Also, the increased near-wall spanwise velocity gradient causes an apparent greater weakening of the case-2 ejection event than under wall-collateral coordinates. Since the buffer layer lies nearly between the bulge and the wall, the theoretical maximum translational w' created by sweeps and ejections is within an order of magnitude. However, the sweep still generates substantially more translational w'. Thus, $(w'^2)^+_{4\text{-}8}$ remains larger than $(w'^2)^+_{2\text{-}6}$ but by a much smaller degree.

This dynamic model introduces the notion that the case-2 sweep octant may lose higher originating sweeps in the 3DTBL because of "shifting" or "retardation" in reaction to the large translational w' that would result. Thus, the model predicts that near the wall, one should expect a population difference between sweep octants under wall-collateral coordinates; i.e., the case-1 sweep octant should have a larger number of events than case-2 sweep octant. In fact, that is the case. In wall-collateral coordinates, the population ratio of octant 8 (case-1 sweep) to octant 4 (case-2 sweep) is 55%/45% (see section 6.4.1). In free-stream coordinates, the population ratio of octant 4 (case-1 sweep) to octant 8 (case-2 sweep) is 62%/38%. A similar argument can also be used for the ejections. Those ejections originating very close to the wall would be affected. These low originating ejections would create moderate translational w' which either "shift" or "retard" events that would fall into the case-1 ejection. This results in a slightly larger population of case-2 ejections over case-1 ejections. In wall, collateral coordinates, the population of octant 2 (case-2 ejection) to octant 6 (case-1 ejection) is 54%/46% on average. In free-stream coordinates, the population of octant 6 (case-2 ejection) to octant 2 (case-1) ejection is 66/34.

The population ratios for ejections and for sweeps are nearly equal under both coordinate systems. The equality in population ratios emphasizes that the difference between $(w'^2)^+_{2\text{-}6}$ and $(w'^2)^+_{4\text{-}8}$ is primarily based on the different size of the potential translational w' associated with "shifted" or "retarded" events. Examination of the same differences for $v'^2$ contributions corroborates the equality in population difference. Since v' is directly related to the mechanism of fluid transport, the near-equal disparity in octant populations between ejections and between sweeps should manifest itself as a nearly equal disparity in $v'^2$ contributions. In wall-collateral coordinates, the disparity in $v'^2$ contributions between ejections $[(v'^2)^+_{2\text{-}6}]$ is 24% of the case-2 ejection; the disparity between sweeps $[(v'^2)^+_{4\text{-}8}]$ is 22% of the case-1 sweep. In free-stream coordinates, $(v'^2)^+_{2\text{-}6}$ is 22.4% of the case-2 ejection; $(v'^2)^+_{4\text{-}8}$ is 29.5% of the case-1 sweep. Given the $v'^2$ uncertainty of 11%, both sets of numbers can be described as approximately equal.

Because the transport of w' occurs by the same ejection/sweep mechanism as the traditional transport of u', w' events as described above correlate with large u' and v' events. Thus, the loss of higher-originating case-2 sweeps also causes a loss of case-2 sweep events with large positive u'. This decreases $u'^2$ and u'v' contributions from case-1 sweeps while potentially increasing the contributions in the case-1 sweep octant if shifting occurs. Thus, the case-1 sweep octant will contribute more to $u'^2$ and u'v' than the case-2 sweep. In wall-collateral coordinates, octant 4 (case-2 sweep) produces a 17% smaller $u'^2$ contribution and a 22% smaller u'v' contribution than octant 8 (case-1 sweep). In free-stream coordinates, octant 8 (case-2 sweep) produces a 34.7% smaller $u'^2$ contribution and a 38.4% smaller u'v' contribution than octant 4 (case-1 sweep). Similarly, the

loss of near-wall-originating case-1 ejection events also results in a loss case-1 ejection events with the large u'. The case-1 ejections experience a decrease in their contribution to $u'^2$ and u'v'; if shifting occurs, the case-2 ejection will gain very large u' events at the expense of the case-1 ejection. Thus, the case-1 ejection will contribute less to $u'^2$ and u'v' than the case-2 ejection. In wall-collateral coordinates, octant 6 (case-1 ejection) has a 10% smaller contribution to $u'^2$ and a 19% smaller contribution to u'v than octant 2 (case-2 ejection). In free-stream coordinates, octant 2 (case-1 ejection) has a 58% smaller contribution to $u'^2$ and a 41% smaller contribution to u'v' than the case-2 ejection.

Unlike the differences in contributions to $w'^2$, the differences in contributions to $u'^2$ and u'v' between sweeps are not larger than the differences between ejections under both coordinate systems. The contribution disparity for sweeps is only larger in wall-collateral coordinates; the contribution disparity for ejections exceeds that for sweeps in free-stream coordinates. The difference reflects the difference in the streamwise and spanwise profiles and how u' and w' are generated. In wall-collateral coordinates, the near-wall streamwise velocity gradient is large and slowly moderates as one enters the outer layer whereas the spanwise velocity gradient is near-zero close to the wall and grows quickly in the upper log and outer region. Thus, the generation of moderate to large u' values in the buffer layer depends less on fluid being moved over large distances than does the generation of moderate to large w'. Since v' reflects the mechanism of vertical fluid transport, large v' values are more likely to be associated with fluid traveling large distances. Therefore, moderate to large w' caused by sweeps and ejections will often be associated with moderate to large u' and large v'. However, moderate to large u' created by sweeps and ejections does not necessarily correlate with large w' nor does it require association with large v' values. The v' values associated with moderate to large u' can be much smaller than the v' values associated with moderate to large w' because the streamwise gradient near the wall is much larger. Since w' is the factor that defines the split of quadrants into octants, events with moderate to large w' (and, thus, large v') are clustered further away from the U axis than many events with moderate to large u'. Given the moderate angles involved in rotating from free-stream to wall-collateral coordinates, events with large w' and v' are likely to remain in the same octant after the coordinate rotation. Therefore, the primary mechanism that changes the representation of $w'^2$ octant contributions with coordinate rotation is the rotation itself. Thus, trends in $w'^2$ contributions that are compared against the spanwise velocity profile remain consistent with coordinate rotation. The octant contributions to $v'^2$ change slightly with coordinate rotation since the coordinate rotation does not affect v' or move many of the larger v' events across octants; thus, trends in octant contributions to $v'^2$ remain consistent with coordinate rotation. However, moderate to large u' events are moved across the U axis; therefore, the population exchange between octants that occurs with coordinate rotation is the major influence on octant contributions to u'-based Reynolds stresses. Therefore, the population ratios better reflect the relative size of $u'^2$ and u'v' contributions between sweeps and between ejections.

The population ratio for sweeps is slightly wider than the ratio for ejections in wall-collateral coordinates; in free-stream coordinates, the opposite is true. The primary influence of the population ratios on u'-based Reynolds stress contributions is corroborated by examination of the u'v' octant

stresses (not contributions). The octant stresses provide a "population neutral" view of the sweep and ejection events in an octant. The octant stress averages the Reynolds stress by the octant's weighted population; the octant stress contribution is the product of the octant stress and the ratio of the octant's weighted population to the total weighted population. Under both coordinate systems coordinates, the strength of -w' and +w' ejections based on u'v' octant stresses are approximately equal in the buffer layer though the free-stream coordinate stresses diverge more quickly as one moves away from the wall. The strength of the sweeps have a small disparity. The disparity is wider in free-stream coordinates than wall-collateral coordinates. The almost equal strength of u'v' octant stresses reveals that the contribution differences for u'-based Reynolds stresses between coordinate systems primarily results from the change in population distribution. The coordinate rotation's effect on u' values and the streamwise velocity profile are lesser effects. The influence of population distribution on octant contributions to u'-based Reynolds stresses is a reminder of the coordinate system problem discussed in section 6.3.1. The population distribution becomes important because only one of the two coordinate systems is more closely aligned with the coherent structures associated with sweeps and ejections. The octant analysis alone cannot address the problem. Therefore, this problem will be discussed further in the upcoming comparison with other 3DTBL experiments.

Octant contributions in the remaining two Reynolds stresses, u'w' and v'w', show the effects identified previously. For both stresses, the stronger contributors are the case-1 sweep and the case-2 ejection. In wall-collateral coordinates, the ejection disparities, given as a percentage of the case-2 ejection, are 15% for u'w' and 20% for v'w' on average in the buffer layer. The sweep disparities, given as a percentage of the case-1 sweep, are 25% for u'w' and 29% for v'w'. In free-stream coordinates, the disparity in u'w' is 61% for ejections and 49% for sweeps. The disparity in v'w' is 41% for sweeps and 34% for ejections. The stronger ejection and sweep contributors to u'w' and v'w' produce v'w' and u'w' contributions with the same sign. Thus, the asymmetry in contribution to u'w' and v'w' results in total u'w' and v'w' values that are non-zero. Under both coordinate systems, the v'w' contribution disparity between sweeps is greater than that between ejections. As discussed earlier, the translational w' weakens the overall production of w' in case-2 sweeps more than in case-1 ejections; but it weakens the production of v' nearly equally between the case-2 sweep and case-1 ejection. Since it is likely for large w' and large v' to be correlated, the case-2 sweep will experience a larger loss in the production of v'w' than the case-1 ejection. This trend appears in both coordinate systems because the large w' values do not cross octant boundaries during the coordinate rotation. For the u'w' contribution disparities, the comparison between sweeps and ejections is mixed. In wall-collateral coordinates, the disparity between sweep contributions is larger than the disparity in ejection contributions; however, the opposite is true in free-stream coordinates. This is the same behavior exhibited by the contribution disparities in $u'^2$ and u'v'. The disagreement between the two coordinate systems is an artifact of the population exchange. The exchange of moderate to large u' events between octants with coordinate rotation overwhelms the weakening of case-1 ejections and case-2 sweeps caused by the potential translational w'. Thus, trends in u'w' cannot be explored more deeply without resolving the coordinate system problem.

In 2DTBLs, sweeps and ejections produce u' by moving fluid vertically across the streamwise velocity gradient. Since 3DTBLs also exhibit a spanwise velocity gradient, sweeps and ejections should also produce w' through the vertical motion of fluid. This translational w' mixes with the rotationally induced w' characteristic of sweeps and ejections to produce an asymmetry in the overall production of w'. The asymmetry weakens the Reynolds stress production and octant population in the case-2 sweep and case-1 ejection octants. Thus, the case-1 sweep and case-2 ejection octants contain larger Reynolds stress contributions than their respective, companion octants, the case-2 sweep and case-1 ejection. These trends are evident in both coordinate systems. The asymmetry also explains the emergence of non-zero u'w' and v'w'; the stronger ejection and sweep produce u'w' and v'w' contributions of the same sign. The shape of the spanwise velocity profile determines that the contribution difference for $w'^2$ and v'w' is greater between sweeps than between ejections. Since the spanwise velocity gradient does not grow appreciably until one enters the log layer, the potential translational w' for sweeps is greater than for ejections. Thus, the potential it has for weakening the case-2 sweep is greater than for the case-1 ejection. The contribution differences in $v'^2$ are nearly the same size between sweeps and between ejections. Since $v'^2$ reflects the mechanism of vertical fluid transport, the near equality in $v'^2$ contribution disparities reinforces the hypothesis that the wider disparity for sweep contributions to $w'^2$ and v'w' does develop from the shape of the spanwise velocity profile. Examination of the disparities for Reynolds stresses containing u' reveals that relative size of the disparities between sweeps and ejections is coordinate system dependent. The population exchange across the U axis with coordinate rotation has a greater effect on the octant contributions to Reynolds stresses containing u' than the weakening effect from translational w'. Thus, a more detailed examination of these stresses cannot be made without resolving the coordinate system problem.

### 6.5.2 Revisiting The Coordinate System Problem

Many of the 3DTBL coherent structure experiments summarized in section 6.2 employed techniques, such as flow visualization and DNS, that better identify the qualitative behavior of near-wall structures while still capable of producing quantitative results. A comparison with these experiments may uncover more detail about the near-wall flow dynamics. However, these experiments present their results in the context of the QSV model; Fleming, et. al. (1994 & 1995) are the exception. The QSV model cannot be definitively mapped to the octant analysis without solving the coordinate system problem (see section 6.3). Thus, part of the comparison with these experiments will be used to investigate the coordinate system problem further. The octant analysis under both coordinate systems will be examined for trends that approach the important results from the third-party experiments. The comparison will use the QSV-octant mapping presented by Figure 6-1. Population distribution and Reynolds stress contribution differences provide the best evidence that one of the coordinate systems is more closely aligned with the QSV structures. That coordinate system is wall-collateral coordinates. Having narrowed the coordinate system choices to wall-collateral coordinates, the next section will proceed with a more in-depth comparison of the results.

The population ratios of QSV events provide the clearest separation between coordinate systems. They provide the strongest evidence that the wall-collateral coordinate system is more closely aligned with the QSVs than free-stream coordinates. In free-stream coordinates, events in octants 2 and 8 (-QSV ejection and +QSV sweep) occur with, at worst, twice the frequency as those of octants 4 and 6 (-QSV sweep and +QSV ejection). The conclusions of Sendstad and Moin (1992) remotely allow for this possibility. They found that a positive spanwise velocity gradient weakens +w' ejections (case-1 or -QSV) and -w' sweeps (case-2 or +QSV) more than their counterparts. However, this interaction should have a greater impact on the size of velocity fluctuations than on the octant population distribution. The 3DTBL studies of Flack and Johnston (1993,1995) and Chiang and Eaton (1993) concur. They counted nearly equal ejection events from QSVs of both signs. They attributed the reduction of Reynolds stresses to changes in the trajectories of some ejections rather than population differences. In Chiang and Eaton's experiment, the percentage ratio of case-1 ejections to case-2 ejection was 48/52. In Flack and Johnston's experiments, the ratios were 48/52 (30° bend flow, 1993), 49/51 to 54/46 (step flow with bubbles introduced at $y^+ = 3$, 1993), and 49/51 to 47/53 (30° bend flow, 1995). Thus, the ratio of ejection populations seems exaggerated in the free-stream coordinate system. In wall-collateral coordinates, the ratios are narrower. The percentage ratio between the case-1 and case-2 ejections is 46/54; this is nearly the same level of "equality" found in the flow visualization experiments. Moreover, the wall-collateral coordinate system produces three profiles (120c-125c) where the population ratios are closer to equal, 52/48 for ejections and 48/52 for sweeps.

The near-equal ejection ratios present in the wall-collateral profiles extend through most of the inner layer ($y^+ < 70$, at least). This region reflects the average height of ejections recorded in the flow visualization experiments. Flack and Johnston (1993) recorded average ejection heights of $y^+ \approx 46$ (30° bend) and $y^+ \approx 76$ (45° step flow). Flack and Johnston (1995) recorded average ejection heights of $y^+ \approx 70$. Chiang and Eaton's (1993) ejections had an average height of $y^+ \approx 84$. (These average ejection heights were taken using the smaller average of the case-1 or case-2 ejections since it is the range of equal number ejections that is being compared. The average heights for both Flack and Johnston experiments were taken from the results of bubbles introduced at the buffer layer edge.) In free-stream coordinates, the population ratios do narrow with increasing height. They are nearly even at the sixth measurement point of all profiles; however, this point exists in the upper log layer. Near the wall, only the wall-collateral coordinate system presents a flow field with near-equal ejection ratios that remain steady into the log layer.

2DTBL research has shown that sweep and ejection events tend to occur in side-by-side pairs (Robinson, 1991); this occurs 80% of the time (Kline, 1992). If this observation changes moderately in 3DTBLs, the population ratios of sweeps to ejections accompanying the same sign QSV should be near equal; at worst, they should be 45/55. The ratios of +QSV sweeps to +QSV ejections and of -QSV sweeps to -QSV ejections only approaches equality in wall-collateral coordinates; the medians of these ratios are 45/55 and 44/56, respectively. In free-stream coordinates, the median ratios are much wider. At the lowest point in the profiles, the average ratio for the +QSV is 35/65; the average ratio for the -QSV is 61/39. If the ejection ratio is nearly equal and

80% of ejections and sweeps occur in side-by-side pairs, then the population ratio between sweeps should also be near equal. The median ratio of -w' sweeps to +w' sweeps demonstrates near equality only in wall-collateral coordinates with a value of 55/45. In free-stream coordinates, the value is 38/62. As with the ejection ratios, all of the population ratios presented in this paragraph maintain near constant averages into the log layer under wall-collateral coordinates. The free-stream coordinate ratios follow the behavior detailed earlier for the ejection ratios; they narrow with increasing height until one reaches the upper log layer where they are near even. The near equal and steady population ratios better reflect the results of the flow visualization experiments and are the first evidence that favors the wall-collateral coordinate system over the free-stream coordinate system for observing near wall coherent structures.

The differences in Reynolds stress contributions between QSV octants is another point for comparison. The flow visualization experiments of Flack and Johnston (1993 and 1995) and Chiang and Eaton (1993) determine the relative strength of ejections by measuring ejection heights and categorizing ejection trajectories as stronger or weaker producers of Reynolds stresses. This data qualitatively suggests that contribution differences should be moderate between ejection induced by QSVs of opposing signs. The octant contributions to $u'^2$, $v'^2$, and u'v' should reflect the ejection heights and trajectory distribution to some degree. Without a clear relationship between these criteria and the octant contributions, the comparison can only use very broad generalities and, thus, presents a weak argument in favor of one coordinate system over the other. The DNS study of Sendstad and Moin (1992) provides a more direct comparison with the octant analysis of the present flow. Sendstad and Moin performed their own octant analysis to examine the differences between the upstream 2DTBL and the downstream 3DTBL. Differences between octant contributions in a 3DTBL can be extracted from this data and compared with the results of the present experiment. Overall, this series of comparisons will continue to suggest that the wall-collateral coordinates are more closely aligned with the QSV structures.

The 30° bend and swept-step flow visualization studies of Flack and Johnston (1993) focused on the behavior of ejections; they compared the ejection trajectories of an upstream 2DTBL with a downstream 3DTBL. They concluded that case-2 ejections are stronger than case-1 ejections; the octant analysis of the present flow agrees with this finding in both coordinate systems. In their experiment, they classified ejection trajectories into four categories: normal, equal, switch-to, and pull-from. Normal is a single QSV event; the remaining events are attributed to multi-QSV interactions. The switch-to and pull-from trajectories arise from the interaction of two QSVs of differing heights. The lower QSV in a switch-to event is weaker than the upper QSV; the upper QSV in a pull-from event is weaker than the lower QSV. The experiments used two criteria to judge the strength of case-1 and case-2 QSVs by their ejections: the average ejection height and the composition of ejection trajectories attributed to each QSV type. The average case-1 ejection height was shown to be, at worst, 10% lower than the case-2 ejection height in the bend flow and 21% lower than the case-2 ejection height in the step flow. When examining the composition of the ejections, the number of case-2 ejection trajectories identified as "switch-to" increased in comparison to the case-1 ejections; also, the number of case-2 "pull-from" ejections decreased in

comparison with the case-1 ejections. However, the differences represented less than 22% of the events in the bend flow and less than 7% of the events in the step flow.

Chiang and Eaton (1993) examined the ejection trajectories in a spinning disk flow using bubble visualization. As did Flack and Johnston (1993), Chiang and Eaton determined the relative strength of case-1 and case-2 QSVs by examining the heights of the ejections and the composition of the ejection trajectories. Chiang and Eaton composed their own classification for QSV trajectories which was very similar to that of Flack and Johnston but used different terminology. However, their mechanism for meandering trajectories was the interaction of a single QSV with the crossflow, rather than multi-QSV interaction. They concluded that the case-1 QSV was stronger. This contradicts the octant analysis of the present flow under both coordinate systems. Although this disagreement appears to eliminate any meaningful comparison with their results, their results do corroborate the notion that the difference in ejection strengths is moderate in 3DTBLs. There results showed that the average case-2 ejection height was 15% lower than the case-1 ejection height. Compared to the case-2 ejection, the case-1 ejection also exhibited more of the "stronger than normal trajectories" and fewer of the "weaker than normal trajectories". Overall, the differences accounted for only 20% of the events. Thus, the qualitative difference in ejection strength is moderate in the Chiang and Eaton flow.

Though the ejection heights and trajectory classifications cannot quantitatively reveal the exact size for the disparity between case-1 and case-2 ejection contributions to $u'^2$ and u'v', they do qualitatively suggest that the difference should be moderate, on the order of 10-30%. The free-stream coordinate system fails to meet that criteria; the average $u'^2$ "gap" is 57% of the case-2 ejection contribution; for u'v', the gap is 41% of the case-2 ejection contribution. The wall-collateral gap can better be described as moderate; the average $u'^2$ gap is 10% of the case-2 ejection contribution. For u'v', the gap is 17% of the case-2 ejection contribution. The contribution "gaps" presented above where calculated by averaging the contribution differences of the first four points of all the profiles.

Flack and Johnston revisited the bend flow in 1995. Their conclusions depart a little from that of the 1993 experiments. They conclude that case-2 and case-1 QSV ejections remain equal in number and strength in the 3DTBL. The mechanism that reduces the Reynolds stress is a decrease in the frequency of ejection events. The octant analysis of the present flow mostly disagrees with the equality of ejection contributions. As mentioned earlier in this section, three wall-collateral coordinate profiles (120c-125c) have ejection (48/52) and sweep (52/48) population ratios closest to equality. In each one of these profiles, the ejection contributions to $u'^2$ are approximately equal, agreeing with Flack and Johnston's conclusions. However, the sweep contributions remain significantly different. The octant stress ($\tau_i$), which does not contain population distribution effects, emphasizes this trend (see Figures 118-127). Examination of the octant stress may be more appropriate for comparative purposes since it examines each octant in isolation from the others. This is more similar to the method employed in this flow visualization experiment. The ejection heights and ejection populations are calculated separately within their own categories (case-1 and case-2); each criteria has its own uncertainty. A representative uncertainty in ejection

contributions would reflect the combined uncertainty of these two criteria, which cannot be determined. This representative contribution uncertainty could be large enough to declare that the ejection contributions in the present experiment are statistically equivalent. This fact clouds direct comparison between Flack and Johnston's results and the octant contribution data. The uncertainty in the octant stress would reflect only the uncertainty in ejection height. Thus, a stronger comparison can be made between ejection height and octant stress. The $u'^2$ octant stresses for ejections and sweeps are statistically equal under wall-collateral coordinates. This does not hold true for free-stream coordinates. The ejection and sweep stresses remain far apart for $u'^2$.

While $u'^2$ is heavily influenced by the QSVs, the u'v' contributions and stresses are a better measure of ejection strength. Large u'v' events better correlate with ejections and sweeps than large u' events alone. In the three profiles with near-equal population values for QSV octants, the ejection "gap" for u'v' is 9.8% of the larger ejection contribution. This falls below the 11% uncertainty in u'v'; thus, these ejection contributions are statistically equal. In these same profiles, the sweep gap is 15.5% of the larger sweep contributions. Although the ejections may be equal, the sweeps are not. Thus, u'v' uncertainty allows a level of agreement with both of Flack and Johnston's experiments (1993 and 1995). The stronger contribution from the case-2 ejection agrees with the 1993 experiment. But, the contribution difference in the "near-equal-population" profiles is not larger than the uncertainty in u'v'; thus, the possibility that the ejection strengths are equal remains. The octant stress ($\tau_i$) plots, which avoid population distribution affects, show a closer level of equality. In wall-collateral coordinates, the ejection u'v' stresses are nearly equal throughout the buffer layer. The sweep stresses are closer in value compared to their contributions; however, they remain distinctly separate in profiles 105a and 123a. In free-stream coordinates, ejection and sweep stresses have a considerably smaller gap than their contributions. In fact, the ejection stresses are nearly equal in the lower buffer layer; however, unlike the wall coordinate stresses, this equality does not extend throughout the buffer layer. The ejection stresses begin to diverge after a couple of measurement locations. The sweep stresses maintain a distinct gap in profiles where $\alpha_{wc}$ is large (130a, 125b, and 123c). Thus, the octant analysis can be interpreted as having the same equality of ejection strength as uncovered by Flack and Johnston (1995). The wall-collateral coordinate system contains statistically strength ejections in both contribution and stress profiles. The longer extent of the octant stress equality in wall-collateral coordinates better reflects the typical height of near wall ejections. In Flack and Johnston's flow, the average height of ejections from the sublayer was $y^+ < 50$. Thus, the wall-collateral coordinates, once again, displays characteristics that are in better agreement with third-party experiments than free-stream coordinates. The evidence that the ejection contributions converge as the populations in octants 2 and 6 approach equality provides a compelling reason to, in future work, explore coordinate systems where the ejection and sweep populations are even.

Thus far, only contribution differences for $u'^2$ and u'v' have been discussed. These stresses are influenced by a number of factors outside of ejection height and trajectory. The most important of these is coordinate system choice. Therefore, these stresses clearly separate the coordinate systems and add value to the examination of the coordinate system problem. Since v' values are

invariant to coordinate rotation normal to the wall, the coordinate rotation affects contributions to $v'^2$ only through the octant population changes it causes. The octant analysis of $v'^2$ may not provide clear evidence favoring either coordinate system. Therefore, it is being examined separately. Since $v'^2$ is indicative of the mechanism of fluid transport, a close relationship should exist between it and the ejection height. The flow visualization experiments of Chiang and Eaton (1993) and Flack and Johnston (1993) both demonstrated that average ejection heights differed between case-1 and case-2 QSVs. The average ejection heights differed by 3% to 22% of the stronger QSV ejection. In the current experiment, the average difference between +QSV and -QSV ejections contributions is ~14% of the case-2 ejection contribution; this is true under both coordinate systems. Flack and Johnston (1995) determined that the number and strength of ejections remained equal between +QSV and -QSV events in a 3DTBL. In the three, wall-collateral profiles where the population ratio of ejection events remain most equal (120c-125c), the average contribution difference drops to ~9.5% of the larger contributor. As with the $u'^2$ and u'v' contributions, the difference in sweep contributions for these three profiles remains slightly larger, ~10.9%. Compared to the 7.8% uncertainty in $v'^2$, the difference between ejection contributions remains barely significant. It can be argued that the "random" events (i.e., non-QSV events) populating the two ejection octants increase the uncertainty enough to declare them statistically equal. Moreover, $v'^2$ has a weaker correlation with ejections than u'v', and u'v' exhibits a smaller gap under wall-collateral coordinates. The octant stress ($\tau_i$) plots, which are not affected by population distribution, demonstrate that the $v'^2$ stresses in ejection octants are closer to equality than the contribution values. In wall-collateral coordinates, the difference in ejection octant stresses is ~10% or smaller. In free-stream coordinates, the differences are wider apart in profiles with large $\alpha_{wc}$. Under both coordinate systems, the $v'^2$ stresses in the sweep octants are approximately equal throughout the boundary layer. Although the $u'^2$ and u'v' results demonstrate a clear separation between octants that favors the wall-collateral coordinates, the $v'^2$ results show very small differences between coordinate systems. They provide no additional evidence favoring either the wall-collateral or free-stream coordinate systems.

Comparing the octant analysis with flow visualization experiments reveals some evidence that the wall-collateral coordinates are more closely aligned with the QSV structures. However, this evidence relies on a weak and uncertain relationship between ejection heights/ejection trajectories and octant contributions. The DNS study of Sendstad and Moin (1992) contains an octant analysis. Their octant analysis can be used to generate reasonable differences (a.k.a. "gaps") between ejection contributions and between sweep contributions in the 3DTBL. A more meaningful comparison can, thus, be made with the octant analysis of the present experiment. Sendstad and Moin's DNS study demonstrated that the spanwise velocity gradient weakens certain QSV events more than the others. A positive spanwise velocity gradient will more greatly weaken the -QSV ejections (octant 2) and +QSV sweeps (octant 8). Presumably, the opposite would also hold in a flow field with a negative velocity gradient; i.e., a spanwise pressure gradient weakens the case-1 ejection and the case-2 sweep. The current experiment agrees with this statement; therefore, a detailed comparison between with the DNS study is meaningful. Sendstad and Moin compared the octant decomposition of an upstream 2DTBL with a downstream 3DTBL during its initial

development. The coordinate system was aligned with the channel centerline in both cases. The equivalent $\alpha_{wc}$ of the 3DTBL at this early stage should have been less than a couple of degrees; any skewing of the results due to coordinate system choice should be minimal. (Their report does not contain the required data to quantify $\alpha_{wc}$.) Although the DNS study presented octant plots of the contribution difference between a 2DTBL and 3DTBL, the data can be used to generate approximate differences between ejection contributions and between sweep contributions in a 3DTBL if one assumes that ejections and sweeps are nearly equal in the 2DTBL. If one also assumes that $u^+$ is an appropriate scaling factor for the near-wall Reynolds stress, then a loose comparison can be made between the "gaps" in Sendstad and Moin's experiment and the "gaps" present in the current experiment. Table 6-3 presents the comparison. The "gap" averages from the prolate spheroid flow were computed using the buffer layer measurements (first four points) of all the profiles. The DNS numbers represent the maximum difference between ejection and between sweep octants extracted from the report's plots. All numbers were normalized by $u_\tau^2$.

**Table 6-9: Comparison Of Octant Contribution Gaps**

| Reynolds Stress | Free-stream | | Wall-Collateral | | DNS | |
|---|---|---|---|---|---|---|
| | Ejection | Sweep | Ejection | Sweep | Ejection | Sweep |
| $u'^2$ | 1.10 | 0.74 | 0.14 | 0.27 | 0.30 | 0.40 |
| $v'^2$ | 0.025 | 0.030 | 0.022 | 0.028 | 0.003 | 0.005 |
| $w'^2$ | 0.220 | 0.250 | 0.057 | 0.104 | 0.030 | 0.060 |
| $u'v'$ | 0.120 | 0.100 | 0.041 | 0.062 | 0.025 | 0.025 |

The wall-collateral coordinate "gaps" in $u'^2$, $w'^2$, and $u'v'$ are closer to the DNS study values than the "gaps" in free-stream coordinates. The free-stream coordinate values are more than double the DNS results for these three Reynolds stresses except the $u'^2$ sweep gap. For these same Reynolds stresses, the largest difference between the DNS study and the wall-collateral coordinates is the $u'v'$ sweep gap, which is 2.5 times larger than the DNS gap. However, the free-stream coordinate system gap is four times larger for the same case. Thus, the numbers for these three Reynolds stresses favor the wall-collateral coordinate system as the preferred reference. For $v'^2$, the contribution gaps in this experiment are nearly an order of magnitude larger than the DNS study. Sendstad and Moin performed their octant analysis on a 3DTBL whose spanwise boundary layer had not grown above the buffer layer. Thus, it did not engulf the QSVs and its effect on $v'^2$ may have been limited. This difference in flow evolution provides a reason to cast doubt on the results of the comparison.

A preliminary comparison between other 3DTBL structure experiments and the present experiment suggest that the wall-collateral coordinate system is more closely aligned with the QSV structures that the free-stream coordinate systems. The strongest evidence supporting the wall-collateral coordinate system is the near and persistent equality of the QSV-mapped octants throughout the buffer and lower log layers. This result agrees with the flow visualization studies

of Chiang and Eaton (1993) and Flack and Johnston (1993,1995). It also remains consistent with the behavior of ejections and sweeps in 2DTBLs (Robinson, 1991; Kline, 1992). Further supporting evidence can be found by examining the contribution differences between sweeps and between ejections. These differences are very large in free-stream coordinates; in wall-collateral coordinates, the differences can be categorized as moderate. The studies of Chiang and Eaton and Flack and Johnston demonstrate a moderation of change in the flow structure of a 3DTBL compared to a 2DTBL. However, a weak and uncertain relationship exists between octant contribution differences and the structural differences in the flow visualization experiments (i.e., ejection heights and ejection trajectory distributions). Although the moderation in structural changes appears to support the moderate contribution differences in the wall-collateral coordinate system, the weak correlation between these two criteria lessens this evidence that favors the wall-collateral coordinate system. The DNS study of Sendstad and Moin (1992) does contain an octant analysis from which contribution differences can be extracted and compared more directly with the current experiment. The differences show a level of moderate change similar to that displayed under wall-collateral coordinates. However, this octant analysis was performed on a 3DTBL during its initial stages of development. Thus, doubt is cast on the comparison. The evidence favoring the wall-collateral coordinate system as the preferred reference for viewing the near-wall structure is not conclusive. But, it is consistent. Therefore, the QSV-octant mapping will be applied to the octant analysis under wall-collateral coordinates when comparing results with third-party 3DTBL experiments that rely on the QSV structural model.

### 6.5.3 Comparison With 3DTBL Structure Experiments

A number of comparisons with the 3DTBL experiments cited in section 6.2 have already been made in the previous section. These comparisons established that the wall-collateral coordinates system was preferable to the free-stream coordinate system in comparison with experiments that based their results on the QSV model. Therefore, only wall-collateral coordinate results will be used in this section. The discussion will first compare the present results with those of Chiang and Eaton (1993) and Flack and Johnston (1993, 1995). Many of the details of this comparison were presented in the previous section. The discussion in this section will summarize the similarities and will provide a more detailed examination of the disagreements which were given only brief mention. The discussion will then focus on the evolution of non-zero u'w' and v'w'. The only third-party experiment that supplies quantitative data is Sendstad and Moin's (1992) DNS study. Simpson and Devenport (1990) also proposed a model that explains the evolution of non-zero u'w' and v'w'. The results of the present experiment will be applied against the conclusions of these two papers. The discussion will end with a comparison between Sendstad and Moin's (1992) structural model introducing four weakening mechanisms and the w'-model introduced in section 6.5.1. Striking similarities emerge between these two models.

In wall-collateral coordinates, the population distributions among ejection and sweep octants is nearly equal; in the worst case, the ratio is 54/46. Moreover, the relative distributions remain nearly constant throughout the buffer and lower log layers. The near and persistent equality of ejection events agrees with the findings of Chiang and Eaton (1993) and Flack and Johnston

(1993, 1995). However, disagreement emerges among the experiments concerning the relative strength of Reynolds stress contributions between case-1 and case-2 ejections. In the present experiment the case-2 ejection is a stronger contributor than the case-1 ejection. Flack and Johnston's 1993 study and the DNS study of Sendstad and Moin (1992) come to the same conclusion. In fact, the DNS study also agrees with the present experiment's conclusion that the case-1 sweep is a stronger contributor than the case-2 sweep; the other experiments do no address the relative strength of sweeps. Chiang and Eaton come to the opposite conclusion; i.e., the case-1 ejection is stronger than the case-2 ejection. In their own comparison with Chiang and Eaton's experiment, Flack and Johnston (1993) point out that Chiang and Eaton introduce their hydrogen bubbles at $y^+ = 37$, which is outside the buffer layer. Therefore, there is a greater possibility that the bubbles will be influenced coherent structures in the log layer including vortical arches. The point of introduction is close to the location, as determined in section 6.3.2, where the QSV-octant mapping begins to break down ($y^+ \approx 50$). Chiang and Eaton's results cover an area of the flow field where correlating the octant analysis with structural dynamics becomes nearly impossible.

In their 1995 experiment, Flack and Johnston conclude that ejections have equal strength. Overall, the present experiment disagrees. The case-2 ejection is a stronger contributor to all six Reynolds stresses than the case-1 ejection. This is true under both free-stream and wall-collateral coordinates. However, several factors can account for the disagreement. Flack and Johnston based their conclusion on measurements of ejection height and distribution of ejection trajectories. The conclusion of equal ejection strengths is based on equality of ejection heights and population within the uncertainty for their experiment. Although ejection heights and trajectories are indicative of Reynolds stress production, the relationship between them is not clearly defined. Therefore, their uncertainties cannot be translated into similar uncertainties for octant contributions. Also, Flack and Johnston must treat the two criteria of population and ejection height as mathematically separate entities. The contribution values would be affected by both criteria. The combined uncertainty of these criteria could be reflected as a large uncertainty in Reynolds stress contributions. Coordinate system choice could also possibly account for the difference. The differences in u'v' contributions between case-1 and case-2 ejections are smallest at the three measurement locations where the population ratio of these two octants are closest to equal (120c - 125c). In fact, the difference (~9.5%) is slightly more than the uncertainty in u'v' (~7.8%). A coordinate system, that minimizes the population difference between case-1 and case-2 ejections, could produce u'v' contributions that are approximately equal. The octant stress ($\tau_i$) plots support this conjecture. The octant stress is the Reynolds averaged stress within an octant; the octant contribution is the product of the octant stress and the octant population as a percentage of the total population. Thus, the octant stress provides a more population neutral assessment of the velocity events in an octant. The octant stress plots show small differences in u'v' stress between case-1 and case-2 ejection octants. These differences are smaller than the uncertainty in u'v' so the stresses are statistically equal. Therefore, the octant stresses also indicate that the contributions may be statistically equal in a coordinate system where the population differences are minimal. Although the results provide a clearer argument that the case-2 ejection is stronger than the

case-1 ejections, the results do not rule out the possibility that case-1 and case-2 ejections have equal strength.

The published results from 3DTBL structure experiments contain very little quantitative correlation between v'w', u'w', and structural events. Only Sendstad and Moin (1992) provide such data, a quadrant analysis of v'w' and u'w'. In the case of u'w', Sendstad and Moin observed that the quadrants producing negative u'w' moderately increase their contribution. Those contributions producing positive u'w' experience a small decrease in their contribution. Unfortunately, u'w' quadrants mix QSV and interaction octants together so it is difficult to assign these trends to a particular structure. However, the octant analysis of the present flow supports this trend. In free-stream coordinates, the negative u'w' octants (and, thus, quadrants) contribute more than the positive u'w' octants. The octant 4/6 pair is, by far, the major contributor. Assuming the opposite trends would surface in flow where the spanwise velocity is negative, then the wall-collateral coordinates system supports the same trend. The positive u'w' octants (and, thus, quadrants) contribute more than the negative u'w' octants. The octant 2/8 pair contributes much more positive u'w' than the octant 3/5 pair. Thus, the octant analysis points to the ejection and sweep octants as the major source of u'w' changes under both coordinate systems.

In the case of v'w', Sendstad and Moin observed that the quadrants producing negative v'w' moderately decrease their contribution shortly after the flow experiences the spanwise pressure gradient. Those contributions producing positive v'w' experience a small increase in their contribution. Unfortunately, v'w' quadrants also mix QSV and interaction octants together so it is difficult to assign these trends to a particular structure. However, the octant analysis of the present flow supports the quadrant findings. In free-stream coordinates, the positive v'w' octants (and, thus, quadrants) contribute more than the negative v'w' octants in the inner layer. The QSV octant 4/6 pair is, by far, the major contributor. Assuming the opposite trends would surface in flow where the spanwise velocity is negative, then the wall-collateral coordinates system also support the trend. The positive v'w' octants (and, thus, quadrants) contribute less than the negative v'w' octants. The octant 2/8 pair dominates. The QSV octant 2/8 pair contributes much more larger negative v'w' than the octant 3/5 pair. Thus, the octant analysis points to the QSV octants as the major source of v'w' changes under both coordinate systems.

Simpson and Devenport (1990) proposed a comprehensive model that explains the non-zero u'w' in 3DTBLs. When a sweep displaces low speed fluid in a 3DTBL, some of that fluid, rather than ejecting upward, "ejects" in the spanwise direction due to the influence of the spanwise pressure gradient. This spanwise displaced fluid would populate octants 6 and 7 in a flow field with a positive spanwise pressure gradient. Under a negative pressure gradient, the displaced fluid would occupy octants 2 and 3. Simpson and Devenport explain the predicted effects from the model in octant terms; thus, the model can be evaluated using the data of the current experiment. Without a picture of the entire flow field and direct pressure measurements, it is difficult to determine the actual pressure gradient in the different coordinate systems applied to this flow. However, one can usually assume that the spanwise pressure gradient has the opposite sign of spanwise velocity gradient. Also, Chesnakas and Simpson (1996) presented pressure measurements on the same

prolate spheroid model under similar experimental conditions. The prolate spheroid flow has a positive angular pressure gradient at x/L = 0.7722 & $\alpha = 10°$ over the range of $\phi$ examined in this experiment. This becomes a negative spanwise pressure gradient in body surface coordinates since the Z axis points in the opposite direction to increasing $\phi$. Of the two coordinate systems, the free-stream coordinates are closer in alignment to the body surface coordinate system and display a positive spanwise velocity gradient as expected from the negative pressure gradient. Thus, if spanwise ejections where taking place, they would show up in octants 2 and 3 under free-stream coordinates. However, octant 3 is the weakest contributor to $u'^2$, $w'^2$, and u'w'; thus, it shows no sign of this displaced fluid. In wall-collateral coordinates, the spanwise velocity gradient is negative indicating that the coordinate rotation has resulted in a positive spanwise pressure gradient. This would result in the expectation of a significant increase in the u'w' contribution of octants 6 or 7. Once again, the octant analysis reveals that this is not the case. Octant 6 represents the case-1 ejection, which is the weaker contributor of the two ejection octants. Octant 7 many times falls behind octants 1 and 5 in contributions to Reynolds stresses. The octant analysis does not necessarily rule out this spanwise ejection. In fact, Sendstad and Moin's (1992) model of the near-wall structure contains such spanwise displacements. Rather than contribute significantly to u'w', these spanwise displacements weaken the ejection and sweep contributions. Any u'w' generated by the spanwise ejection mechanism is dwarfed by the QSV contributions. In section 6.5.1, a model was presented in which the QSVs transport w' in the same manner they transport u'. In a 3DTBL with a moderate spanwise profile, such as the current flow, dW/dy can be fairly large. The sweep and ejection of fluid creates substantial w' fluctuation in addition to u' fluctuations. The size of these fluctuations dwarf those caused by spanwise "ejections " of fluid.

As summarized in section 6.2, Sendstad and Moin (1992) proposed four mechanisms that weaken ejections and sweeps in a 3DTBL compared to a 2DTBL. Evidence of all four mechanism appears in the results of the current experiment. The first two mechanisms are the most dominant. Fluid swept toward the wall by case-2 QSVs (i.e., the case-2 sweep) will not get as close to the wall as in a 2DTBL. Ejections by case-1 QSVs generate lower velocity fluctuations because the fluid originates at further from the wall than in 2D flow. The octant analysis of the current experiment immediately agrees on the point that the case-2 sweep and case-1 ejection appear severely weakened in comparison to the case-1 sweep and case-2 ejection. The similarities become deeper with the examination of the w'-model introduced in section 6.5.1. In the w' model, the translational displacement of fluid caused by sweeps and ejections creates a w' fluctuation by virtue of the spanwise velocity gradient. Sweeps and ejections have a streamwise rotation that creates its own w' fluctuation. When these effects combine, it results in a weakening of the case-1 ejection and the case-2 sweep. The creation of w' by translational displacement mirrors the creation of u' by the same mechanism. Thus, large w' fluctuations have a high probability of accompanying large u' fluctuations (though the opposite is not necessarily true). Since the ejection origin is limited by the wall and the velocity gradient near the wall is very small, only those case-1 ejections which would have originated very close to the wall are affected by the translational w' mechanism. In wall-collateral coordinates, these ejections would also produce large +u'. Thus, case-1 ejections are weakened because they lose the most positive u' values associated negative

w'. Sendstad and Moin's analysis revealed that quadrant 2 u'v' reductions resulted from "the most negative u' correlated with positive w'". Sendstad and Moin's flow has a positive spanwise velocity gradient. The present flow has a negative spanwise velocity gradient. Assuming that the results are symmetric with the sign of the spanwise velocity gradient, then the w'-model and Sendstad and Moin's first mechanism agree on the underlying effect that weakens case-1 ejection. Sweeps have fewer limitations than ejections. They can originate over a larger range of height, up to the boundary layer edge. Also, the spanwise velocity gradient increases rapidly in the log layer as the streamwise velocity gradient begins to moderate. Thus, case-2 sweeps originating over a larger portion of the boundary layer are affected by the translational w' mechanism. These sweeps would have produced moderate to large -u'. Thus, the case-2 sweep is weakened by a loss of medium to large -u' associated with +w'. This same effect is witnessed by Sendstad and Moin. Reductions in quadrant four u'v' resulted from the reduction of "positive u' correlated with negative w'". Once again, the DNS trends are the mirror opposite of those in the current flow due to the sign of the spanwise velocity gradient. The w'-model and the first two mechanisms of Sendstad and Moin agree on the underlying effect that weakens the case-1 ejection and case-2 sweep.

Sendstad and Moin's other two mechanisms are less prominent. They affect the case-2 QSV ejection and case-1 QSV sweep. In the third mechanism, the streamwise QSVs are tilted with respect to the near wall streaks. The resulting interaction causes the QSVs to eject high-speed fluid from the high speed streaks rather than low speed fluid from the wall. This mechanism primarily affects case-2 QSV ejections. In octant terms, these high-speed ejections should show up in octant 1 ($u' > 0, v' > 0, w' > 0$) or octant 5 ($u' > 0, v' > 0, w' < 0$). The octant analysis reveals that octant 1 may contain such high speed ejections. As stated in the introduction to this section (6.5), one of the octant analysis trends common to both coordinate systems is the surprising strength of contributions to w'-based stresses in octant 1. Under wall-collateral coordinates, octant 1 is the second largest contributor to $w'^2$ for $y^+ < 15$. As shown in section 6.4.2, octant 1 was also the largest $u'^2$ contributor among the interaction octants under wall-collateral coordinates; thus, octant 1 contains some moderate u' events. The octant analysis of u'w' shows that these large w' events correlate with the moderate u' events. In the buffer layer, the octant 1 contribution to u'w' surpasses the strength of the case-1 ejection in over half of the profiles under wall-collateral coordinates. In these profiles, octant 1 is the fourth largest contributor to u'w'. Similarly, in the buffer region, octant 1 surpasses the case-1 ejection contribution to v'w' in five profiles; in all other profiles it is the fifth largest contributor. The strength of octant 1 is accentuated by the octant stress plots (Figures 118-127). Octant 1 contains the largest $w'^2$ stress in the buffer layer. It comes in first or second for stress value of u'w' and is among the top three octants for v'w'. This is true under both coordinate systems. These characteristics are expected from a "high speed" ejection induced by a QSV. Because ejections transports "high speed" flow to regions of faster moving flow, the resulting u' is large close to the ejection's origination and moderates as the fluid rises. The ejection retains the moderate, rotationally induced w' and the signature v' of a normal ejection. Compared to a 2DTBL, a "high speed" ejection octant in a 3DTBL should have a larger number of moderate w' events correlated large to moderate u' events. These events occur close to the wall since the relative u' of the fluid will decrease as it rises. These events should also have a correlation between v' and w' which are on par with normal ejections. However, the "high speed" ejection occurs with

much less frequency than normal ejections so its contribution to the Reynolds stresses will be small although its stress value will be large. The data reflects this assessment although the w' fluctuations in octant 1 appear to be larger than those in the normal ejections given the strength of octant 1 in $w'^2$ contributions. The population changes that occur with coordinate rotation reflect these large w' events. The high speed ejection events do not appear to cross octant boundaries during the coordinate system rotation even though the normal ejections events cross between octants 2 and 6. There is almost no population transfer between octants 1 and 5. Large w' events would account for the lack of population transfer; these events fall outside of the region swept by the coordinate rotation. Only random events get transferred into and out of octants 1 and 5; this leads to a very small net difference in population. Lastly, Sendstad and Moin state that the "high speed" ejection has the largest affect on the case-2 QSV ejections. The case-2 QSV produces -w' in free-stream coordinates and +w' in wall-collateral coordinates. Only octant 1 shows signs of containing these "high speed" ejection events; octant 1 contains +w' events. Only under wall-collateral coordinates could these events be caused by a case-2 QSV. This provides further evidence that could be added to section 6.5.2; the evidence favors the wall-collateral coordinates for examination of near wall structure.

In the fourth mechanism, the spanwise mean flow retards near-wall penetration of high speed sweeps produced by case-1 QSVs. In combination with mechanism I, this implies that all sweeps terminate further from the wall than in 2DTBLs. Fleming, et. al. (1995), and Flack and Johnston (1995) also reported that the ejection/sweep process in a 3DTBL influences fluid dynamics further away from the wall than in the upstream 2DTBL. 2DTBL experiments have shown that sweep contributions become more important than ejection contributions below $y^+ \approx 12$ (Robinson, 1991). Robinson quotes the lowest of the values revealed in a number of experiments. Willmarth and Lu (1972) identified the crossover location at $y^+ \approx 15$. As stated in the introduction to this section (6.5), the sweep quadrant overcomes the ejection quadrant at the same average location in both coordinate systems. This location at $y^+ \sim 20$ is higher than the 2DTBL values. The higher location implies that the influence of sweep events occurs further away from the wall than in 2DTBL.

The w'-model provides a complete description of the flow dynamics as observed in the octant analysis. The model reproduces the experimental results of Flack and Johnston (1993) and the dominant mechanisms of Sendstad and Moin's (1992) DNS study while providing a more simple explanation of asymmetries in QSV events and the emergence of non-zero u'w' and v'w'. Additional results from the octant analysis support the two minor mechanisms in the DNS study and agree with the quadrant analysis of u'w' and v'w' in that same study. The results do not conclusively contradict the equal-strength ejection finding of Flack and Johnston's (1995) experiment. However, the results are contrary to Chiang and Eaton's (1993) conclusion that the case-1 ejection is stronger than the case-2 ejection. The results also fails to match structural model proposed by Simpson and Devenport (1990) for the creation of u'w' and v'w'.

# Chapter 7 Conclusions

A high Reynolds number flow near the separation point of a 6:1 prolate spheroid was observed using a novel LDV probe mounted inside of the model. The probe allowed measurements down to the lower edge of the buffer layer. This region is very sensitive to the calibration of the measurement volume's position. At the time of the experiment, the only acceptable method of calibration depended on visual observation of the measurement volume using a magnifying lens. Thus, a post-processing technique was developed to refine the wall position for each profile. This method rearranges the Spalding continuous wall law to extract two unknowns, the skin friction ($C_f$) and a wall refinement ($\Delta y$). The skin friction was a necessary unknown because no direct skin friction measurements were taken. A least squares fit of the law to the buffer layer data was used to solve for the two unknowns. The technique was applied successfully to the LDV data. Resultant wall-refinement values were reasonable. The skin-friction coefficient values were consistent with the direct measurements reported by Vollmers, et. al. (1984) on a larger scale model and Wetzel, et. al. (1997) on the same model at a later date. The wall-refined profiles of $a_1$ showed a tighter similarity in the buffer layer; self-similarity of $a_1$ was reported by Flack and Johnston (1992). However, the investigation into this technique reveals that the number of measurement points in the buffer layer were barely sufficient for successful application; six or more points are preferred. Also, this technique is only applicable to a flow that also exhibits near-collateral behavior in the buffer layer. It would also be of interest to apply this technique to a flow where the skin friction is measured directly and does need to be solved as another unknown.

The refined data was then used to examine the near-wall structure of the flow using octant analysis. The investigation introduced a dynamic model that explains the octant results. In 2DTBLs, sweeps and ejections produce u' by moving fluid vertically across the streamwise velocity gradient. Since 3DTBLs also exhibit a spanwise velocity gradient, sweeps and ejections should also produce w' through the same vertical motion. This translational w' mixes with the rotationally induced w' characteristic of sweeps and ejections to produce an asymmetry in the overall production of w'. The asymmetry weakens the Reynolds stress production and octant population in the case-2 sweep and case-1 ejection octants. Thus, the case-1 sweep and case-2 ejection octants contain larger Reynolds stress contributions than their respective, companion octants, the case-2 sweep and case-1 ejection. These trends are evident in both coordinate systems. The asymmetry also explains the emergence of non-zero u'w' and v'w'; the stronger ejection and sweep produce u'w' and v'w' contributions of the same sign. The shape of the spanwise velocity profile determines that the contribution difference for $w'^2$ and v'w' is greater between sweeps than between ejections. Since the spanwise velocity gradient does not grow appreciably until one enters the log layer, the potential translational w' for sweeps is greater than for ejections. Thus, the potential it has for weakening the case-2 sweep is greater than for the case-1 ejection. The contribution differences in $v'^2$ are nearly the same size between sweeps and between ejections. Since $v'^2$ reflects the mechanism of vertical fluid transport, the near equality in $v'^2$ contribution disparities reinforces the hypothesis that the wider disparity for sweep contributions to $w'^2$ and v'w' does develop from the shape of the spanwise velocity profile. Examination of the disparities for Reynolds stresses containing u' reveals that relative size of the disparities between sweeps and ejections is

coordinate system dependent. The population exchange across the U axis with coordinate rotation has a greater effect on the octant contributions to Reynolds stresses containing u' than the weakening effect from translational w'. Thus, a more detailed examination of these stresses cannot be made without resolving the coordinate system problem.

The w'-model provides a complete description of the flow dynamics as observed in the octant analysis. The model reproduces the experimental results of Flack and Johnston (1993) and the dominant mechanisms of Sendstad and Moin's (1992) DNS study while providing a more simple explanation of asymmetries in QSV events and the emergence of non-zero u'w' and v'w'. Additional results from the octant analysis support the two minor mechanisms in the DNS study and agree with the quadrant analysis of u'w' and v'w' in that same study. The results do not conclusively contradict the equal-strength ejection finding of Flack and Johnston's (1995) experiment. However, the results are contrary to Chiang and Eaton's (1993) conclusion that the case-1 ejection is stronger than the case-2 ejection. The results also fails to match structural model proposed by Simpson and Devenport (1990) for the creation of u'w' and v'w'. A close examination of the octant analysis with these third-party experiments also provides evidence that the wall-collateral coordinate system is a better reference system for examining the near-wall structures than the free-stream coordinate system. The strongest evidence involves the octant population distribution. Chiang and Eaton (1993) and Flack and Johnston (1993, 1995) reported that case-1 and case-2 ejections occur with equal frequency. The population distribution under wall-collateral coordinates places a nearly equal number of events in both ejection octants; in free-stream coordinates, the case-2 ejection has nearly twice the population of the case-1 ejection. Moreover, the near-equality in wall-collateral coordinates extends well into the log layer; this reflects the typical ejection heights witnessed in the flow visualization experiments. However, the prolate spheroid flow has a near-collateral region where the flow, gradient, and intensity angles converge; the stress angle was unpredictable. Thus, the wall-collateral coordinate system may be a less appropriate reference in more complex 3DTBLs.

# Chapter 8 Figures

The following pages contain all figures referenced within this document.

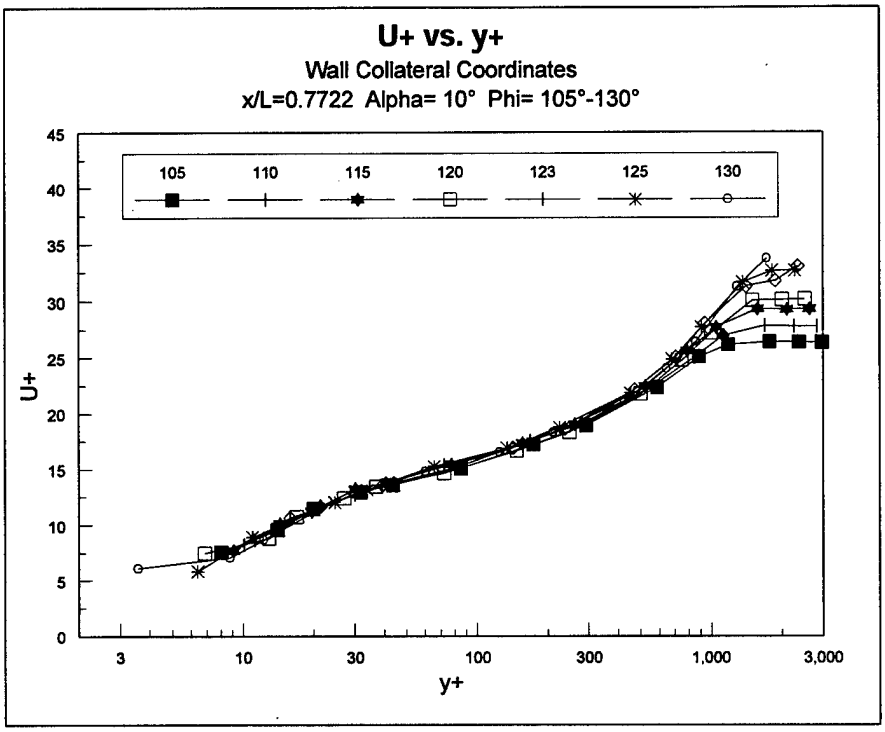


Figure 1. $U^+$ Profiles in Wall-collateral Coordinates at x/L=0.7722.

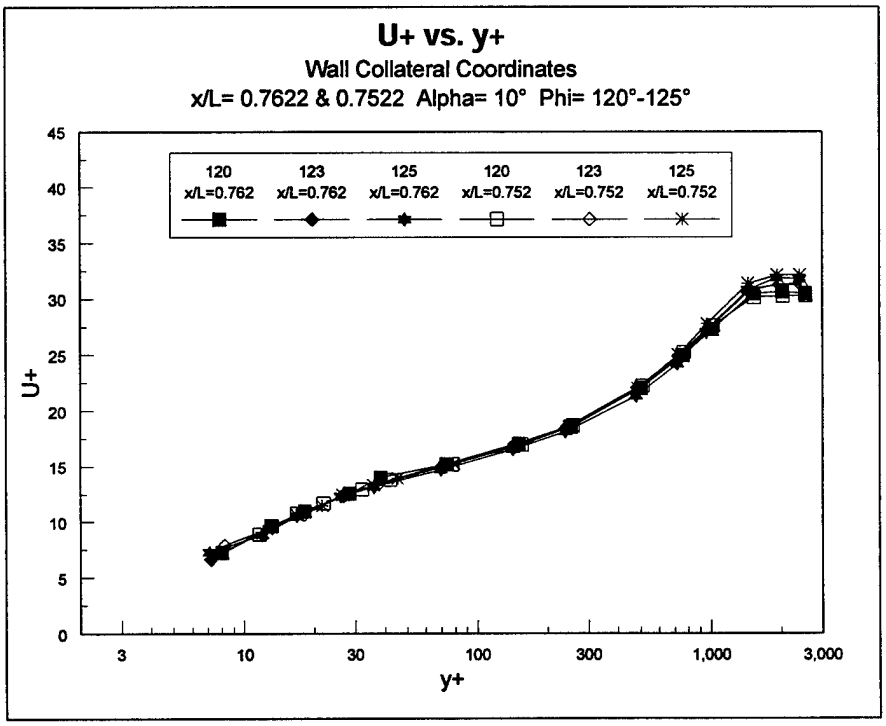


Figure 2. $U^+$ Profiles in Wall-collateral Coordinates at x/L=0.7622 & 7522.

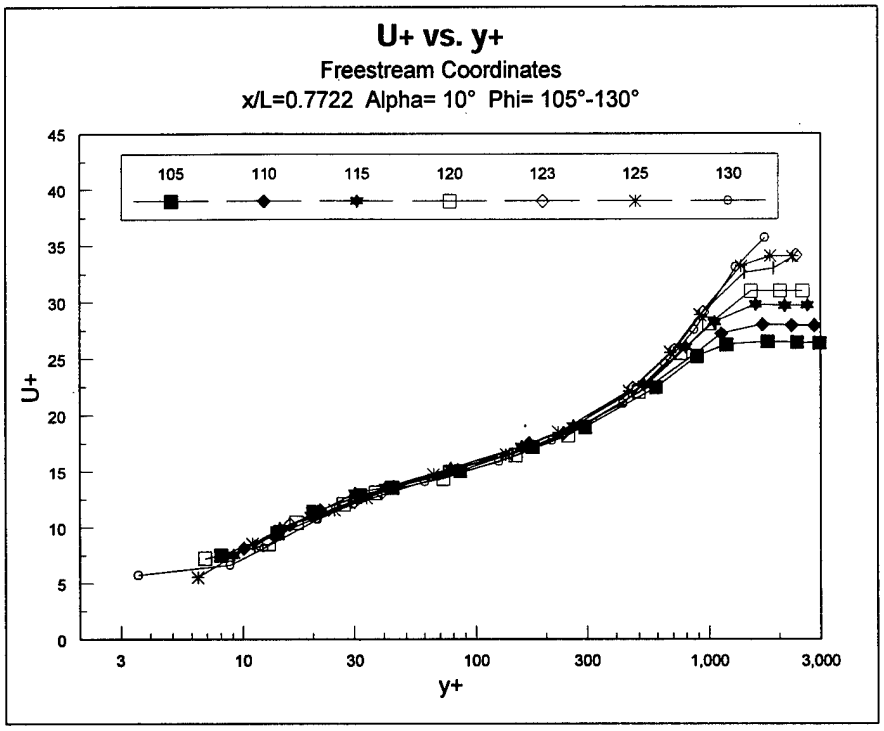


Figure 3. $U^+$ Profiles in Free-stream Coordinates at x/L= 0.7722.

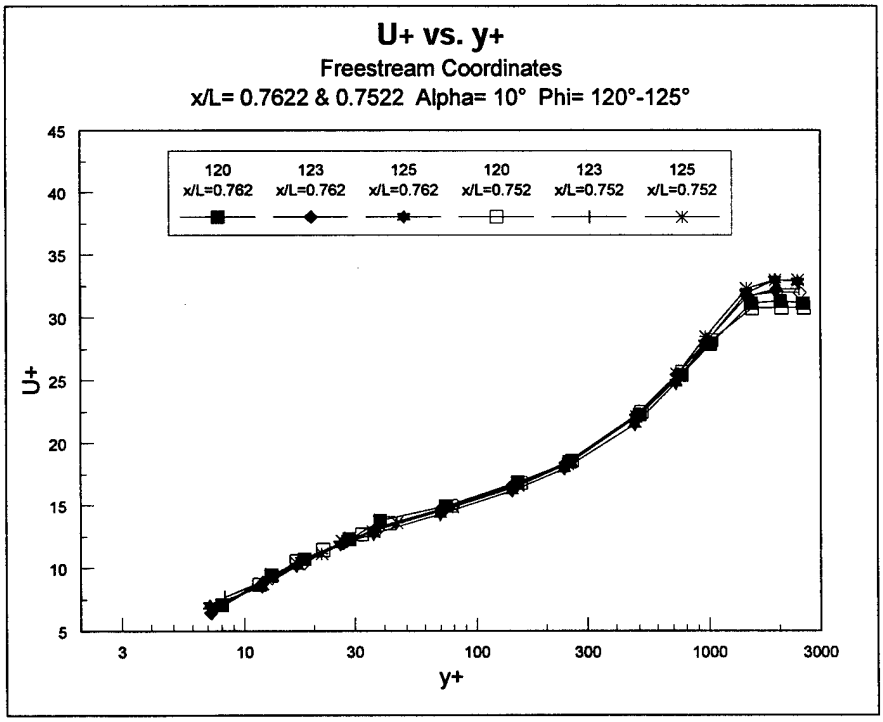


Figure 4. $U^+$ Profiles in Free-stream Coordinates at x/L= 0.7622 & 7522.

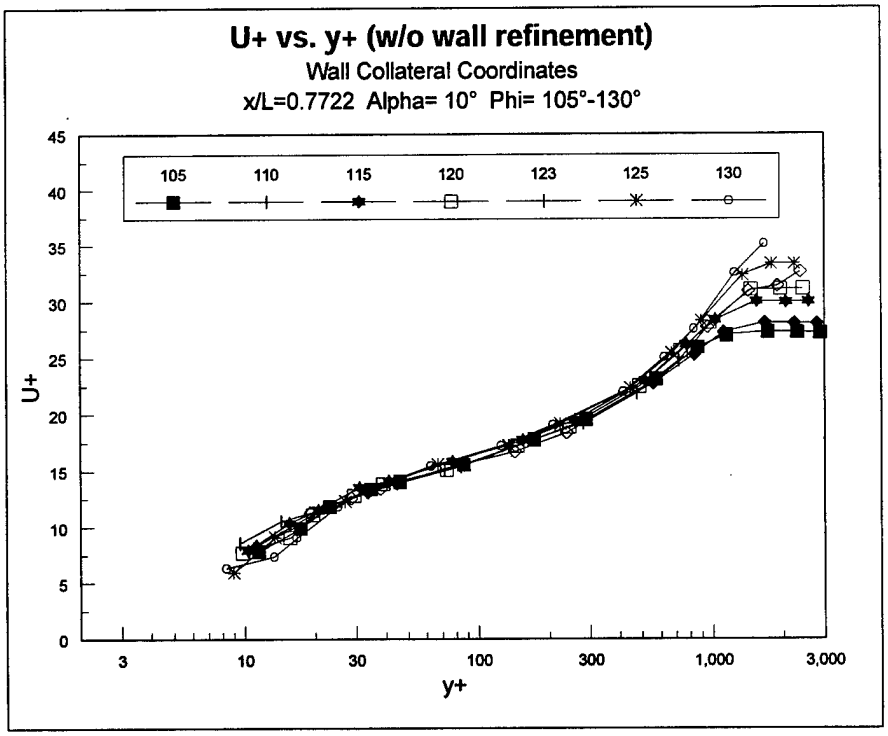


Figure 5. $U^+$ Profiles without Wall Refinement, Wall-collateral Coordinates, x/L= 0.7722.

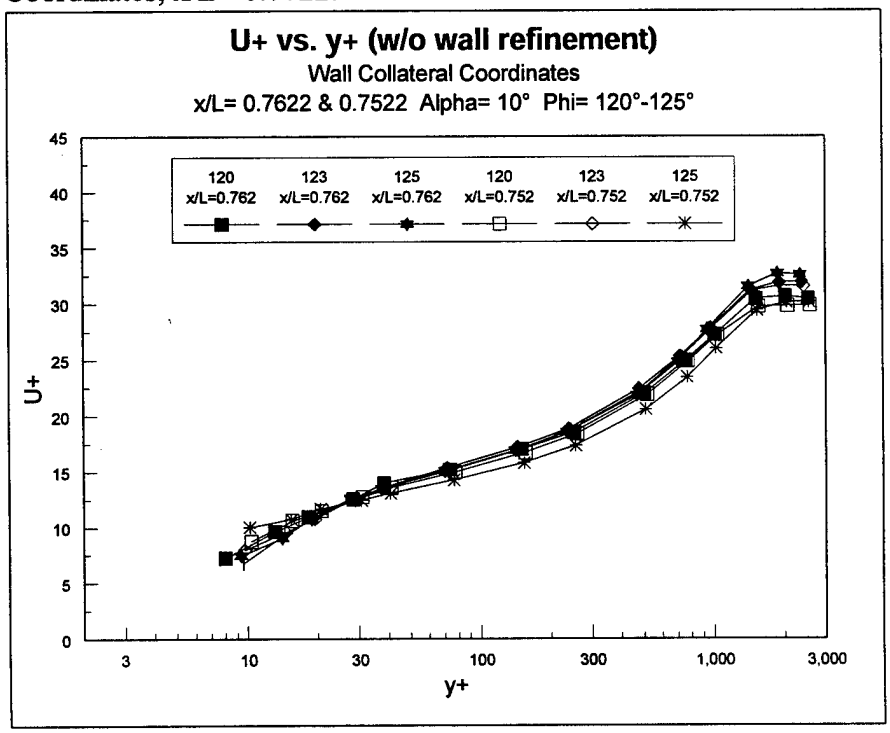


Figure 6. $U^+$ Profiles Without Wall Refinement, Wall-collateral Coordinates, x/L= 0.7762 & 0.7752.

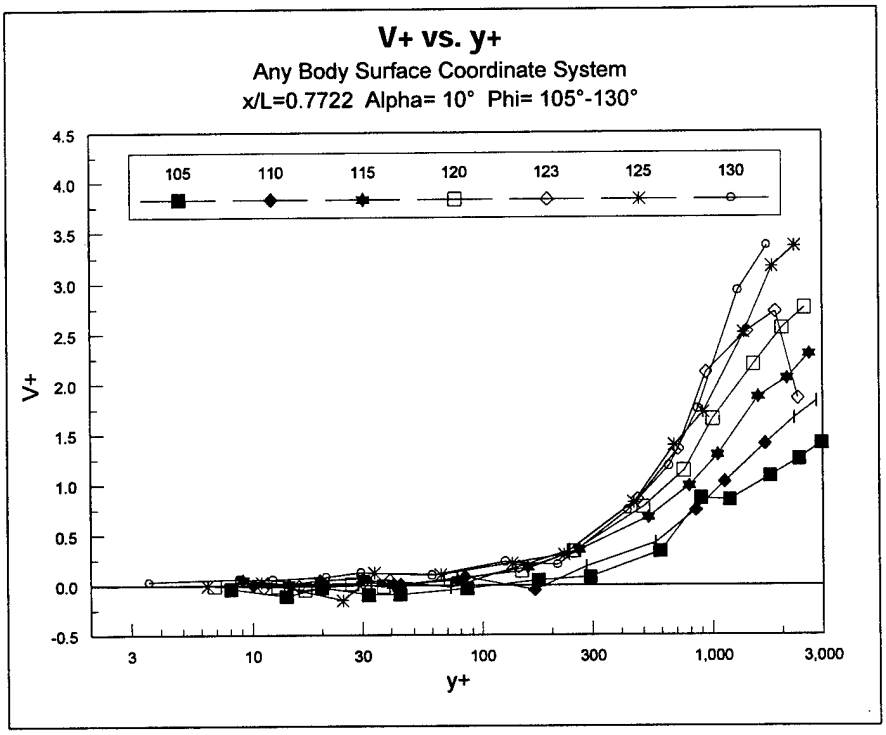


Figure 7. $V^+$ Profile, Normal to Wall, x/L= 0.7722.

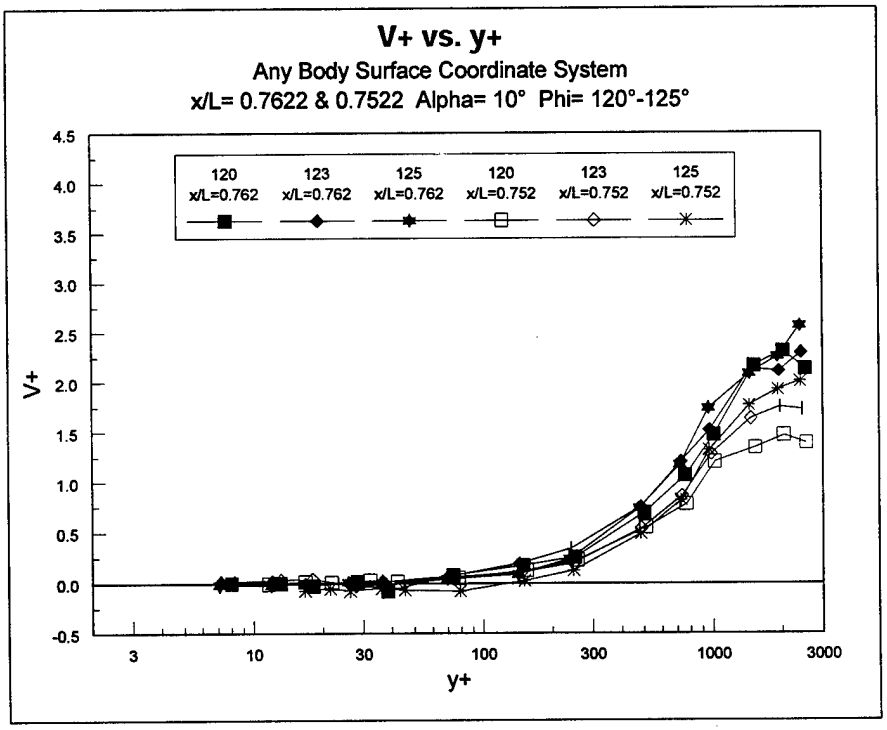


Figure 8. $V^+$ Profile, Normal to Wall, x/L= 0.7622 & 0.7522.

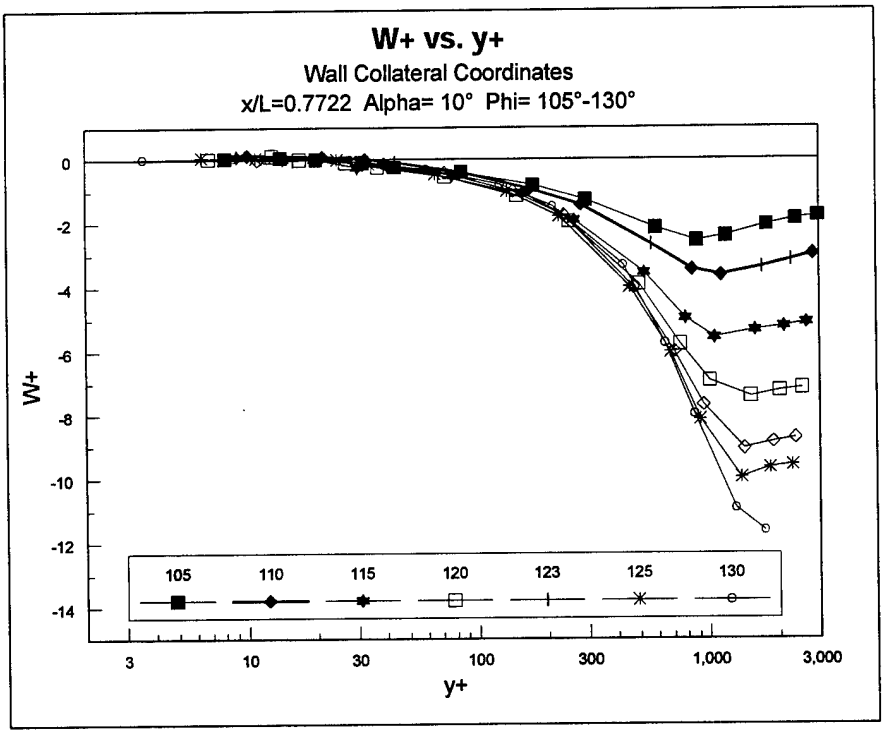


Figure 9. $W^+$ Profiles, Wall-collateral Coordinates, x/L= 0.7722.

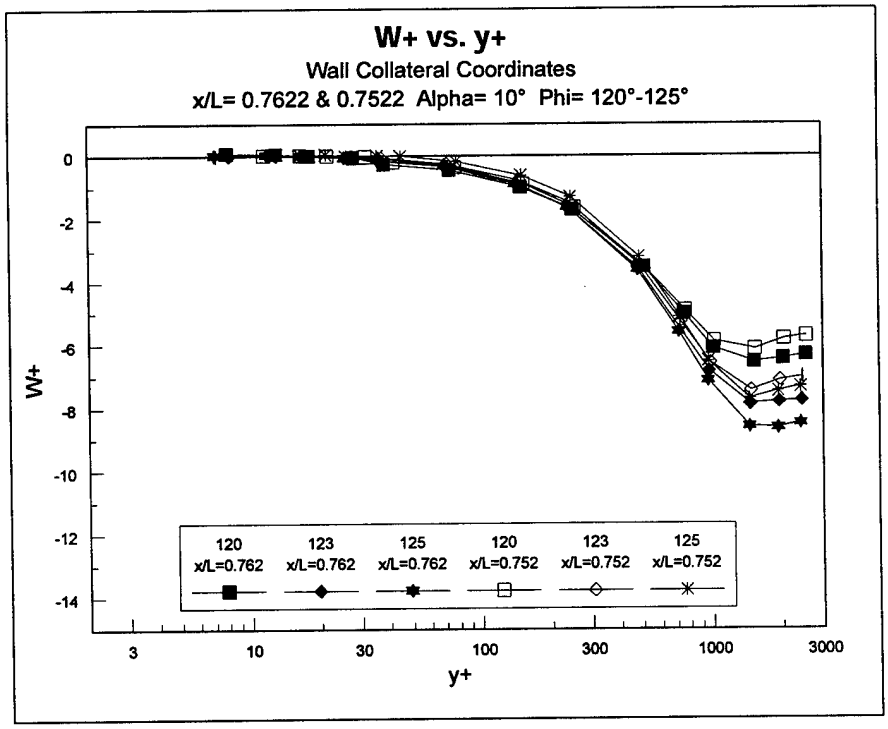


Figure 10. $W^+$ Profiles, Wall-collateral Coordinates, x/L= 0.7622 & 0.7522.

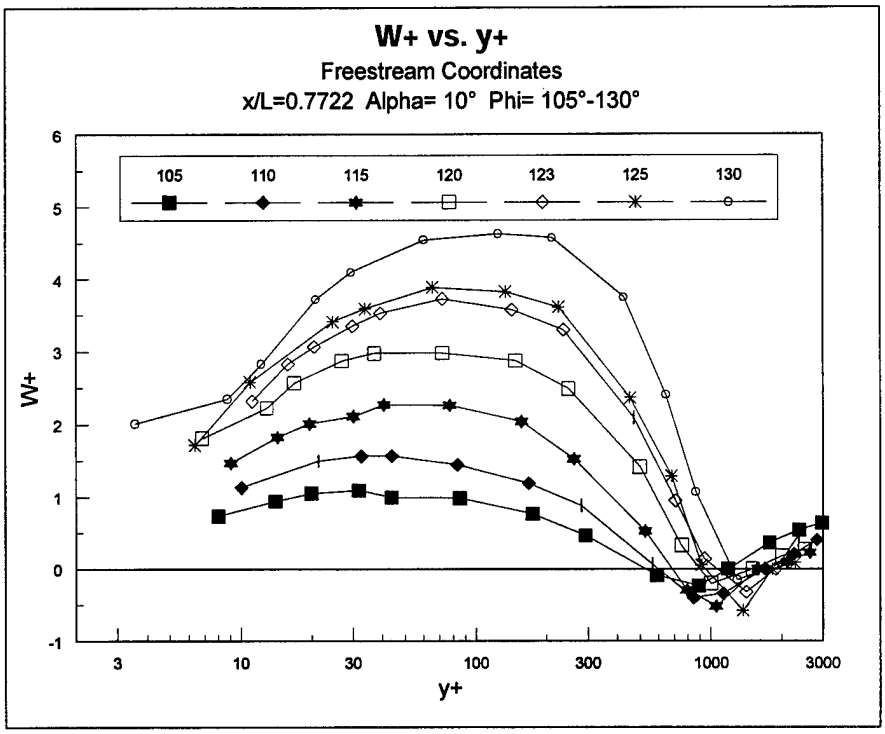


Figure 11. $W^+$ Profiles, Free-stream Coordinates, x/L= 0.7722.

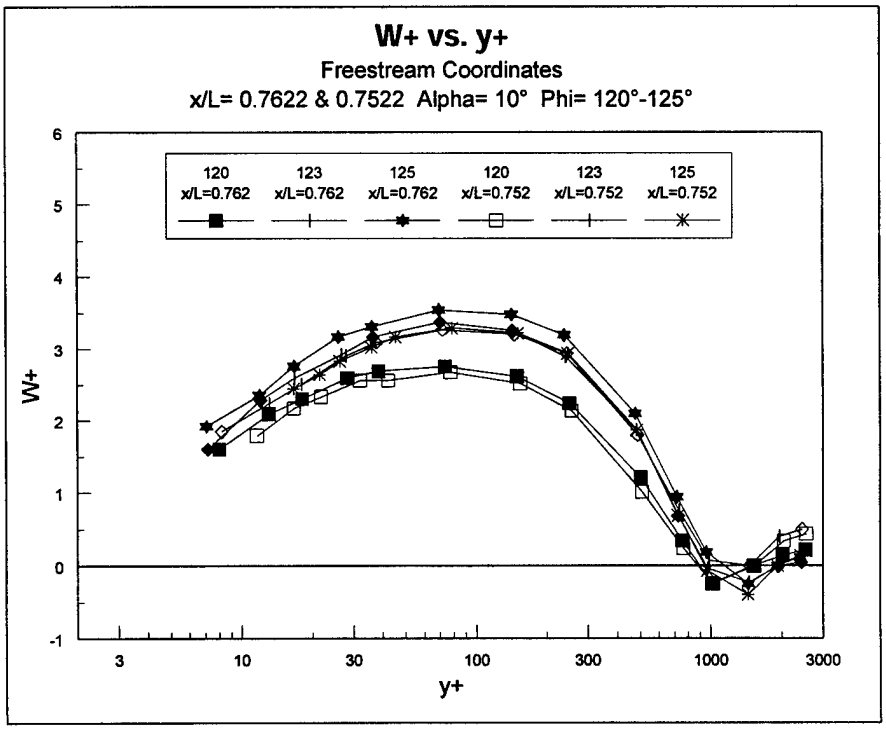


Figure 12. $W^+$ Profiles, Free-stream Coordinates, x/L= 0.7622 & 0.7522.

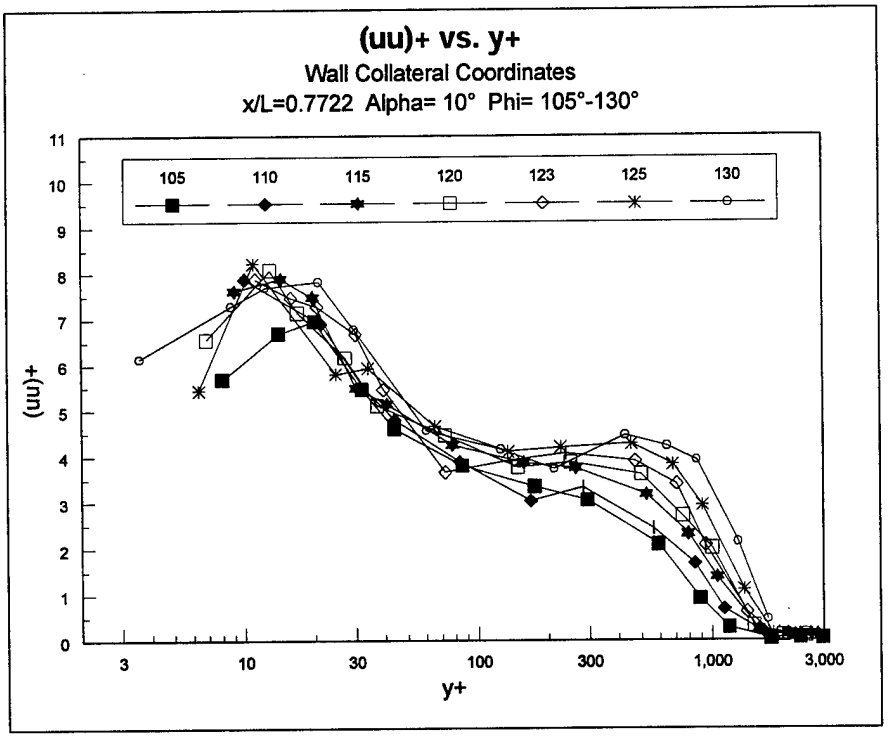


Figure 13. $u'^2$ Profiles, Wall-collateral Coordinates, x/L= 0.7722.

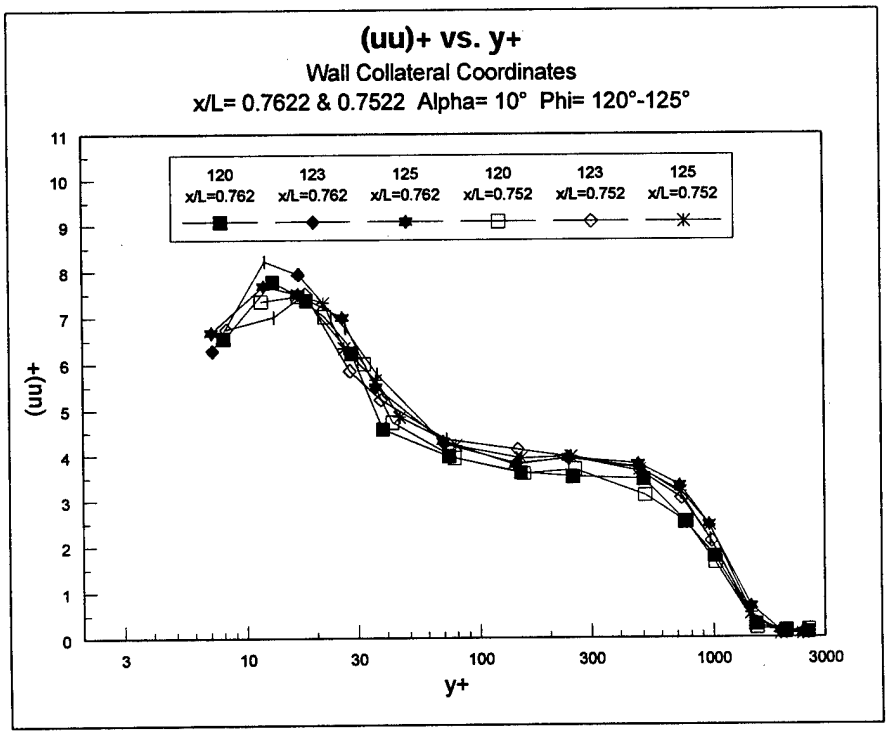


Figure 14. $u'^2$ Profiles, Wall-collateral Coordinates, x/L= 0.7622 & 0.7522.

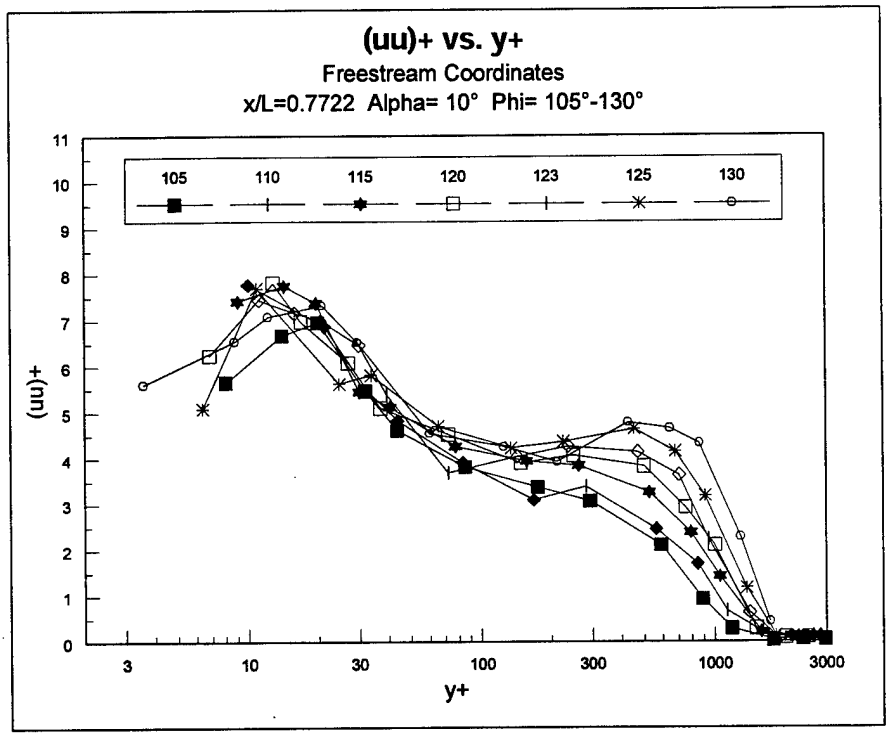


Figure 15. $u'^2$ Profiles, Free-stream Coordinates, x/L= 0.7722.

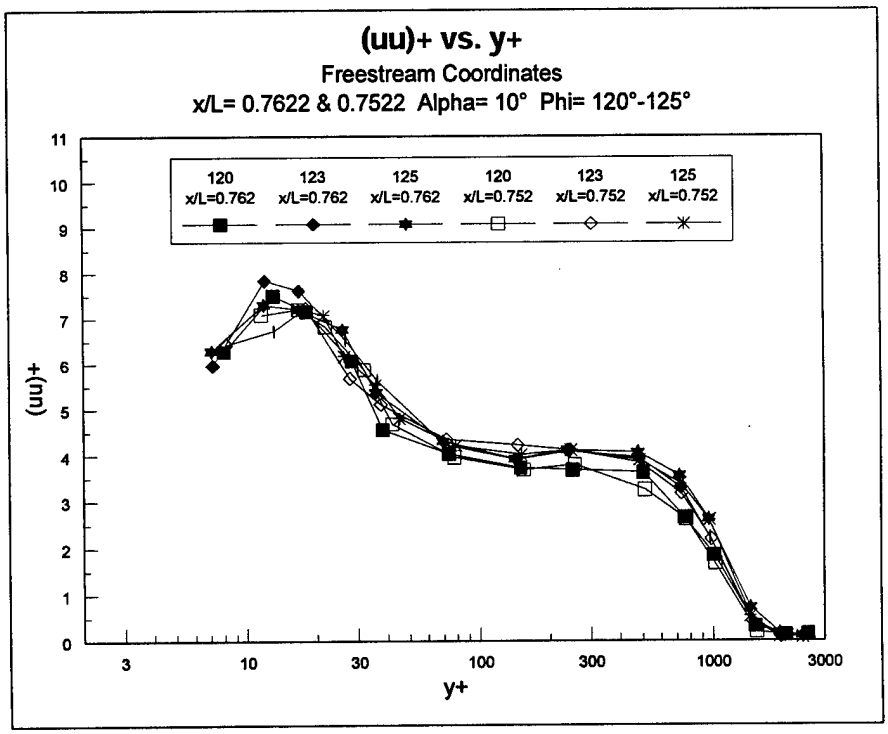


Figure 16. $u'^2$ Profiles, Free-stream Coordinates, x/L= 0.7622 & 0.7522.

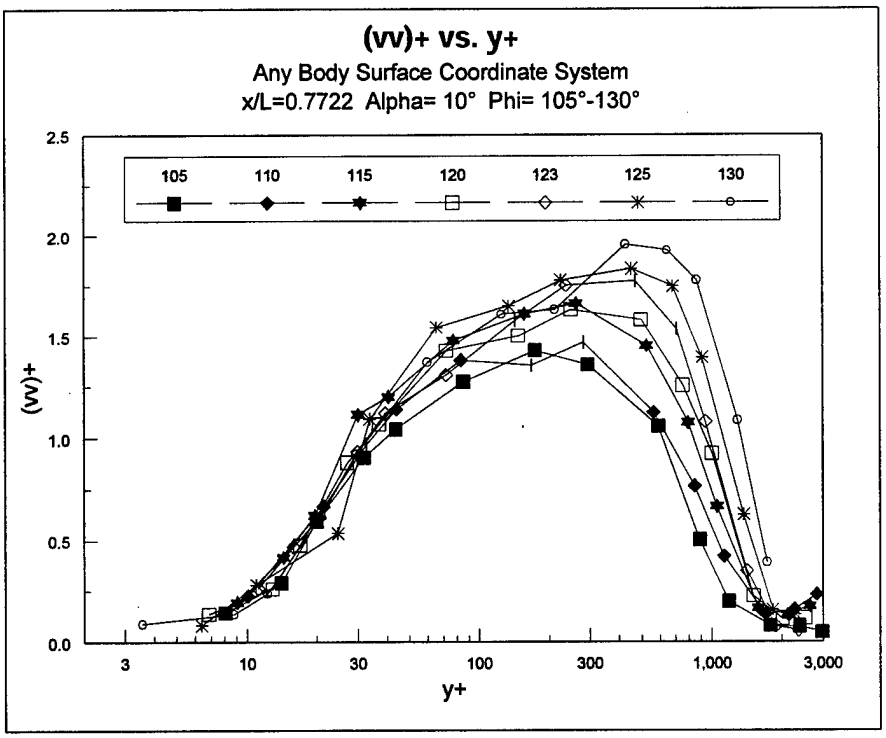


Figure 17. $v'^2$ Profiles, Normal to Wall, x/L= 0.7722.

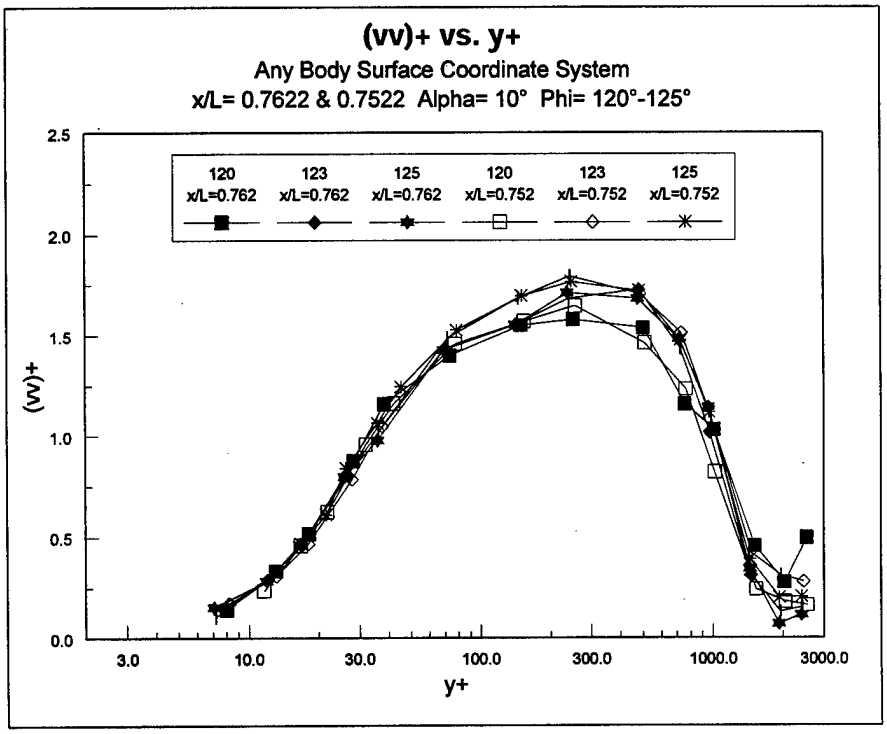


Figure 18. $v'^2$ Profiles, Normal to Wall, x/L= 0.7622 & 0.7522.

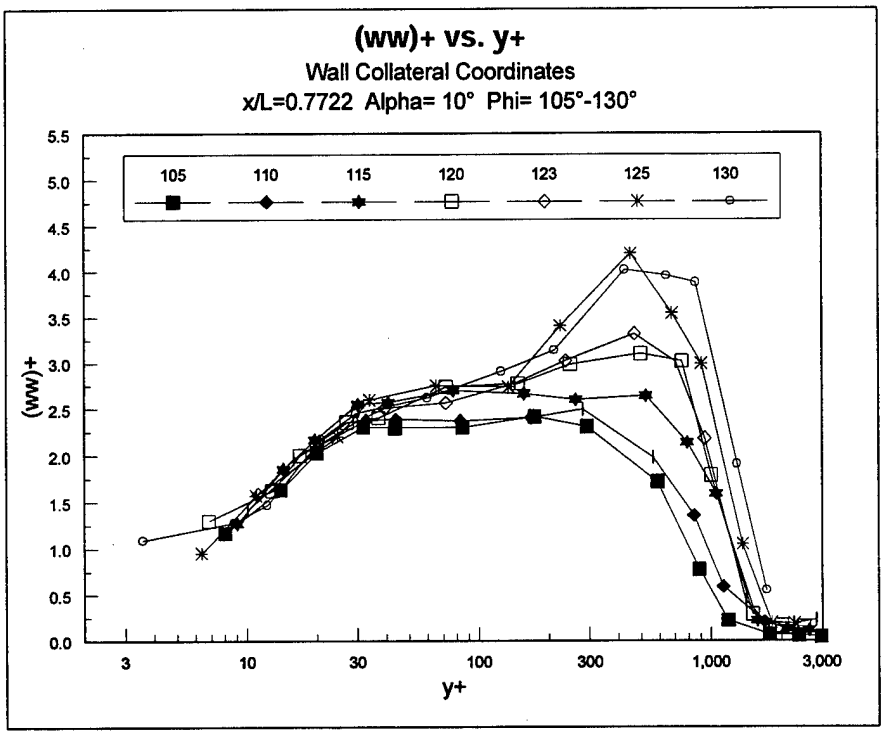


Figure 19. $w'^2$ Profiles, Wall-collateral Coordinates, x/L= 0.7722.

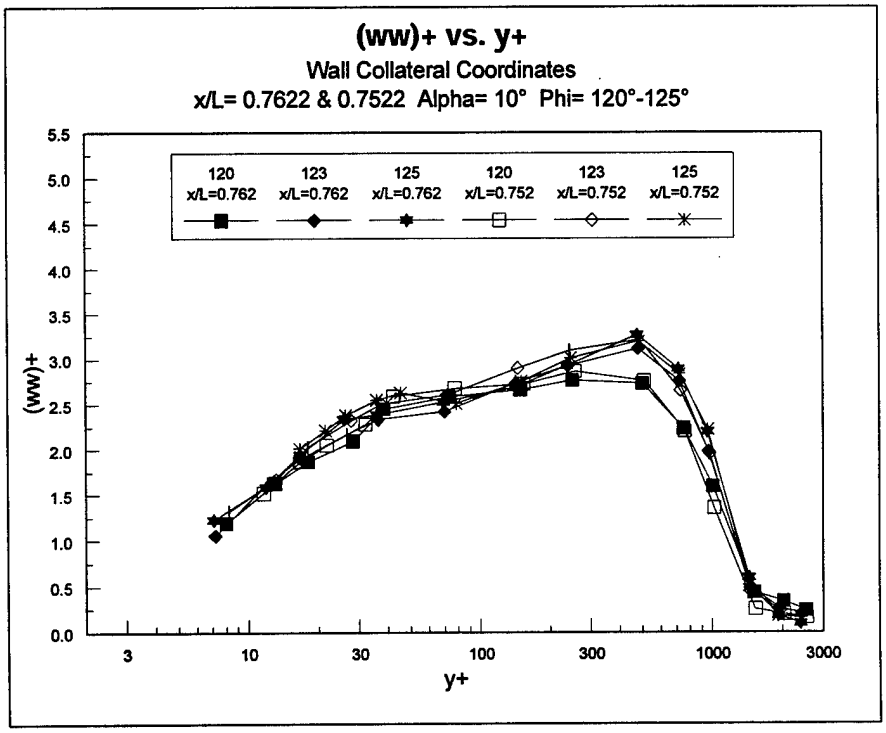


Figure 20. $w'^2$ Profiles, Wall-collateral Coordinates, x/L= 0.7622 & 0.7522.

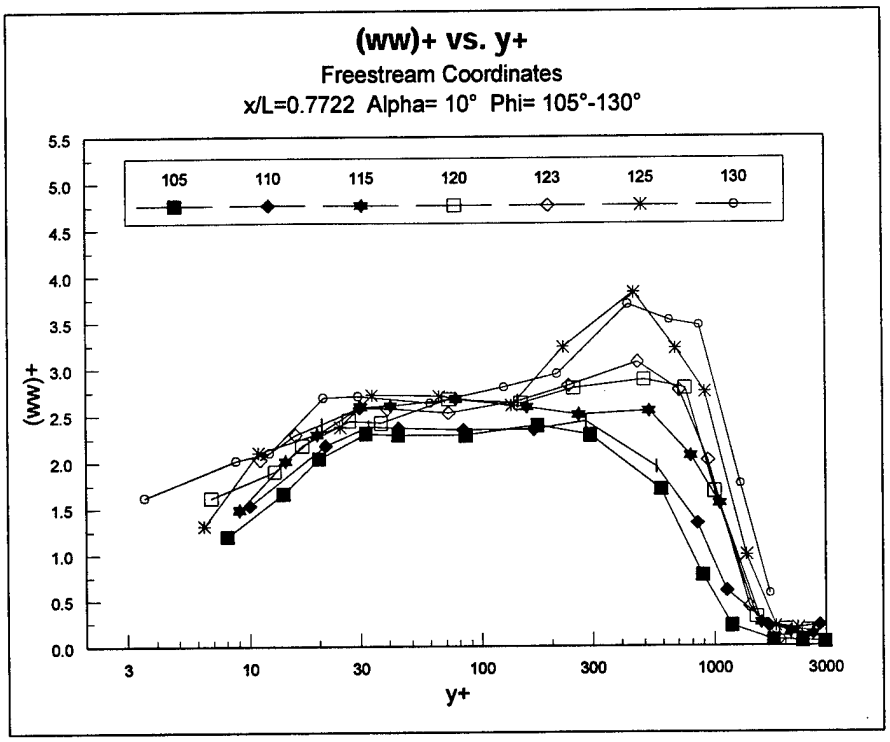


Figure 21. $w'^2$ Profiles, Free-stream Coordinates, x/L = 0.7722.

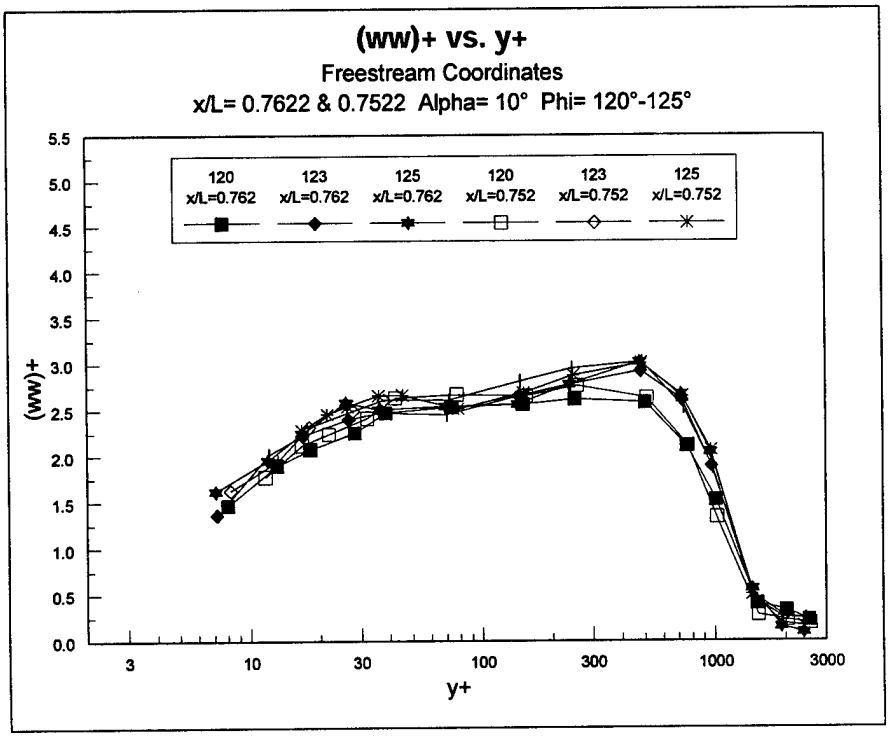


Figure 22. $w'^2$ Profiles, Free-stream Coordinates, x/L = 0.7622 & 0.7522.

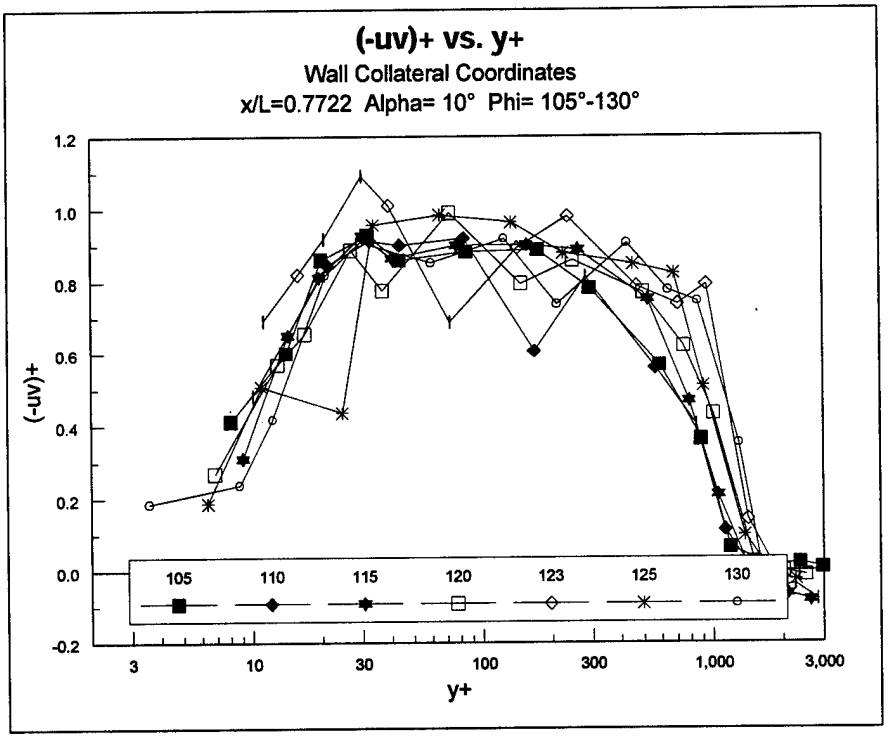


Figure 23. -u'v' Profiles, Wall-collateral Coordinates, x/L= 0.7722.

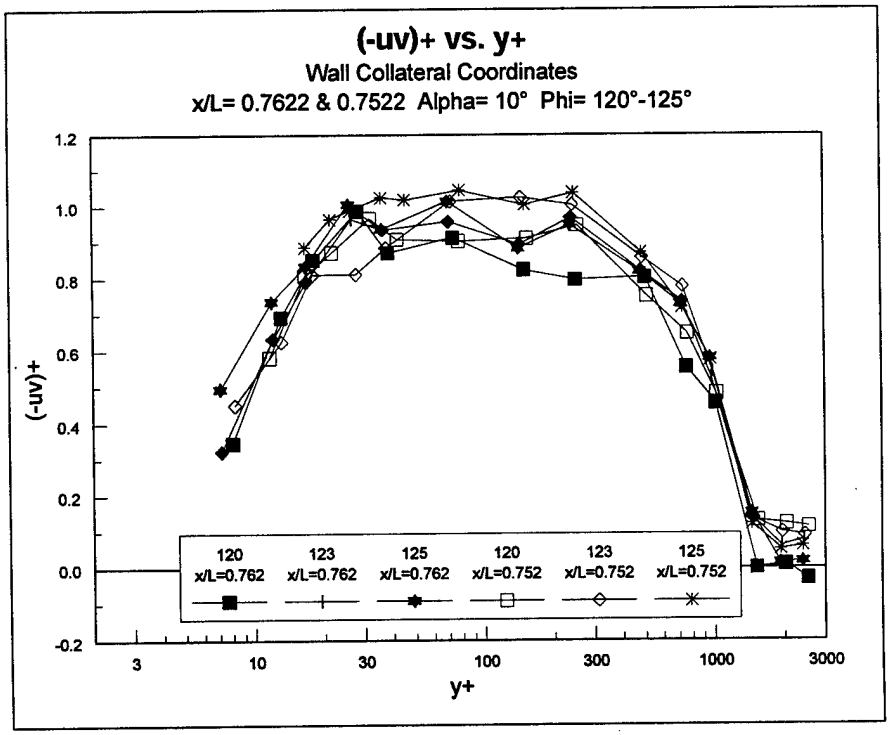


Figure 24. -u'v' Profiles, Wall-collateral Coordinates, x/L= 0.7622 & 0.7522.

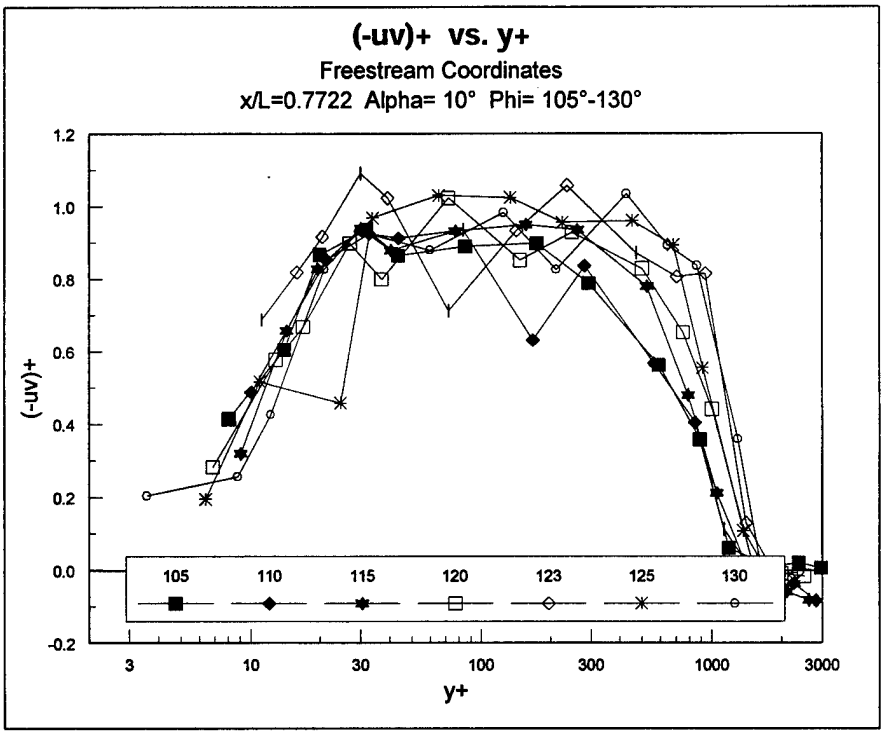


Figure 25. -u'v' Profiles, Free-stream Coordinates, x/L= 0.7722.

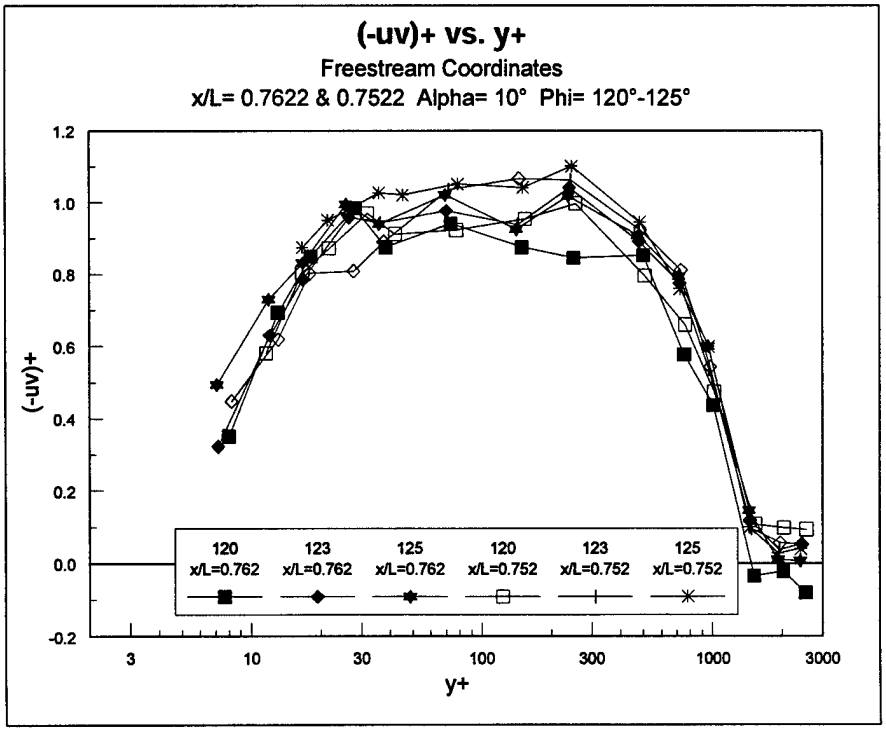


Figure 26. -u'v' Profiles, Free-stream Coordinates, x/L= 0.7622 & 0.7522.

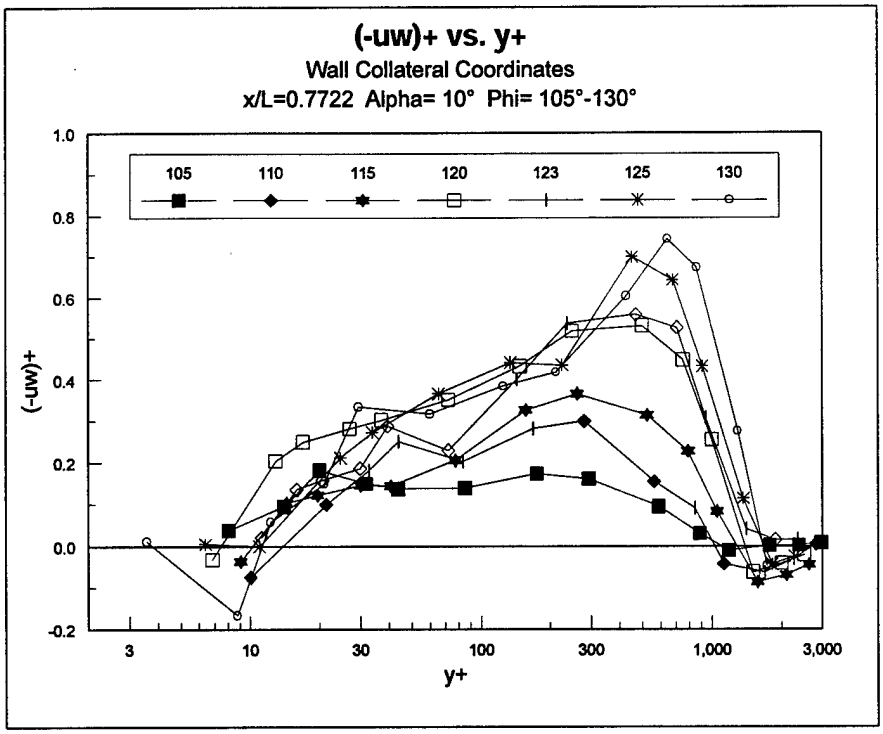


Figure 27. -u'w' Profiles, Wall-collateral Coordinates, x/L= 0.7722.

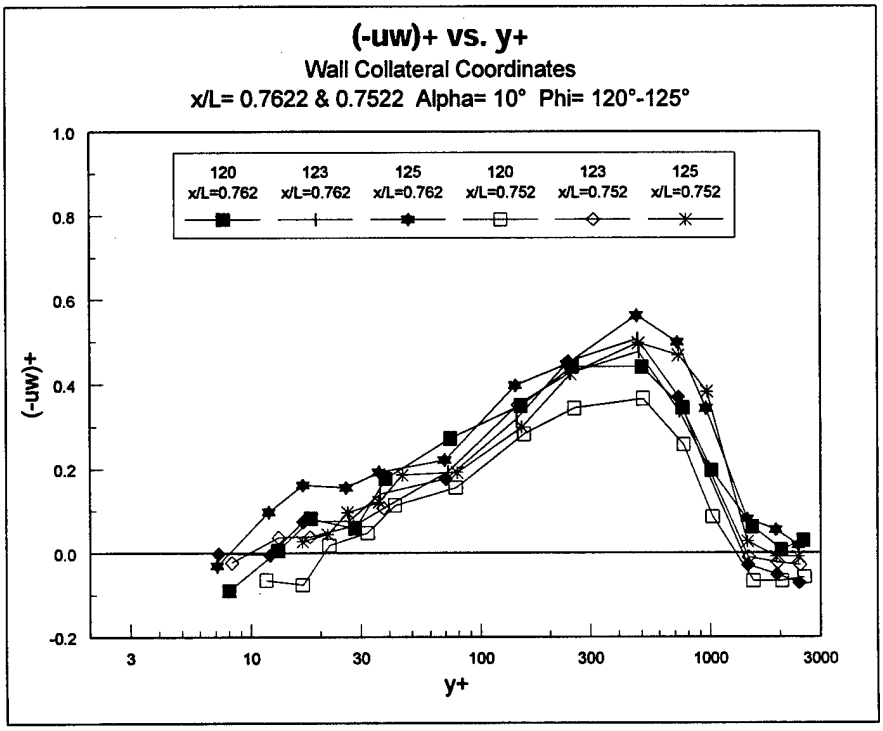


Figure 28. -u'w' Profiles, Wall-collateral Coordinates, x/L= 0.7622 & 0.7522.

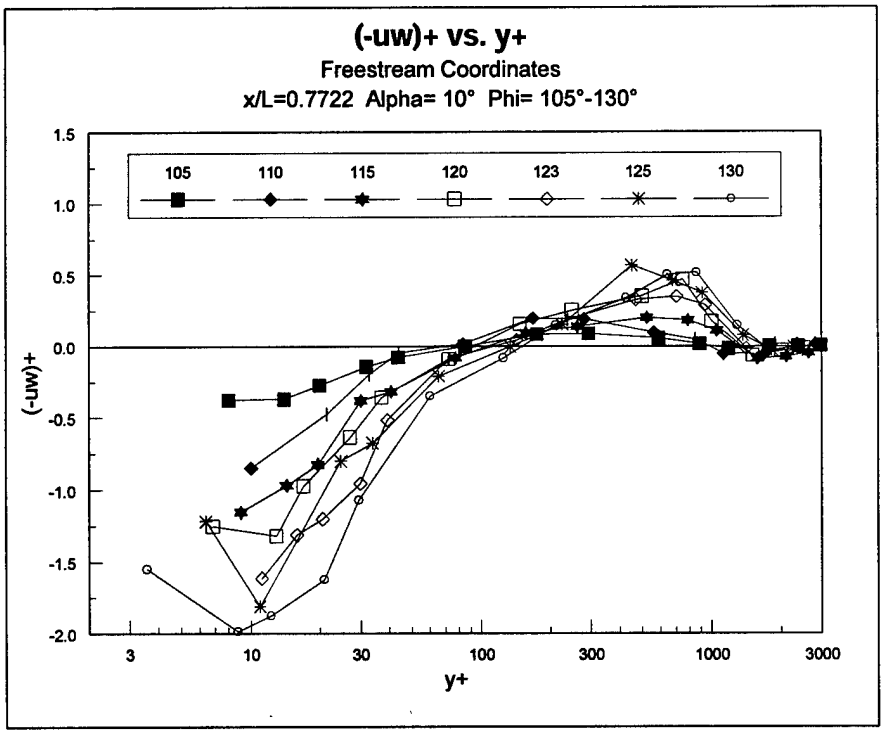


Figure 29. -u'w' Profiles, Free-stream Coordinates, x/L= 0.7722.

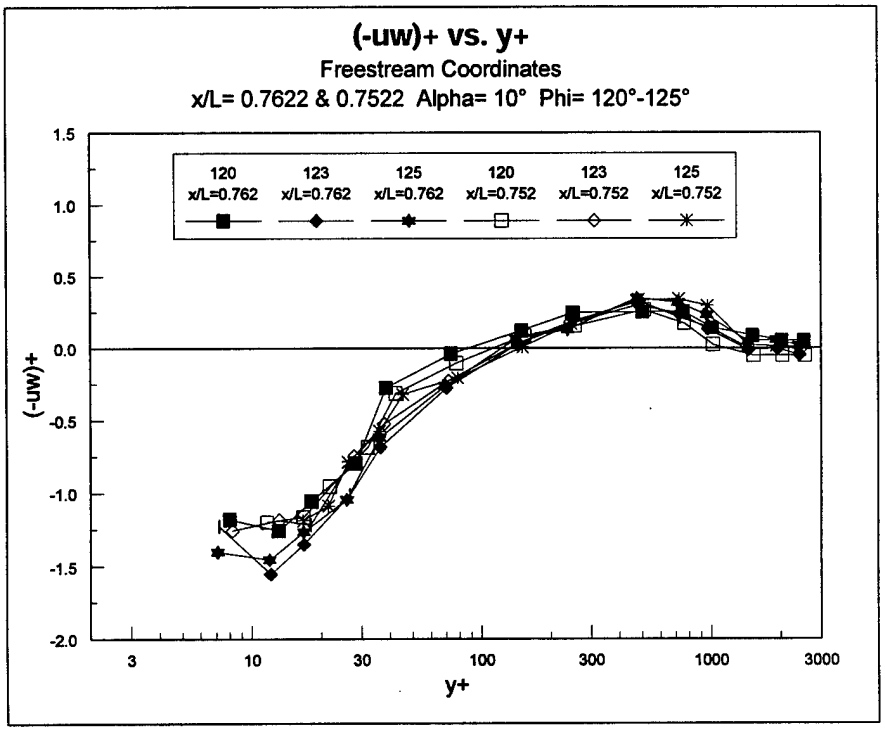


Figure 30. -u'w' Profiles, Free-stream Coordinates, x/L= 0.7622 & 0.7522.

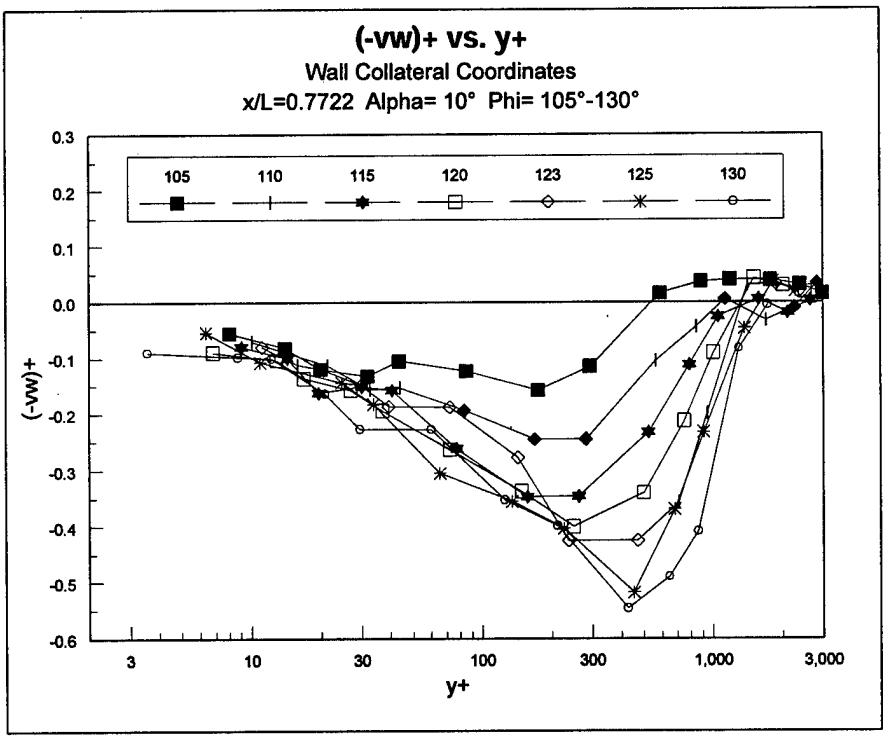


Figure 31. -v'w' Profiles, Wall-collateral Coordinates, x/L= 0.7722.

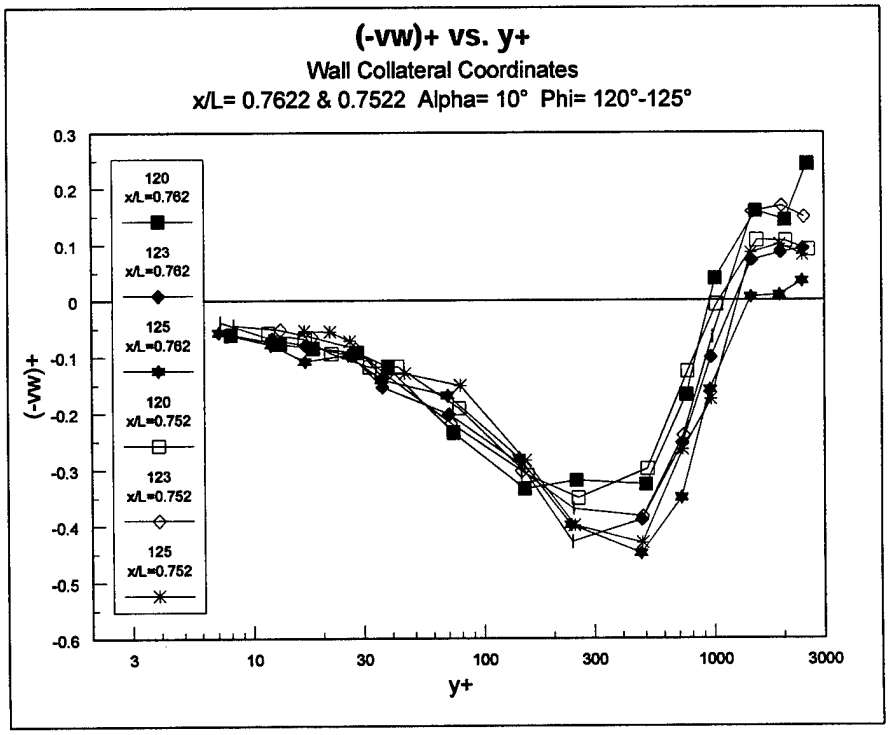


Figure 32. -v'w' Profiles, Wall-collateral Coordinates, x/L= 0.7622 & 0.7522.

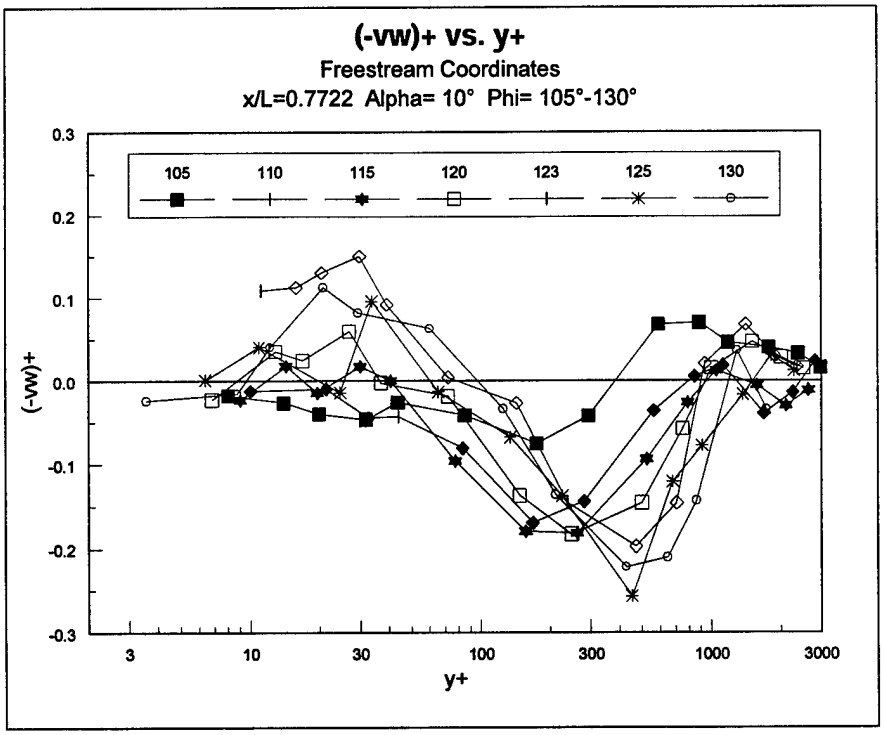


Figure 33. -v'w' Profiles, Free-stream Coordinates, x/L= 0.7722.

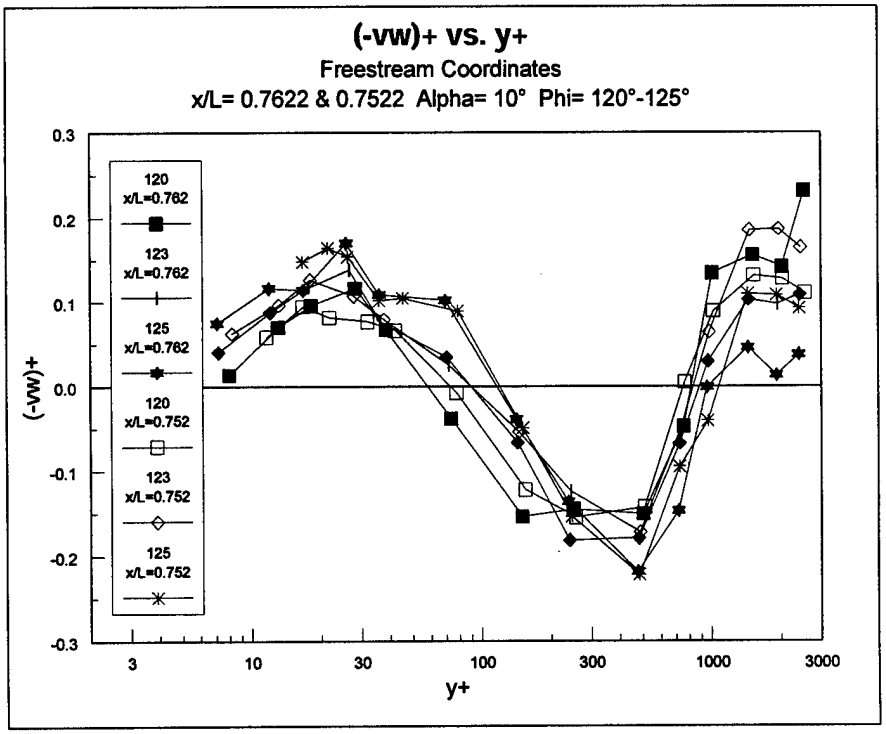


Figure 34. -v'w' Profiles, Free-stream Coordinates, x/L= 0.7622 & 0.7522.

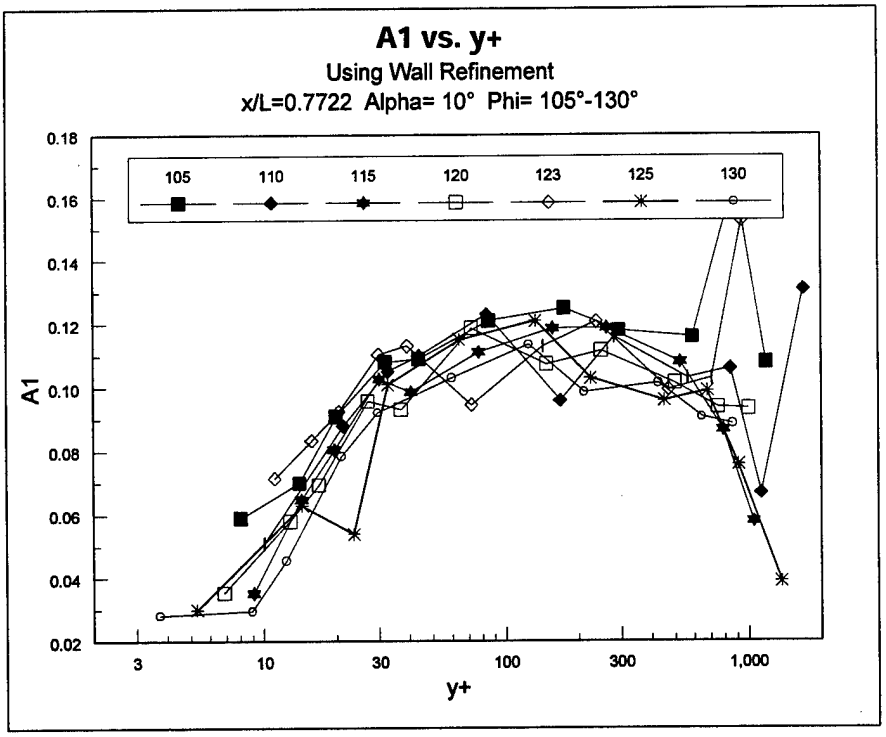


Figure 35. $a_1$ Profiles Using Wall Refinement, x/L= 0.7722.

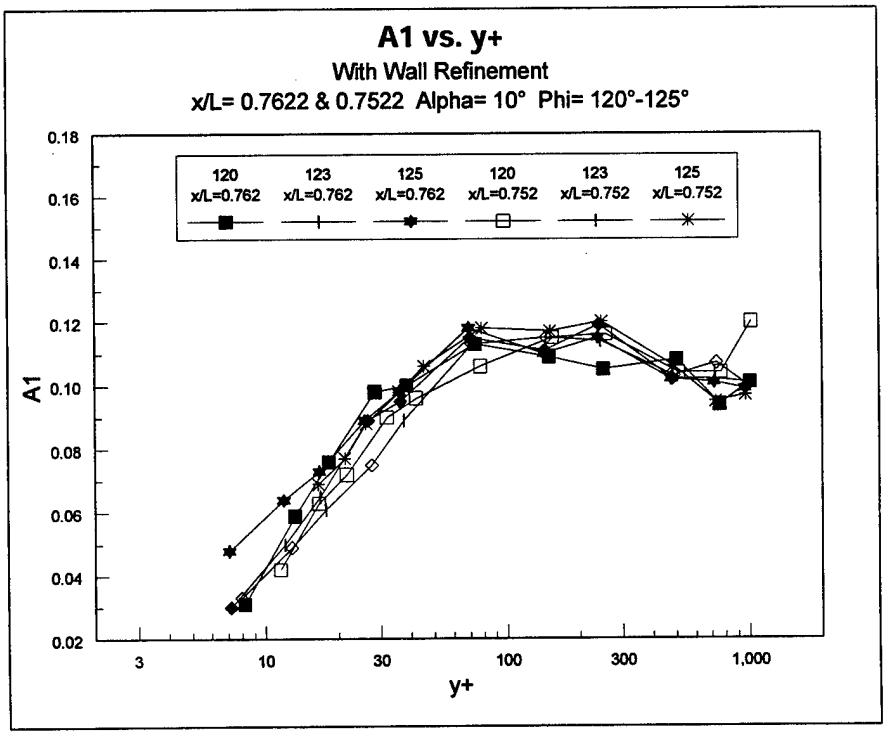


Figure 36. $a_1$ Profiles Using Wall Refinement, x/L= 0.7622 & 0.7522.

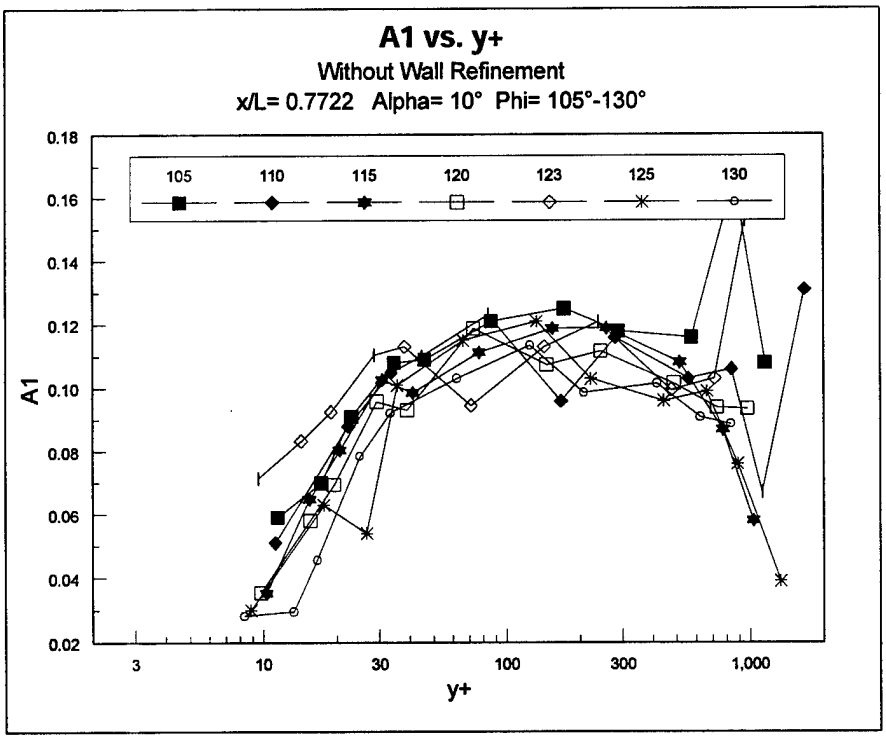


Figure 37. $a_1$ Profiles Without Wall Refinement, x/L= 0.7722.

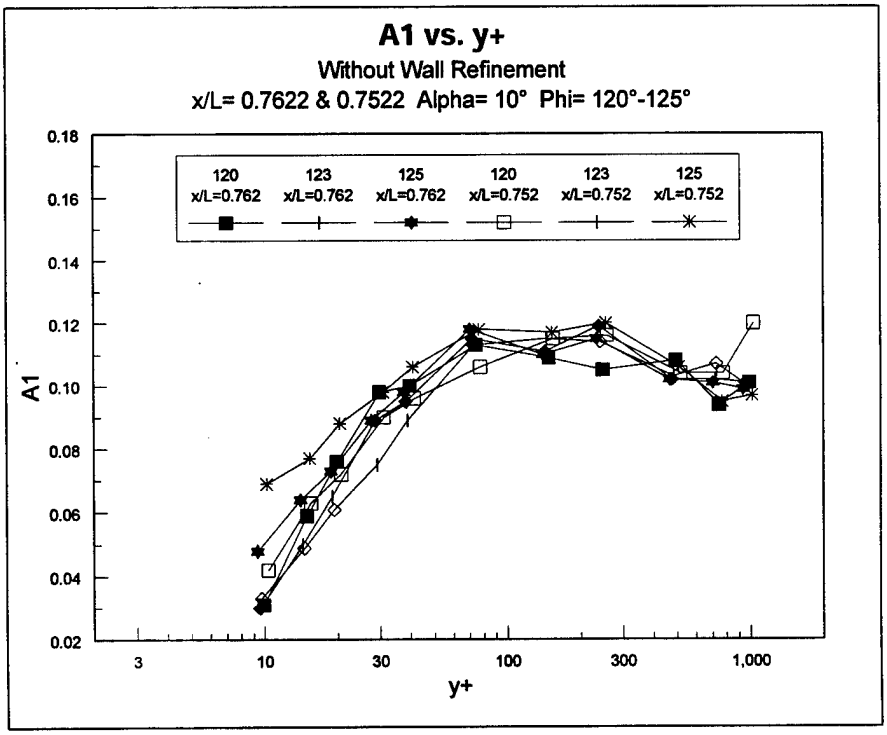


Figure 38. $a_1$ Profiles Without Wall Refinement, x/L= 0.7622 & 0.7522.

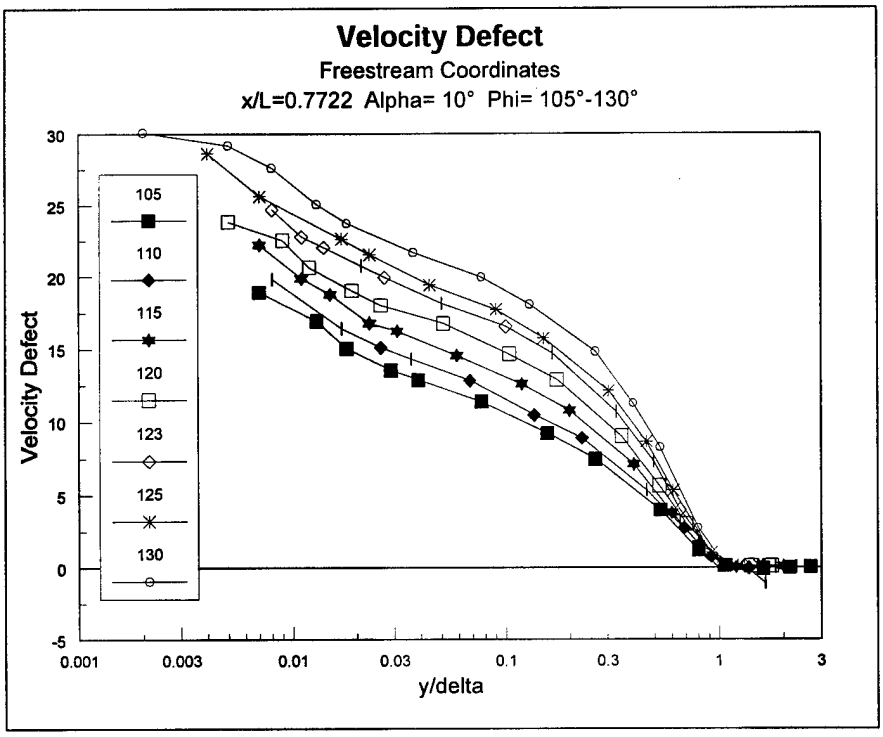


Figure 39. Velocity Defect, Free-stream Coordinates, x/L= 0.7722.

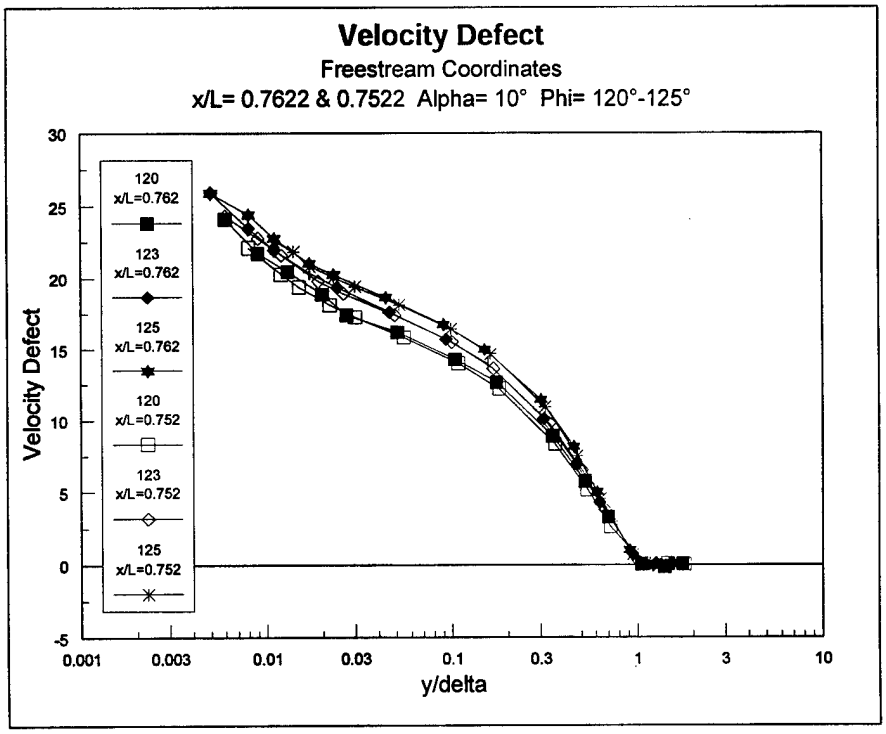


Figure 40. Velocity Defect, Free-stream Coordinates, x/L= 0.7622 & 0.7522.

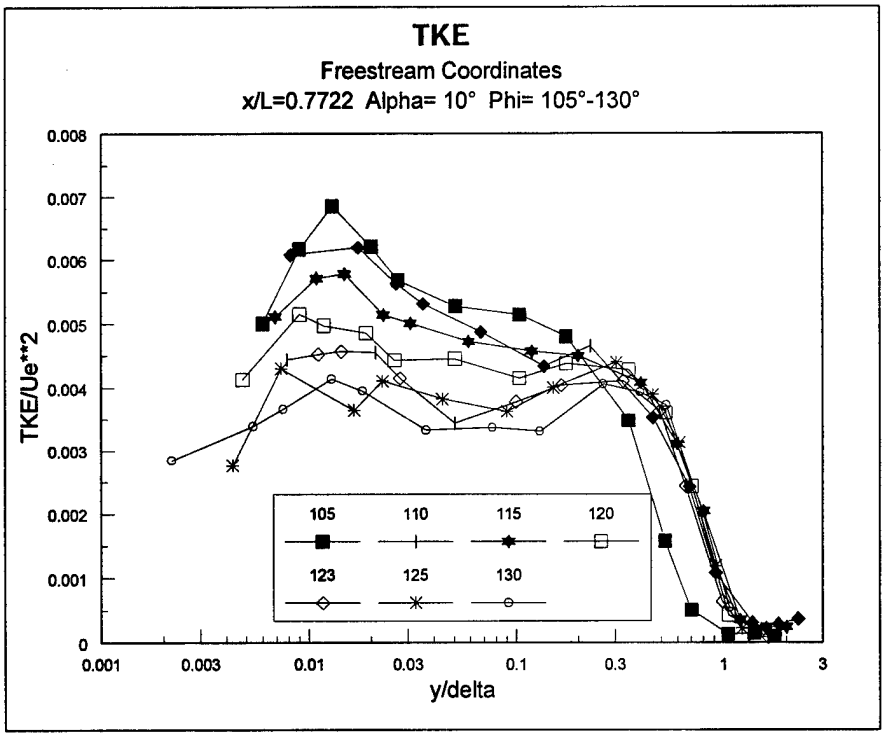


Figure 41. TKE, Free-stream Coordiantes, x/L = 0.7722.

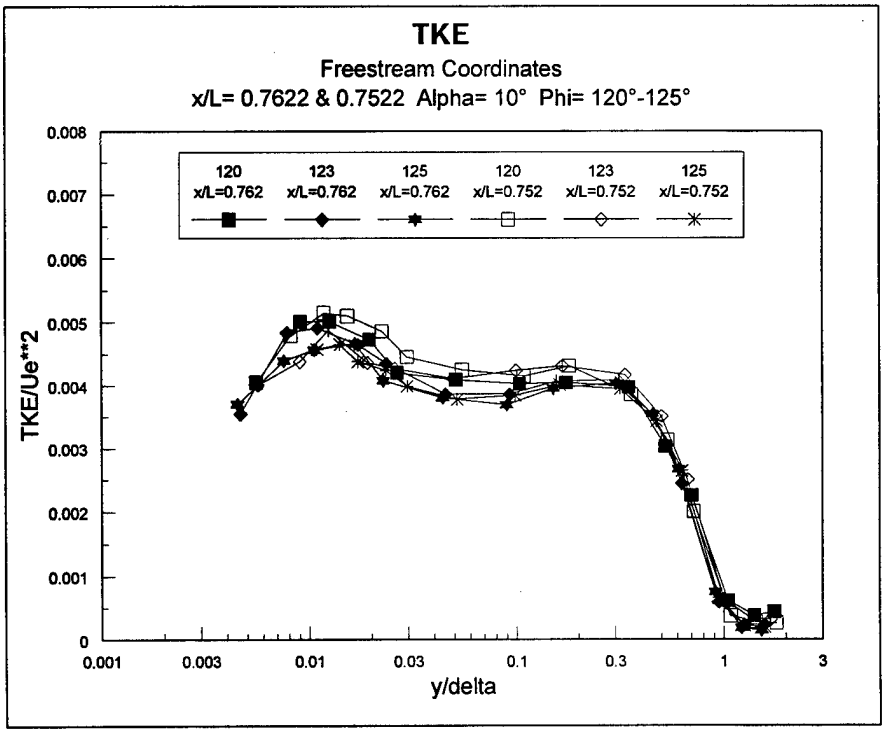


Figure 42. TKE, Free-stream Coordinates, x/L= 0.7622 & 0.7522,

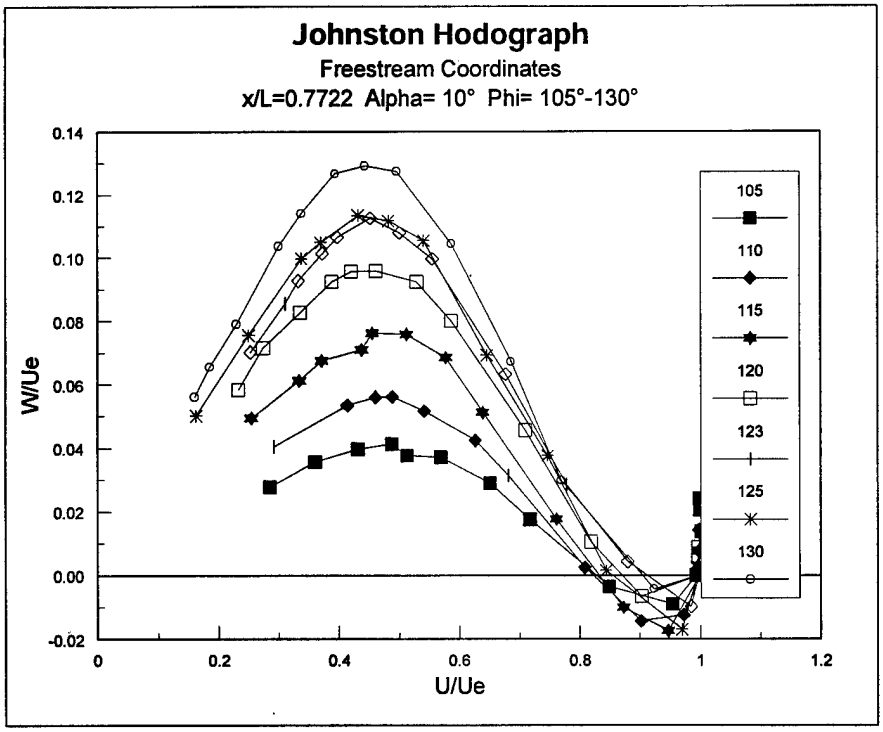


Figure 43. Johnston Hodograph, Free-stream Coordinates, x/L= 0.7722.

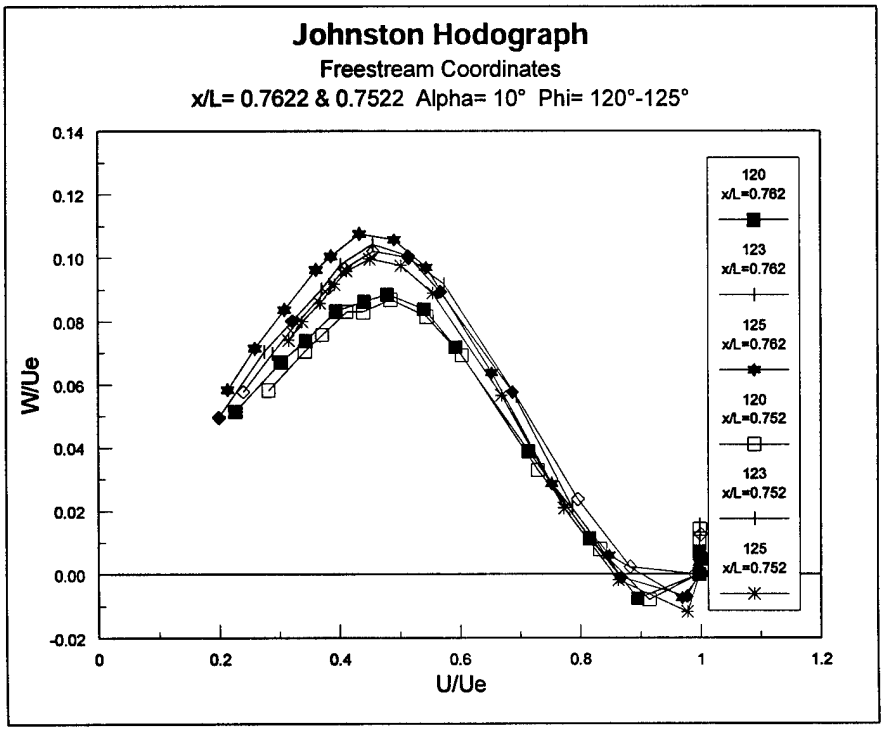


Figure 44. Johnston Hodograph, Free-stream Coordinates, x/L= 0.7622 & 0.7522.

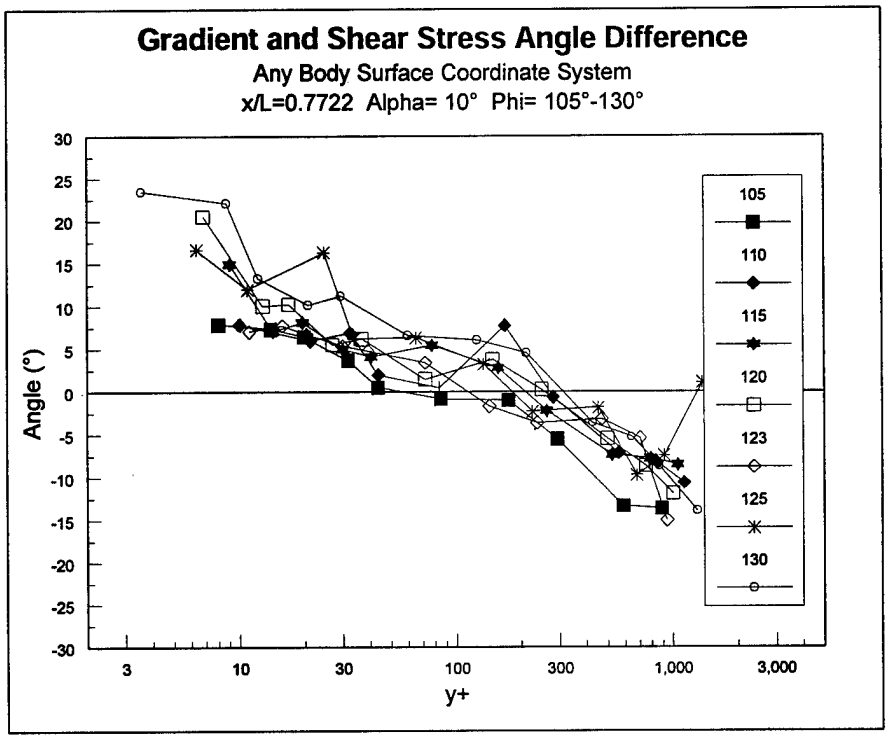


Figure 45. Difference Between Gradient and Shear Stress Angles, x/L= 0.7722.

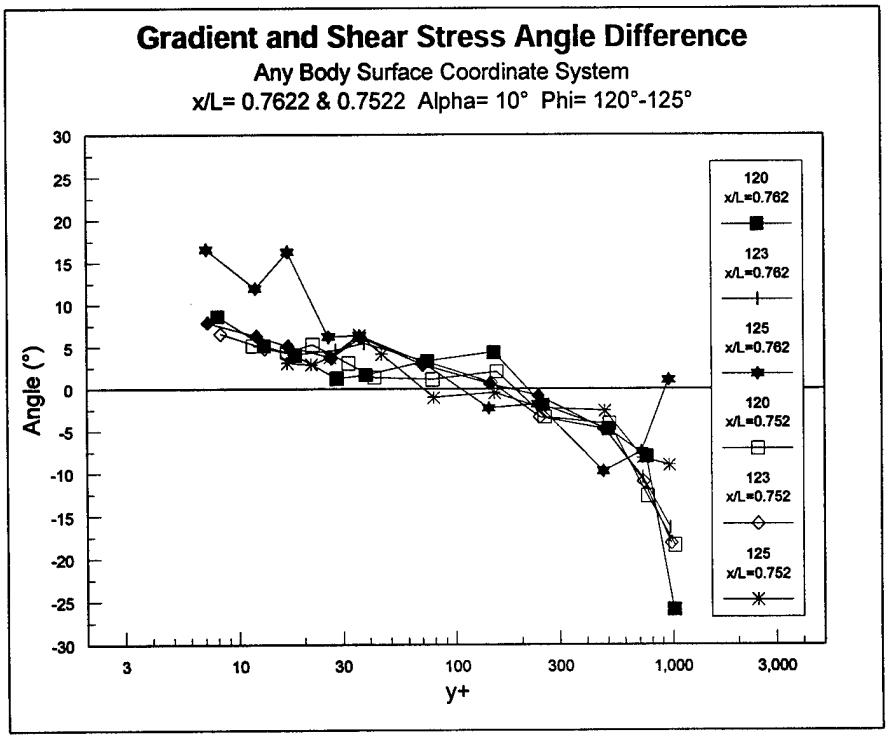


Figure 46. Difference Between Gradient and Shear Stress Angles, x/L= 0.7622 & 0.7522.

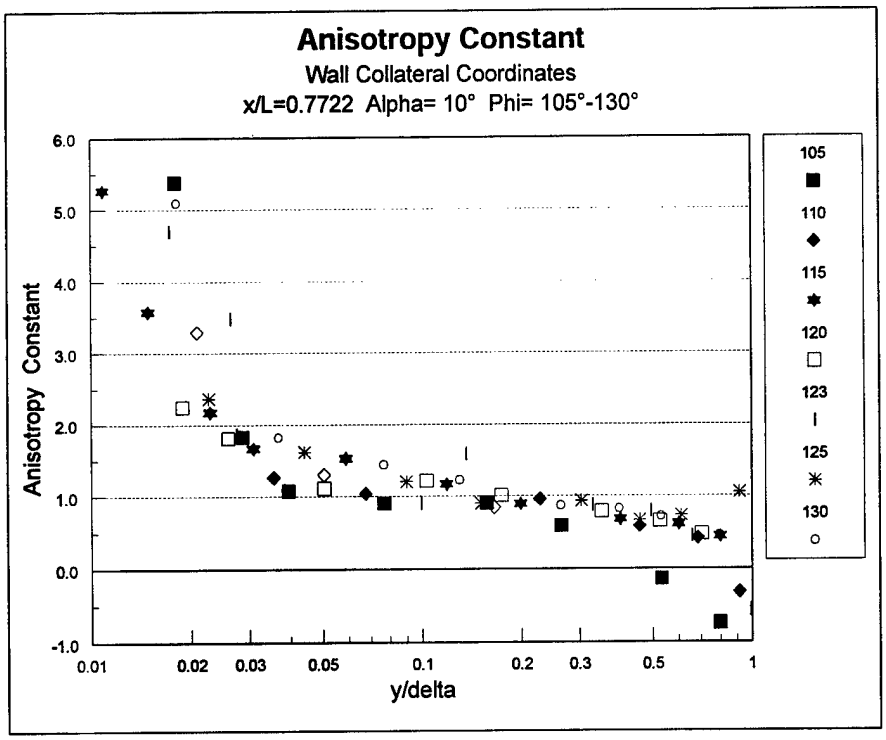


Figure 47. Anisotropy Constant, Wall-collateral Coordinates, x/L= 0.7722.

**Table 8-1: Points Discarded In Figure 47.**

| $\phi = 105°$ | | $\phi = 110°$ | | $\phi = 115°$ | | $\phi = 120°$ | |
|---|---|---|---|---|---|---|---|
| y/d | N | y/d | N | y/d | N | y/d | N |
| 0.007 | -46.99 | 0.008 | 16.28 | 0.007 | -36.63 | 0.005 | -9.19 |
| 0.013 | 16.38 | | | | | 0.009 | 37.16 |
| | | | | | | 0.012 | 7.85 |
| $\phi = 123°$ | | $\phi = 125°$ | | $\phi = 130°$ | | | |
| y/d | N | y/d | N | y/d | N | | |
| 0.008 | -14.94 | 0.004 | -35.88 | 0.002 | 17.80 | | |
| 0.011 | 136.60 | 0.007 | 867.70 | 0.005 | 73.51 | | |
| 0.014 | 10.23 | 0.017 | 19.74 | 0.008 | 43.20 | | |
| | | | | 0.013 | 10.35 | | |

All values above $y/\delta = 1.0$ are unreliable and have been discarded.

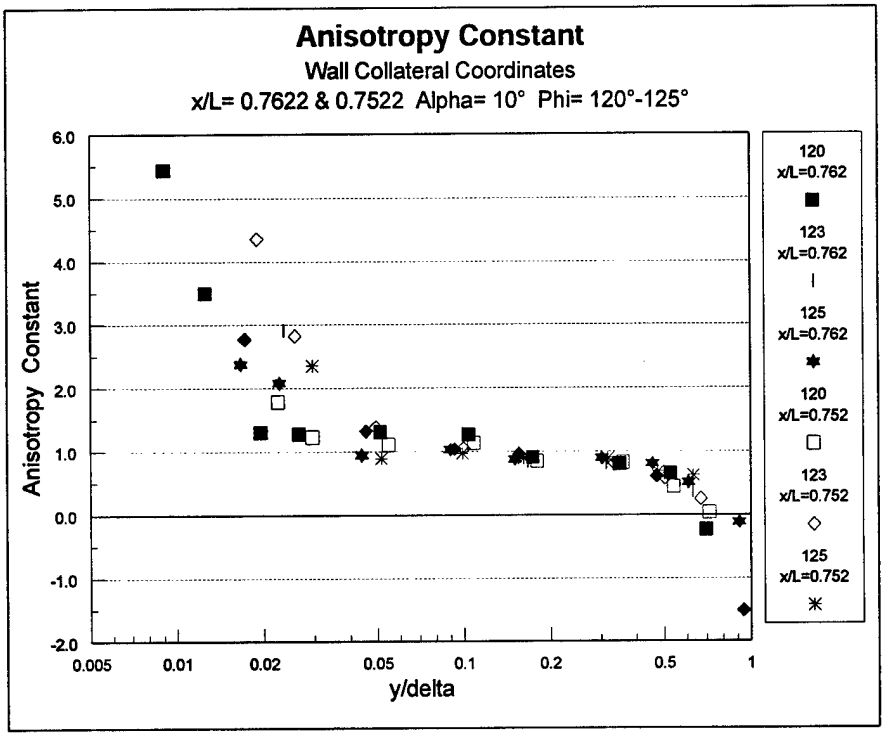


Figure 48. Anisotropy Constant, Wall-collateral Coordinates, x/L= 0.7622 & 0.7522.

**Table 8-2: Points Discarded In Figure 48.**

| x/L = 0.7622 | | | | | |
|---|---|---|---|---|---|
| $\phi$ = 120° | | $\phi$ = 123° | | $\phi$ = 125° | |
| y/δ | N | y/δ | N | y/δ | N |
| 0.006 | 7.79 | 0.005 | -6.22 | 0.005 | -15.59 |
| | | 0.008 | -26.71 | 0.008 | 44.34 |
| | | 0.011 | 9.28 | 0.011 | 9.40 |
| x/L = 0.7522 | | | | | |
| $\phi$ = 120° | | $\phi$ = 123° | | $\phi$ = 125° | |
| y/δ | N | y/δ | N | y/δ | N |
| 0.008 | 9.31 | 0.006 | -5.95 | 0.011 | 9.17 |
| 0.012 | 11.93 | 0.009 | -44.48 | 0.014 | 8.97 |
| 0.015 | 6.94 | 0.012 | 8.87 | 0.017 | 10.99 |
| | | | | 0.023 | 7.31 |
| | | | | 0.950 | -2.23 |

All values above y/δ = 1.0 are unreliable and have been discarded.

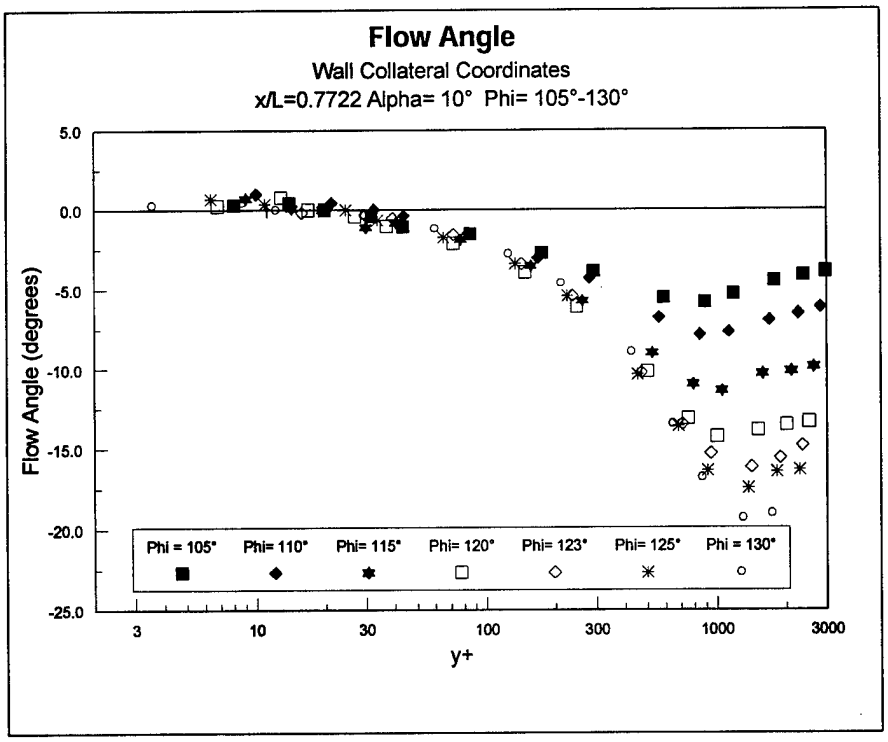


Figure 49. Flow Angle, Wall-collateral Coordinates, x/L= 0.7722.

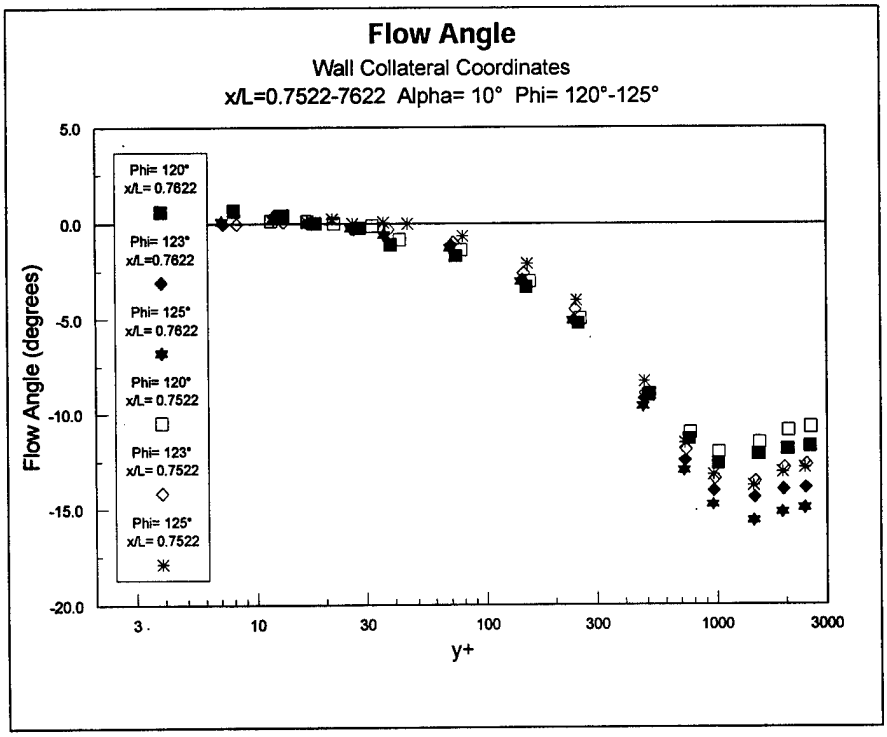


Figure 50. Flow Angle, Wall-collateral Coordinates, x/L= 0.7622 & 0.7522.

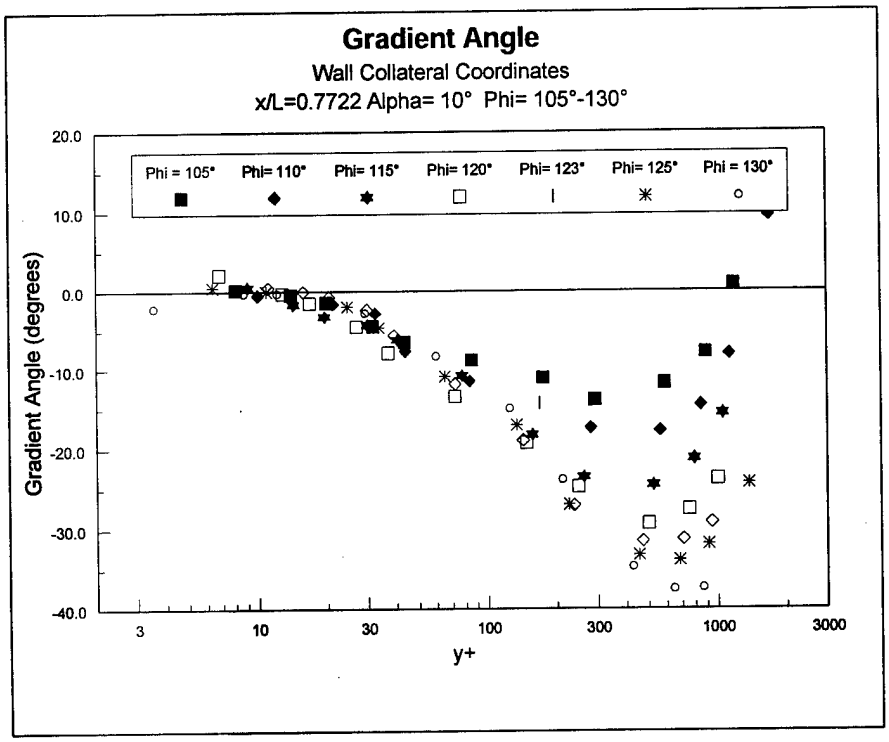


Figure 51. Gradient Angle, Wall-collateral Coordinates, x/L= 0.7722.

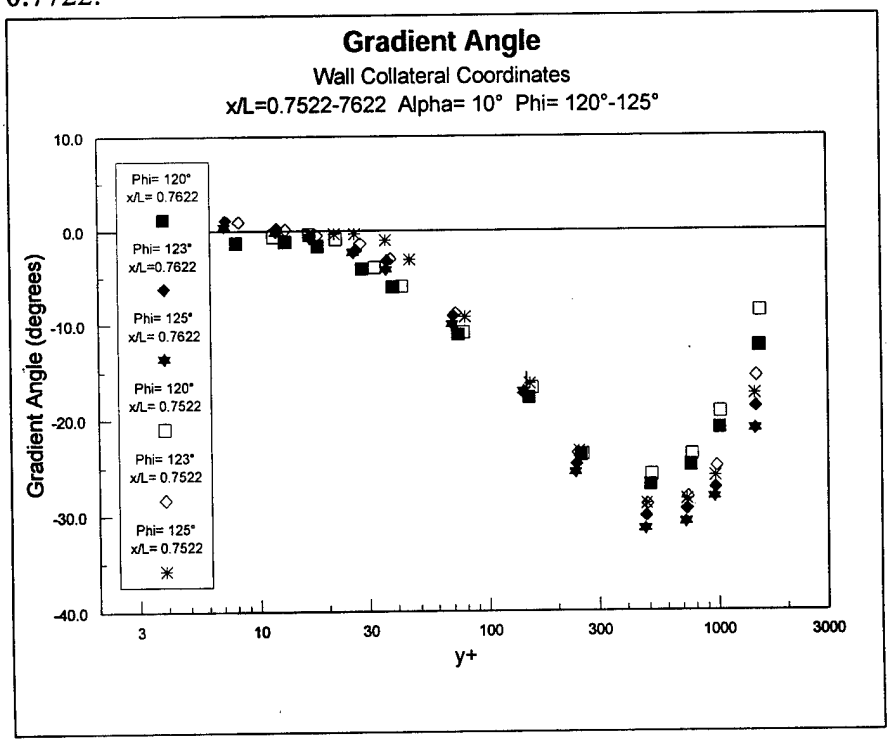


Figure 52. Gradient Angle, Wall-collateral Coordinates, x/L= 0.7622 & 0.7522.

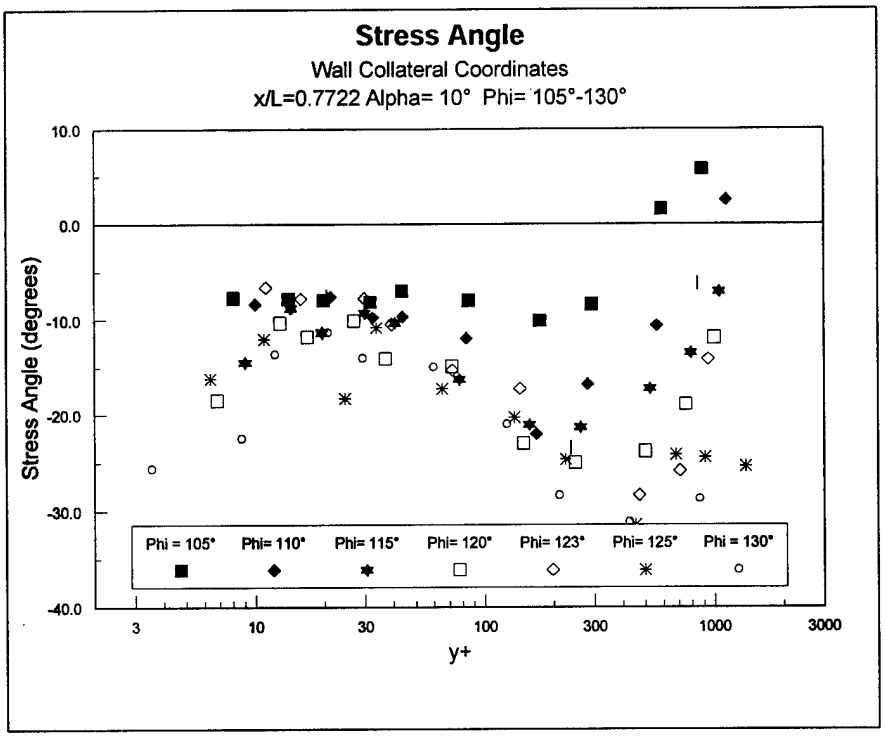


Figure 53. Stress Angle, Wall-collateral Coordinates, x/L = 0.7722.

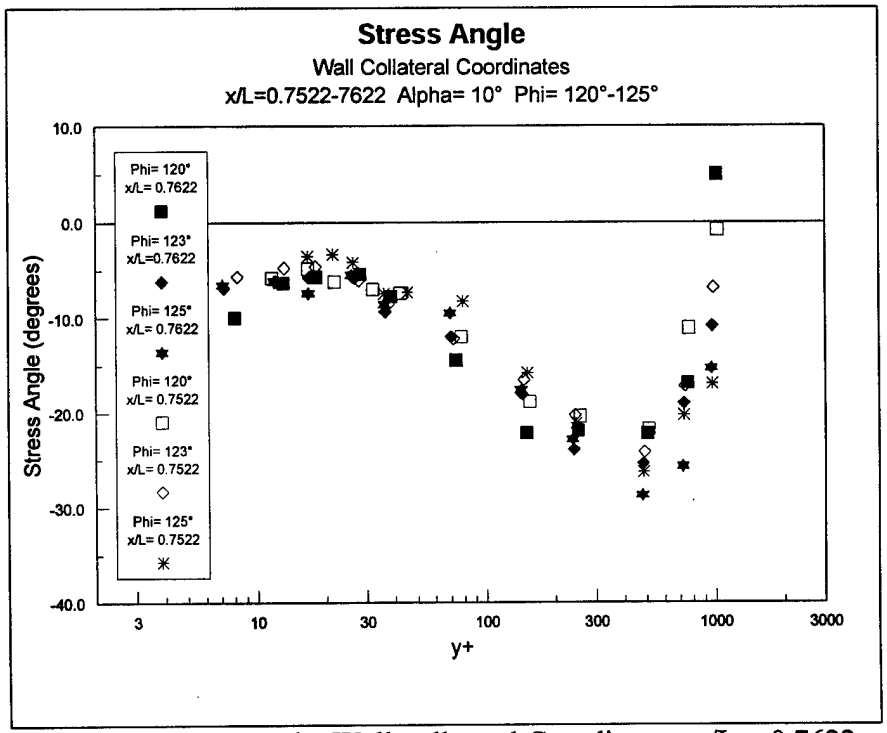


Figure 54. Stress Angle, Wall-collateral Coordinates, x/L = 0.7622 & 0.7522.

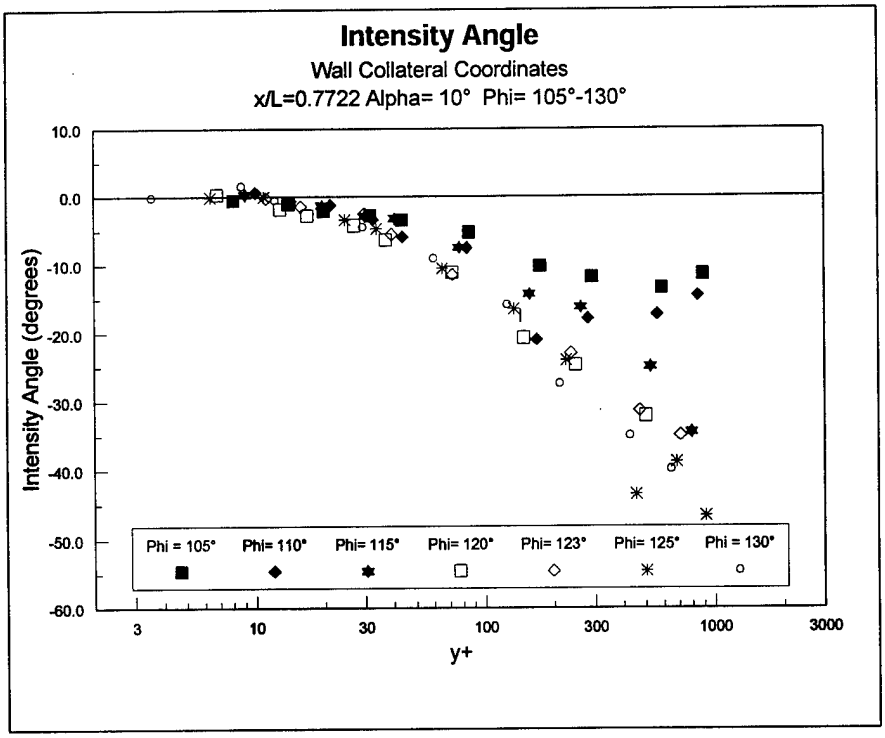


Figure 55. Intensity Angle, Wall-collateral Coordinates, x/L = 0.7722.

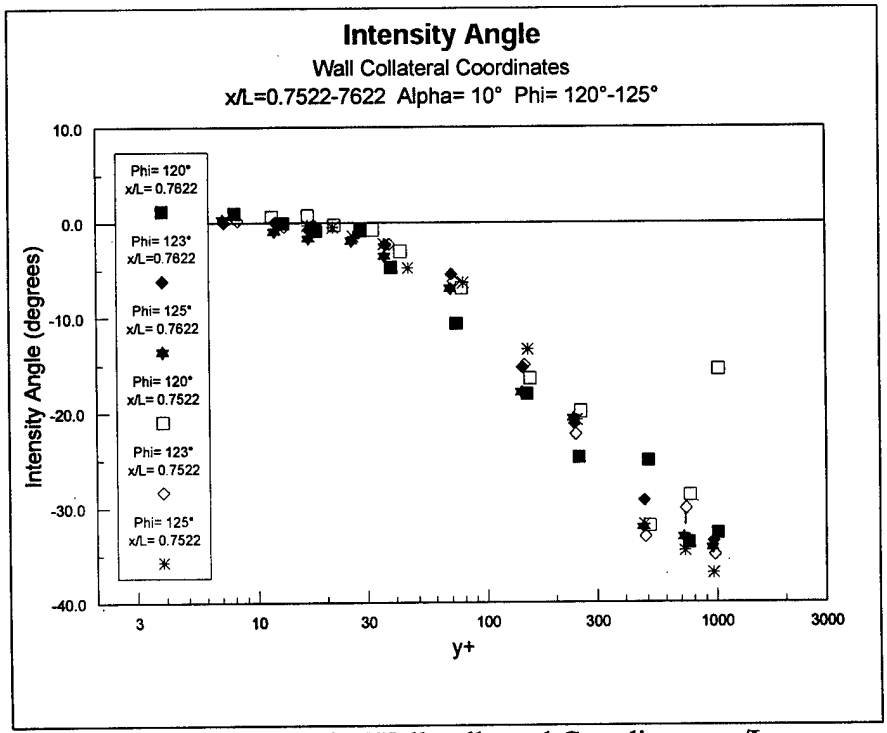


Figure 56. Intensity Angle, Wall-collateral Coordinates, x/L = 0.7622 & 0.7522.

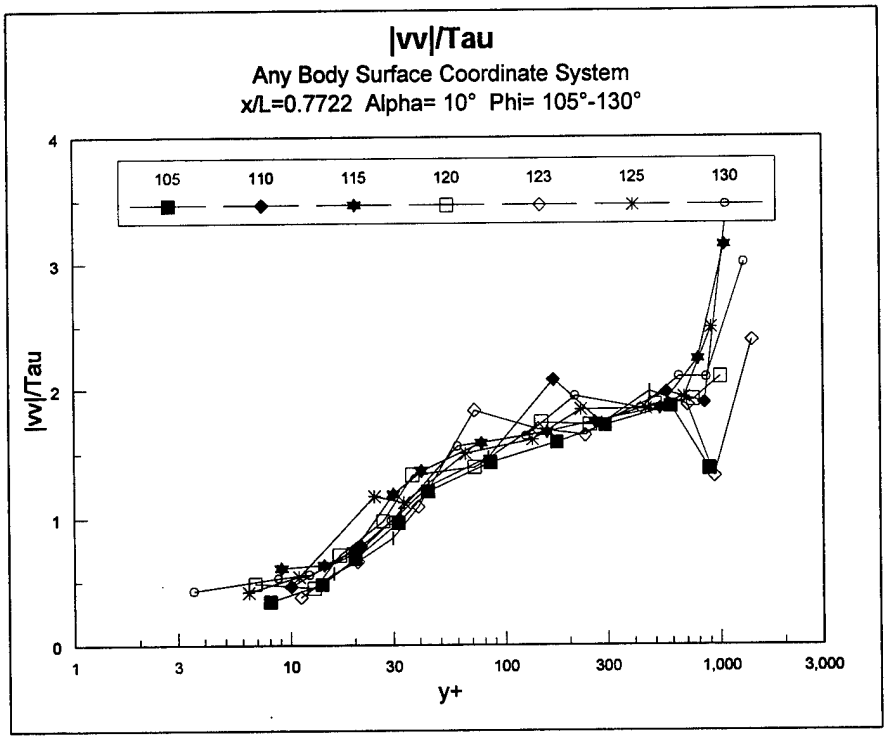


Figure 57. $v'^2/\tau$, Normal to Wall, x/L = 0.7722. Collateral

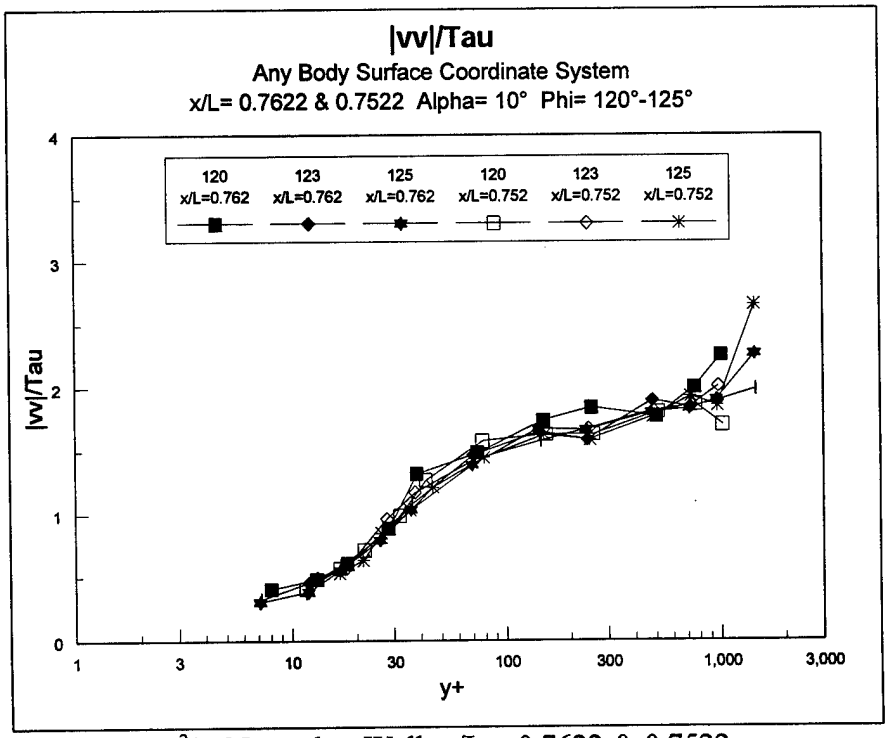


Figure 58. $v'^2/\tau$, Normal to Wall, x/L = 0.7622 & 0.7522.

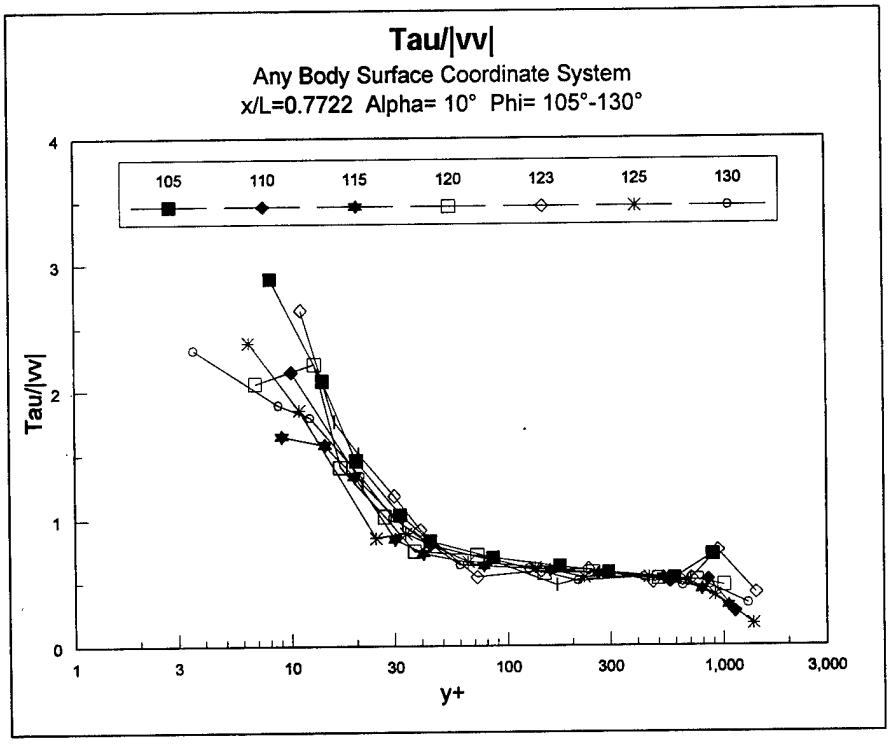


Figure 59. $\tau/v'^2$, Normal to Wall, x/L = 0.7722..7722.

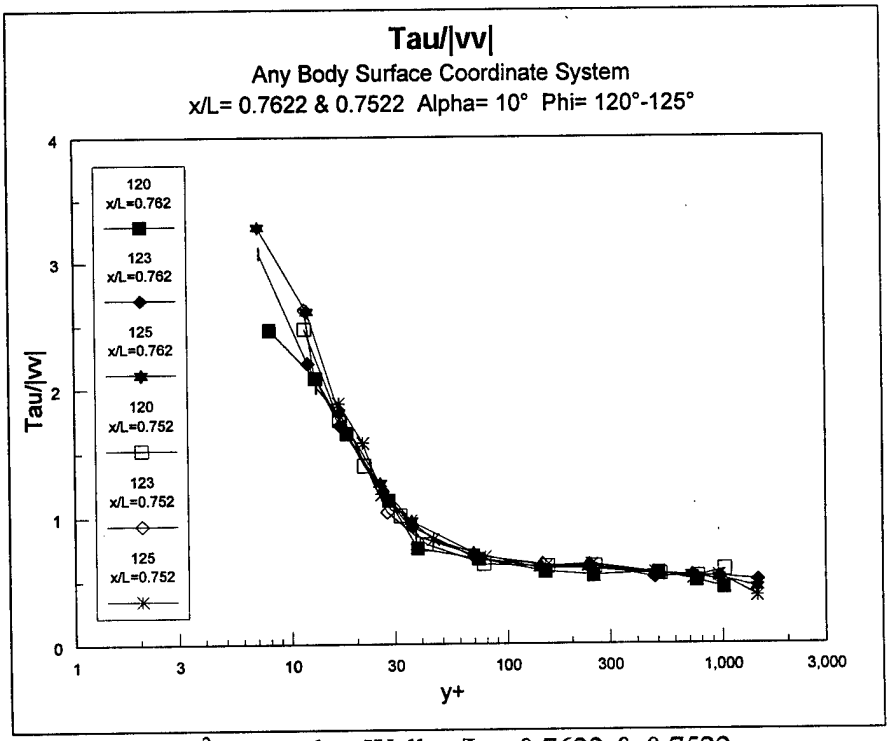


Figure 60. $\tau/v'^2$, Normal to Wall, x/L = 0.7622 & 0.7522.

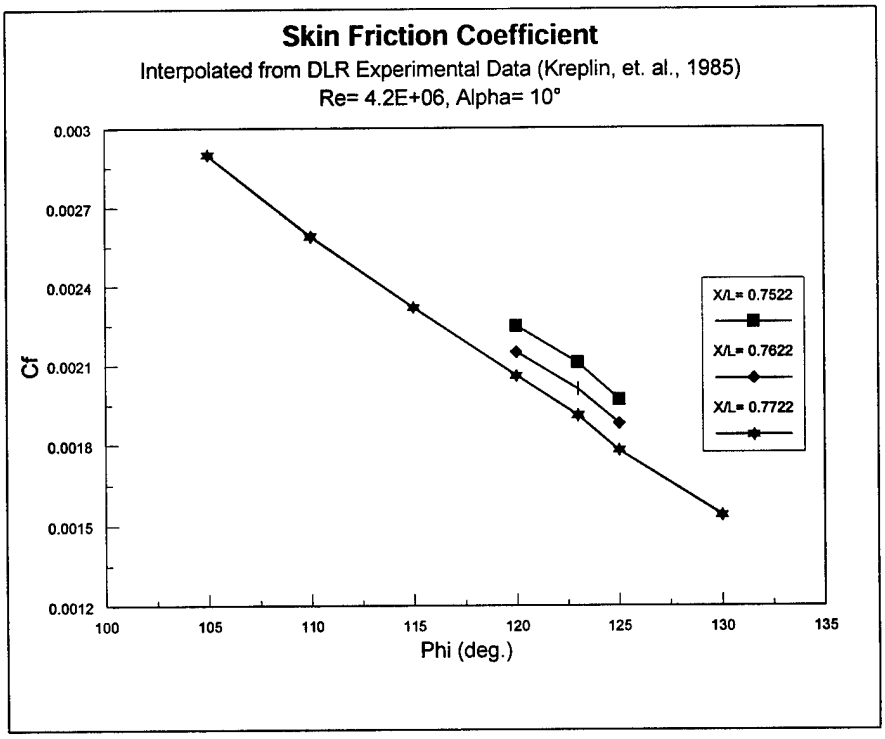


Figure 61. $C_f$ interpolated form DLR experiment data (Kreplin, et al., 1985).

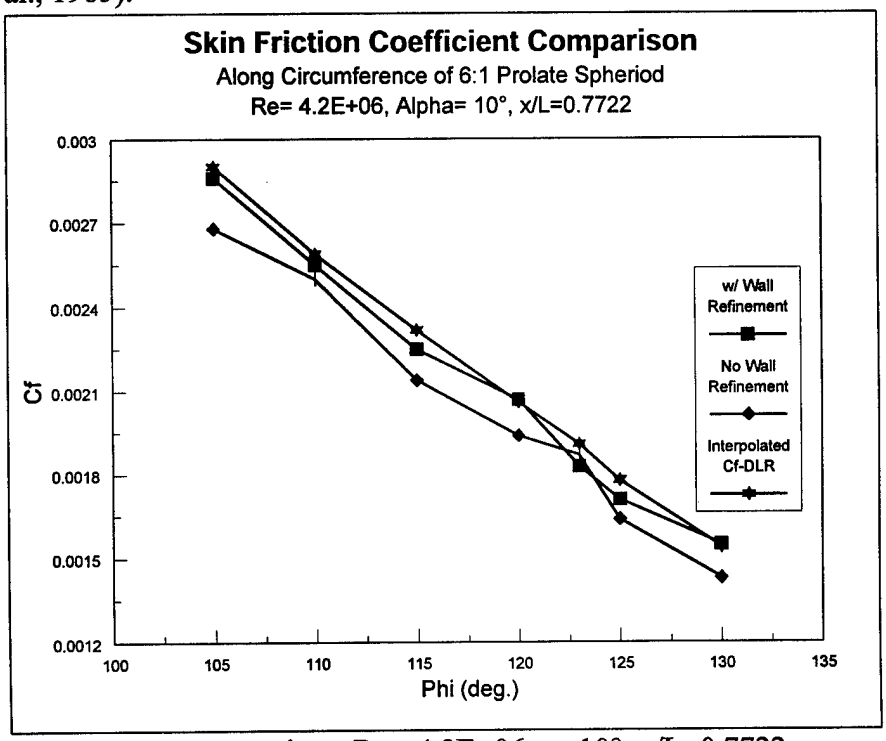


Figure 62. $C_f$ comparison, $Re_L$=4.2E+06, $\alpha$=10°, x/L=0.7722.

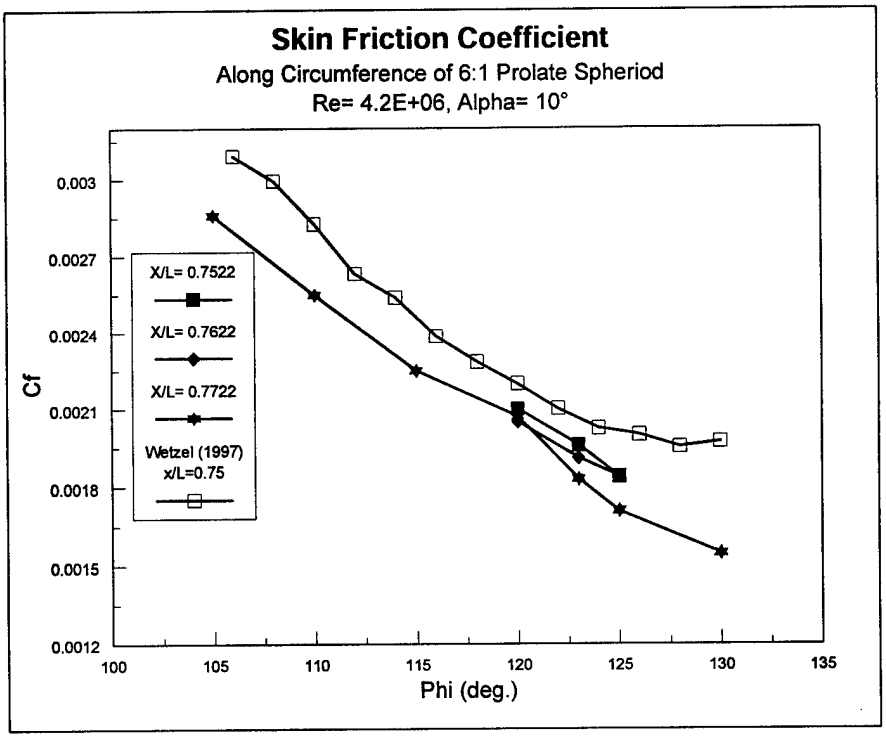


Figure 63. $C_f$ calculated without wall refinement, all locations.

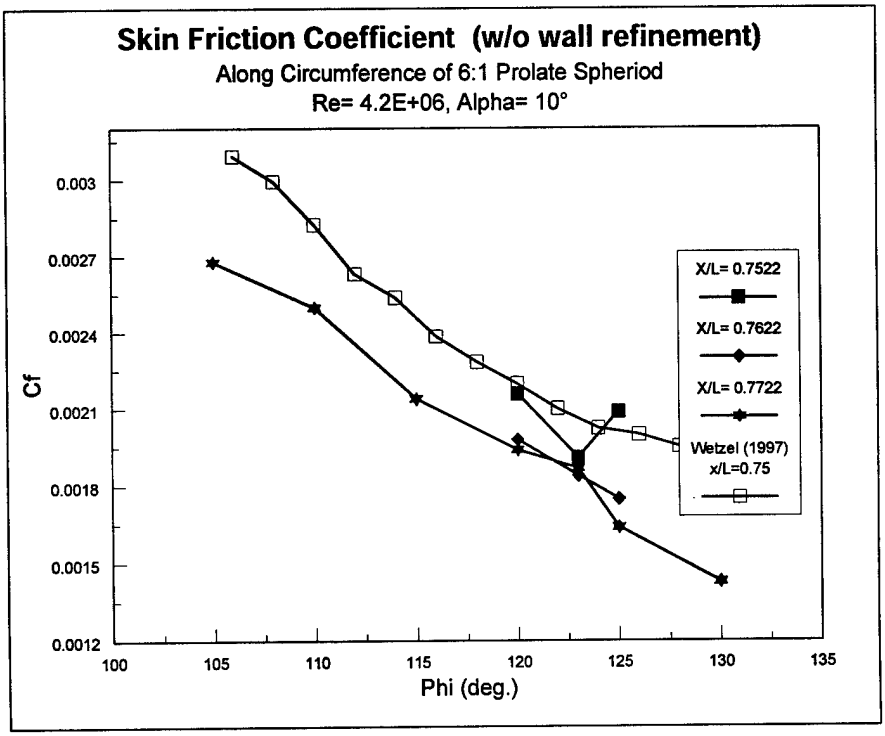


Figure 64. $C_f$ calculated with wall refinement, all locations.

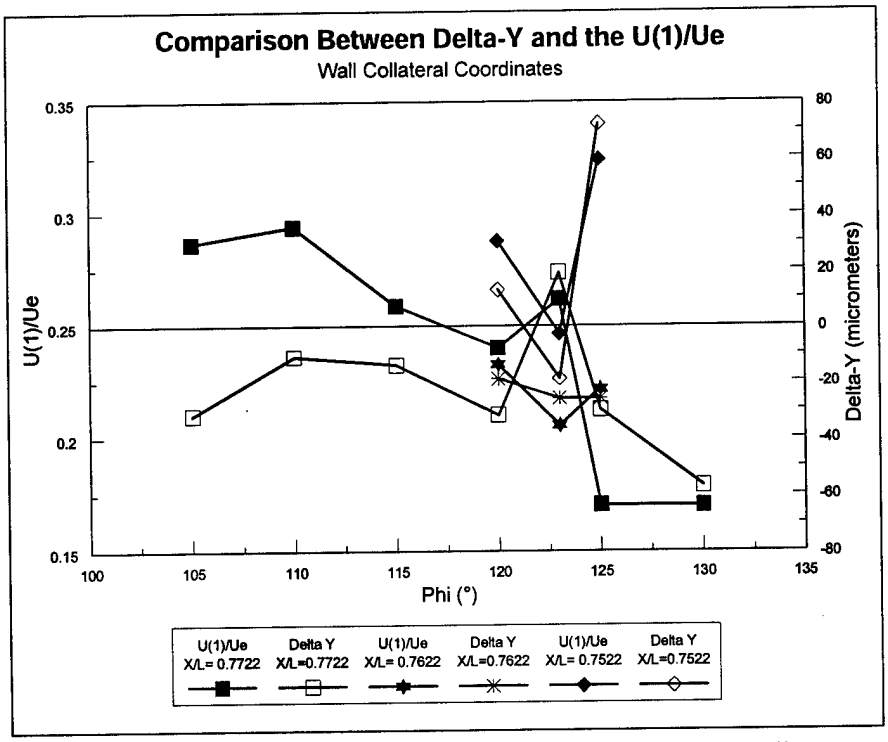


Figure 65. Comparison of $U_1$ and the wall refinement ($\Delta y$), all locations.

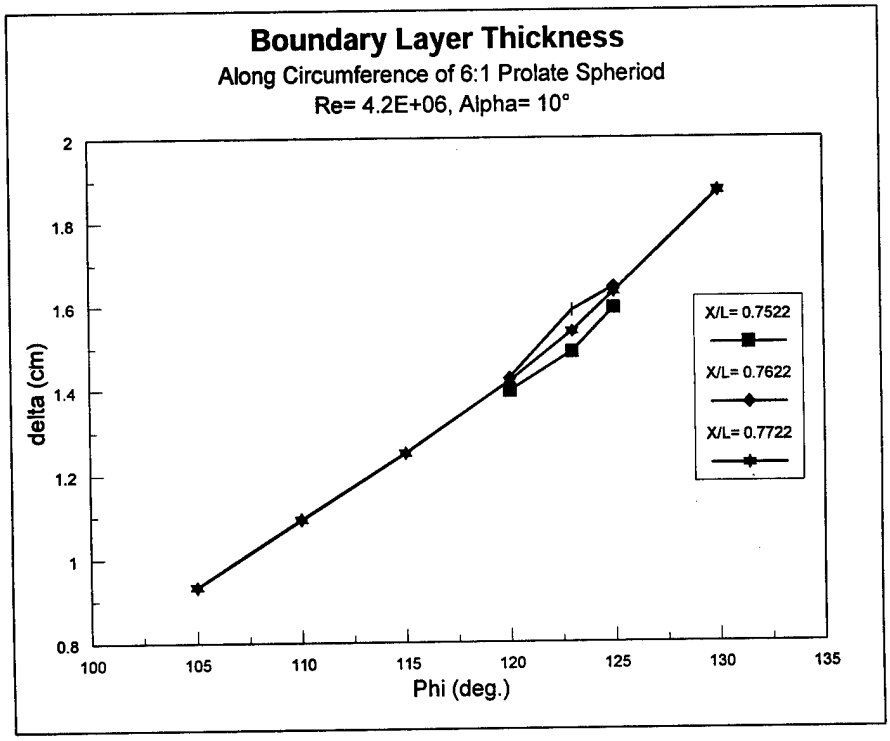


Figure 66. Boundary Layer Thickness, all locations.

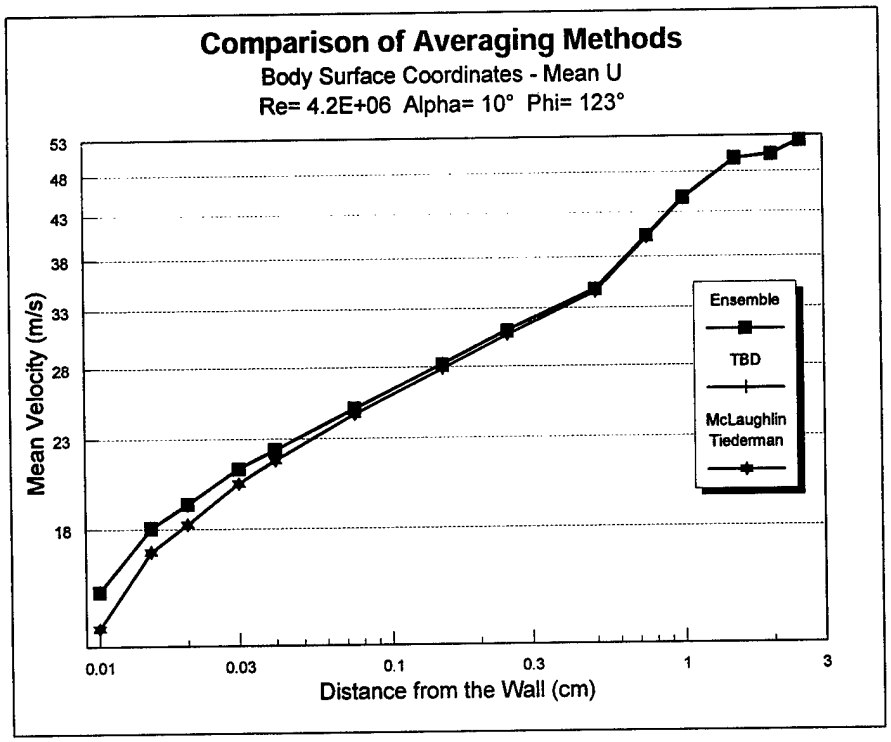


Figure 67. Comparison of Averaging Methods, Re = 4.2E+06, $\alpha$ = 10°, $\phi$ = 123°, x/L = 0.7722.

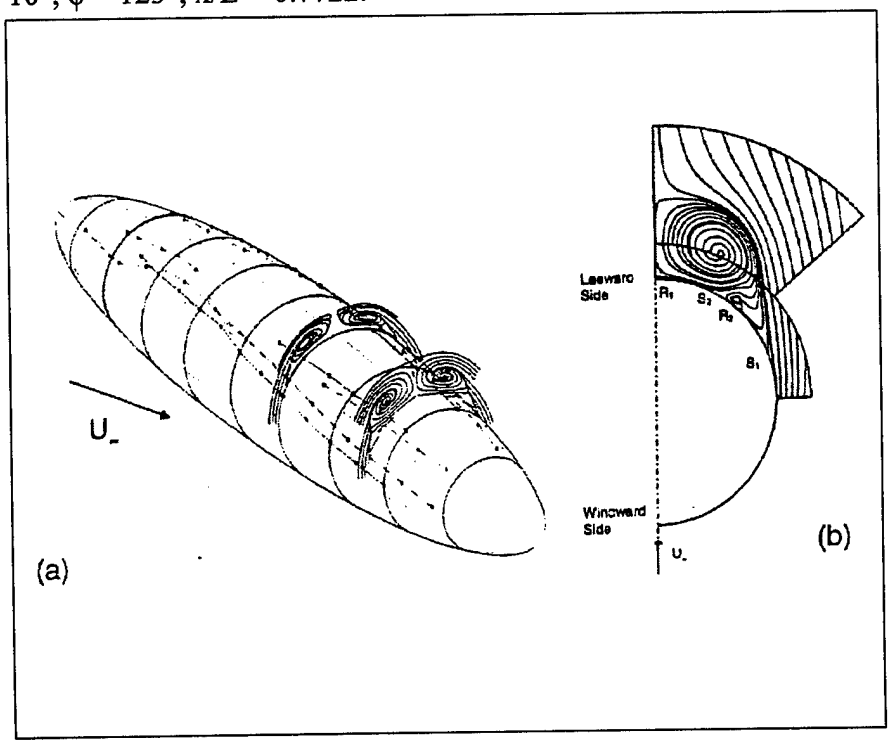


Figure 68. Flow field on the leeward side of a 6:1 Prolate Spheroid. (Wetzel, et. al., 1997)

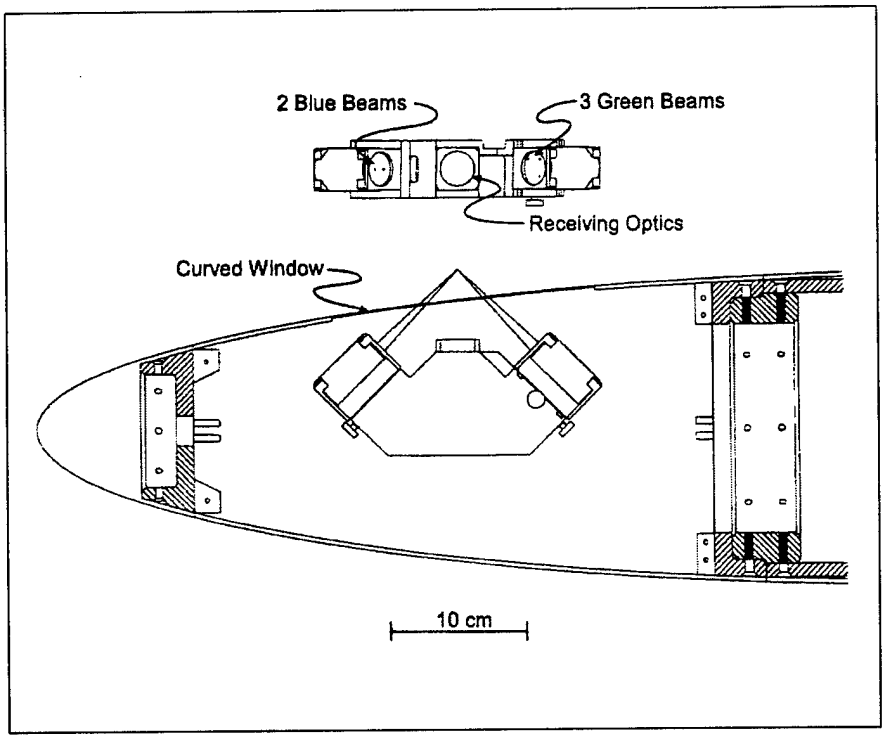


Figure 69. Schematic of LDV probe and prolate spheroid model.

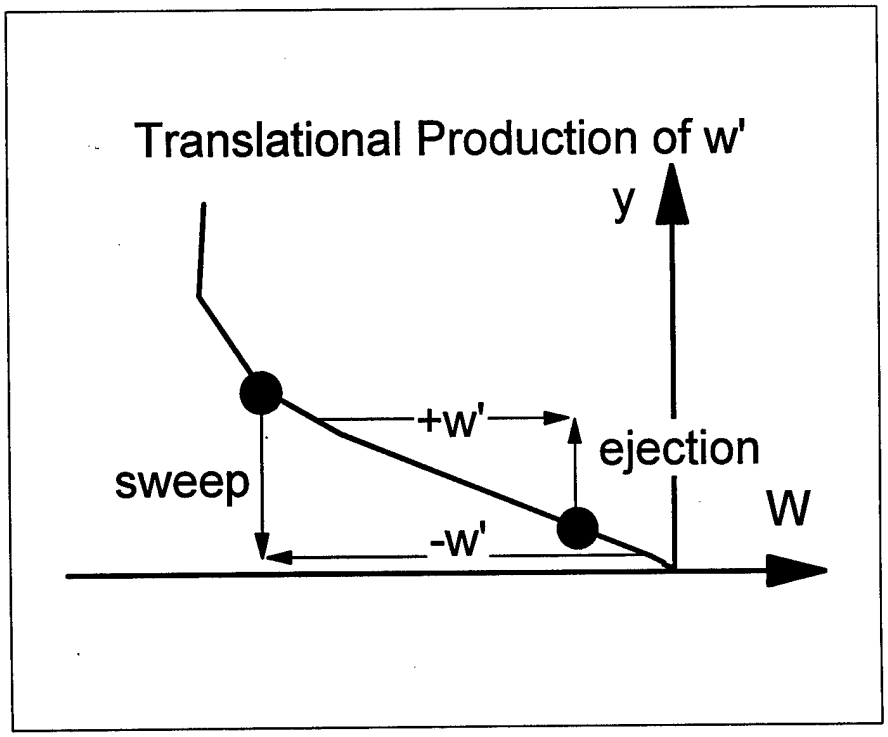


Figure 70. Illustration of translational production of w' in the bursting process.

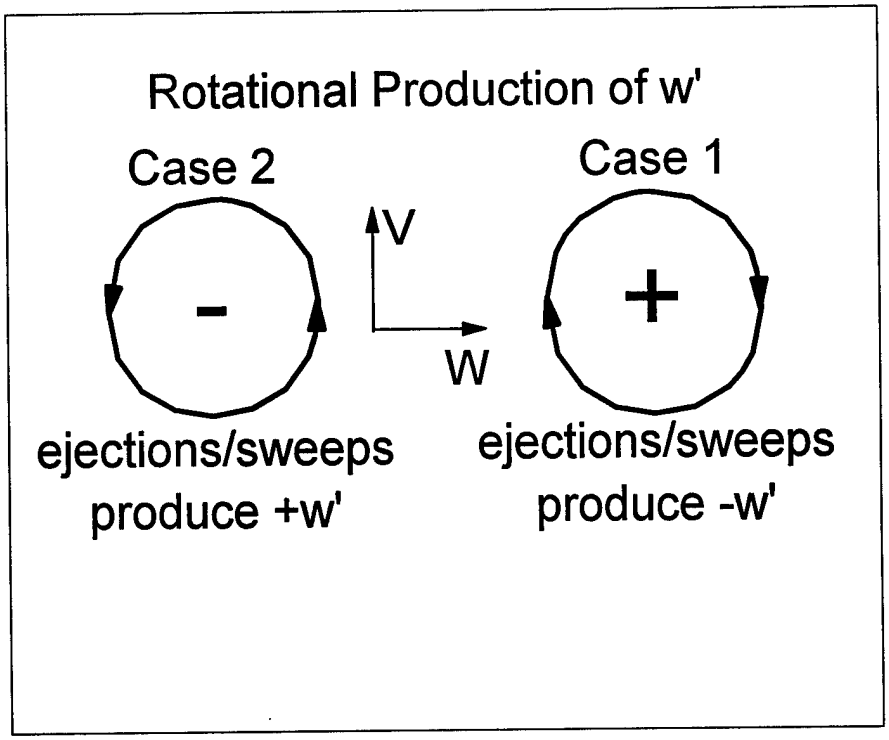


Figure 71. Illustration of rotational production of w' by QSVs.

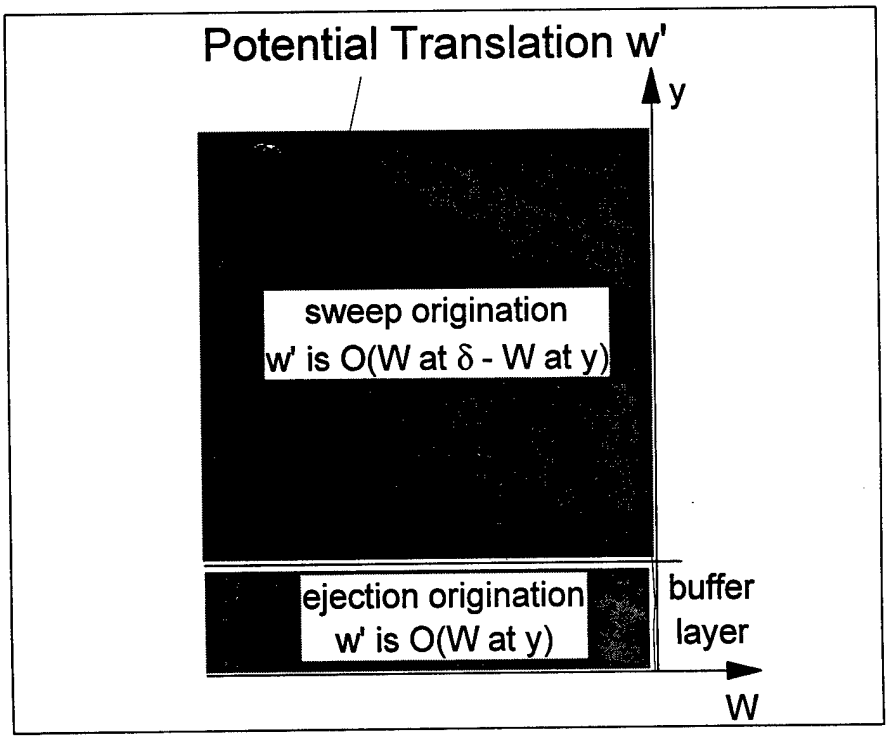


Figure 72. Illustration depiciting the potential translation w' for ejections and sweeps as seen from the buffer layer edge.

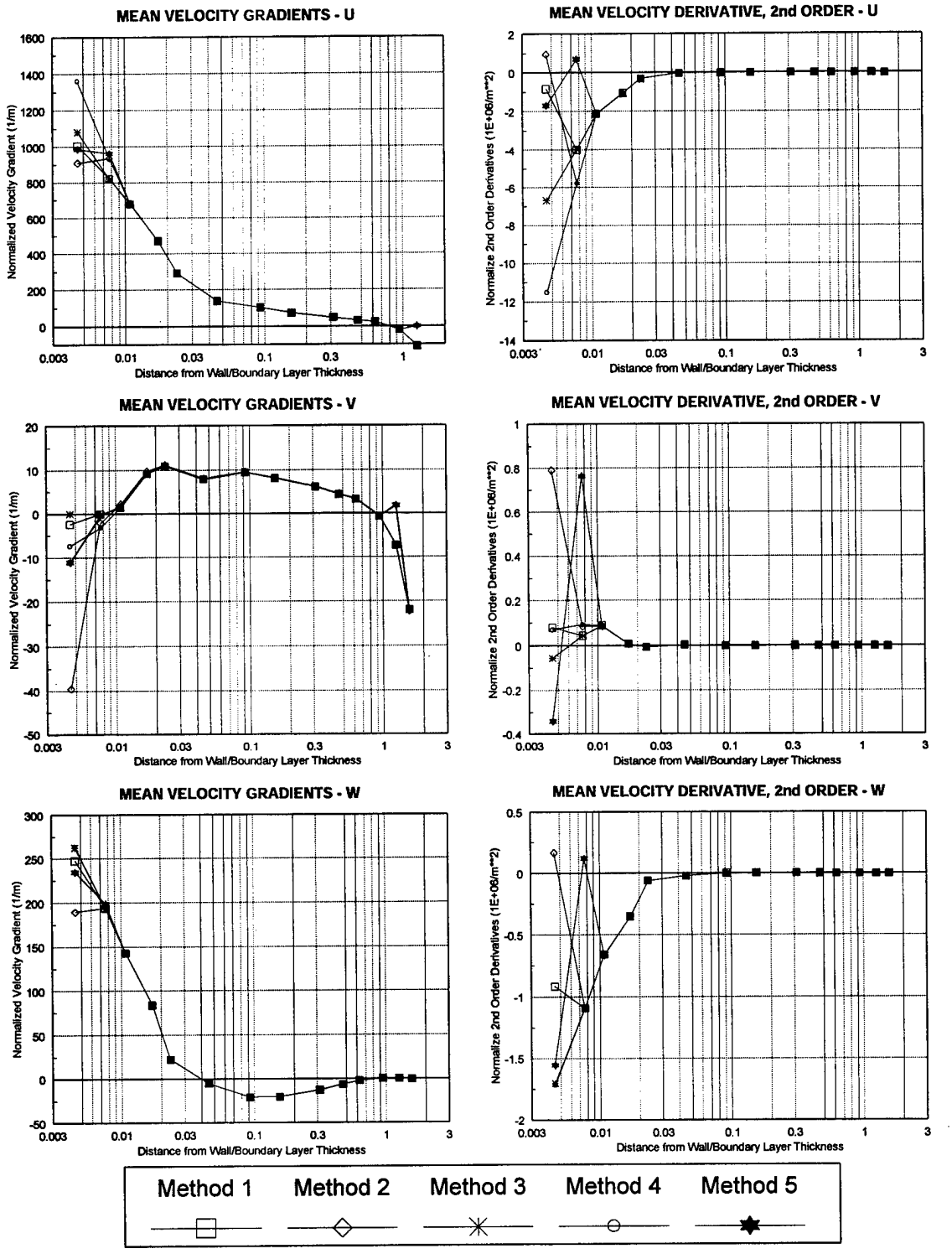


Note: All Derivatives Normalized by $U_e$.

Figure 73. Comparison of derivative generation methods for mean velocities, x/L = 0.7622 & $\phi = 123°$, Free-stream Coordinates.

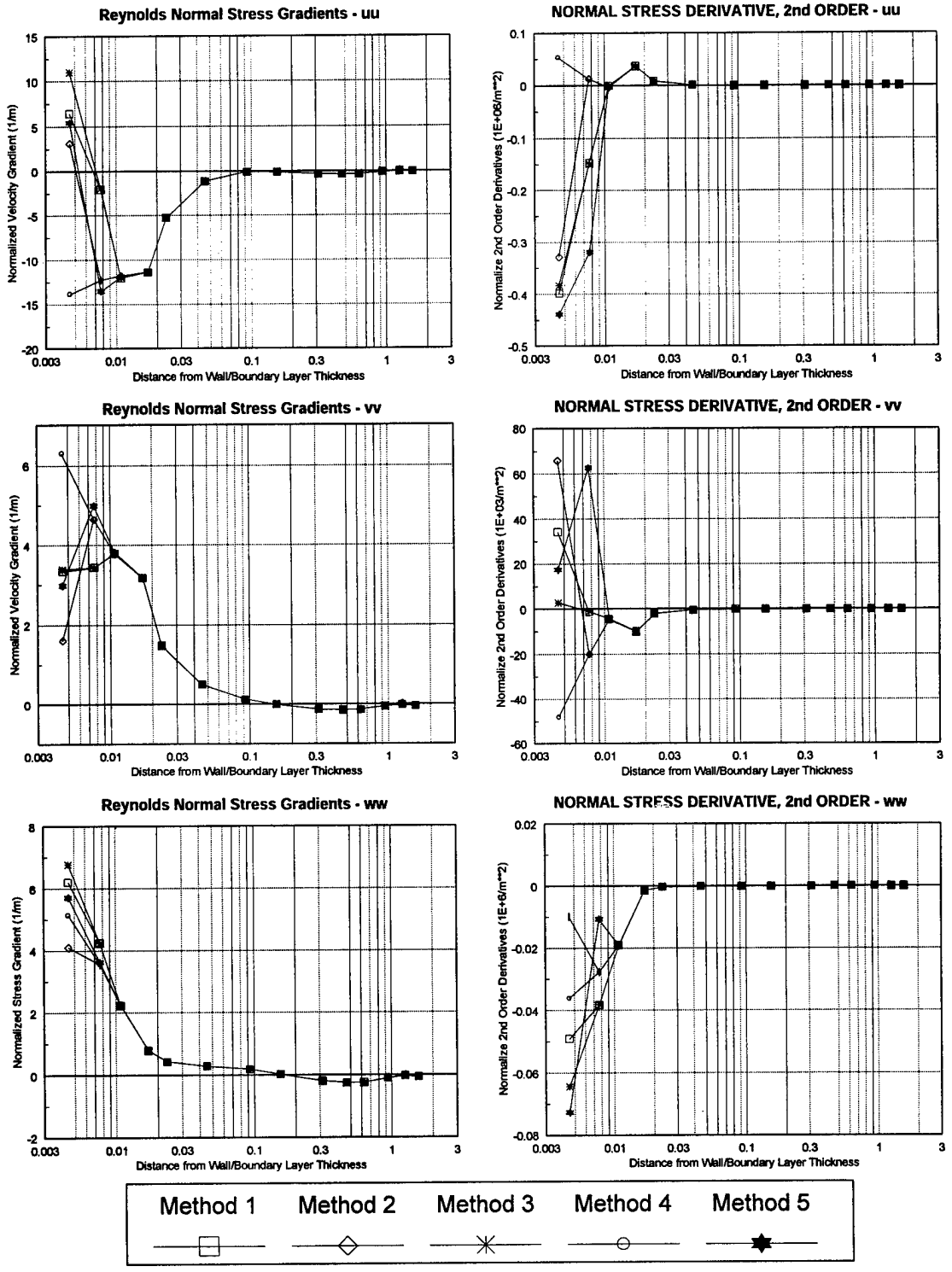


Note: All Derivatives Normalized by $U_e^2$.

Figure 74. Comparison of derivative generation methods for Reynolds normal stress, x/L = 0.7622 & $\phi$ = 123°, Free-stream Coordinates.

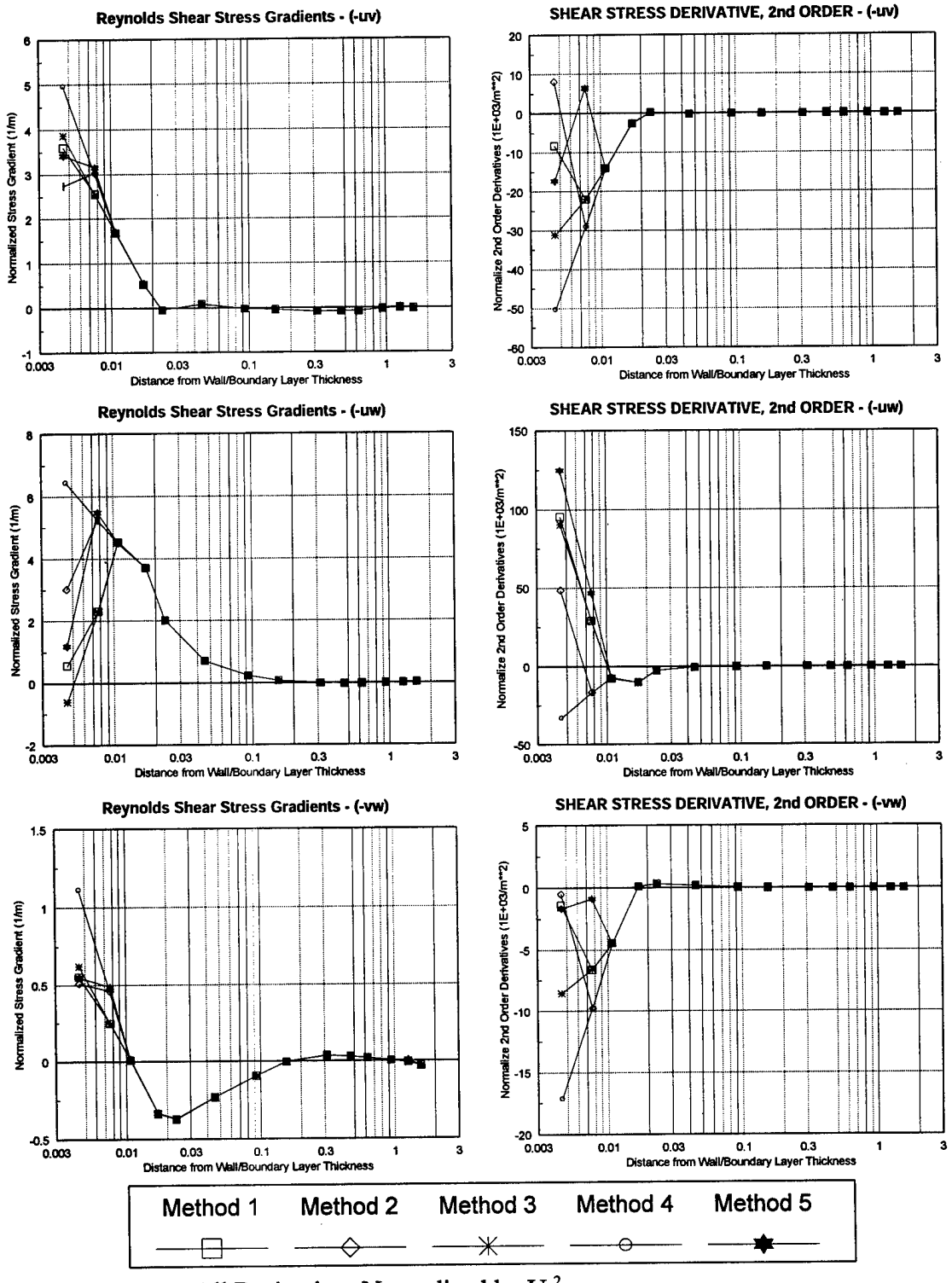


Note: All Derivatives Normalized by $U_e^2$.

Figure 75. Comparison of derivative generation methods for Reynolds shear stress, x/L = 0.7622 & $\phi = 123°$, Free-stream Coordinates.

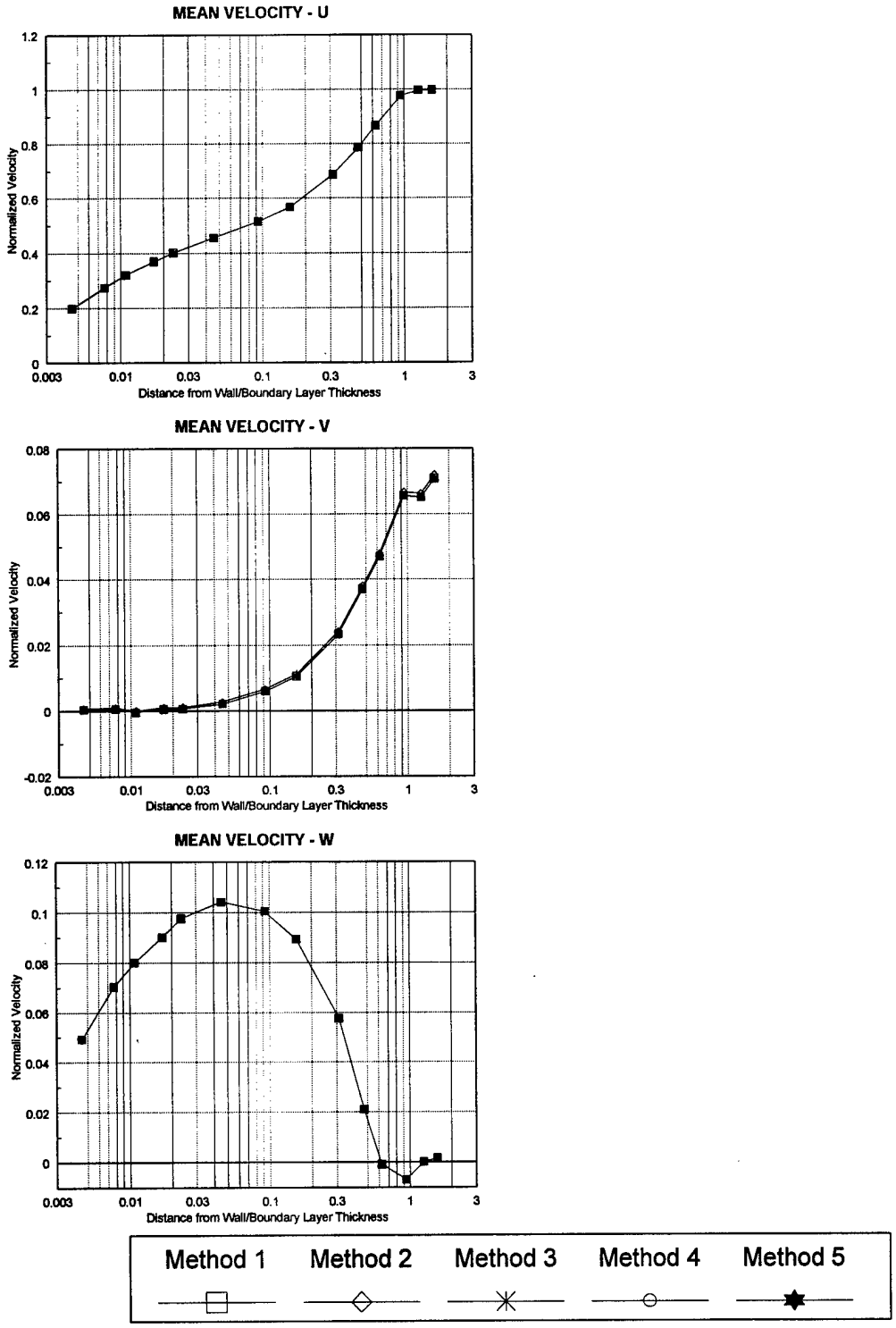


Note: All Derivatives Normalized by $U_e$.

Figure 76. Mean velocities with gradient broadening corrections, x/L = 0.7622 & $\phi$ = 123°, Free-stream Coordinates.

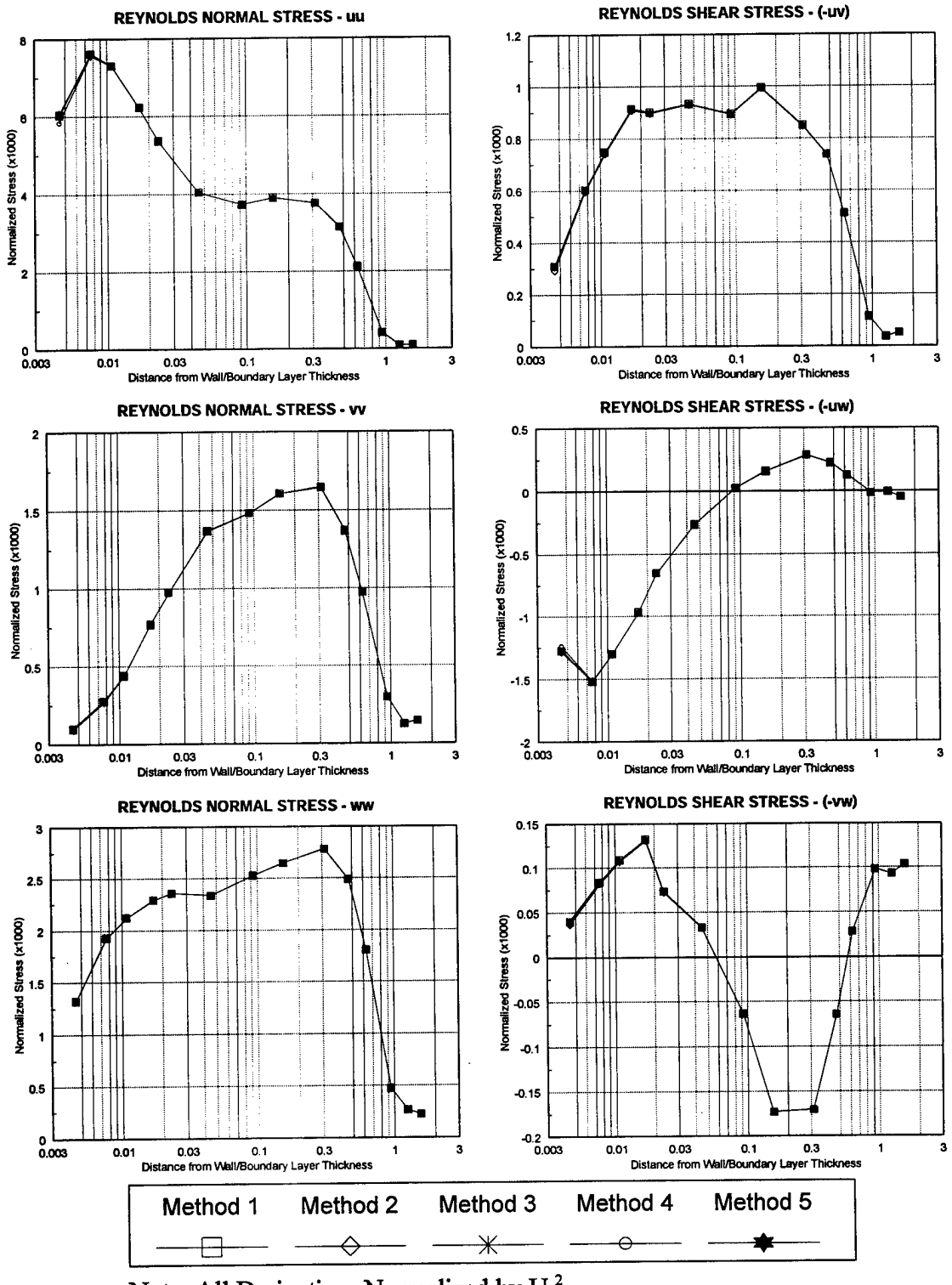


Note: All Derivatives Normalized by $U_e^2$.

Figure 77. Reynolds stresses with gradient broadening corrections, x/L = 0.7622 & $\phi$ = 123°, Free-stream Coordinates.

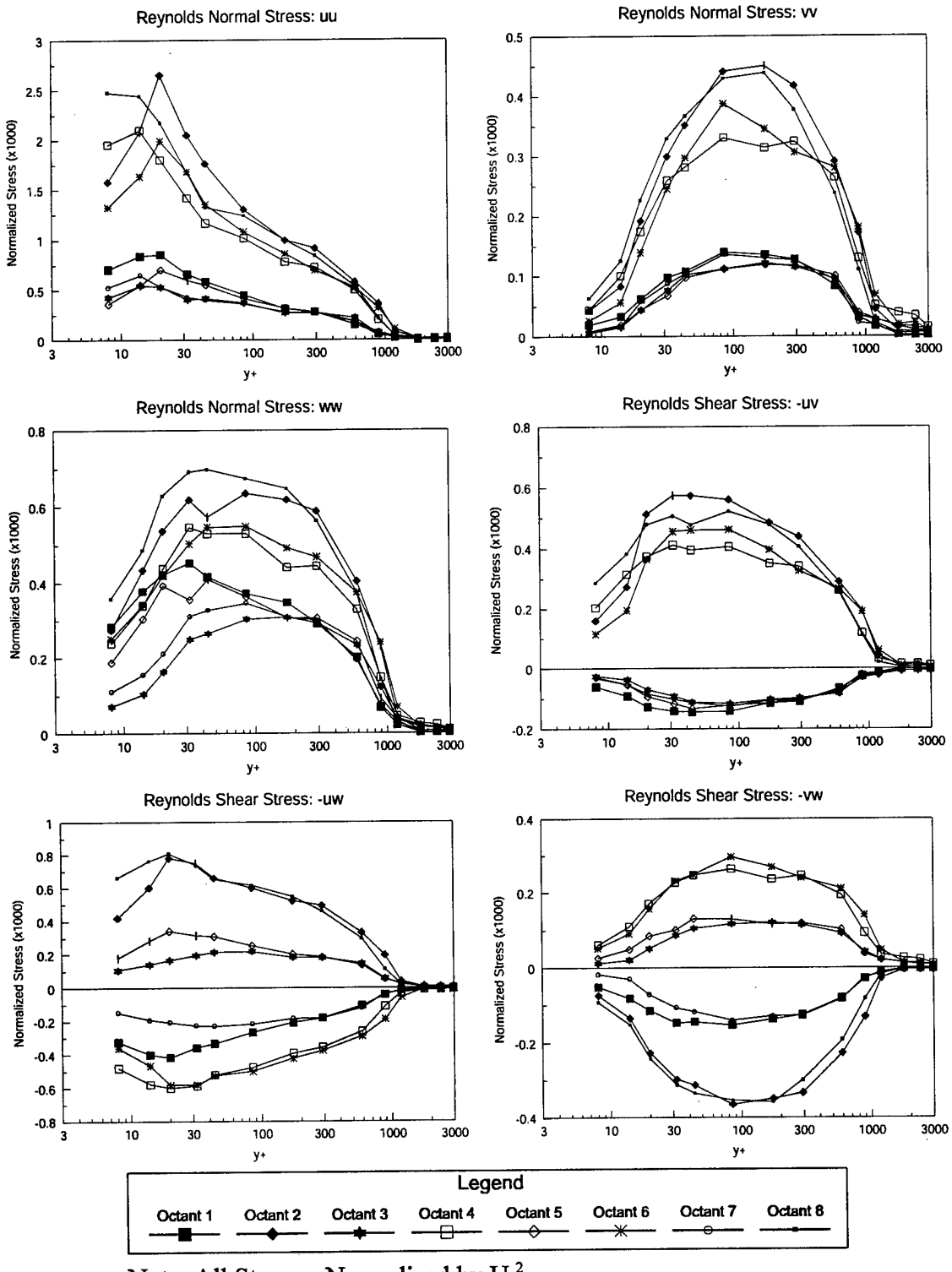


Note: All Stresses Normalized by $U_e^2$.

Figure 78. Octant Contributions to the Reynolds Stresses, x/L = 0.7722 & $\phi$ = 105°, Wall-collateral Coordinates.

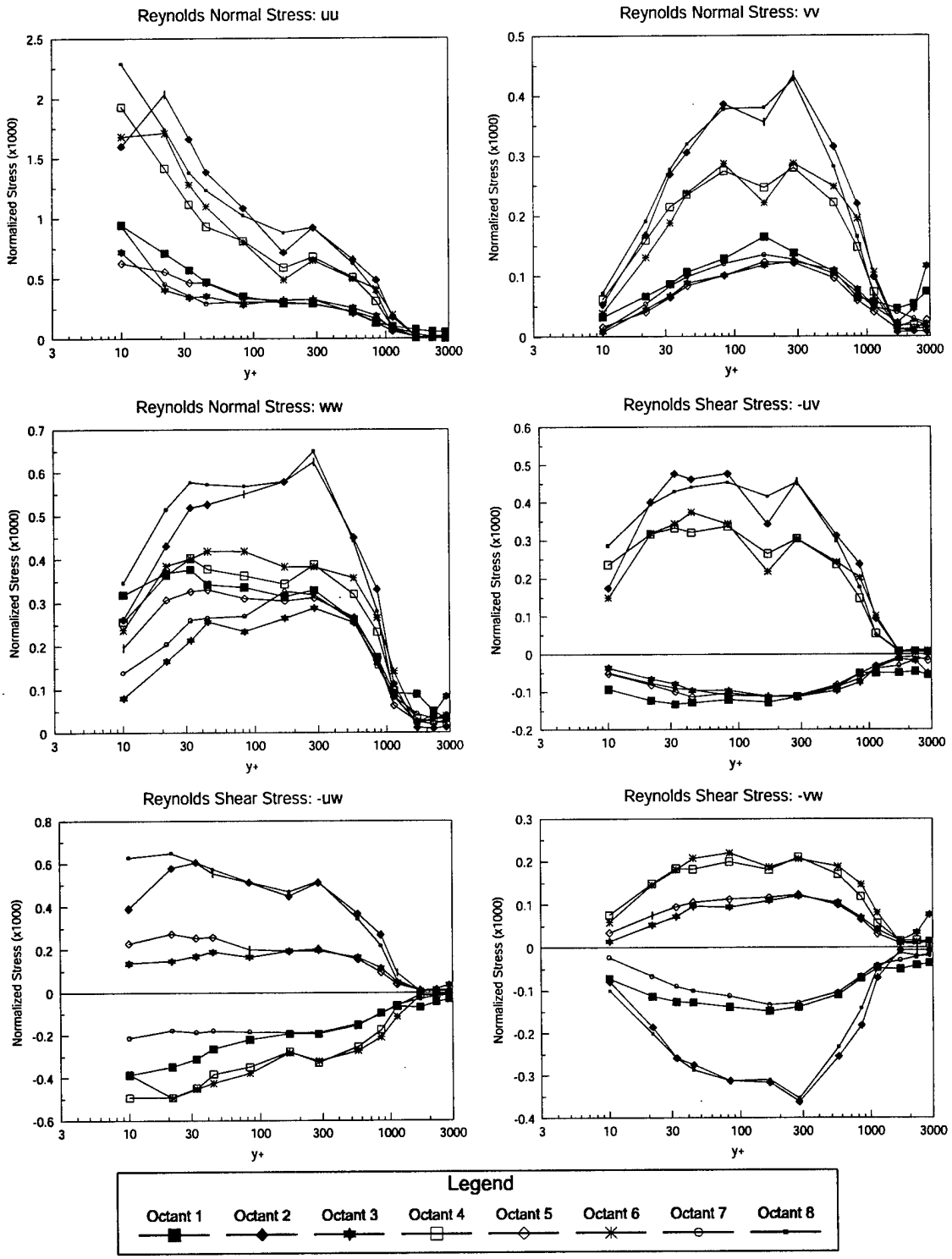


Note: All Stresses Normalized by $U_e^2$.

Figure 79. Octant Contributions to the Reynolds Stresses, x/L = 0.7722 & $\phi = 110°$, Wall-collateral Coordinates.

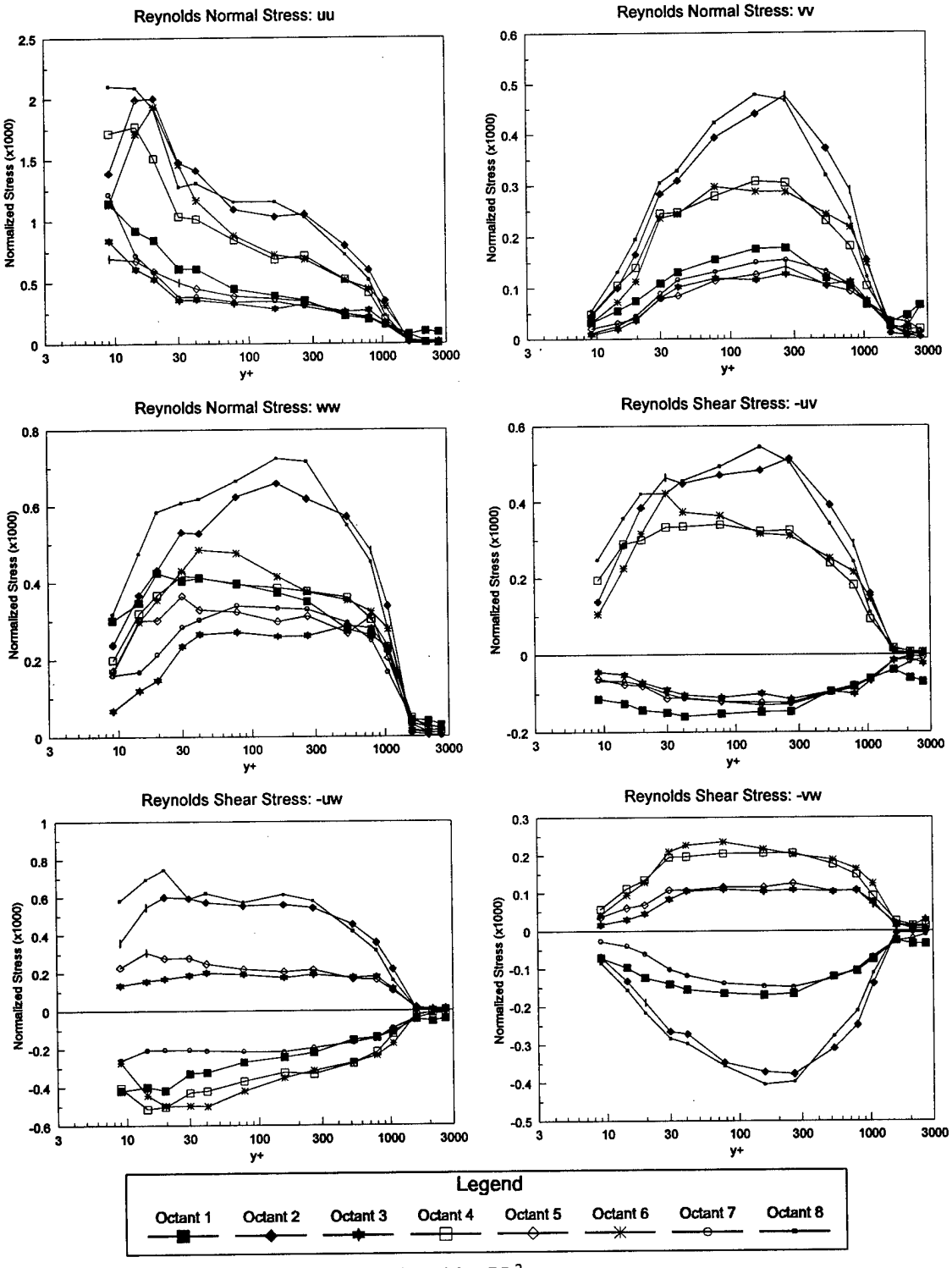


Note: All Stresses Normalized by $U_e^2$.

Figure 80. Octant Contributions to the Reynolds Stresses, x/L = 0.7722 & $\phi$ = 115°, Wall-collateral Coordinates.

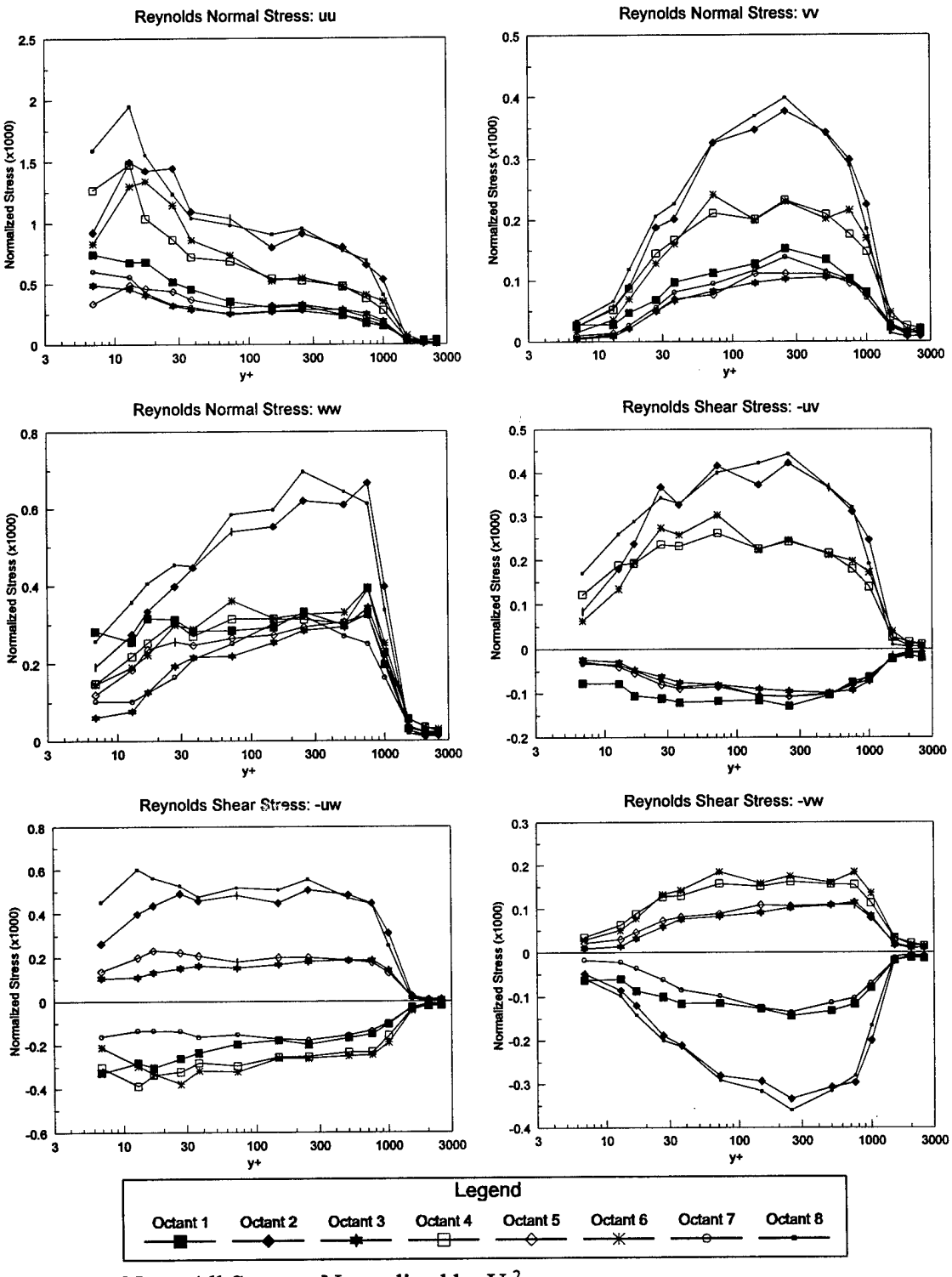


Note: All Stresses Normalized by $U_e^2$.

Figure 81. Octant Contributions to the Reynolds Stresses, x/L = 0.7722 & $\phi$ = 120°, Wall-collateral Coordinates.

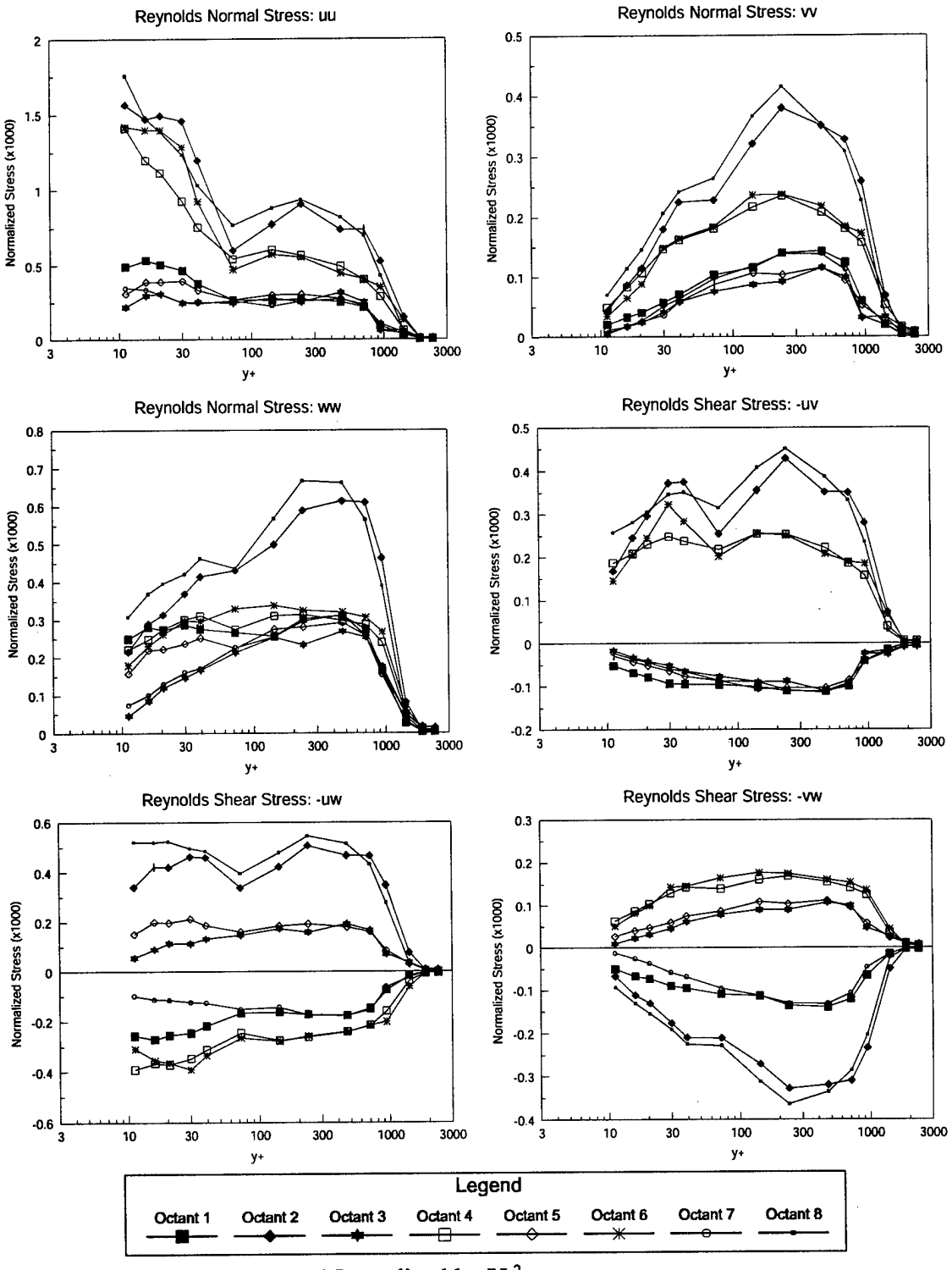


Note: All Stresses Normalized by $U_e^2$.

Figure 82. Octant Contributions to the Reynolds Stresses, x/L = 0.7722 & $\phi$ = 123°, Wall-collateral Coordinates.

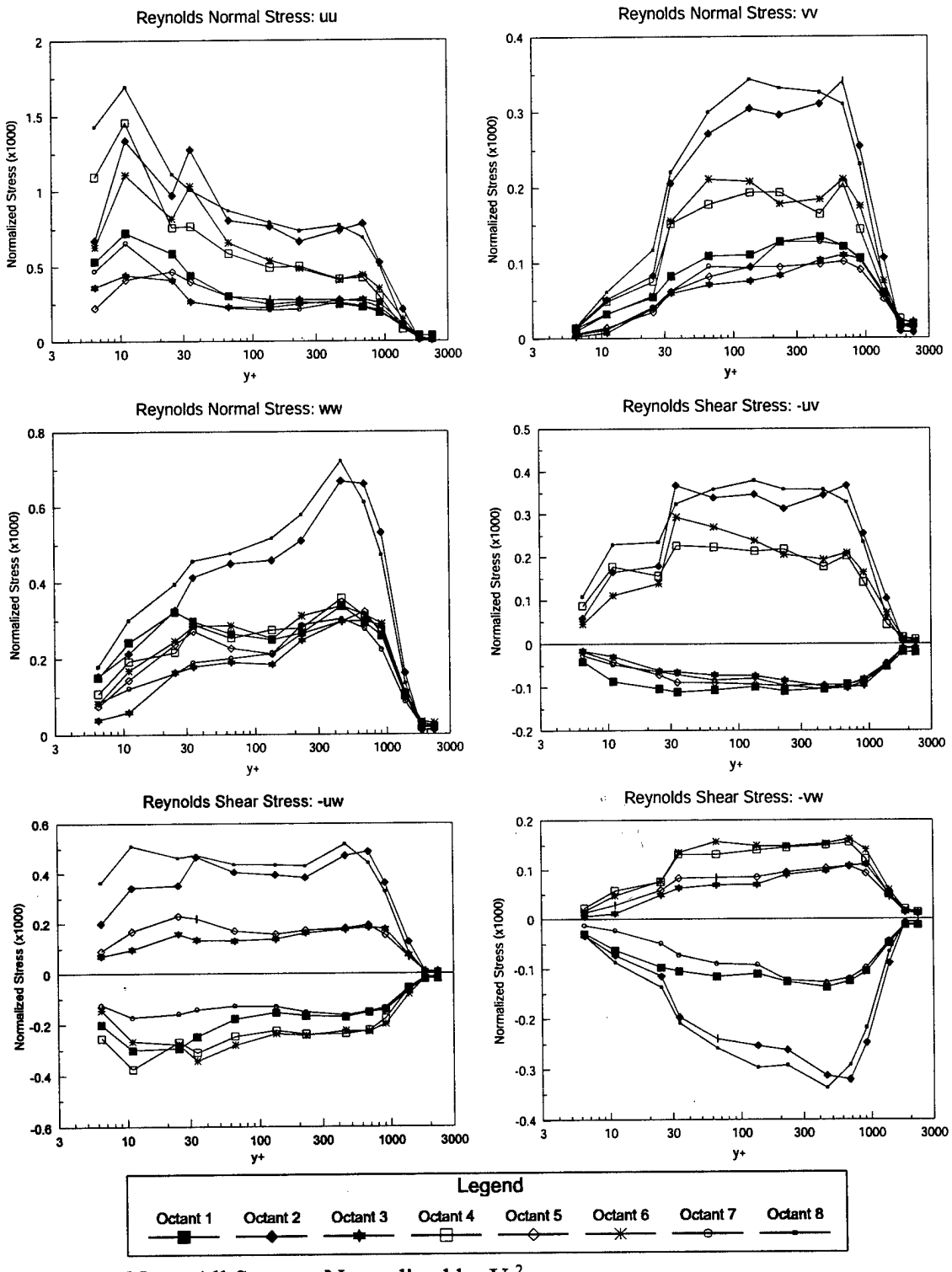


Note: All Stresses Normalized by $U_e^2$.

Figure 83. Octant Contributions to the Reynolds Stresses, x/L = 0.7722 & $\phi$ = 125°, Wall-collateral Coordinates.

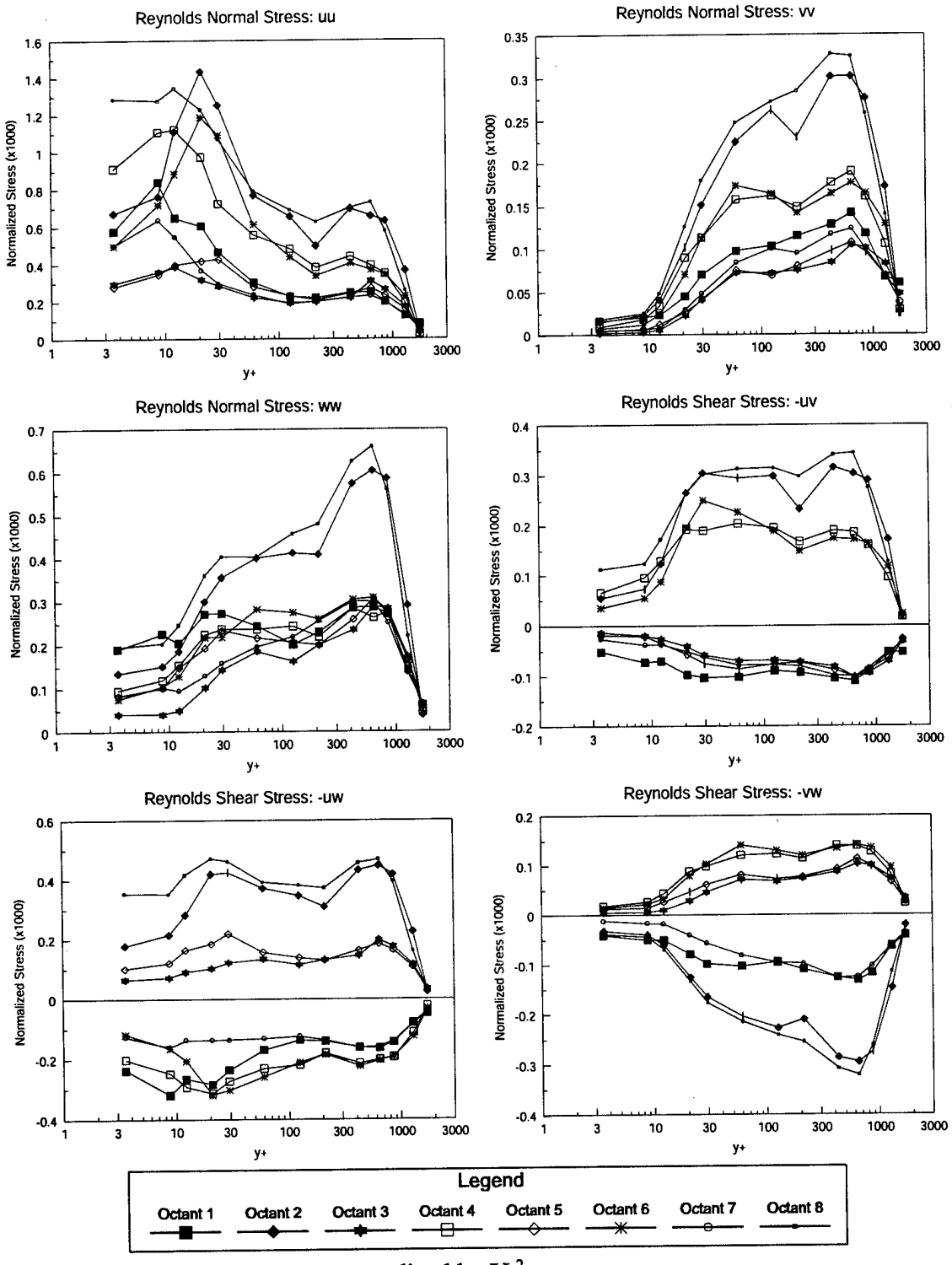


Note: All Stresses Normalized by $U_e^2$.

Figure 84. Octant Contributions to the Reynolds Stresses, x/L = 0.7722 & $\phi$ = 130°, Wall-collateral Coordinates.

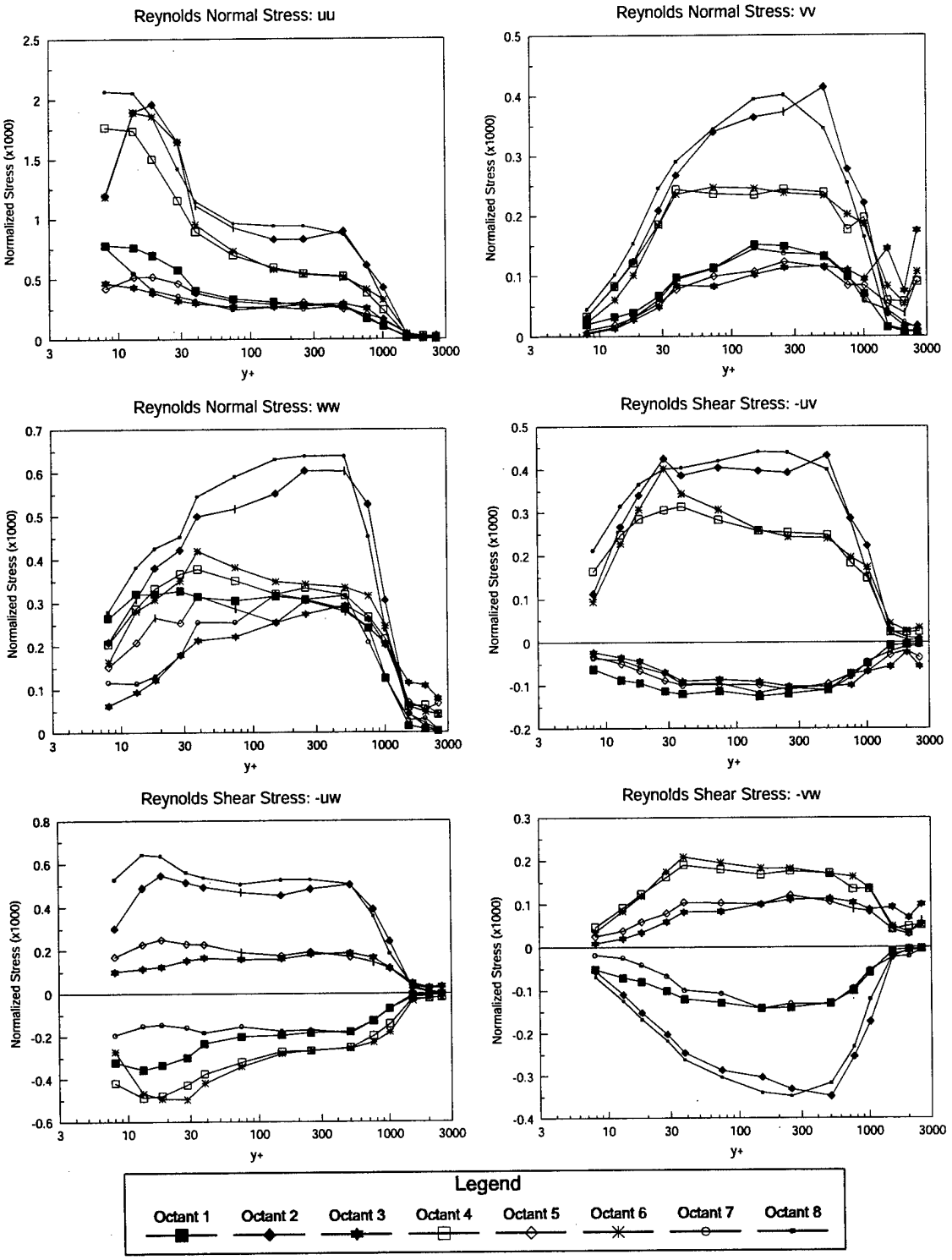


Note: All Stresses Normalized by $U_e^2$.

Figure 85. Octant Contributions to the Reynolds Stresses, x/L = 0.7622 & $\phi$ = 120°, Wall-collateral Coordinates.

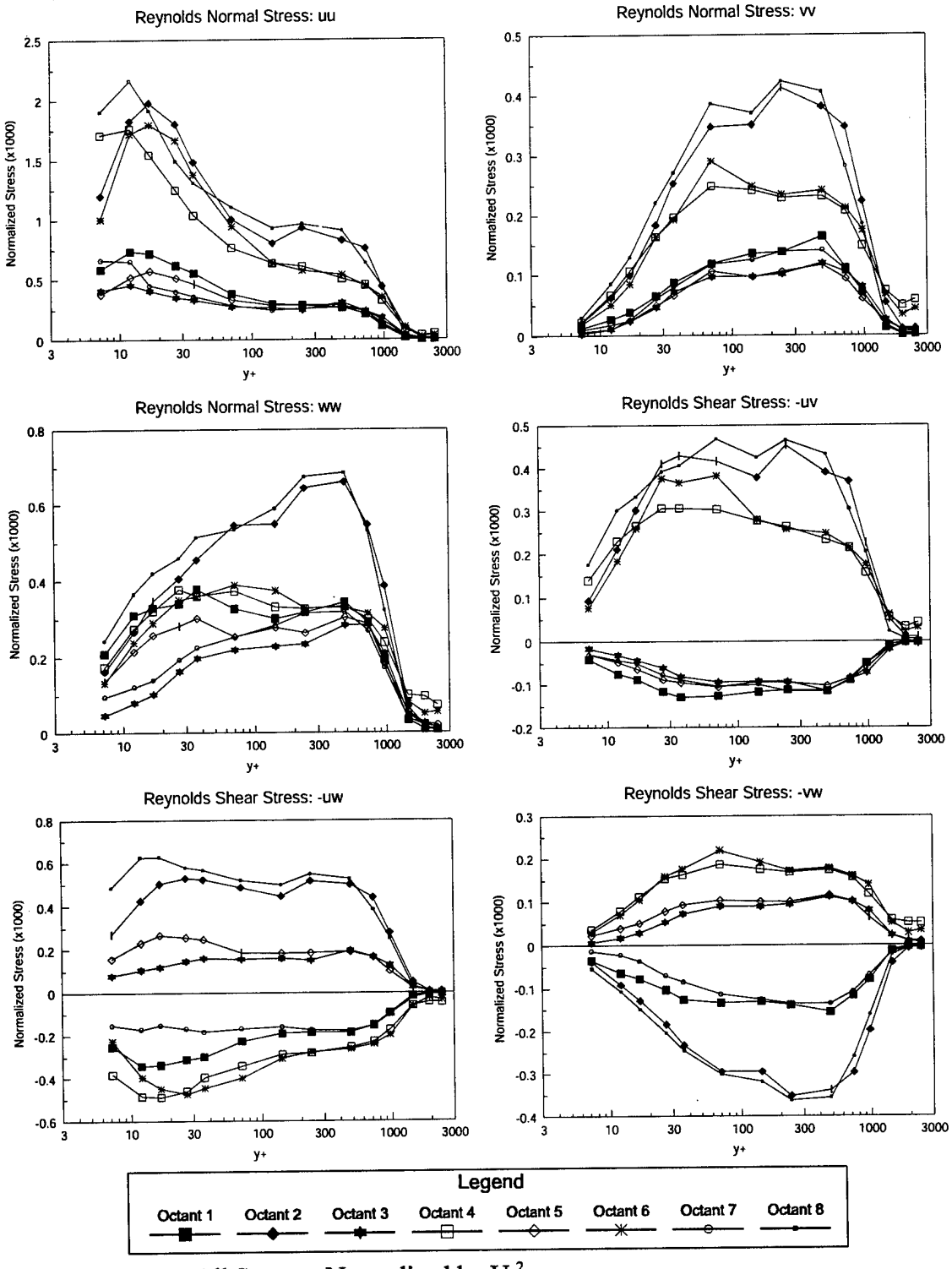


Note: All Stresses Normalized by $U_e^2$.

Figure 86. Octant Contributions to the Reynolds Stresses, x/L = 0.7622 & $\phi$ = 123°, Wall-collateral Coordinates.

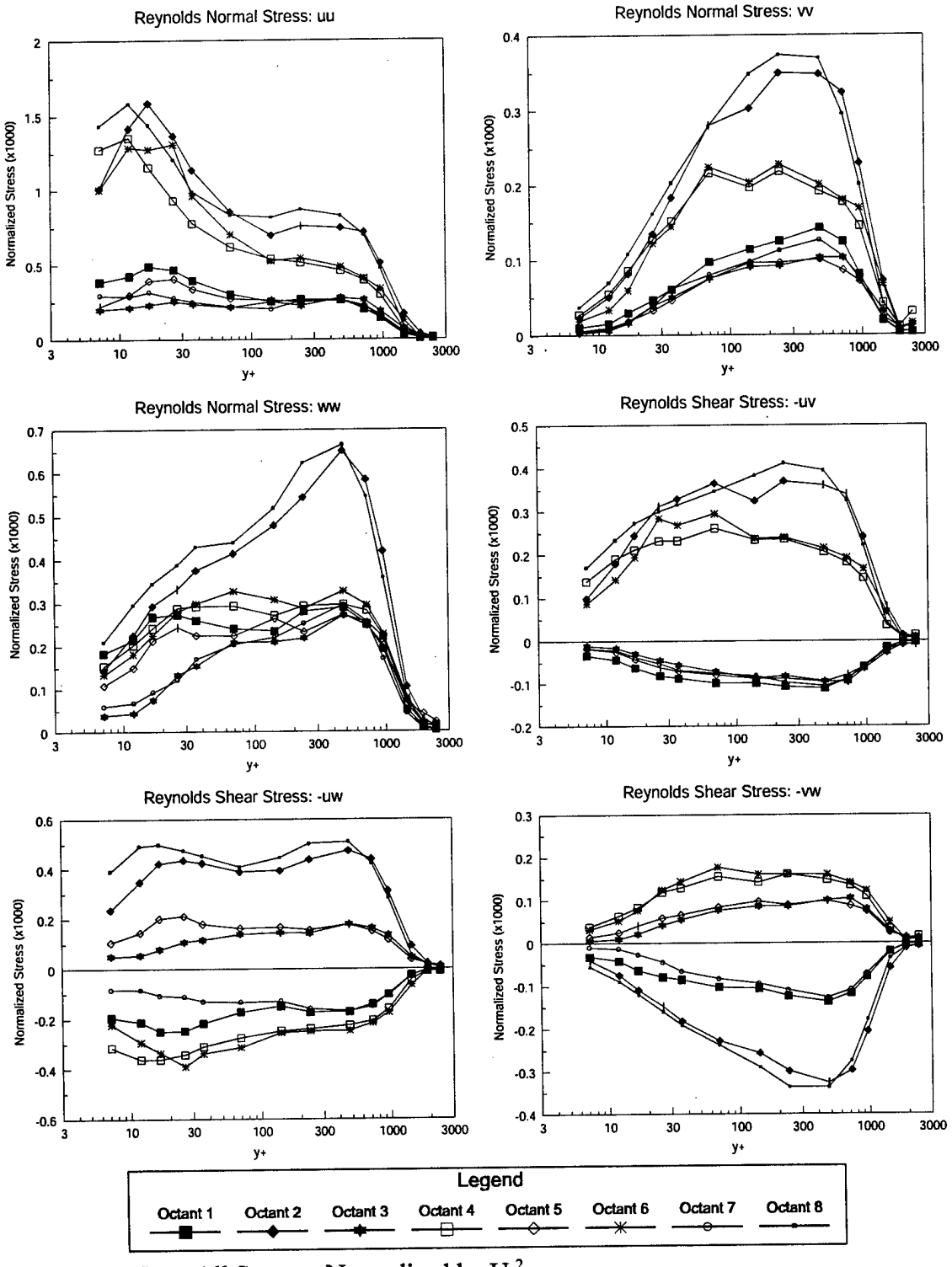


Note: All Stresses Normalized by $U_e^2$.

Figure 87. Octant Contributions to the Reynolds Stresses, x/L = 0.7622 & $\phi$ = 125°, Wall-collateral Coordinates.

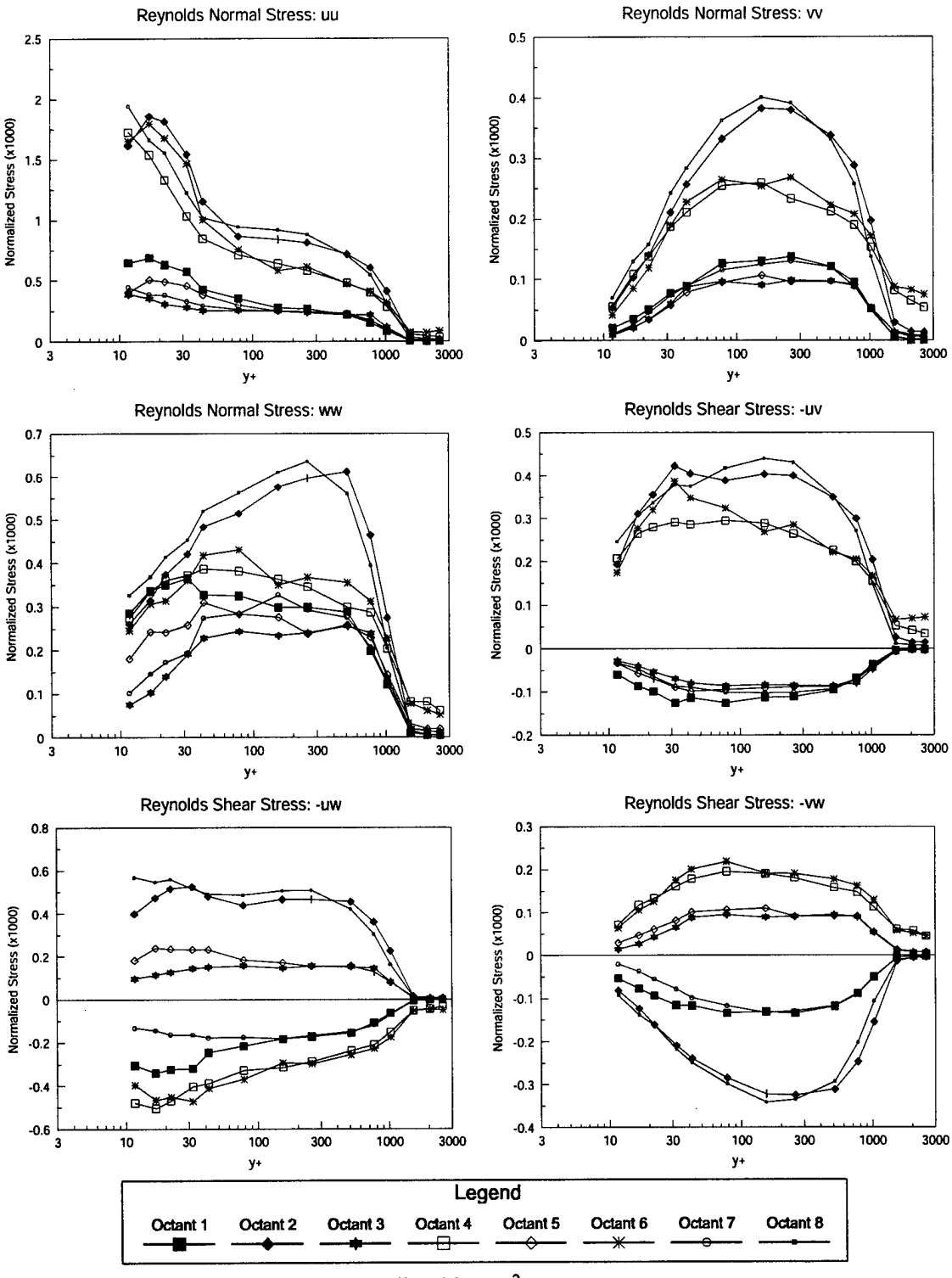


Note: All Stresses Normalized by $U_e^2$.

Figure 88. Octant Contributions to the Reynolds Stresses, x/L = 0.7522 & $\phi = 120°$, Wall-collateral Coordinates.

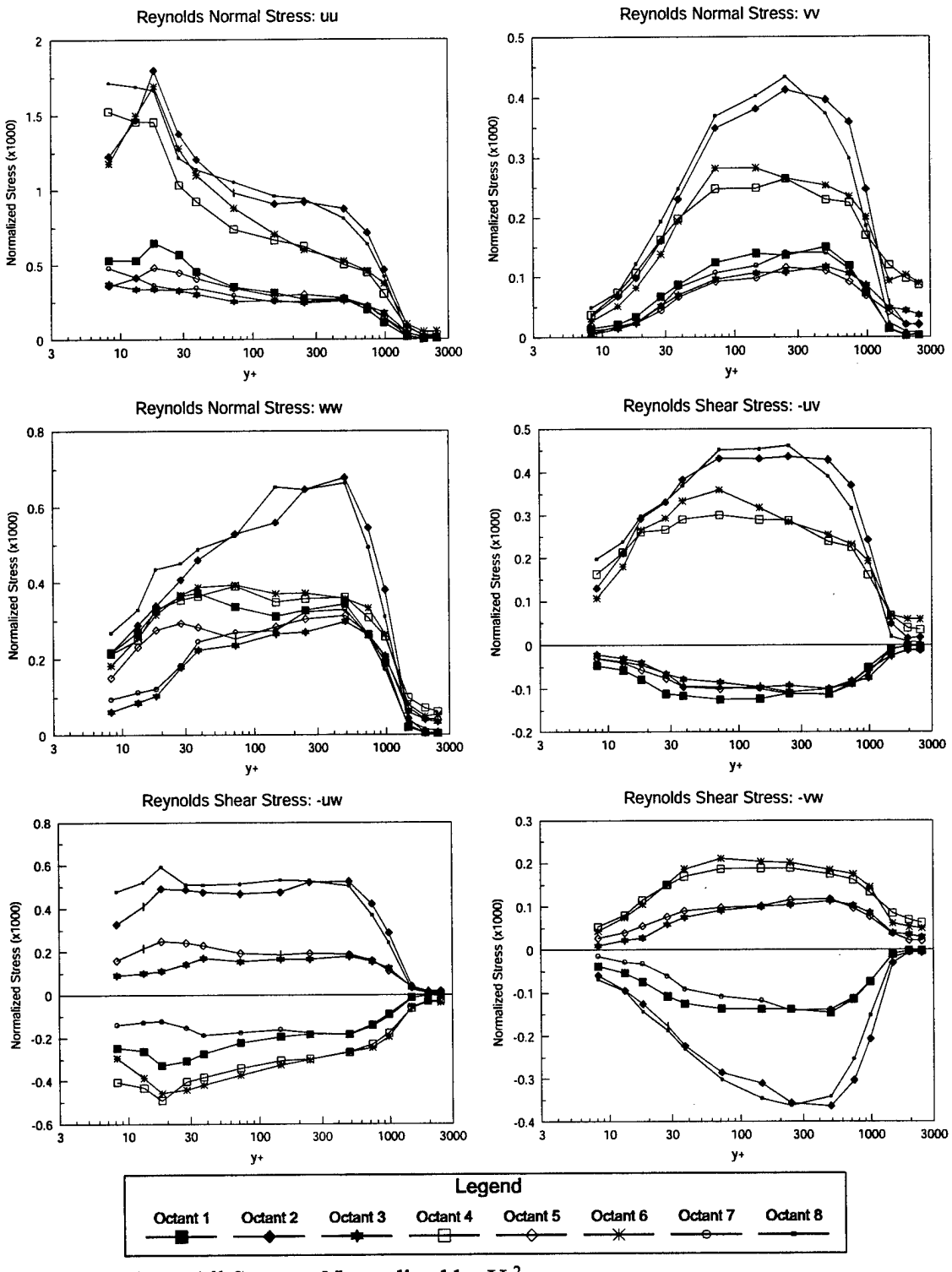


Note: All Stresses Normalized by $U_e^2$.

Figure 89. Octant Contributions to the Reynolds Stresses, x/L = 0.7522 & $\phi$ = 123°, Wall-collateral Coordinates.

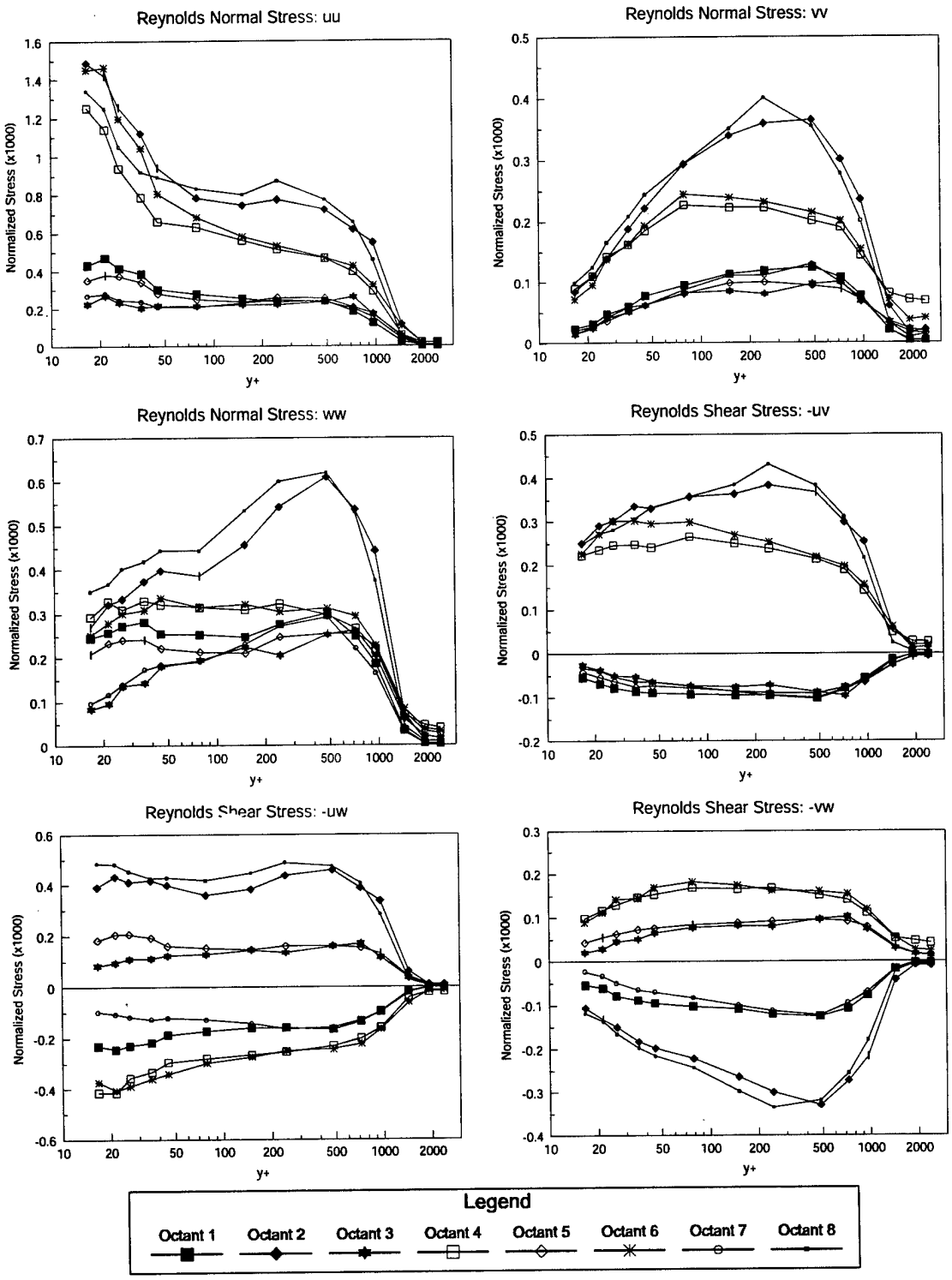


Note: All Stresses Normalized by $U_e^2$.

Figure 90. Octant Contributions to the Reynolds Stresses, x/L = 0.7522 & $\phi$ = 125°, Wall-collateral Coordinates.

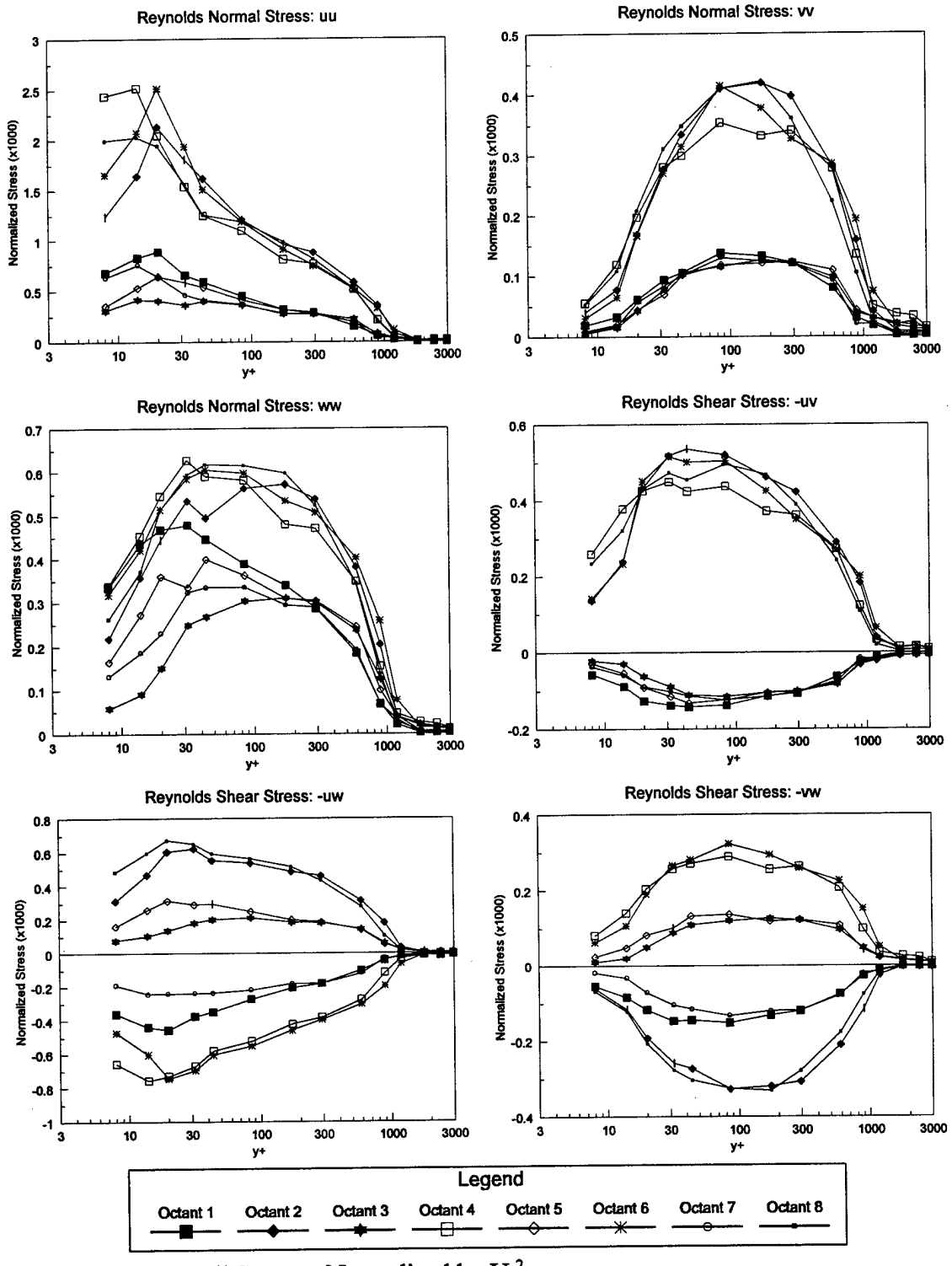


Note: All Stresses Normalized by $U_e^2$.

Figure 91. Octant Contributions to the Reynolds Stresses, x/L = 0.7722 & $\phi$ = 105°, Free-stream Coordinates.

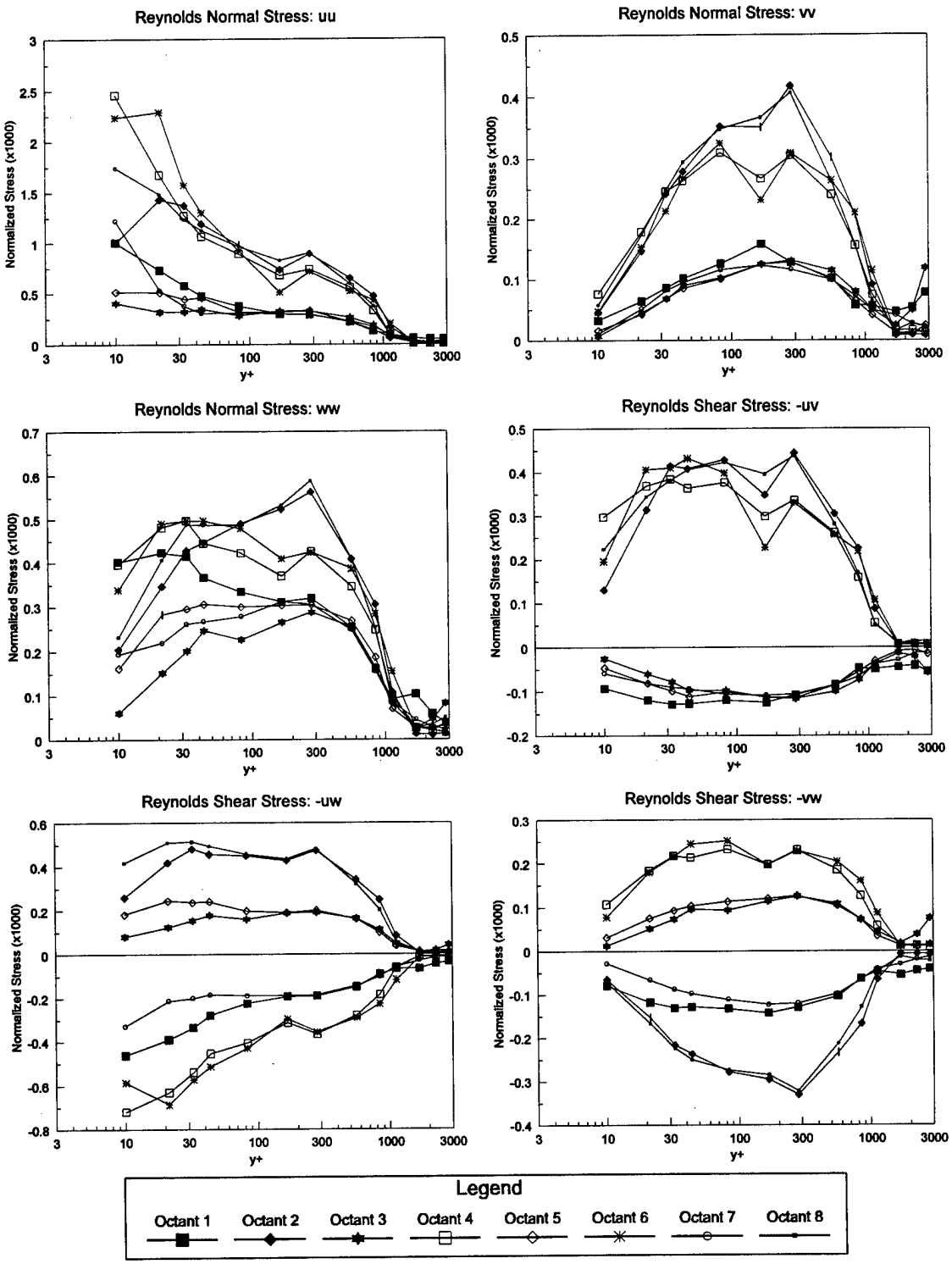


Note: All Stresses Normalized by $U_e^2$.

Figure 92. Octant Contributions to the Reynolds Stresses, x/L = 0.7722 & $\phi = 110°$, Free-stream coordinates.

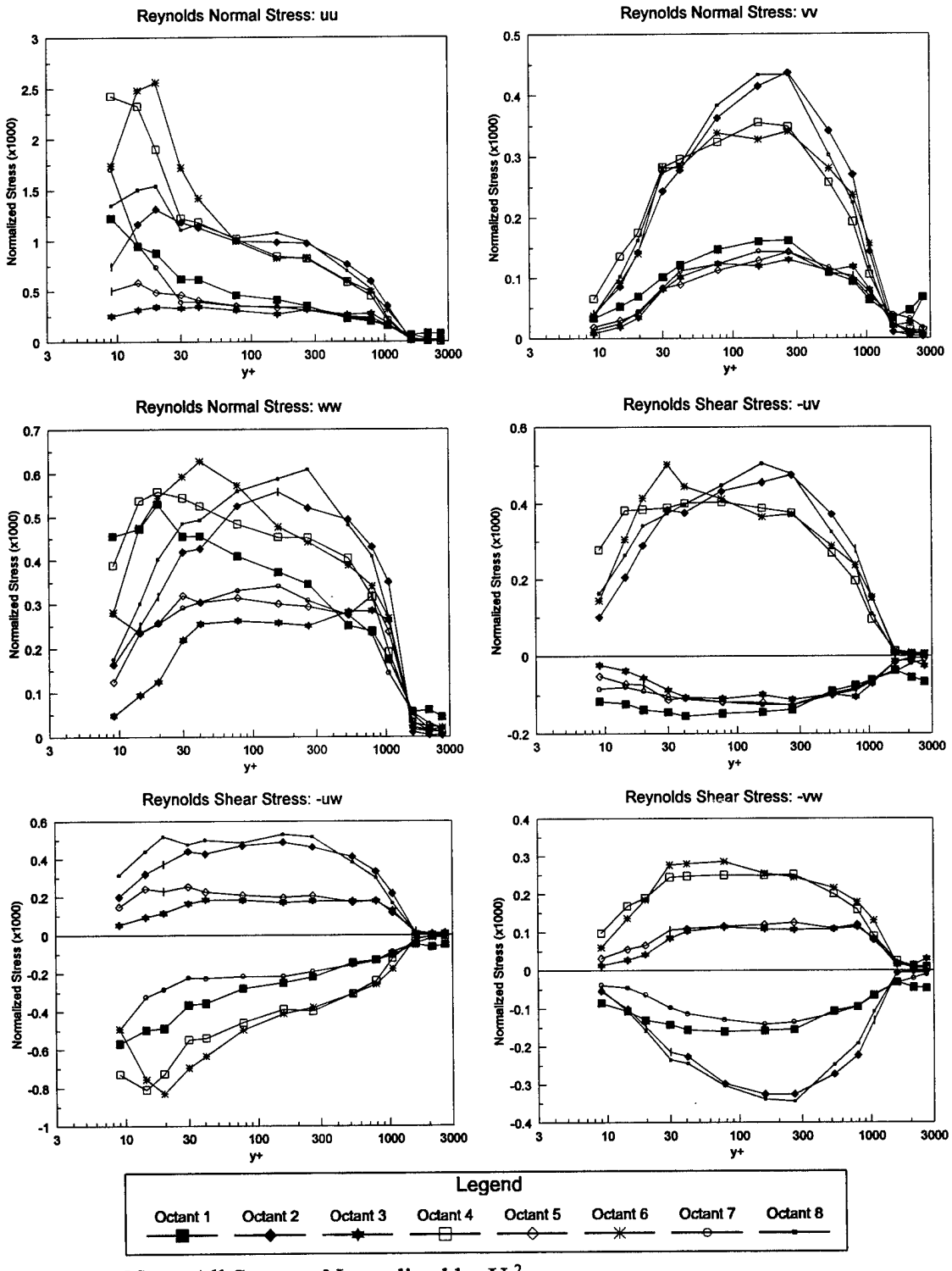


Note: All Stresses Normalized by $U_e^2$.

Figure 93. Octant Contributions from the Reynolds Stresses, x/L = 0.7722 & $\phi$ = 115°, Free-stream Coordinates.

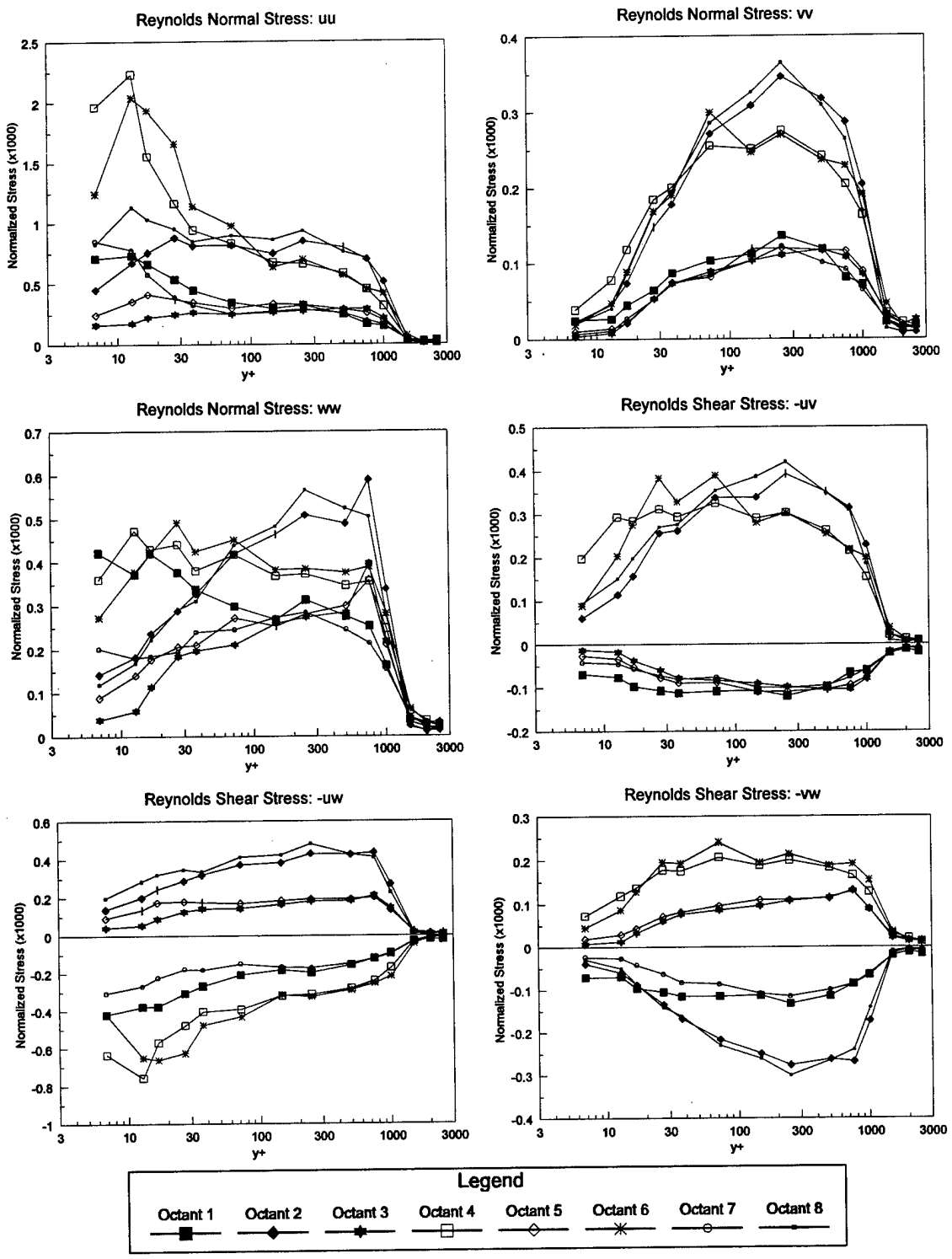


Note: All Stresses Normalized by $U_e^2$.

Figure 94. Octant Contributions from the Reynolds Stresses, x/L = 0.7722 & $\phi$ = 120°, Free-stream Coordinates.

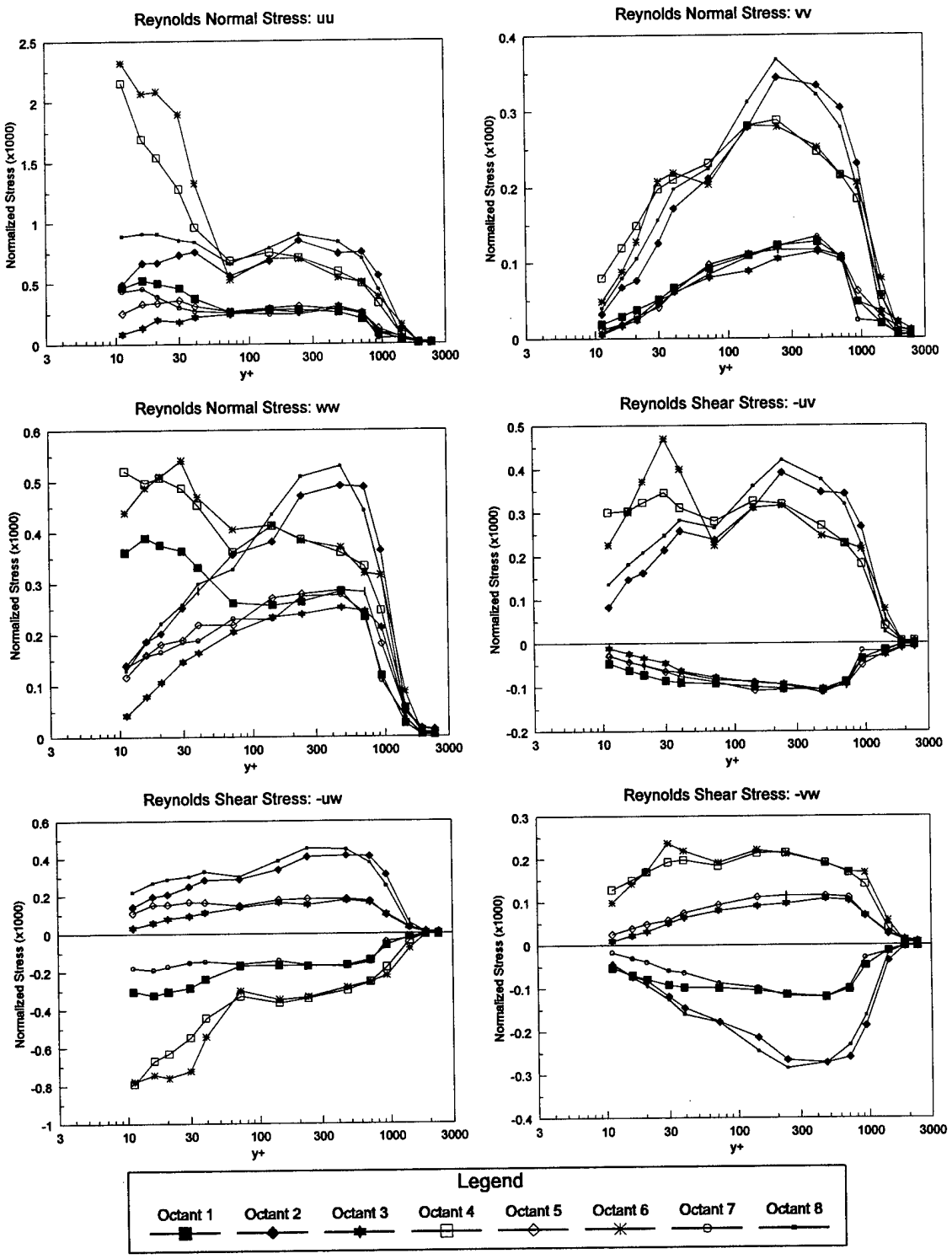


Note: All Stresses Normalized by $U_e^2$.

Figure 95. Octant Contributions from the Reynolds Stresses, x/L = 0.7722 & $\phi$ = 123°, Free-stream Coordinates.

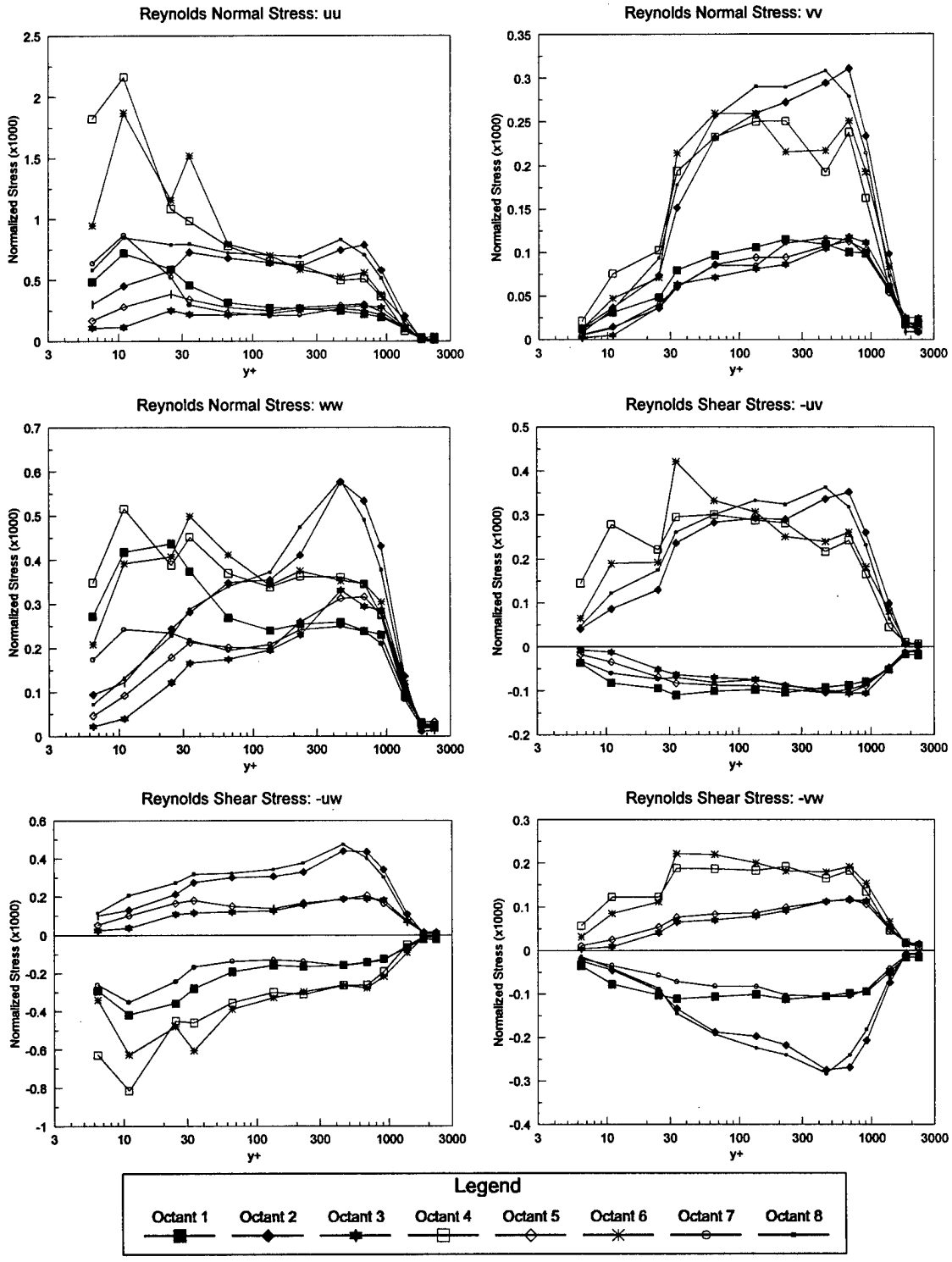


Note: All Stresses Normalized by $U_e^2$.

Figure 96. Octant Contributions from the Reynolds Stresses, x/L = 0.7722 & $\phi$ = 125°, Free-stream Coordinates.

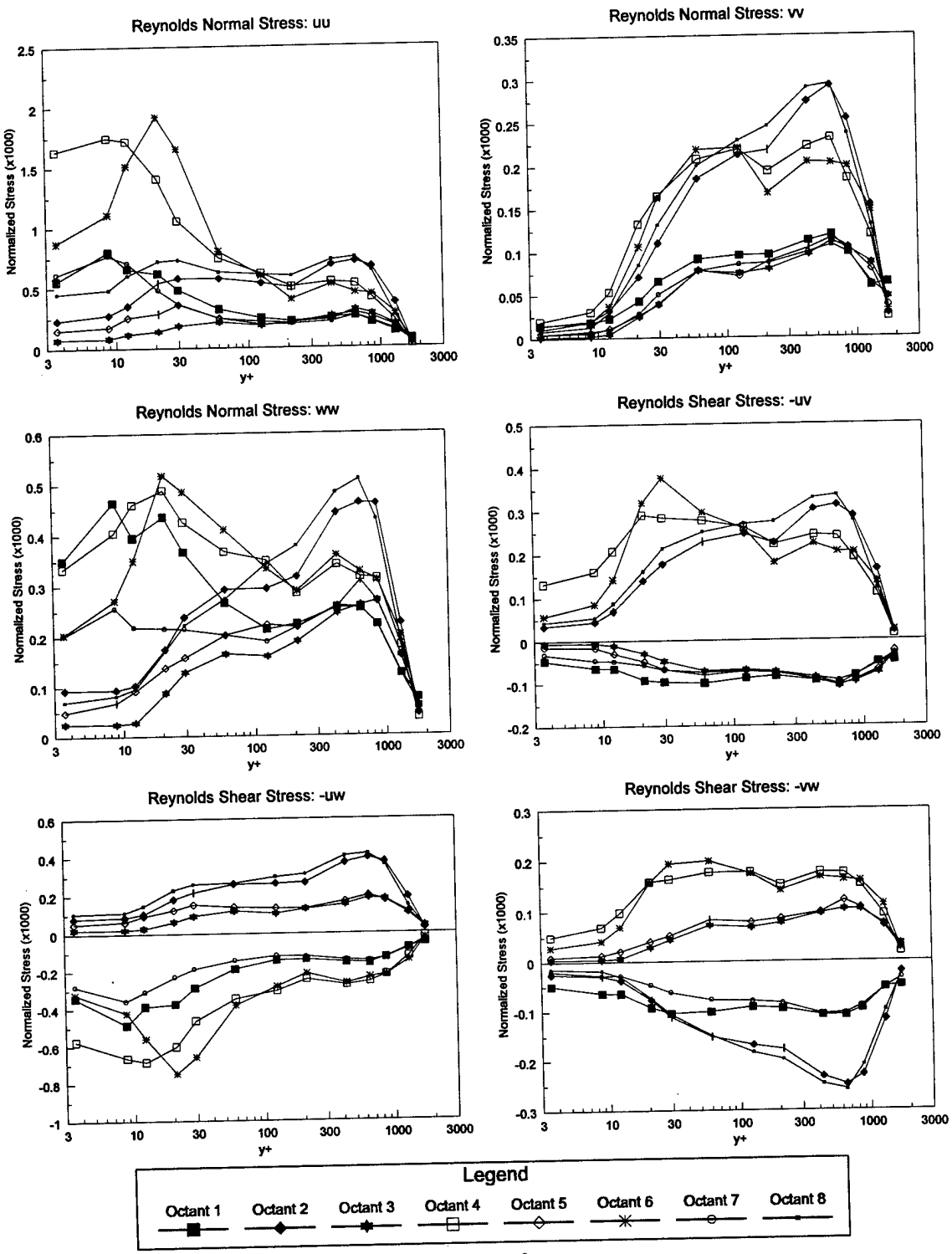


Note: All Stresses Normalized by $U_e^2$.

Figure 97. Octant Contributions from the Reynolds Stresses, x/L=0.7722 & $\phi = 130°$, Free-stream Coordinates.

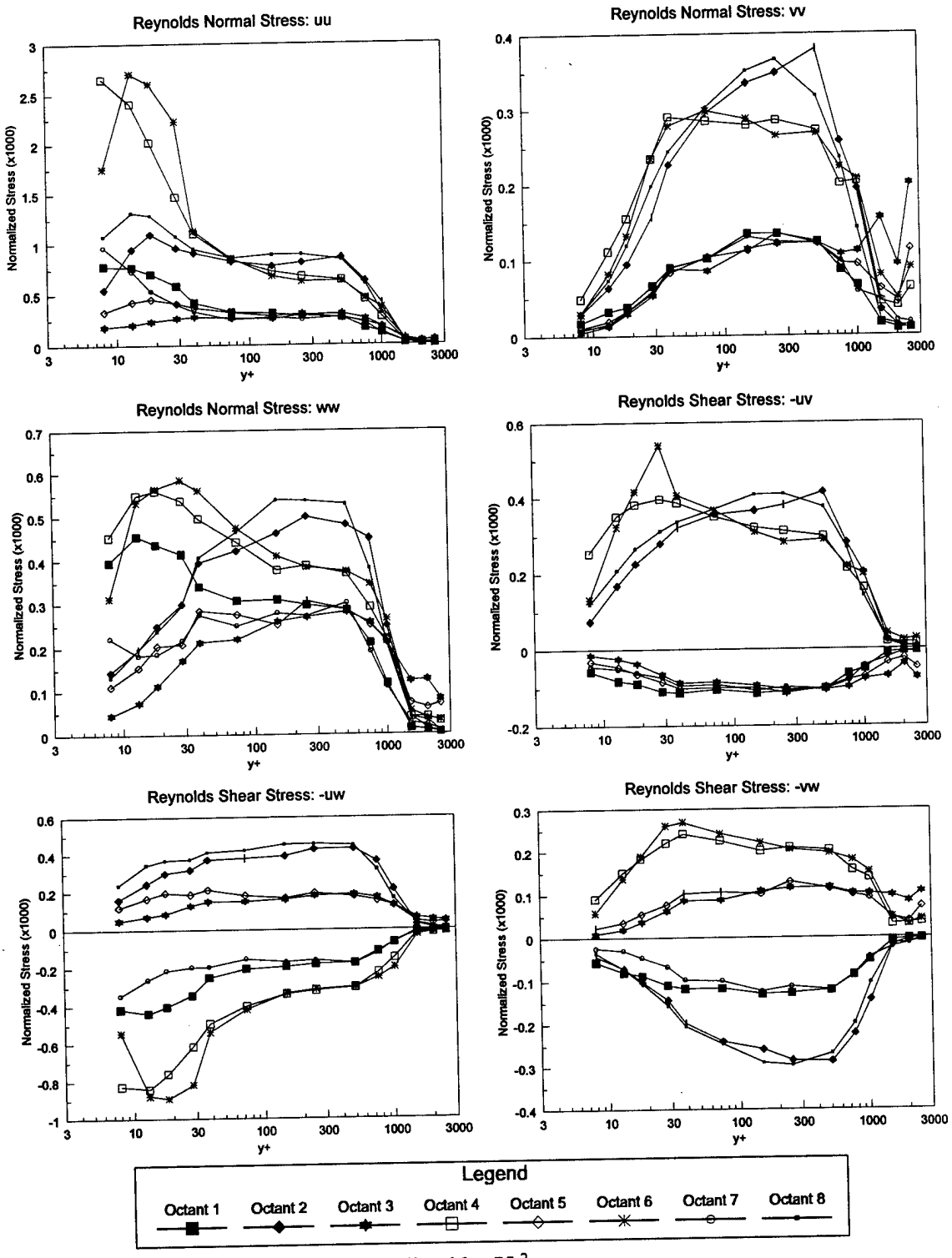


Note: All Stresses Normalized by $U_e^2$.

Figure 98. Octant Contributions from the Reynolds Stresses, x/L=0.7622 & $\phi = 120°$, Free-stream Coordinates.

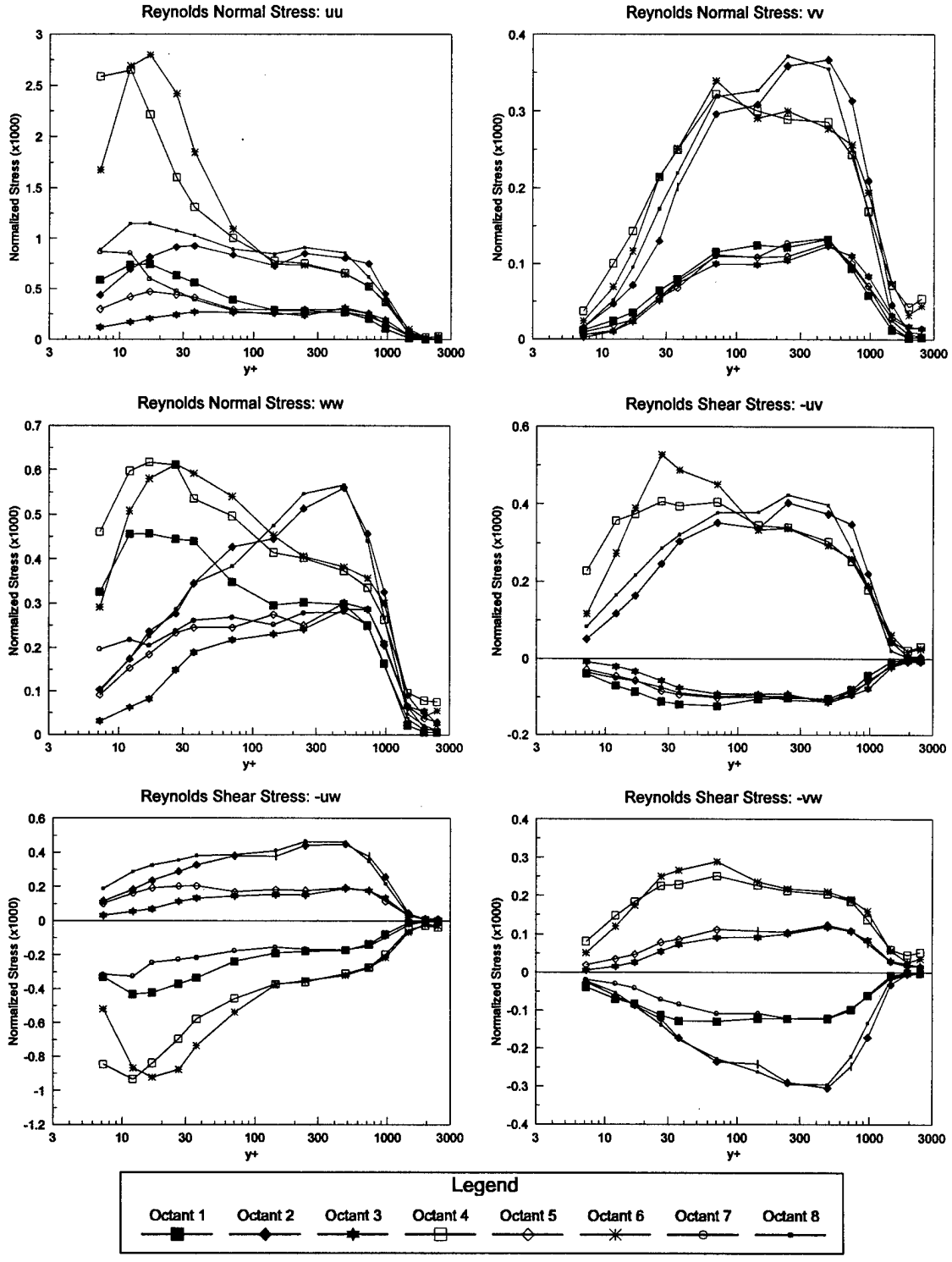


Note: All Stresses Normalized by $U_e^2$.

Figure 99. Octant Contributions from the Reynolds Stresses, x/L = 0.7622 & $\phi$ = 123°, Free-stream Coordinates.

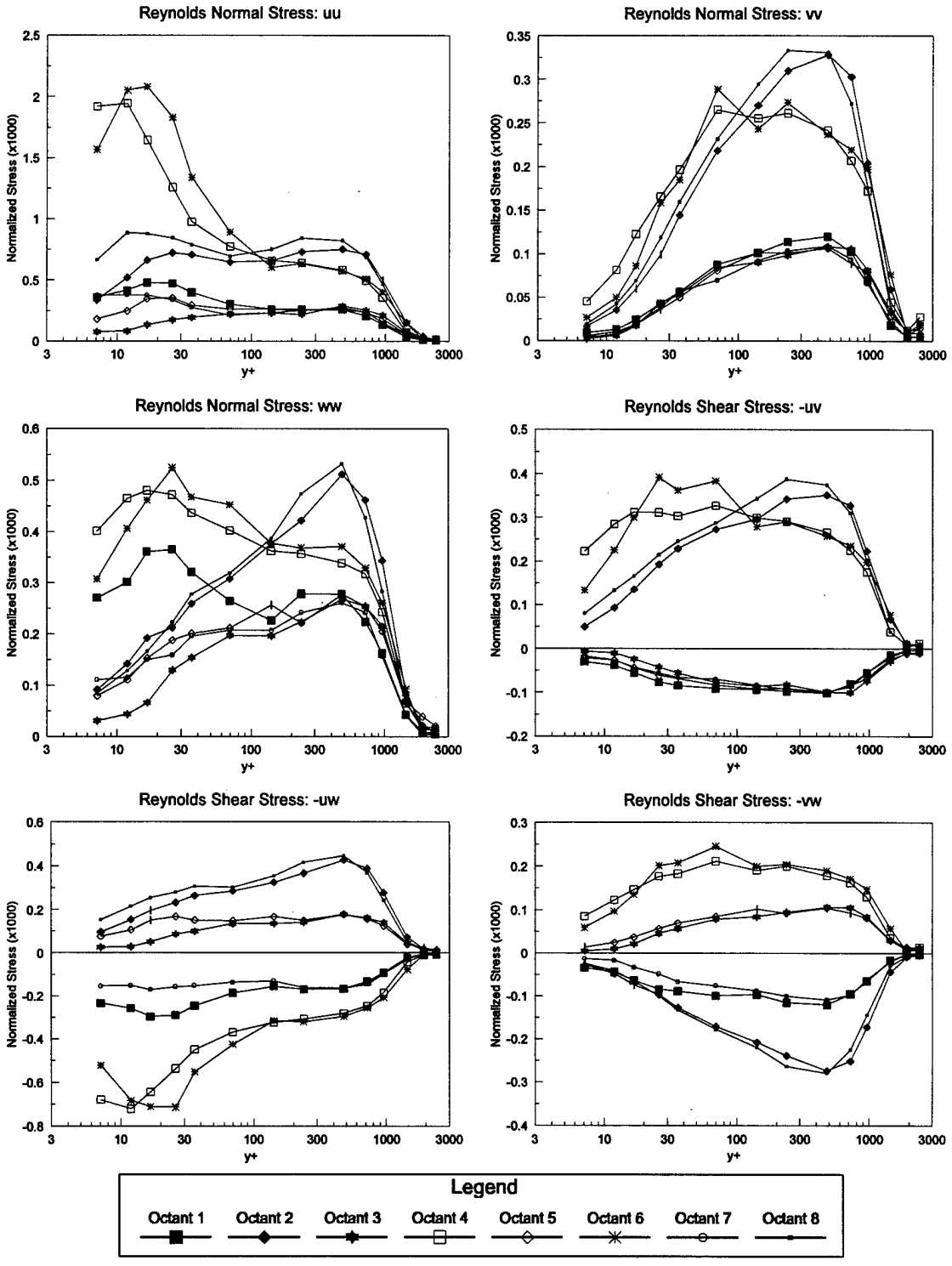


Note: All Stresses Normalized by $U_e^2$.

Figure 100. Octant Contributions from the Reynolds Stresses, x/L=0.7622 & $\phi = 125°$, Free-stream Coordinates.

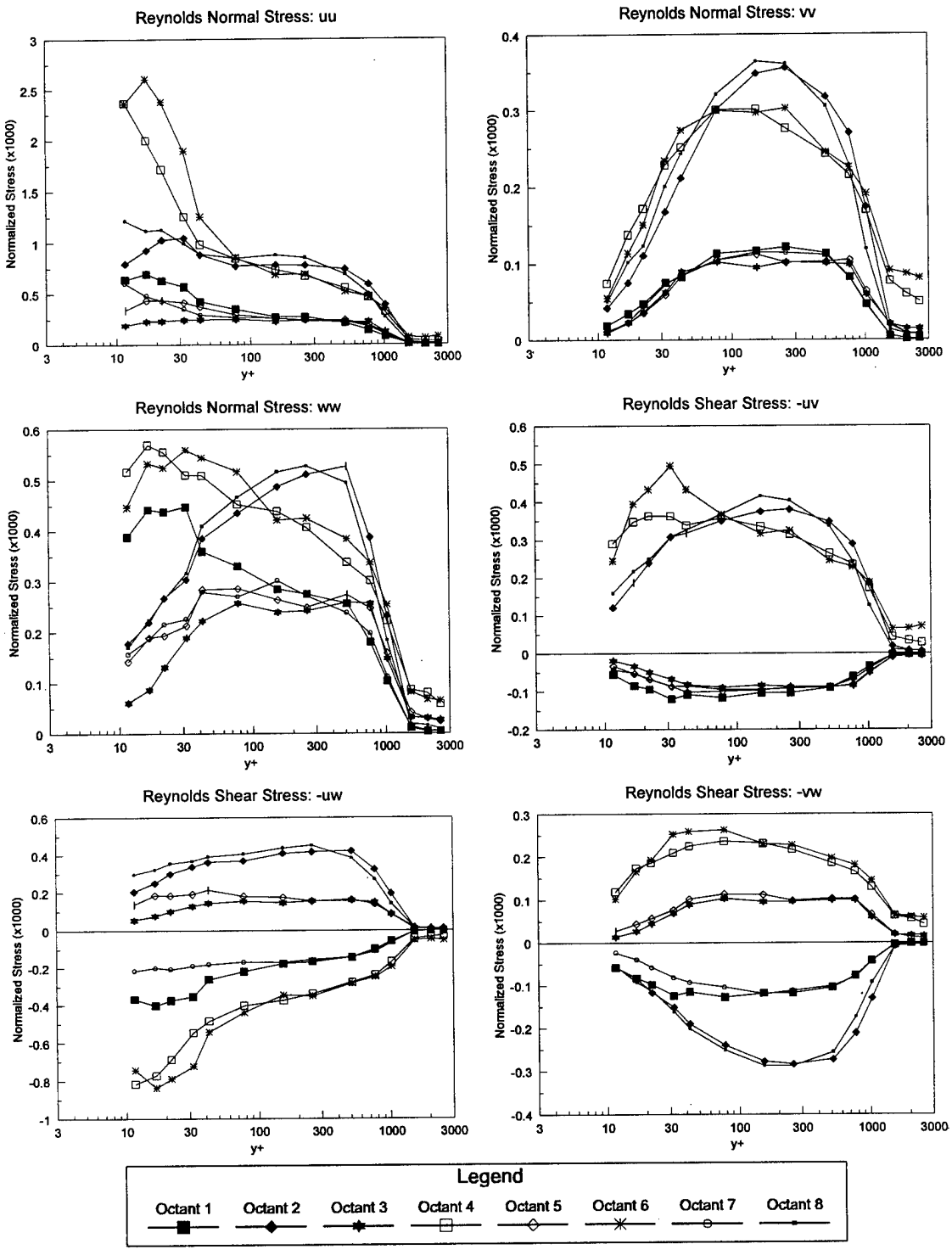


Note: All Stresses Normalized by $U_e^2$.

Figure 101. Octant Contributions from the Reynolds Stresses, x/L = 0.7522 & $\phi$ = 120°, Free-stream Coordinates.

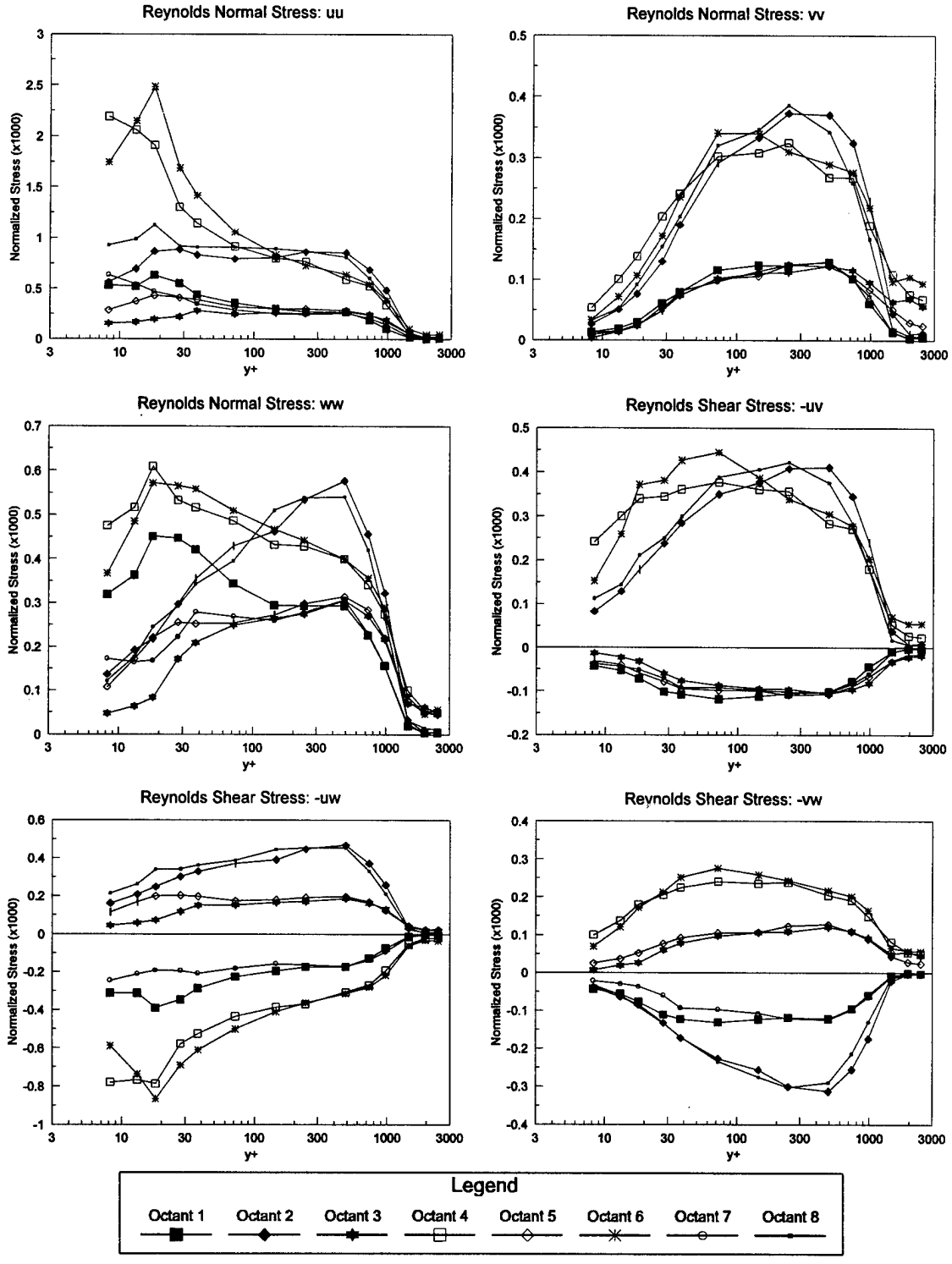


Note: All Stresses Normalized by $U_e^2$.

Figure 102. Octant Contributions from the Reynolds Stresses, x/L = 0.7522 & $\phi$ = 123°, Free-stream Coordinates.

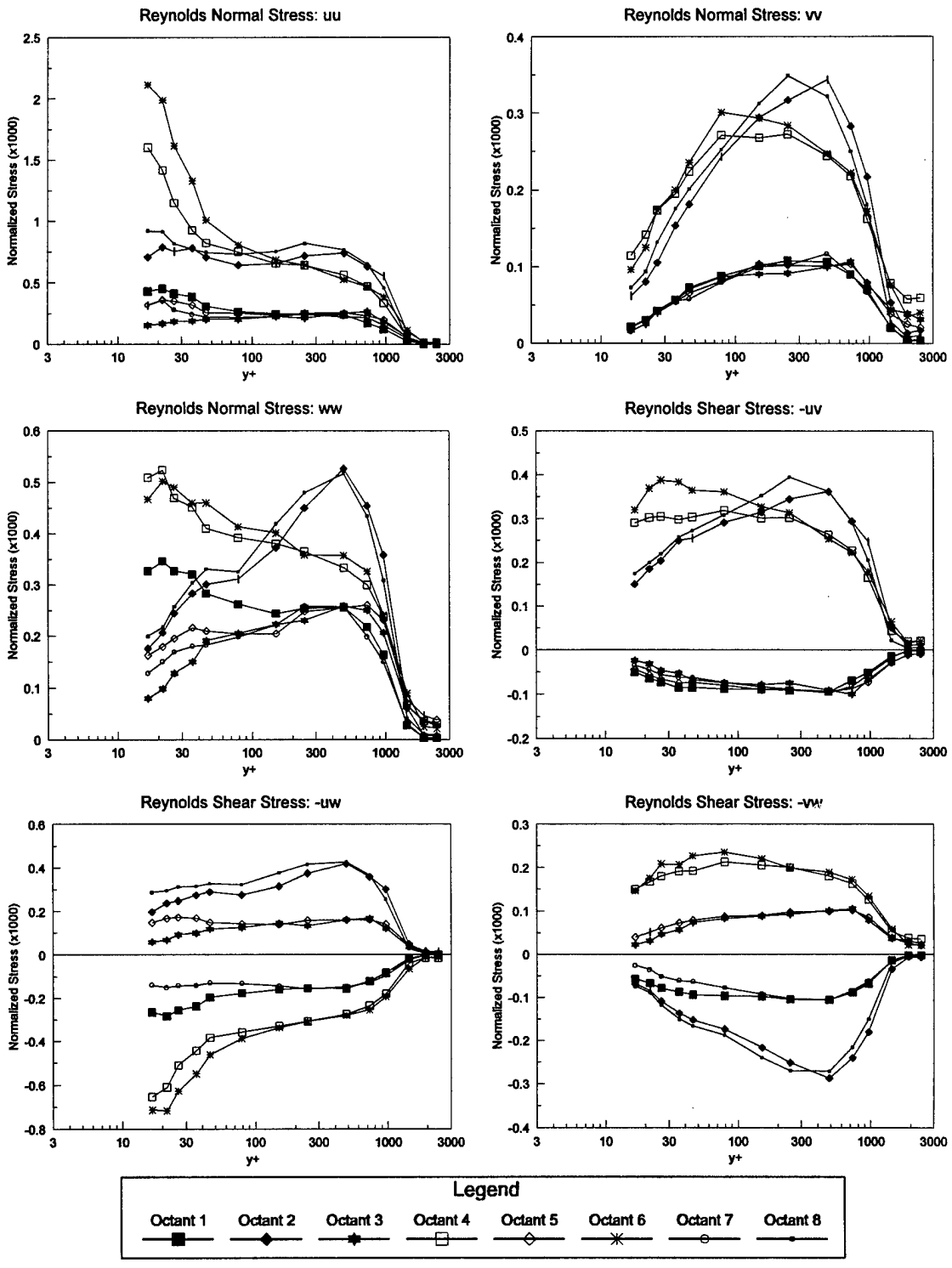


Note: All Stresses Normalized by $U_e^2$.

Figure 103. Octant Contributions from the Reynolds Stresses, x/L = 0.7522 & $\phi$ = 125°, Free-stream Coordinates.

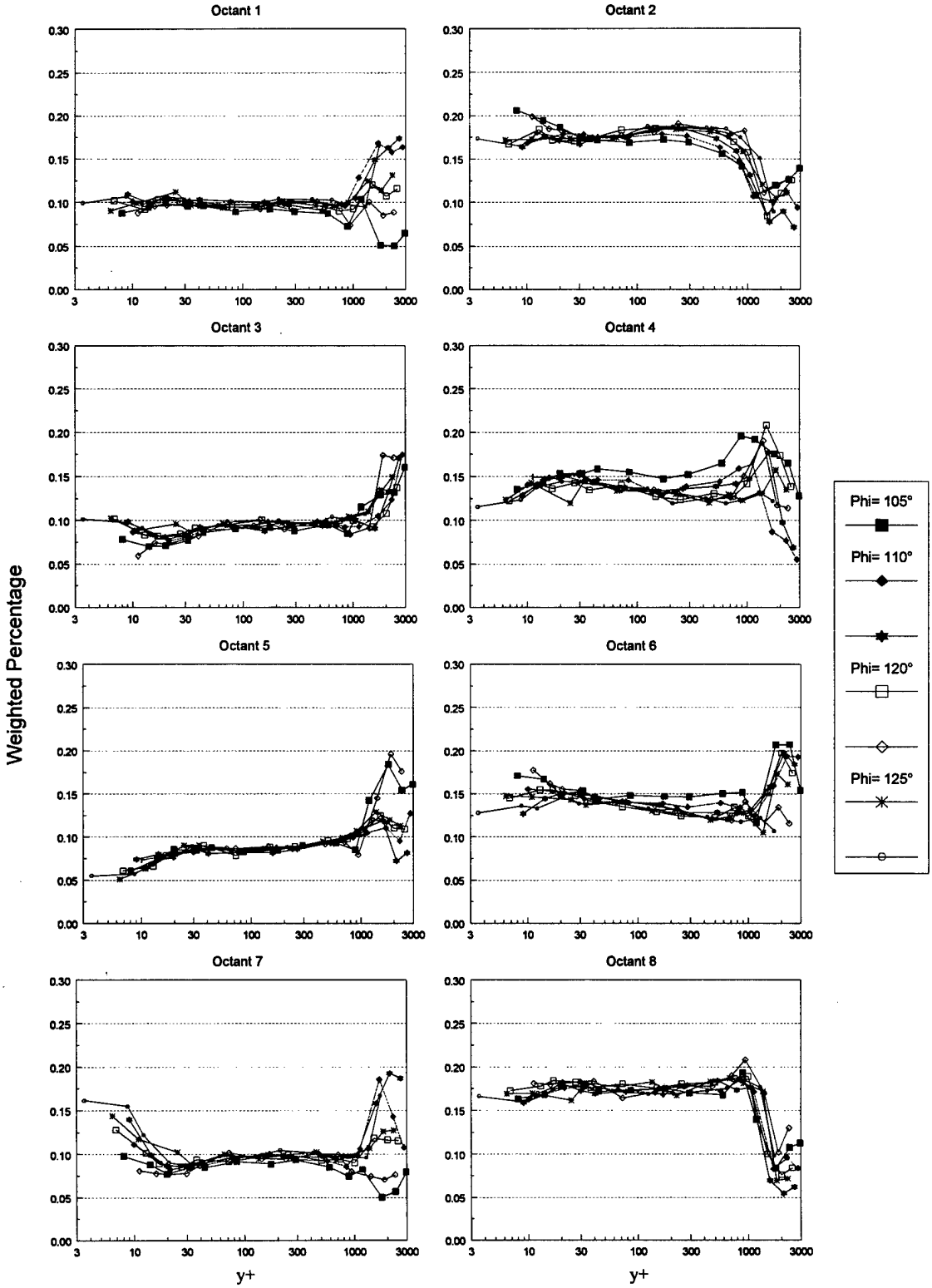


Figure 104. Weighted Octant Population in Wall-collateral Coordinates. x/L=0.7722, $\phi$=105°-130°.

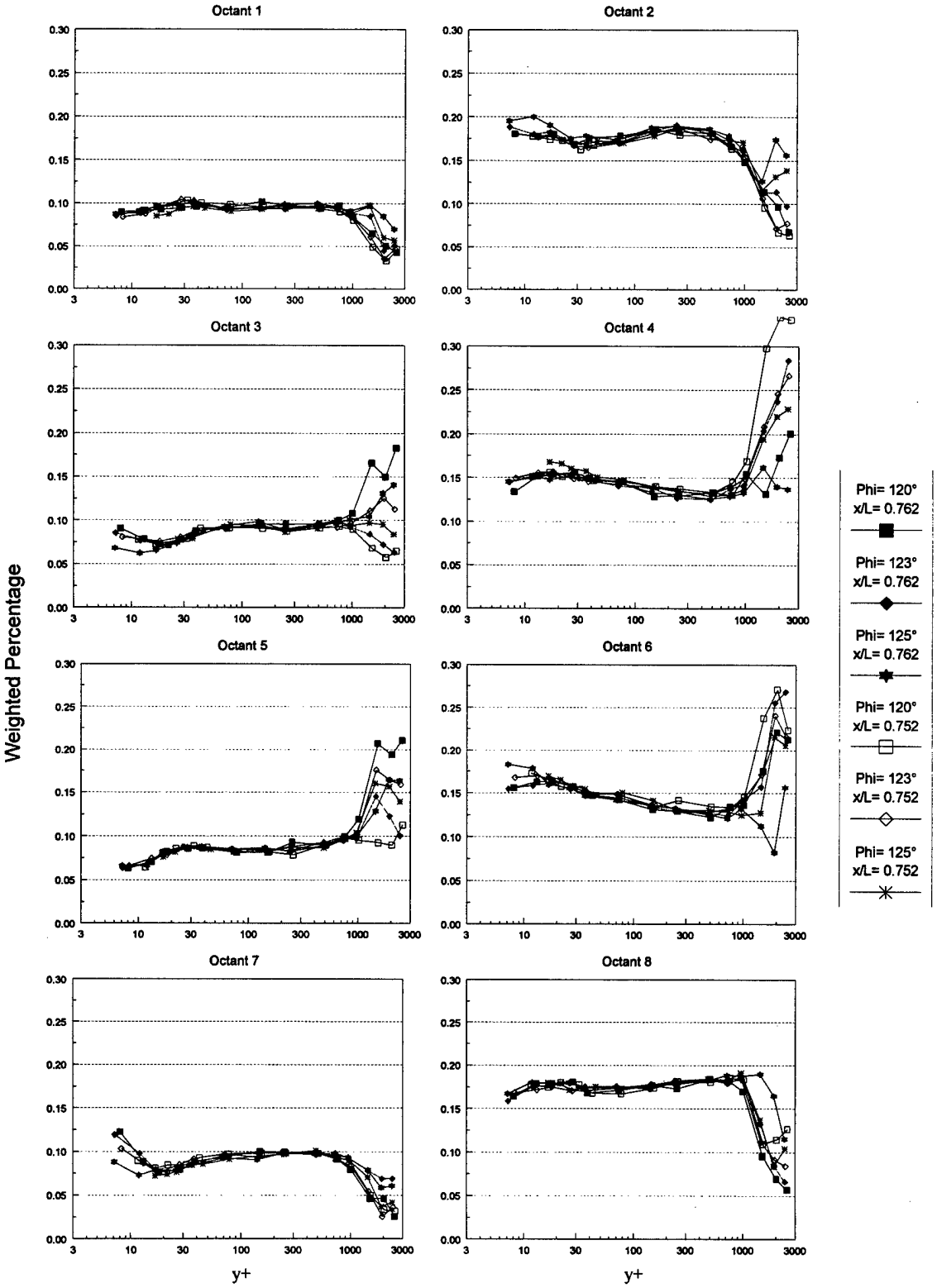


Figure 105. Weighted Octant Population in Wall-collateral Coordinates. x/L=0.7622 & 0.7522, $\phi$=120°-125°.

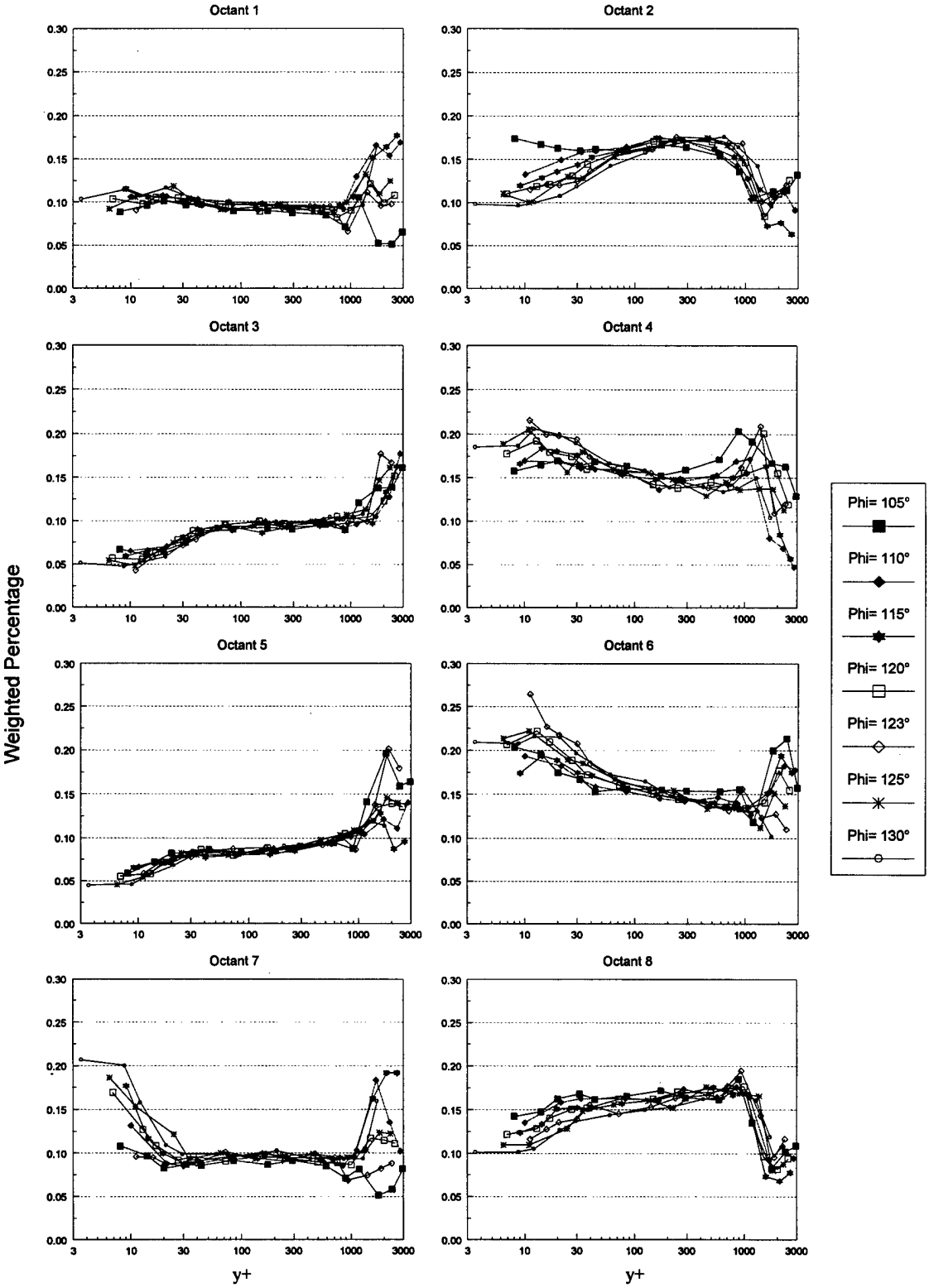


Figure 106. Weighted Octant Population in Free-stream Coordinates. x/L=0.7722, $\phi$=105°-130°.

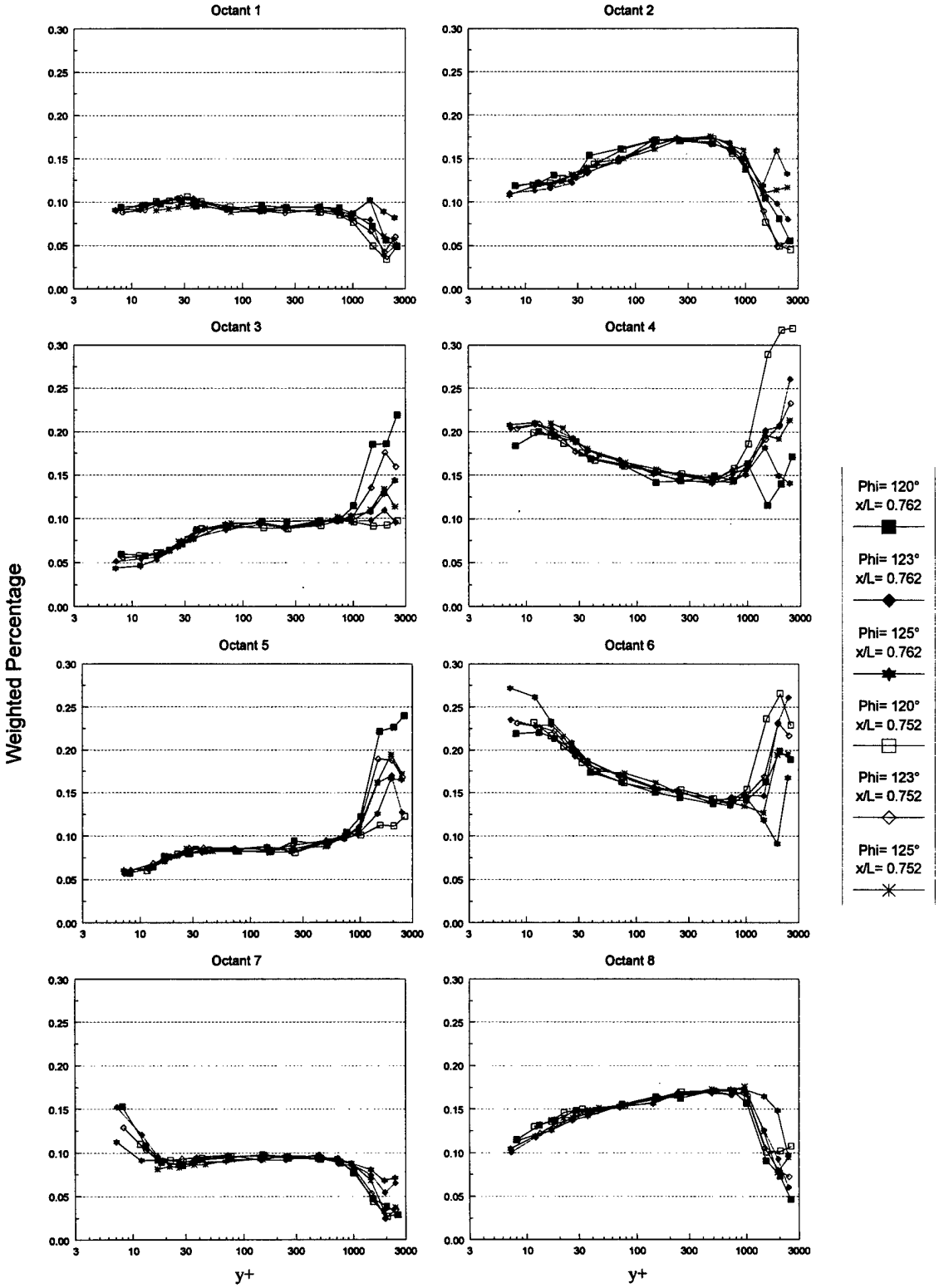


Figure 107. Weighted Octant Population in Free-stream Coordinates. x/L=0.7622 & 0.7522, $\phi$=120°-125°.

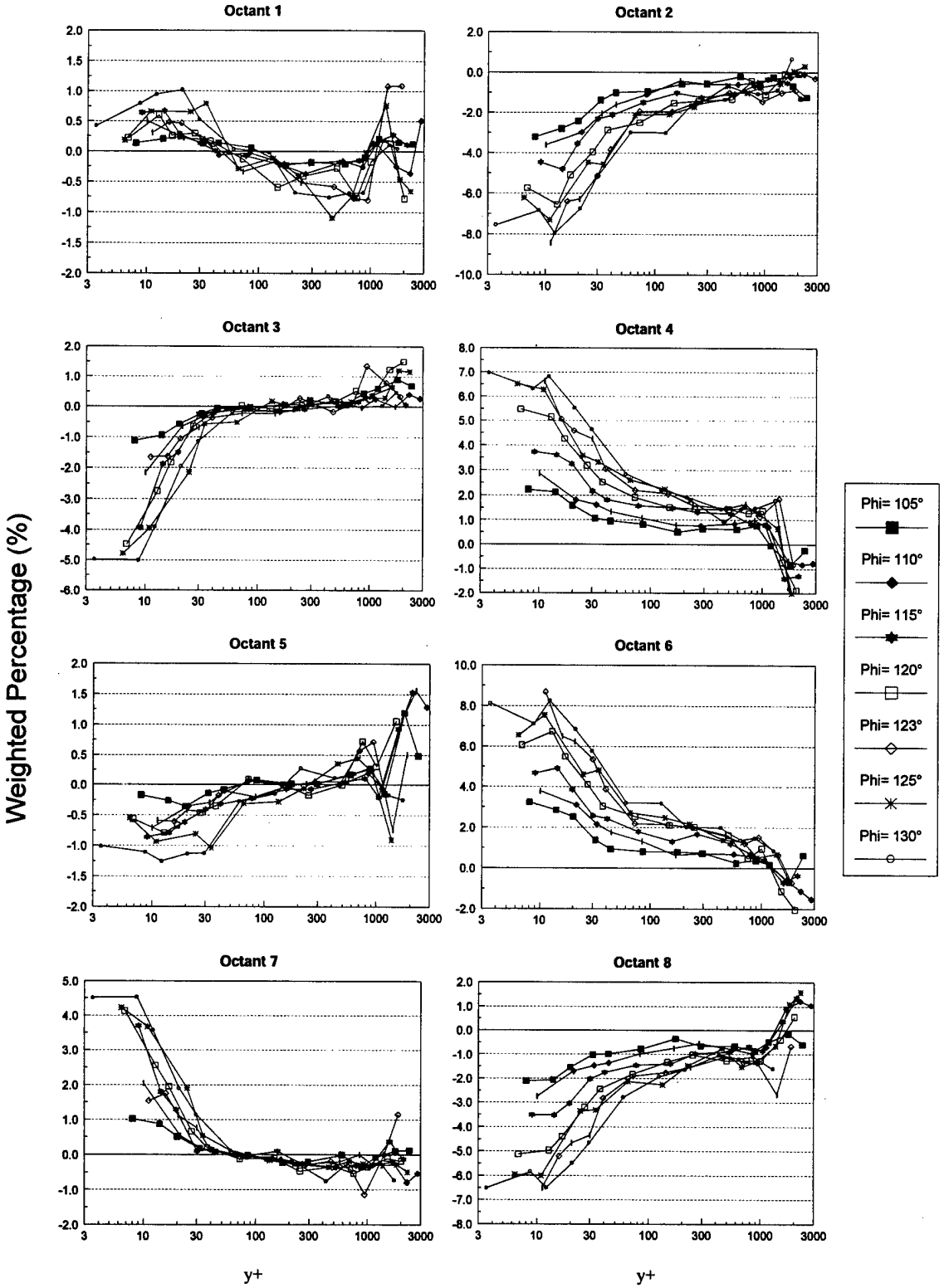


Figure 108. Octant population difference between free-stream and wall-collateral coordinates. x/L=0.7722, $\phi$=105°-130°.

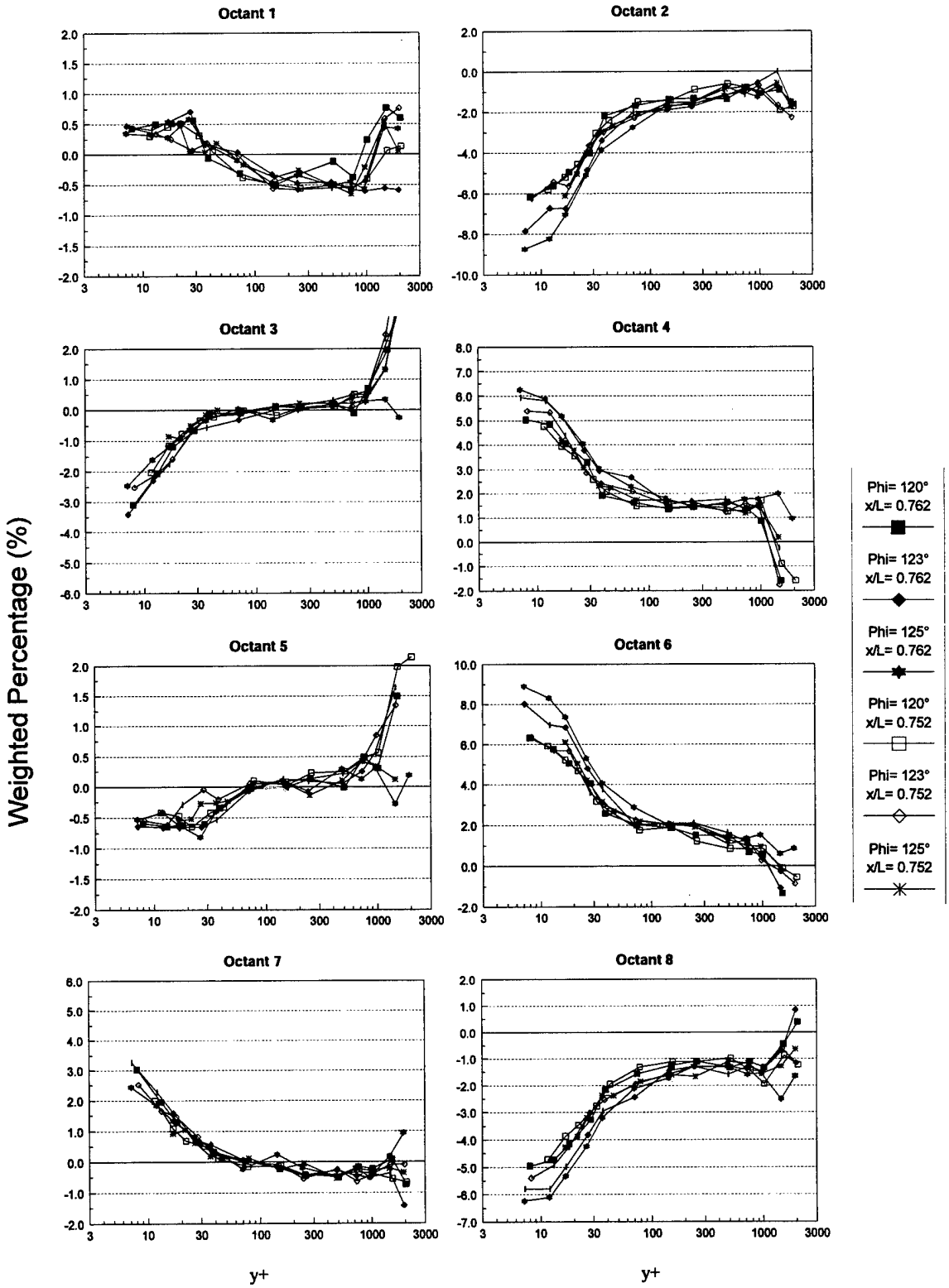


Figure 109. Octant population difference between free-stream and wall-collateral coordinates . x/L=0.7622 & 0.7522, $\phi$=120°-125°.

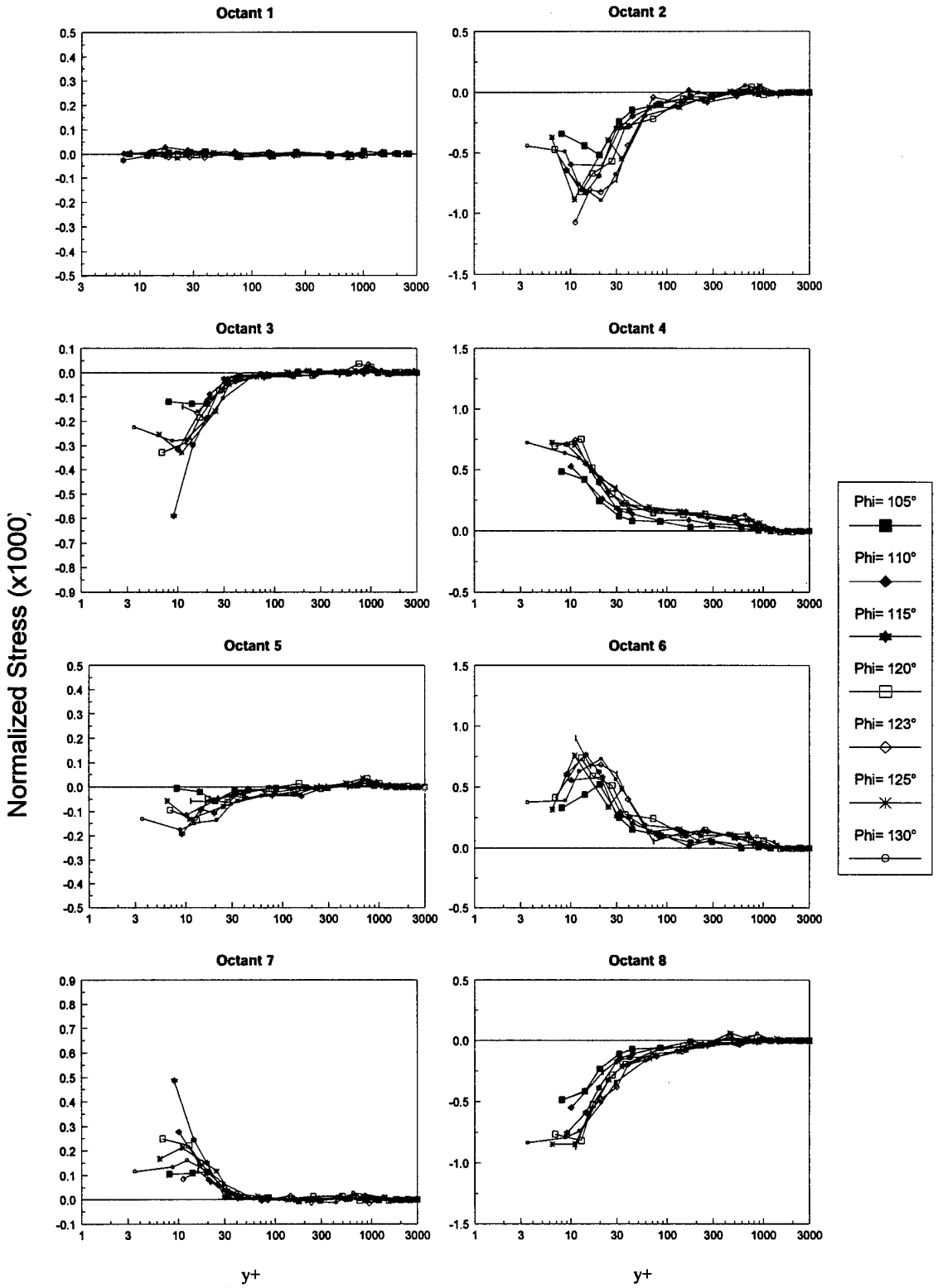


Figure 110. Octant $u'^2$ contribution difference between free-stream and wall-collateral co-ordinates. x/L=0.7722, $\phi$=105°-130°.

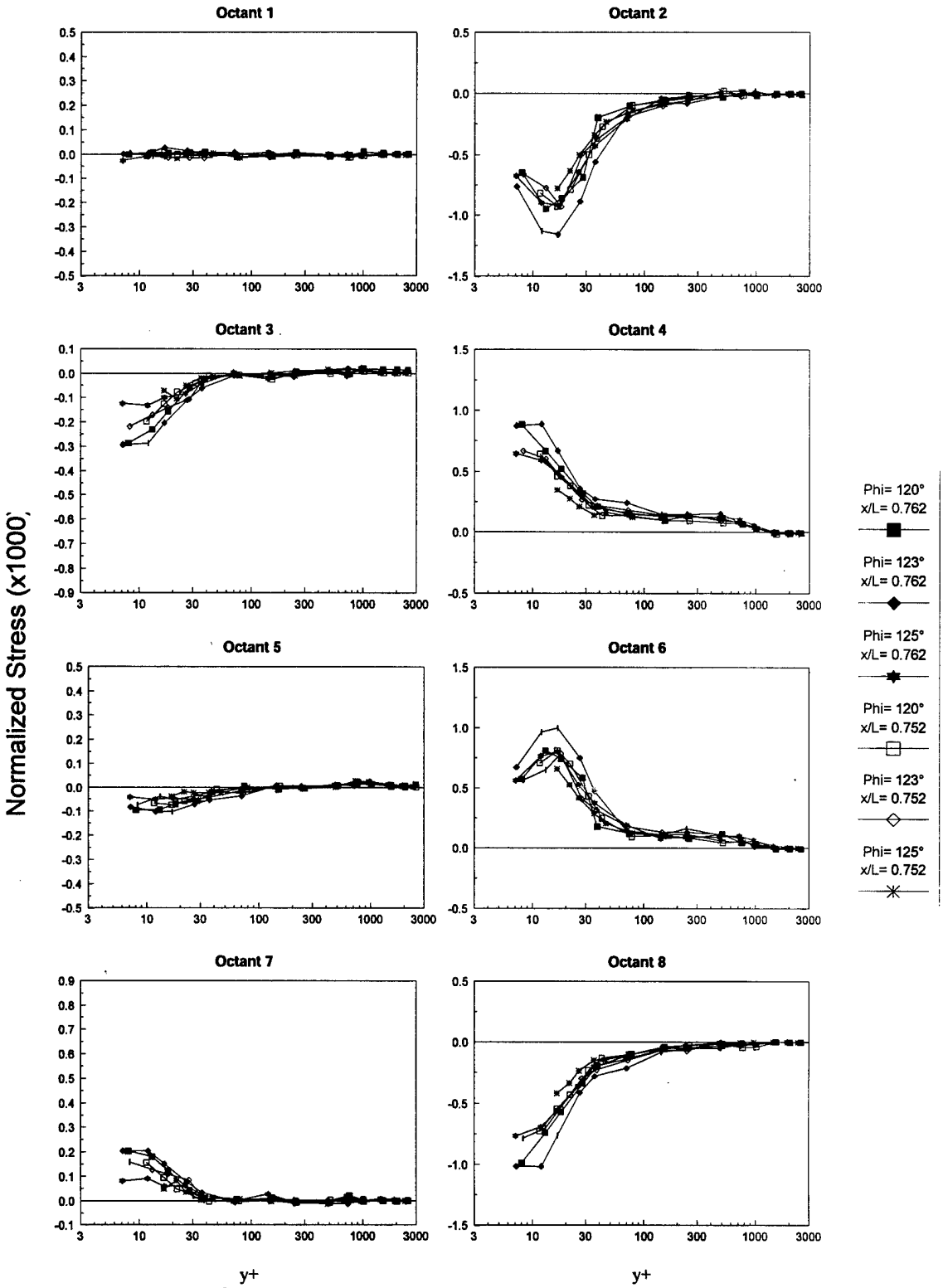


Figure 111. Octant $u'^2$ contribution difference between free-stream and wall-collateral co-ordinates. x/L=0.7622 & 0.7522, $\phi$=120°-125°.

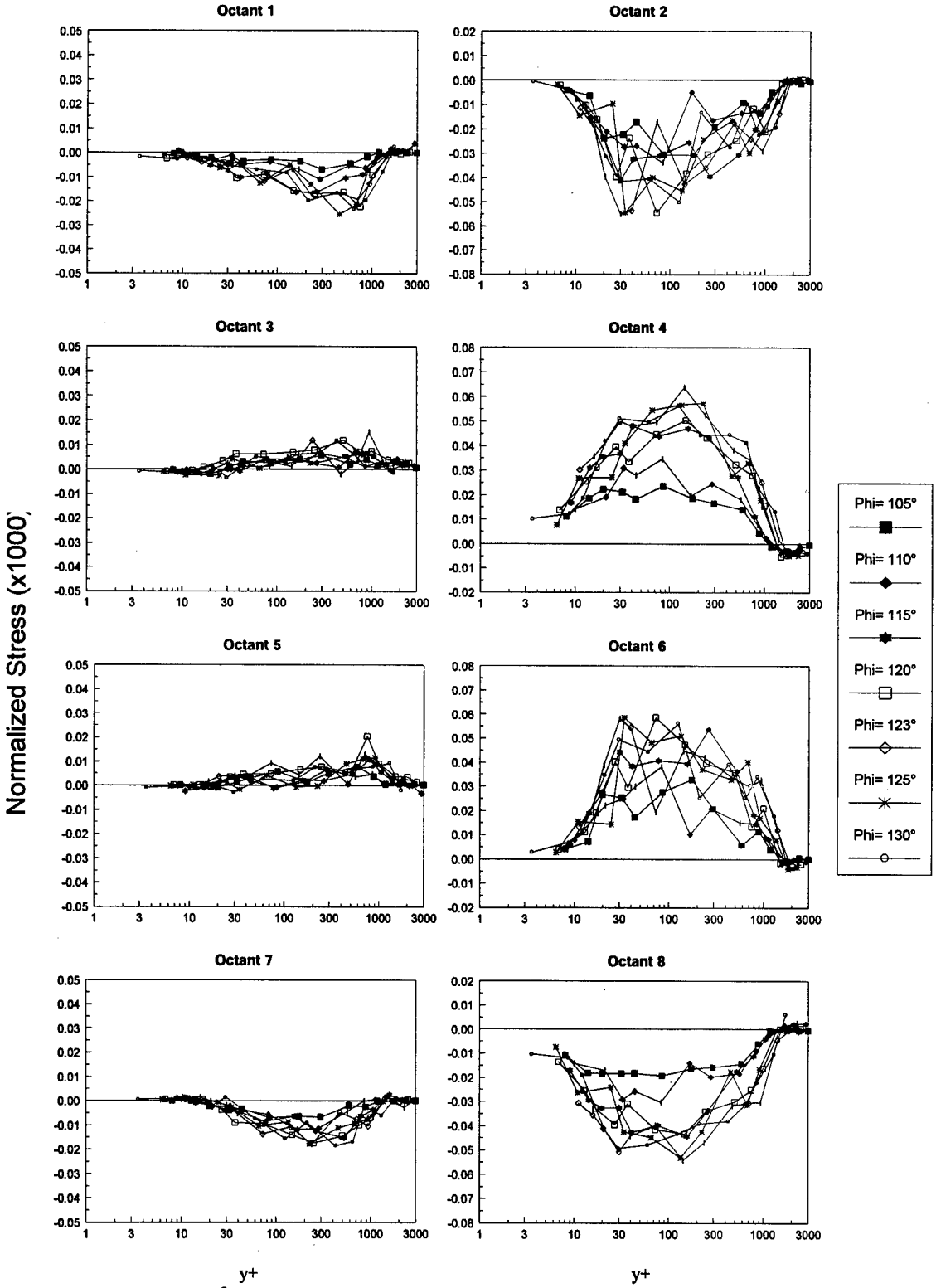


Figure 112. Octant $v'^2$ contribution difference between free-stream and wall-collateral co-ordinates. x/L=0.7722, $\phi$=105°-130°.

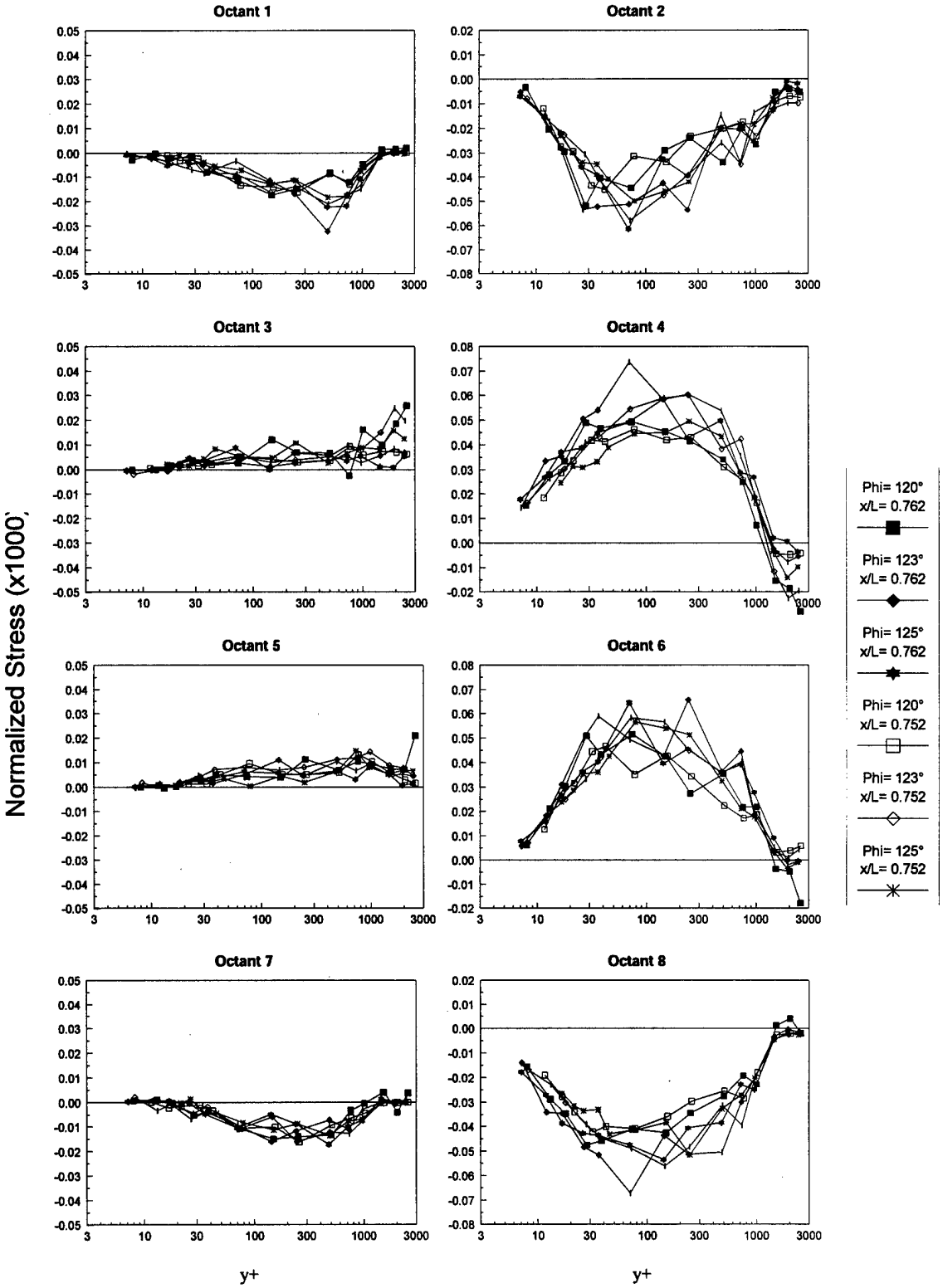


Figure 113. Octant $v'^2$ contribution difference between free-stream and wall-collateral co-ordinates. x/L=0.7622 & 0.7522, $\phi$=120°-125°.

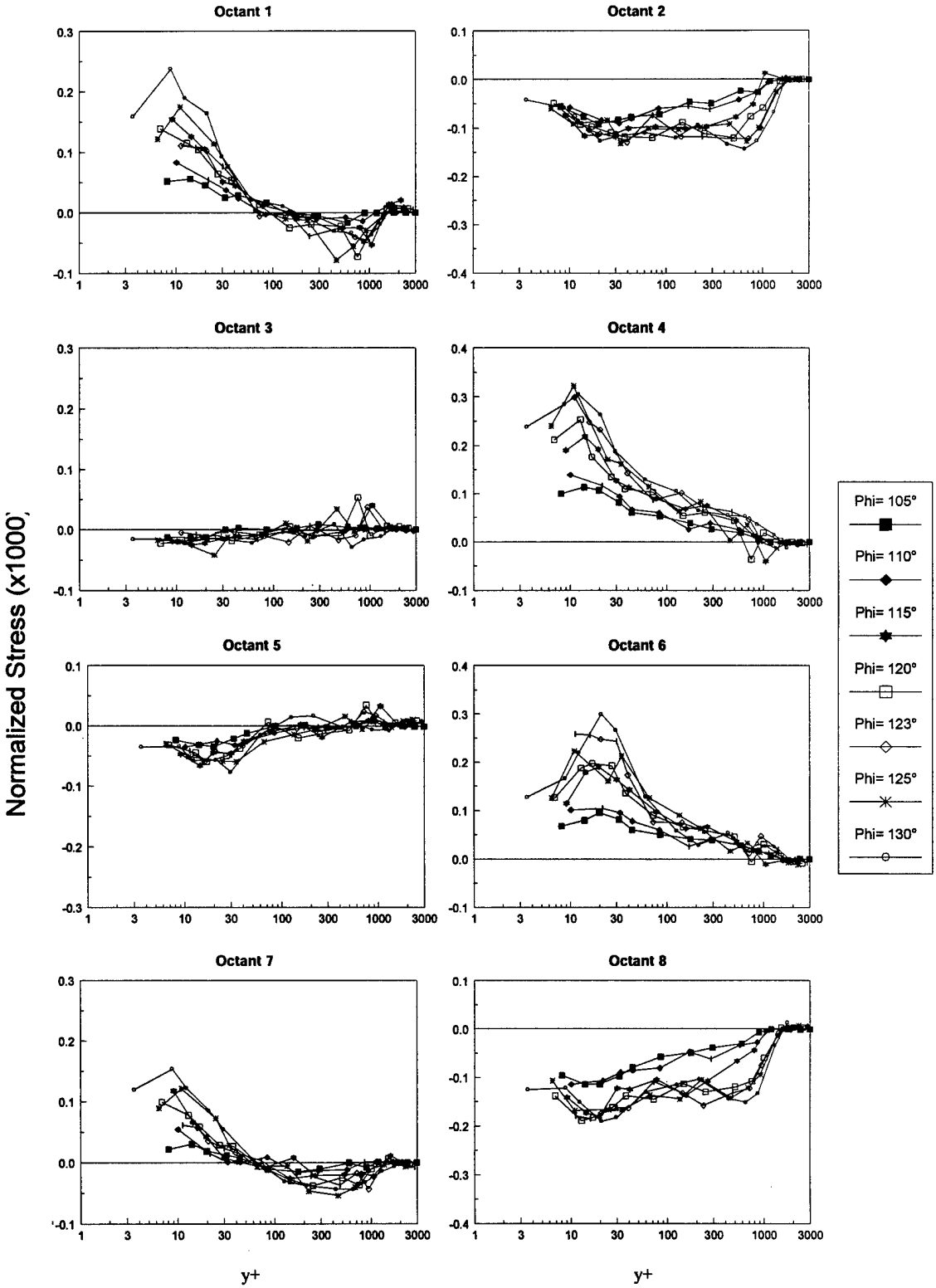


Figure 114. Octant $w'^2$ contribution difference between free-stream and wall-collateral co-ordinates. x/L=0.7722, $\phi$=105°-130°.

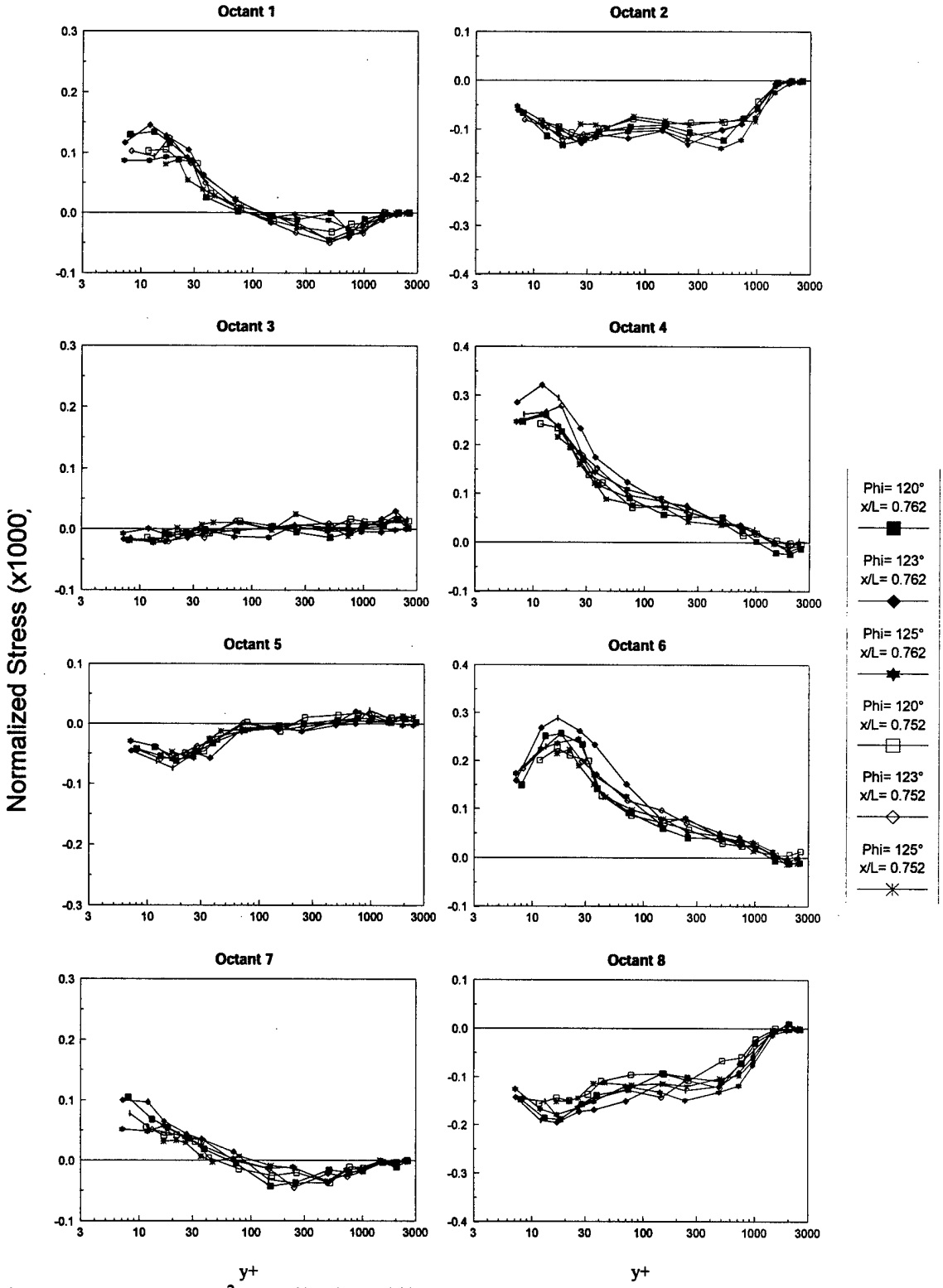


Figure 115. Octant $w'^2$ contribution difference between free-stream and wall-collateral co-ordinates. x/L=0.7622 & 0.7522, $\phi$=120°-125°.

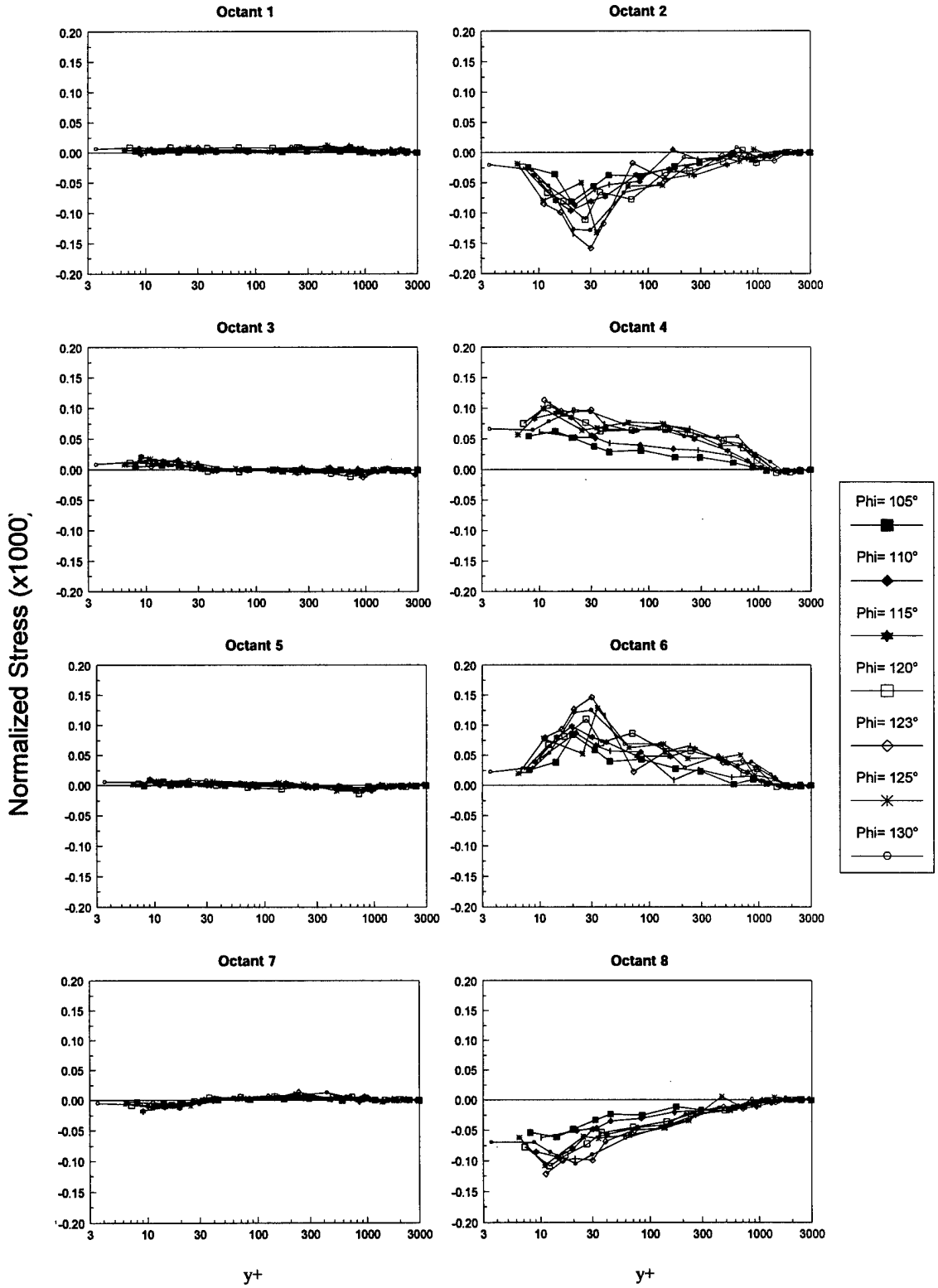


Figure 116. Octant u'v' contribution difference between free-stream and wall-collateral coordinates. x/L=0.7722, $\phi$=105°-130°.

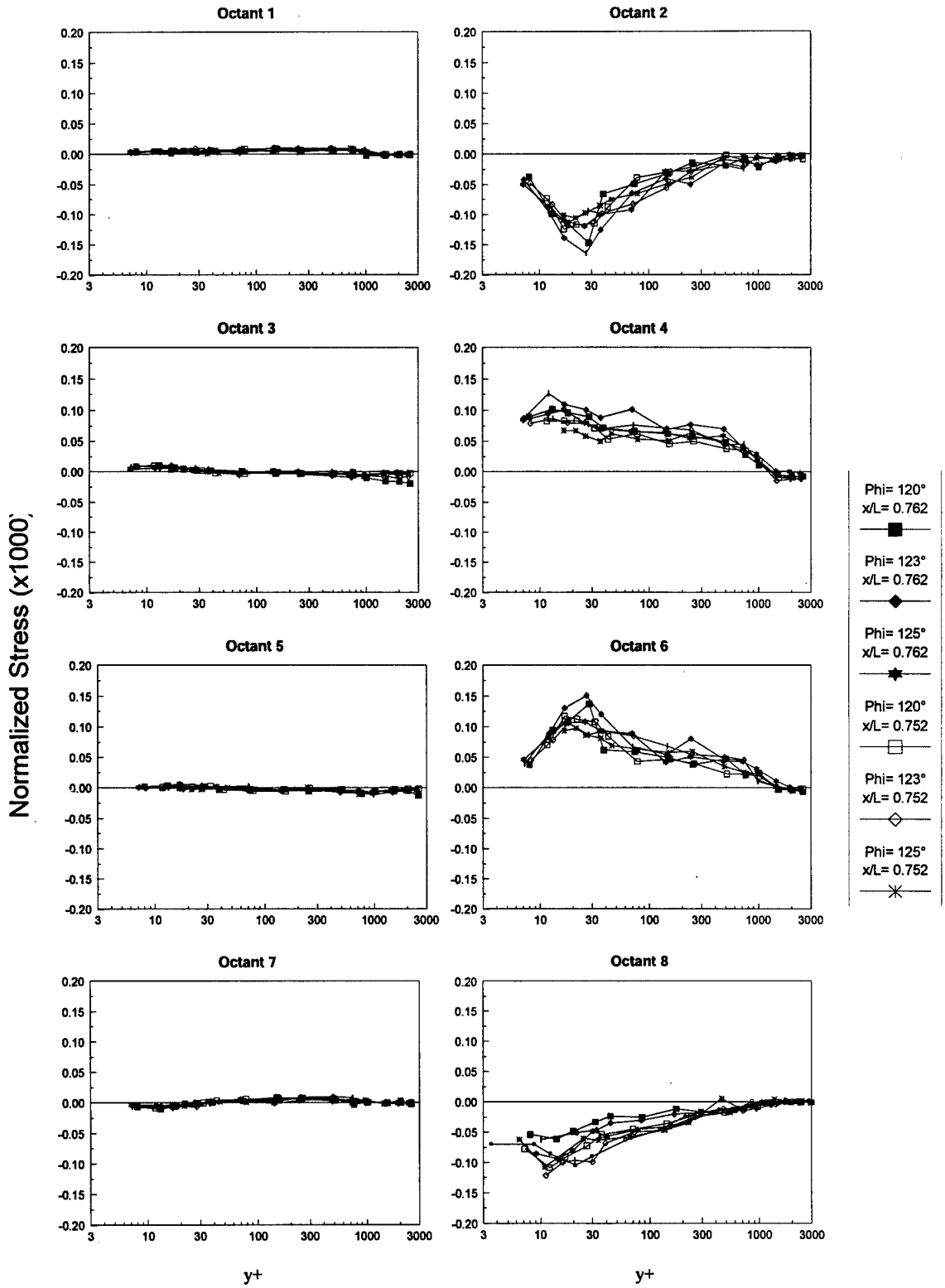


Figure 117. Octant u'v' contribution difference between free-stream and wall-collateral coordinates. x/L=0.7622 & 0.7522, $\phi$=120°-125°.

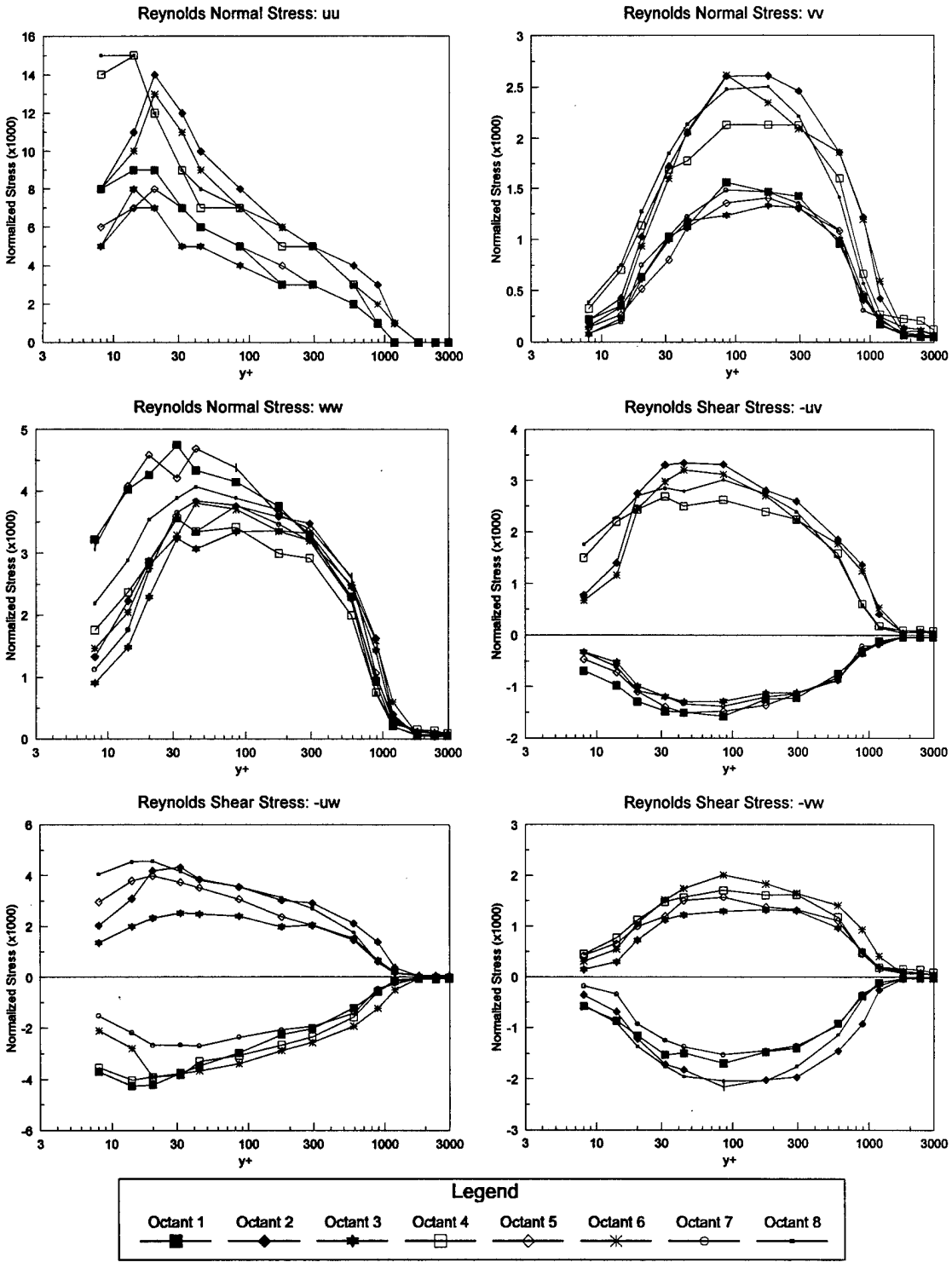


Note: All Stresses Normalized by $U_e^2$.

Figure 118. Octant Reynolds Stresses, x/L = 0.7722 & $\phi$ = 105°, Wall-collateral Coordinates.

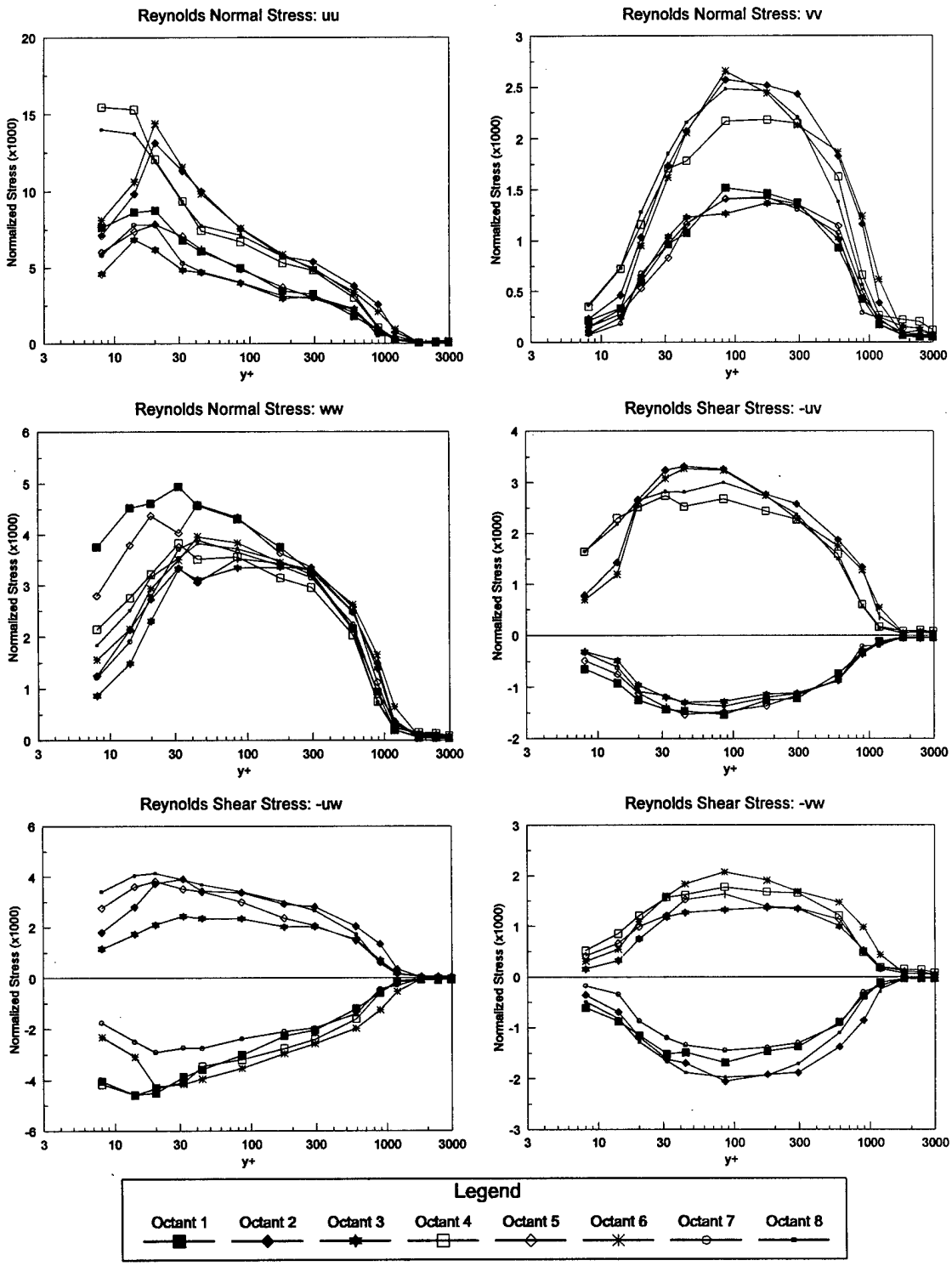


Note: All Stresses Normalized by $U_e^2$.

Figure 119. Octant Reynolds Stresses, x/L = 0.7722 & $\phi$ = 105°, Free-stream Coordinates.

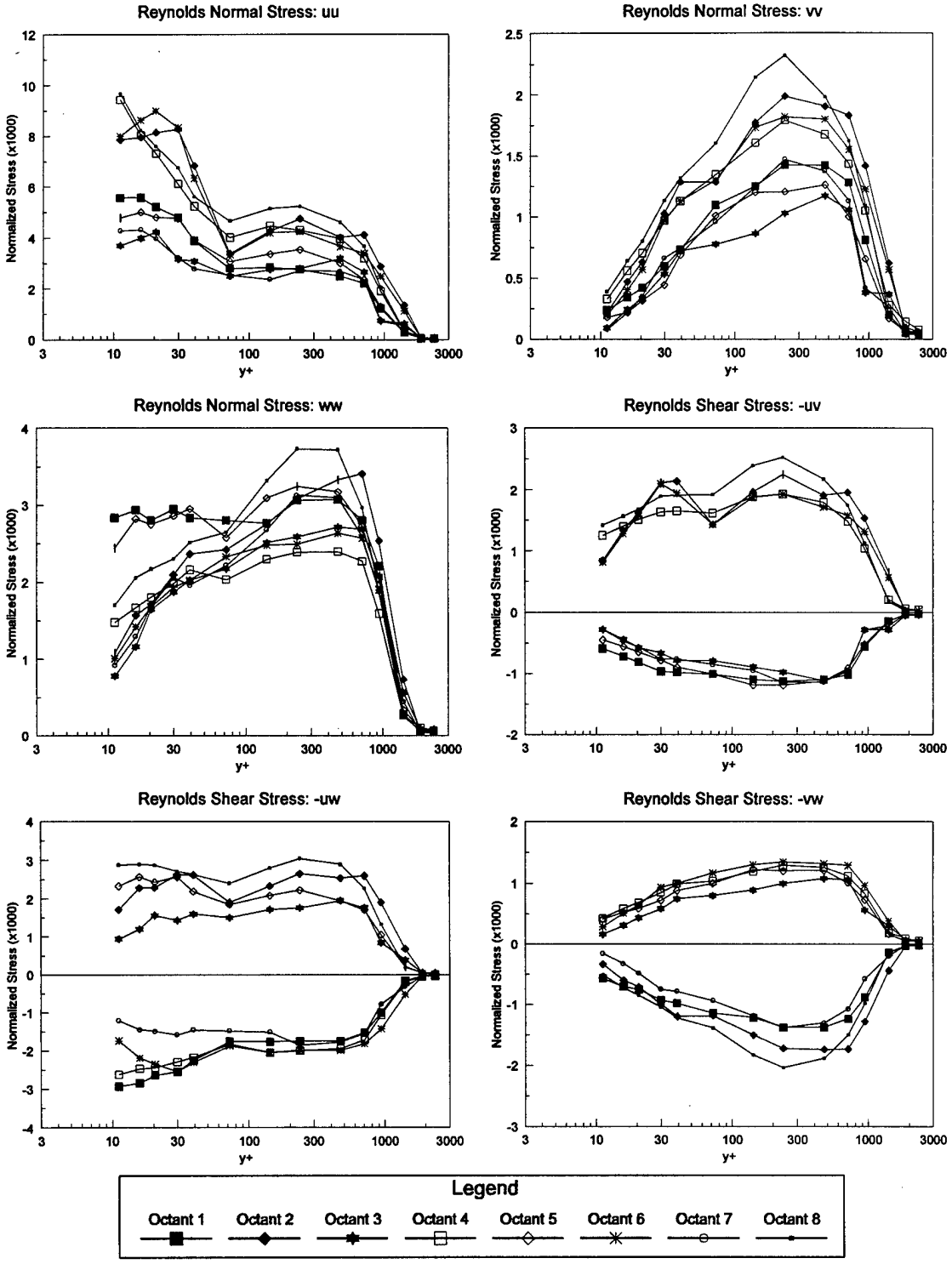


Note: All Stresses Normalized by $U_e^2$.

Figure 120. Octant Reynolds Stresses, x/L = 0.7722 & $\phi$ = 123°, Wall-collateral Coordinates.

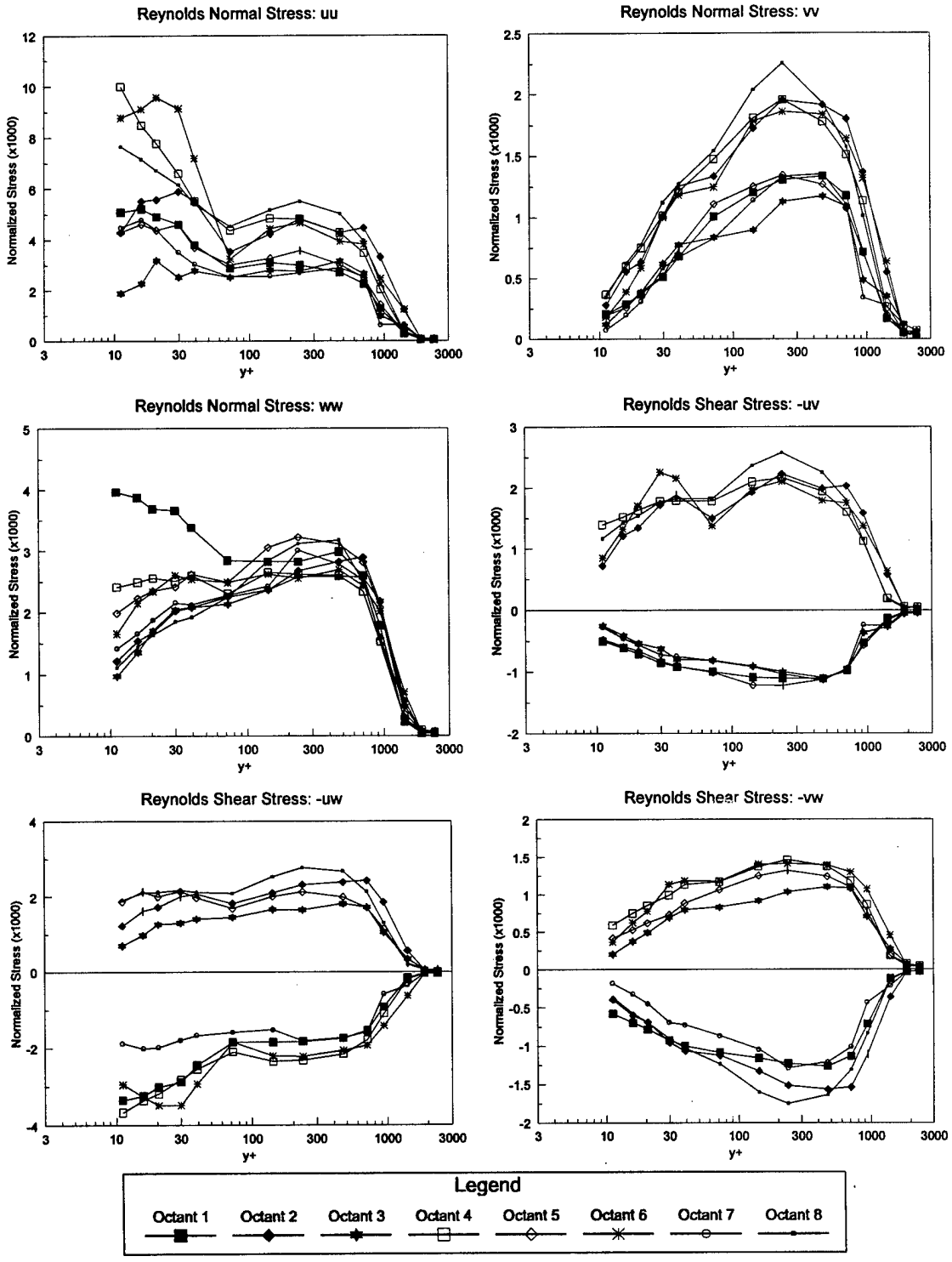


Note: All Stresses Normalized by $U_e^2$.

Figure 121. Octant Reynolds Stresses, x/L = 0.7722 & $\phi$ = 123°, Free-stream Coordinates.

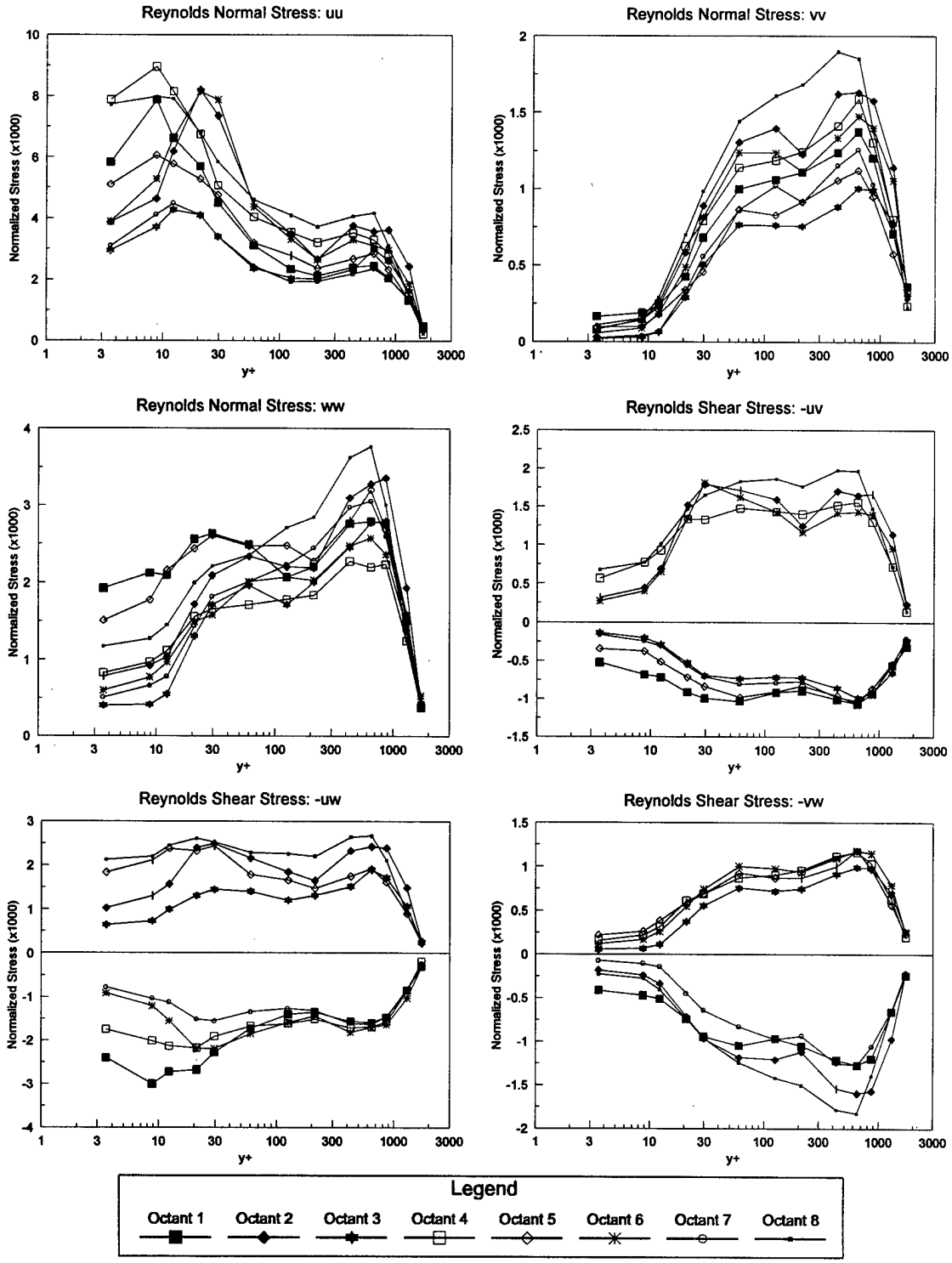


Note: All Stresses Normalized by $U_e^2$.

Figure 122. Octant Reynolds Stresses, x/L = 0.7722 & $\phi$ = 130°, Wall-collateral Coordinates.

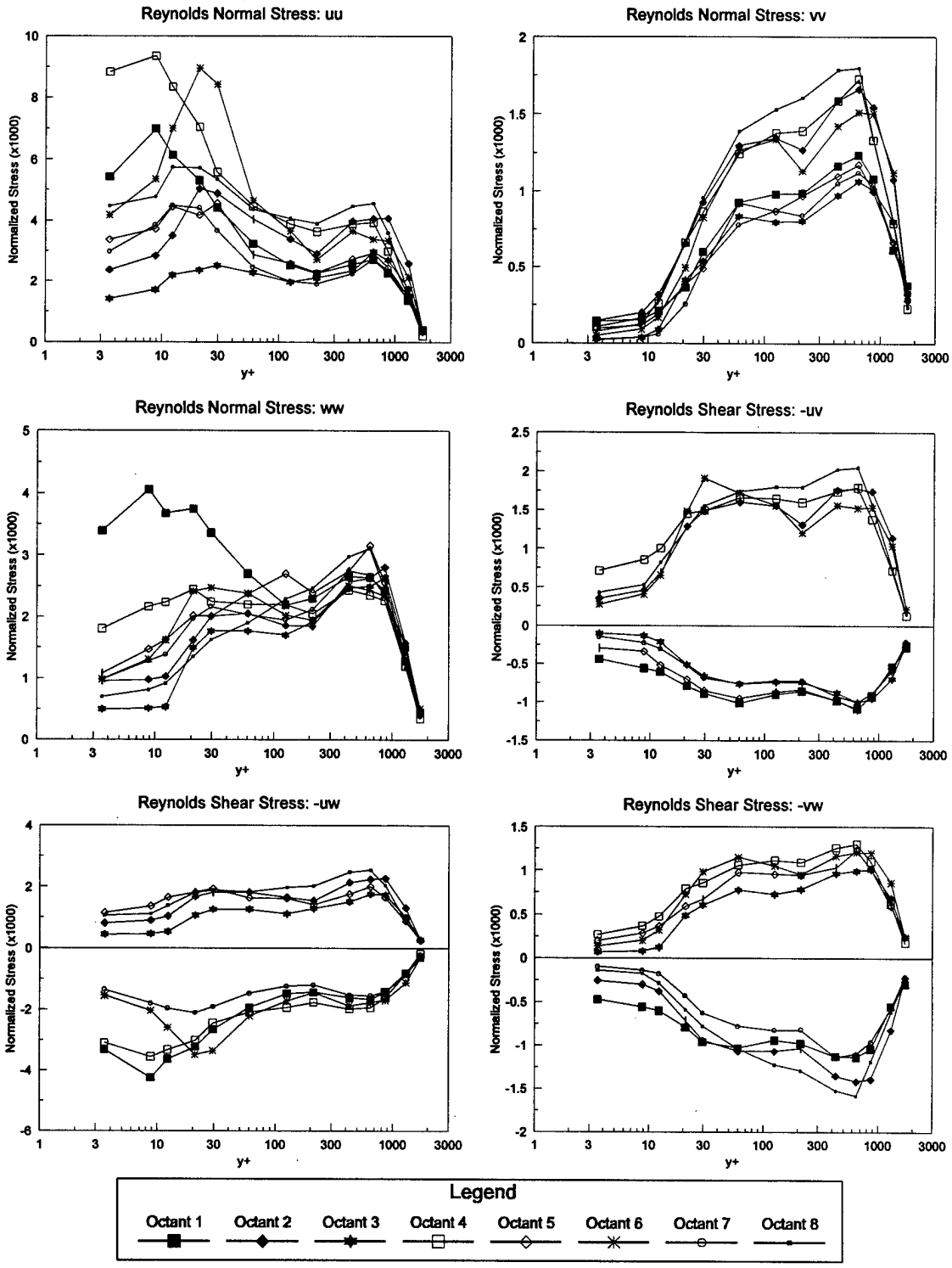


Note: All Stresses Normalized by $U_e^2$.

Figure 123. Octant Reynolds Stresses, x/L = 0.7722 & $\phi$ = 130°, Free-stream Coordinates.

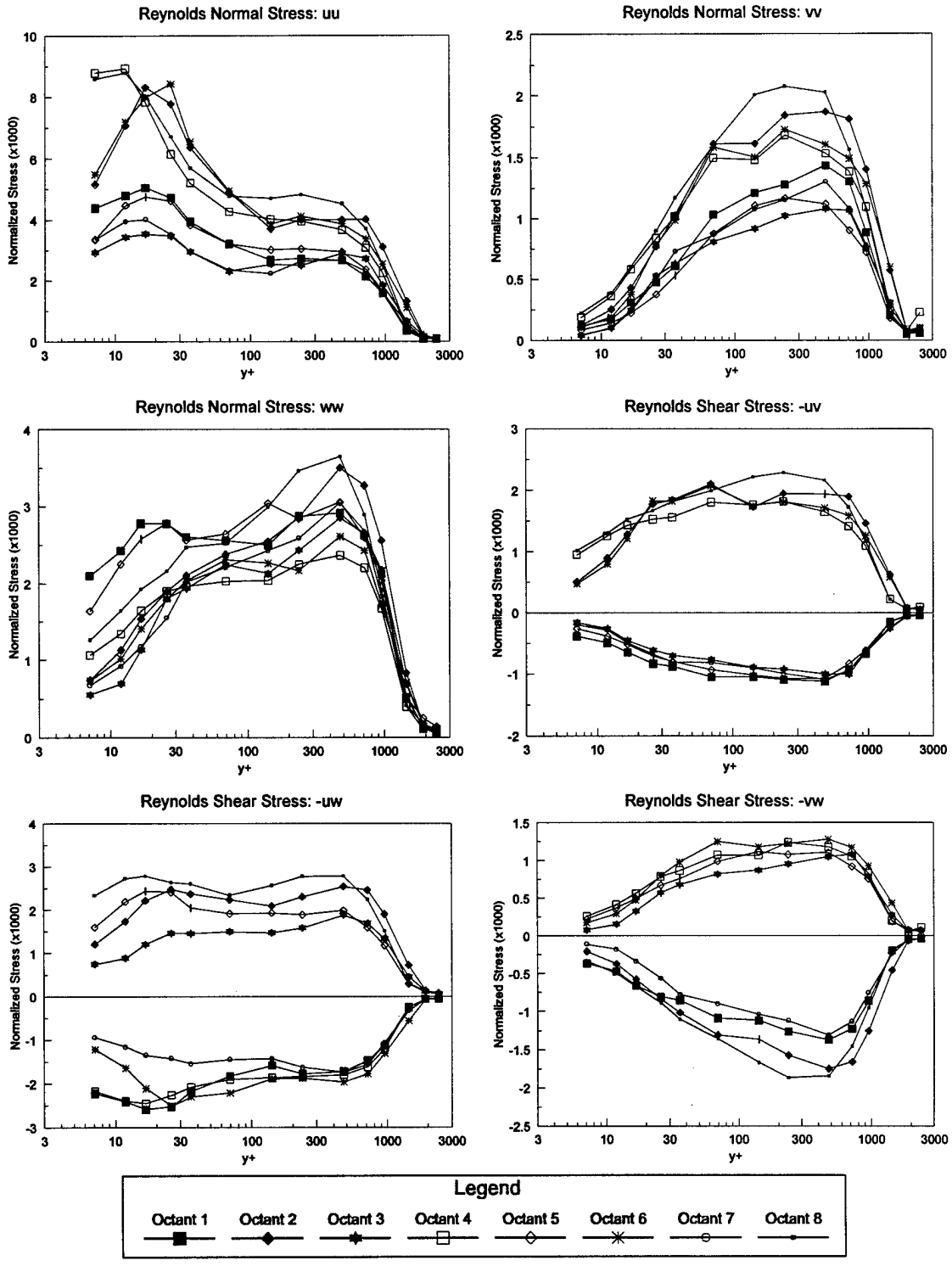


Note: All Stresses Normalized by $U_e^2$.

Figure 124. Octant Reynolds Stresses, x/L = 0.7622 & $\phi$ = 125°, Wall-collateral Coordinates.

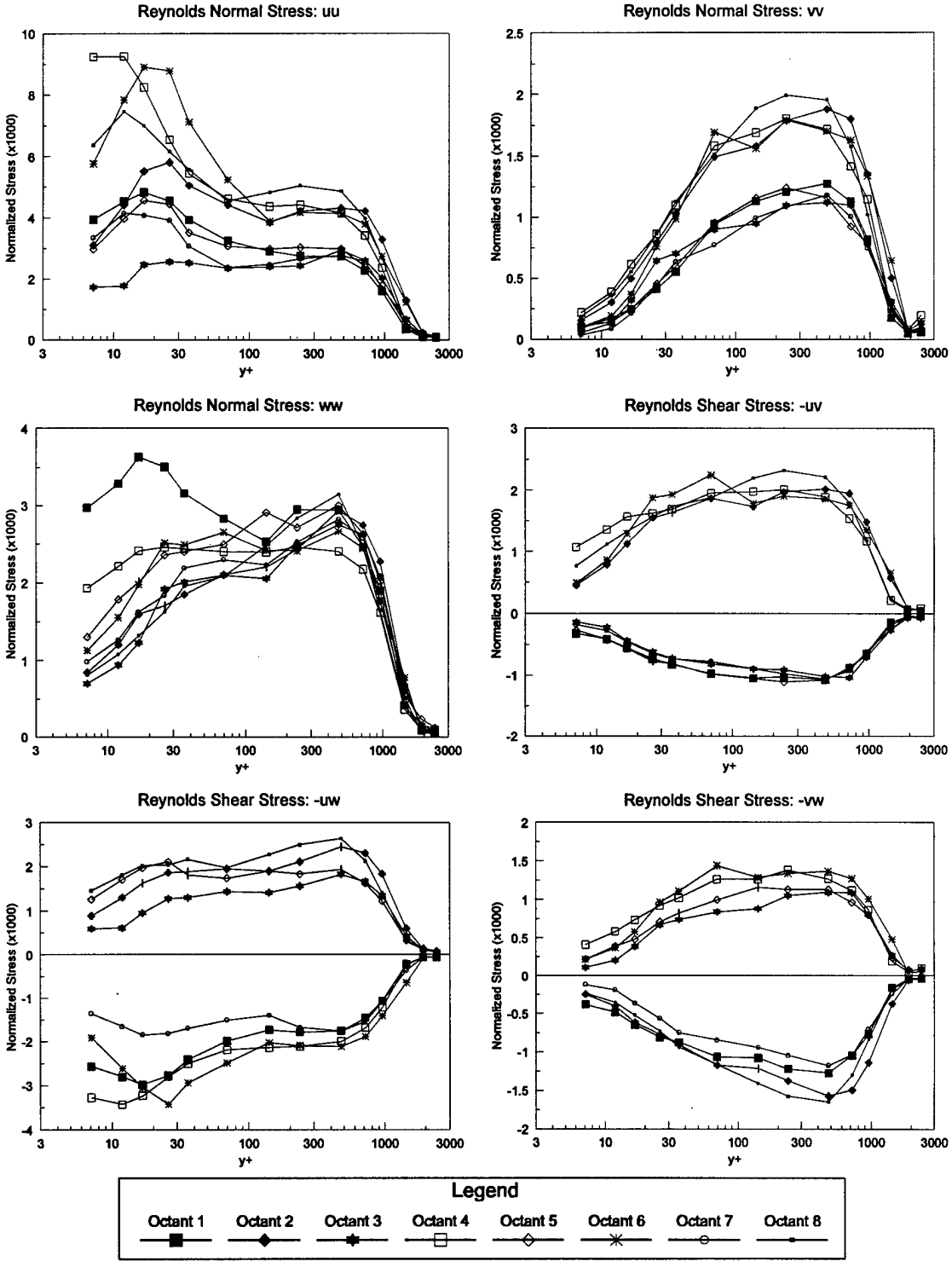


Note: All Stresses Normalized by $U_e^2$.

Figure 125. Octant Reynolds Stresses, x/L = 0.7622 & $\phi$ = 125°, Free-stream Coordinates.

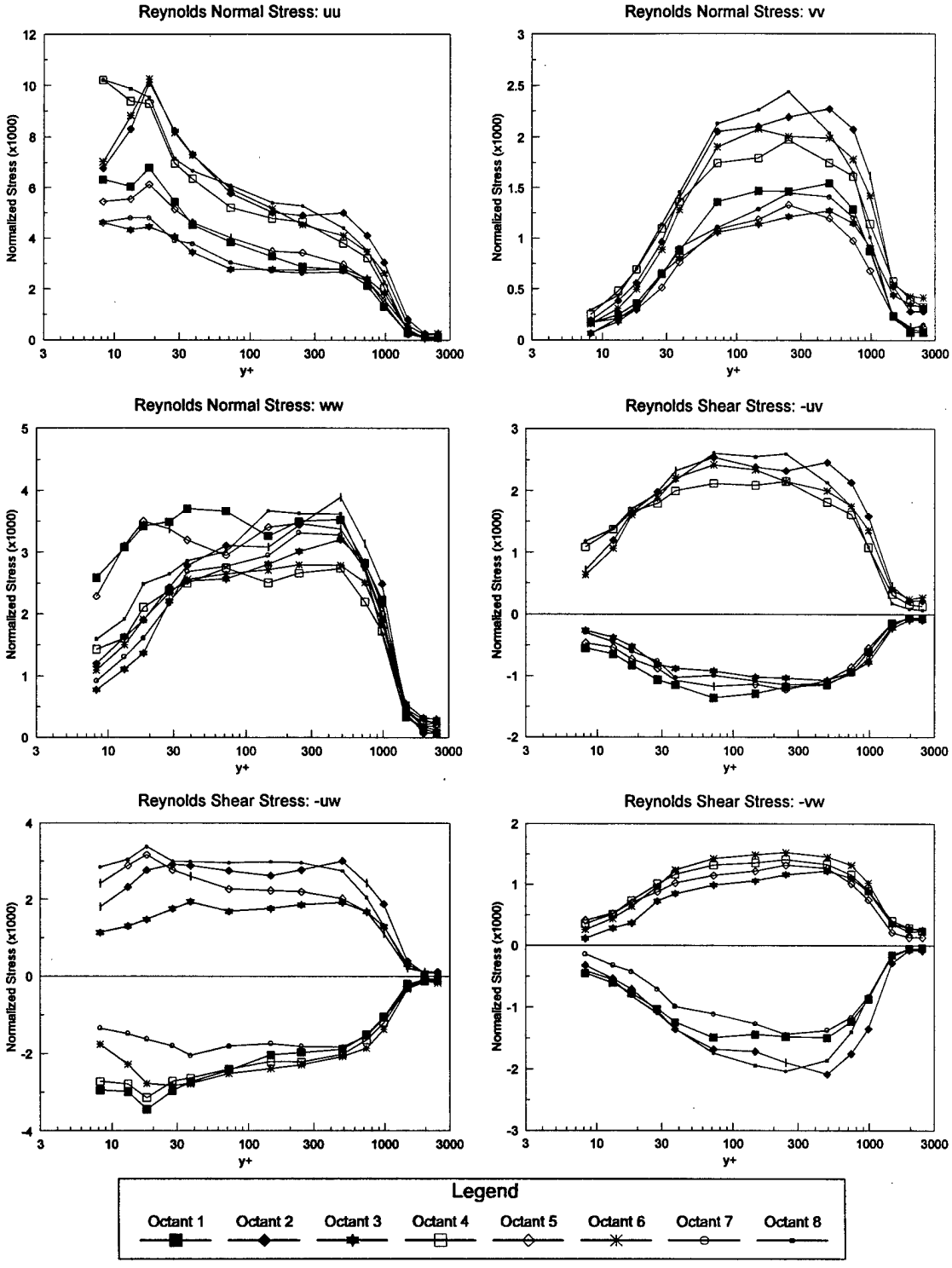


Note: All Stresses Normalized by $U_e^2$.

Figure 126. Octant Reynolds Stresses, x/L = 0.7522 & $\phi$ = 123°, Wall-collateral Coordinates.

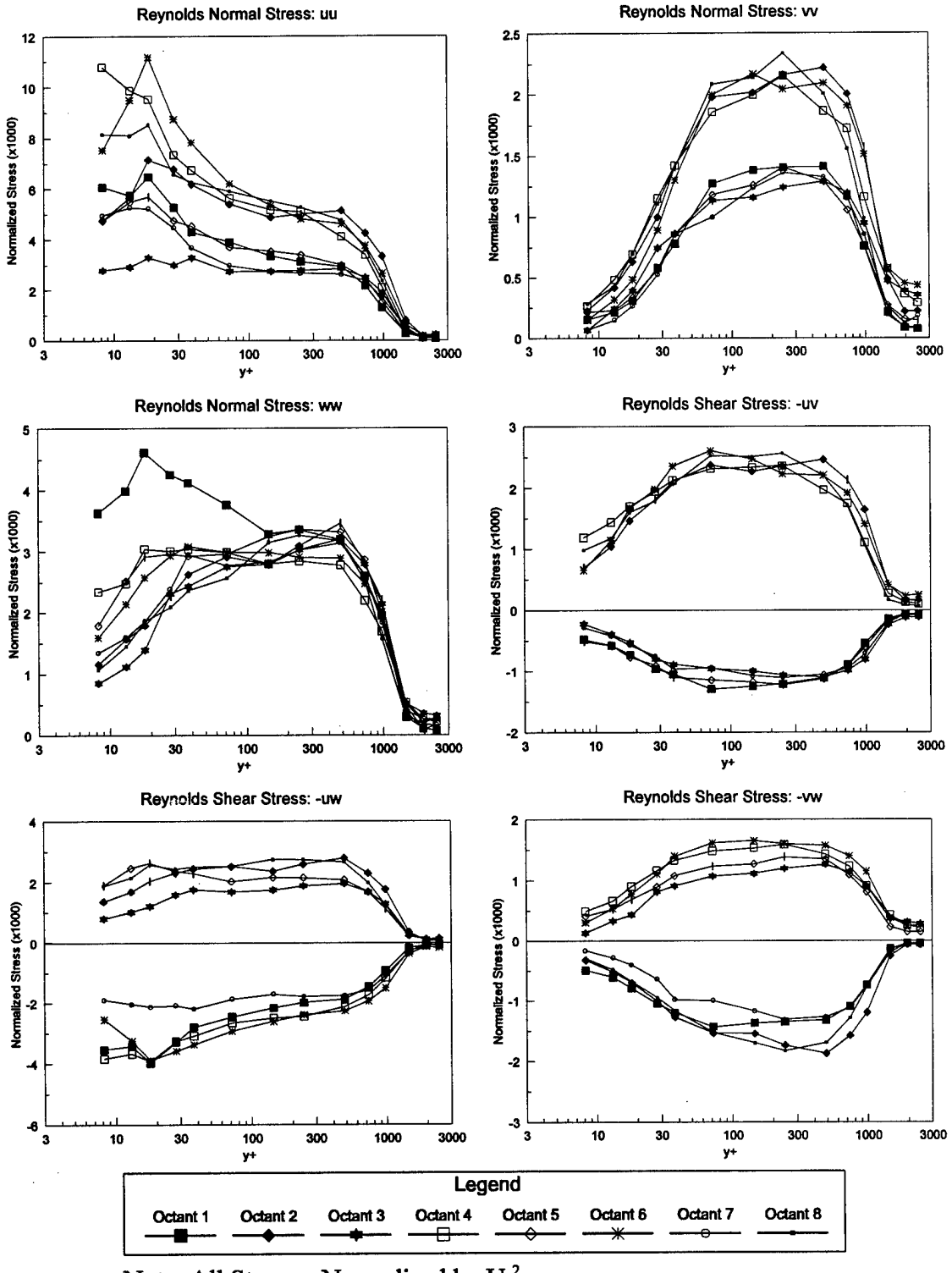


Note: All Stresses Normalized by $U_e^2$.

Figure 127. Octant Reynolds Stresses, x/L = 0.7522 & $\phi$ = 123°, Free-stream Coordinates.

# Appendix A: Data Reduction Methods

## A.1 Velocity Statistics

The LDV device provides coincident measurements of all three velocity over a short period of time. The coincident measurements simplify the process of extracting statistical quantities. Cross correlated statistics such as the Reynolds shear stresses (covariances) can be directly computed using discrete forms of their integral definitions. The formulas used follow:

**Mean**

$$\overline{U} = \frac{\int_0^\infty U(t)w(t)\,dt}{\int_0^\infty w(t)\,dt} \cong \frac{\sum_{i=1}^{N} U_i w_i^t}{\sum_{j=1}^{N} w_i^t} \tag{A.1}$$

w(t) is a weighting factor. In the discrete form, $w_i^t = w_i \times \Delta t$. See Section A.2 for a further discussion of the weighting factors.

**Variance (Reynolds Normal Stress)**

$$\overline{u'^2} = \frac{\int_0^\infty \left(U(t)-\overline{U}\right)^2 w(t)\,dt}{\int_0^\infty w(t)\,dt} \cong \frac{N}{N-1}\left(\frac{\sum_{i=1}^{N} U_i^2 w_i^t}{\sum_{j=1}^{N} w_i^t} - \overline{U}^2\right) \tag{A.2}$$

**Covariance (Reynolds Shear Stress)**

$$\overline{u'v'} = \frac{\int_0^\infty \left(U(t)-\overline{U}\right)\left(V(t)-\overline{V}\right) w(t)\,dt}{\int_0^\infty w(t)\,dt} \cong \frac{N}{N-1}\left(\frac{\sum_{i=1}^{N} U_i V_i w_i^t}{\sum_{j=1}^{N} w_i^t} - \overline{U}\,\overline{V}\right) \tag{A.3}$$

**Third Order Moment**

$$\overline{u'^3} = \frac{\int_0^\infty \left(U(t)-\overline{U}\right)^3 w(t)\;dt}{\int_0^\infty w(t)\;dt} \cong \frac{N}{N-1}\left(\frac{\sum_{i=1}^{N} U_i^3 w_i^t}{\sum_{j=1}^{N} w_i^t} - \overline{U}^3\right) - 3\,\overline{U}\left(\overline{u'^2}\right) \tag{A.4}$$

**Triple Products**

$$\overline{u'^2 v'} = \frac{\int_0^\infty \left(U(t)-\overline{U}\right)^2 \left(V(t)-\overline{V}\right) w(t)\, dt}{\int_0^\infty w(t)\, dt}$$

$$\cong \frac{N}{N-1}\left(\frac{\sum_{i=1}^{N} U_i^2 V_i w_i^t}{\sum_{j=1}^{N} w_i^t} - \overline{U}^2\overline{V}\right) - 2\overline{U}\left(\overline{u'v'}\right) - \overline{V}\left(\overline{u'^2}\right) \qquad \text{(A.5)}$$

## A.2 Velocity Bias

The discrete forms of the time-averaged velocity statistics given in the previous section show that a $\Delta t$ is required for each measurement. Naturally, $\Delta t$ should be the length of registered velocity's existence. However, LDV systems detect a signal only when the particle flies through the measurement volume. The signal lasts no longer than the time the particle is in the volume. The life span of a signal is infinitesimal compared to the total time of the experiment. Plotting the signals versus time reveals a discontinuous function of short realizations widely spaced apart. Thus, $\Delta t$ is approximately constant for all measurements and drops from the equations.

The problem with treating each measurement equally in time is that it does not resemble physical reality. When the flow moves quickly, many particles enter the measurement volume in a short period. As the flow slows down, fewer particles enter the measurement volume during an equal period. The velocities of the faster particles are short-lived compared to the velocities of the slower particles. Equal treatment of all measurements will skew the velocity statistics in favor of the faster velocities. This is the velocity bias problem; McLaughlin and Tiederman (1973) first conceptualized it.

Solving the problem requires a method for weighting each measurement. The weighting schemes must approximate the physics of the flow and have units of time. (This is the reason for using the notation $w_i^t$ in the previous section.) Two methods were examined: time between data (TBD) and McLaughlin-Tiederman (a.k.a. transit time).

TBD assumes that the time intervals between each realization reflect the lifetimes of the measured velocities (DeOtte, Morrison, and Wiedner, 1992). Each measurement is weighted by the time that has elapsed since the previous measurement. TBD works best when the data rate is high; a definite correlation exists between the measured velocities and the time between realizations (Fuchs, Albrecht, Nobach, Tropea, and Graham, 1992). However, as one approaches the model surface, the seed density drops considerably. The data rate decreases and fluctuates. The entrance of a particle into the measurement volume becomes a random event. The relationship

between the measured velocity and the time between realizations breaks down (Fuchs, et. al., 1992).

The McLaughlin-Tiederman scheme weights each measurement by the reciprocal of the magnitude of the velocity vector. The assumption here is that the measured velocities live long enough to span some common length, presumably the diameter of the measurement volume (d). The time that the seed particle would take to cross this length (i.e., d/|V|) better represents the life span of the measured velocity. Since the length is a constant among all realizations, it will drop out of the equations for the velocity statistics. The significant quantity left is the reciprocal of the magnitude of the velocity vector. This method requires correlated velocity component measurements for optimum performance. (These experiments meet that criterion.) It is potentially less accurate than TBD for high data rate events (DeOtte, et. al., 1992). However, it does not depend on the data rate. Thus, it holds for the entire height of the boundary layer.

A plot (Figure 67) of the three averages (ensemble, TBD, and McLaughlin-Tiederman) displays the behavior discussed above and is consistent with the results presented by Fuchs, et. al. (1992). The TBD average deviates little from the ensemble average, which has bias near the wall. The data rate in these experiments is too low ($\prec$ 100 measurements/sec.) for successful application of TBD. The TBD method has no corrective effect for data taken. It was not used in the final data processing. The McLaughlin-Tiederman average consistently differs from the ensemble average throughout the boundary layer. It demonstrates a correction over the physically-flawed ensemble average. Thus, this weighting scheme was used for the final data reduction.

## A.3 Gradient Broadening

The purpose of this experiment is to obtain time-averaged velocity statistics for a set of points within the boundary layer. However, the LDV system records velocity events within the measurement volume, not a point. The flow velocity at one edge of the volume may differ from the flow velocity at the opposite edge. A velocity gradient then exists within the measurement volume. The problem of obtaining velocity statistics at a point from a series of measurements obtained from a small volume is termed gradient broadening or spatial bias.

Durst, Martinuzzi, Sender, and Thevin (1992) analyzed the problem. The statistics containing the spatial bias represent spatially averaged quantities of the measurement volume. (These are the statistics computed using the LDV system output and the discrete equations in Section A.1.) The relationships that define spatial-averaging mirror the equations for time-averaging. For the mean, it is (Durst, et. al., 1992):

$$\langle \overline{U} \rangle = \frac{\int_{y_c-d/2}^{y_c+d/2} U(y)f(y)\,dy}{\int_{y_c-d/2}^{y_c+d/2} f(y)\,dy} \cong \frac{1}{d}\int_{y_c-d/2}^{y_c+d/2} U(y)f(y)\,dy \qquad \text{(A.6)}$$

($Y_c$ is the radial location of the center of the measurement volume.) The weighting function, f(y),

accounts for the distribution of light intensity within the measurement volume. (This assumes that the probability of particle detection is directly proportional to the intensity of the back scattered light.) Durst, et. al., suggest the following probability function,

$$f(y) = \frac{4}{\sqrt{2\pi}} e^{-2\frac{(y-y_c)^2}{d^2}} \tag{A.7}$$

which integrates to one. The integrand of the spatial average is expanded into a Taylor series about the center of the measurement volume (Durst, et. al., 1992).

$$\langle \overline{U} \rangle = \frac{1}{d} \int_{y_c-\frac{d}{2}}^{y_c+\frac{d}{2}} \left( \overline{U}(y_c) + (y-y_c) \left( \frac{d\overline{U}(y)}{dy} \right)_{y_c} + \frac{(y-y_c)}{2} \left( \frac{d^2\overline{U}(y)}{dy^2} \right)_{y_c} \right) f(y)\, dy \tag{A.8}$$

The Taylor series is then integrated (Durst, et. al., 1992).

$$\langle \overline{U} \rangle = \overline{U}_{y_c} + \frac{d^2}{32} \left( \frac{d^2\overline{U}}{dy^2} \right)_{y_c} \tag{A.9}$$

The first term on the right side is the unbiased mean at the point, $y_c$; the equation can easily be re-arranged to deliver a function for the corrected mean. Equations for the remaining statistics are:

$$\overline{u'^2}_{y_c} = \langle \overline{u'^2} \rangle - \frac{d^2}{16} \left( \frac{d\overline{U}}{dy} \right)^2_{y_c} - \frac{d^2}{32} \left( \frac{d^2\overline{u'^2}}{dy^2} \right)_{y_c} \tag{A.10}$$

$$\overline{u'v'}_{y_c} = \langle \overline{u'v'} \rangle - \frac{d^2}{16} \left( \frac{d\overline{U}}{dy} \frac{d\overline{V}}{dy} \right)_{y_c} - \frac{d^2}{32} \left( \frac{d^2\overline{u'v'}}{dy^2} \right)_{y_c} \tag{A.11}$$

$$\overline{u'^3}_{y_c} = \langle \overline{u'^3} \rangle - \frac{3d^2}{16} \left( \frac{d\overline{u'^2}}{dy} \frac{d\overline{U}}{dy} \right)_{y_c} - \frac{d^2}{32} \left( \frac{d^2\overline{u'^3}}{dy^2} \right)_{y_c} \tag{A.12}$$

$$\overline{u'^2v'}_{y_c} = \langle \overline{u'^2v'} \rangle - \frac{d^2}{16} \left( \frac{d\overline{u'^2}}{dy} \frac{d\overline{V}}{dy} \right)_{y_c} - \frac{d^2}{8} \left( \frac{d\overline{u'v'}}{dy} \frac{d\overline{U}}{dy} \right)_{y_c} - \frac{d^2}{32} \left( \frac{d^2\overline{u'^2v'}}{dy^2} \right)_{y_c} \tag{A.13}$$

The size of the correction depends on the magnitude of the derivatives of the velocity statistics; Section A.6 details the derivatives and their influence on the gradient broadening correction.

## A.4 Normalizing Velocity

The gradient broadening corrections require derivatives of the statistical quantities. The methods for getting these derivatives and other important flow properties (like the skin friction coefficient) require mean velocity vectors at multiple points along the profile. Yet, the tunnel conditions at each point are different. A unifying factor must be found. All points do have one flow property in common. The Reynolds number (with respect to the model length) was held constant. This allows a few liberties. This work assumes that the ratio of the flow speed at the edge of the profile to the upstream tunnel flow speed is constant. Given the tunnel flow speeds, a "profile edge" velocity can be computed for each point. Whenever multiple points are used in a calculation, the profile edge velocity, $U_e$, normalizes the velocity vector. (Note: For x/L= 0.7722 and $\phi$= 123°,

the speed of the point just below the top of the profile was used instead. The speed recorded for the top point was 20% larger than the three below it. Using the second point produced better results in those properties that required multiple points in their solution.)

## A.5 Coordinate Transformation Of Velocity Statistics

All coordinate systems used in this paper are invariant with respect to time. And, each measurement consists of three correlated, orthogonal velocity components. Therefore, the transformation of the velocity statistics into different coordinate systems becomes straightforward (although it evolves into complexity). Direction cosine matrices are the preferred method of applying transformations.

$$\begin{Bmatrix} x_1 \\ x_2 \\ x_3 \end{Bmatrix}_A = \begin{bmatrix} l_{11} & l_{12} & l_{13} \\ l_{21} & l_{22} & l_{23} \\ l_{31} & l_{32} & l_{33} \end{bmatrix} \begin{Bmatrix} x_1 \\ x_2 \\ x_3 \end{Bmatrix}_B \tag{A.14}$$

First, the transformation is applied to the velocity vector. Then each velocity component in the integrand of the equations in section A.1 is replaced by the equation for the transformed component. The integral is then expanded and broken into smaller integrals that share a common product of direction cosines. The direction cosines are then moved outside the integrals and integration is performed. The result is a set of algebraic equations containing only direction cosines and velocity statistics. For example,

$$\overline{U}_A = \frac{\int_0^\infty U_A(t)w(t)\,dt}{\int_0^\infty w(t)\,dt} = \frac{\int_0^\infty (l_{11}U_B(t) + l_{12}V_B(t) + l_{13}W_B(t))w(t)\,dt}{\int_0^\infty w(t)\,dt}$$

$$= l_{11}\frac{\int_0^\infty U_B(t)w(t)\,dt}{\int_0^\infty w(t)\,dt} + l_{12}\frac{\int_0^\infty V_B(t)w(t)\,dt}{\int_0^\infty w(t)\,dt} + l_{13}\frac{\int_0^\infty W_B(t)w(t)\,dt}{\int_0^\infty w(t)\,dt}$$

$$= l_{11}\overline{U}_B + l_{12}\overline{V}_B + l_{13}\overline{W}_B \tag{A.15}$$

The remaining equations follow (one example for each statistic):

$$\overline{u'^2}_A = l_{11}^2\overline{u'^2}_B + l_{12}^2\overline{v'^2}_B + l_{13}^2\overline{w'^2}_B + 2\left(l_{11}l_{12}\overline{u'v'}_B + l_{11}l_{13}\overline{u'w'}_B + l_{12}l_{13}\overline{v'w'}_B\right) \tag{A.16}$$

$$\begin{aligned}\overline{u'v'}_A = {} & l_{11}l_{21}\overline{u'^2}_B + l_{12}l_{22}\overline{v'^2}_B + l_{13}l_{23}\overline{w'^2}_B + \\ & \overline{u'v'}_B(l_{11}l_{22} + l_{12}l_{21}) + \overline{u'w'}_B(l_{11}l_{23} + l_{13}l_{21}) + \\ & \overline{u'v'}_B(l_{11}l_{22} + l_{12}l_{21}) + \overline{u'w'}_B(l_{11}l_{23} + l_{13}l_{21}) + \\ & \overline{v'w'}_B(l_{12}l_{23} + l_{B}l_{21})\end{aligned} \tag{A.17}$$

$$\overline{u'^3}_A = l_{11}^3\overline{u'^3}_B + l_{12}^3\overline{v'^3}_B + l_{13}^3\overline{w'^3}_B + 6\,l_{11}l_{12}l_{13}\overline{u'v'w'}_B +$$

$$3(l_{11}^2 l_{12}\overline{u'^2 v'}_B + l_{11}^2 l_{13}\overline{u'^2 w'}_B + l_{12}^2 l_{11}\overline{v'^2 u'}_B + l_{12}^2 l_{13}\overline{v'^2 w'}_B + l_{13}^2 l_{11}\overline{w'^2 u'}_B + l_{13}^2 l_{12}\overline{w'^2 v'}_B) \quad \text{(A.18)}$$

$$\begin{aligned}\overline{u'^2 v'}_A = {} & l_{11}^2 l_{21}\overline{u'^3}_B + l_{12}^2 l_{22}\overline{v'^3}_B + l_{13}^2 l_{23}\overline{w'^3}_B + \\ & \overline{u'^2 v'}_B\left(l_{11}^2 l_{22} + 2 l_{11} l_{12} l_{21}\right) + \overline{u'^2 w'}_B\left(l_{11}^2 l_{23} + 2 l_{11} l_{13} l_{21}\right) + \\ & \overline{v'^2 u'}_B\left(l_{12}^2 l_{21} + 2 l_{11} l_{12} l_{22}\right) + \overline{v'^2 w'}_B\left(l_{12}^2 l_{23} + 2 l_{12} l_{13} l_{22}\right) + \\ & \overline{w'^2 u'}_B\left(l_{13}^2 l_{21} + 2 l_{11} l_{13} l_{23}\right) + \overline{w'^2 v'}_B\left(l_{13}^2 l_{22} + 2 l_{12} l_{13} l_{23}\right) + \\ & 2\,\overline{u' v' w'}_B(l_{11} l_{12} l_{23} + l_{11} l_{22} l_{13} + l_{21} l_{12} l_{13})\end{aligned} \quad \text{(A.19)}$$

From these examples, the remaining equations can be found using the following rules. The subscripts 1, 2, and 3 refer to the velocities u, v, and w respectively. The first subscript of the direction cosine refers to the statistic on the left side of the equation. The second subscript refers to the statistic being multiplied by the product of direction cosines multiplies. For example, in the last three terms of equation A.19, the first subscript of the direction cosine products is a combination of two ones and one two because the term on the left hand side of the equation is $u'^2v'$; the second subscripts of the direction cosine products are a combination of one, two, and three because they are multiplied to the statistic u'v'w'.

## A.6 Obtaining Derivatives Of Flow Quantities

The gradient broadening corrections require first and second order derivatives of the statistical quantities. Also, the formulas of many derived quantities, such as the anisotropy constant or eddy viscosities, contain radial gradients of the mean flow and of the Reynolds stresses. Numerical methods are used to estimate these derivatives from discrete data. The classic (and simplest) algorithm is the finite difference method; it forms the baseline by which other methods are judged. The central difference equations for three points with uneven spacing are:

$$f_1' = \frac{\left((y_1 - y_0)^2 (f_2 - f_1) - (y_2 - y_1)^2 (f_1 - f_0)\right)}{(y_2 - y_0)(y_1 - y_0)(y_2 - y_1)} \quad \text{(A.20)}$$

$$f_1'' = \frac{2((y_1 - y_0) f_2 - (y_2 - y_0) f_1 + (y_2 - y_1) f_0)}{(y_2 - y_0)(y_1 - y_0)(y_2 - y_1)} \quad \text{(A.21)}$$

These equations exhibit the limitation common to all the algorithms evaluated here. The spacing between the points used in obtaining the derivatives must reflect the change in the flow field. If the spacing becomes too large, then the numerical scheme computes derivatives that reflect a function other than the one that physically describes the flow (but which will pass through the data points).

For the bulk of each profile, the derivative at a point was computed by applying a least squares fit of a quadratic function to itself and its four immediate neighbors. The first and second order

derivatives of the 'middle' point are assigned the values of the differentiated quadratic equation. This solution produces a smooth profile of derivatives. The uncertainty of the data has a smaller impact on this scheme than it does on a finite difference method which may deliver a "wavy" derivative profile.

The quadratic fit cannot be used on the first two or last two points of a profile because they do not have four surrounding neighbors. The last two points, usually outside the turbulent boundary layer, do not attract the same importance as the first two points closest to the wall. For these points, only two alternate schemes were examined. The first modified the original scheme. Instead of fitting the curve to five points, the curve was fit to what was available (i.e., four and three points respectively). For example, the derivatives of the last point would be derived from the last point and the two neighbors below it (three points). The other method tested, a three point backward difference scheme, occasionally exhibited erratic behavior with the derivatives of containing V (or v'). (See the top two points of Method 5 on Figures 75-77; these use the finite difference scheme. The other methods use the least squares fit). The modified least squares scheme remained smooth, and it kept the programming simple by utilizing existing code. Therefore, it was used in the final data reduction.

The first two points have the promise of providing insight into the near wall mechanics that affect the flow. The derivatives here are large and can affect the values of the statistical quantities through the gradient broadening correction. Precision must be maintained. Therefore, a wider range of methods for extracting derivatives was examined. One possible advantage that the bottom of the profile has over the top is the emergence of a "free" data point, the wall. All statistical quantities become zero at the wall. However, using the wall as an extra data point could introduce greater error. First, the location of the wall is not precisely known. A curve fit of the Spalding continuous wall law does yield a refinement of the walls initial placement but there is no certainty that this process produces a more accurate result (see Section A.7). Second, the distance between the wall and the first point may be too large; rapid change occurs close to the wall. Three of the schemes described below use the wall in creating their derivatives.

The algorithms tested can be placed into three broad categories: quadratic curve fits, finite difference schemes, and Taylor series extrapolations. To simplify the discussion, the radial position of the wall and the first four points of the profile will be referred to as $r_0$ through $r_4$. Figures 75-77 display the results of using the various schemes at $\phi = 123°$ and $x/L = 0.7622$. (Note that these methods are only used to predict the derivatives for the bottom two points; the quadratic fit is used elsewhere except for the top two points of the method 5 curves. A backward difference scheme is used here.) On these plots, Methods 1 and 2 employ the quadratic curve fits. Method 1 makes use of the wall; Method 2 does not. Thus, Method one fits five ($r_0$-$r_4$) and four ($r_0$-$r_3$) points to the quadratic curve to gain the derivatives at $r_2$ and $r_1$ respectively. Method 2 fits four ($r_1$-$r_4$) and three ($r_1$-$r_3$) points. Method 5 uses a central difference scheme; this includes the wall in the solution at the bottom point.

The Taylor series extrapolation uses a combination of Taylor series expansions and finite difference equations to predict the next derivative. Every continuous, differentiable function can be represented by a Taylor series:

$$f_1 = f_0 + \sum_{i=1}^{\infty} \frac{\partial^i f}{\partial x^i}_{x=0} \frac{(x_1 - x_0)^i}{n!} \tag{A.21}$$

Taking the derivatives of the Taylor series, one gets the following relationships (expanded to fourth order):

$$f_0' = f_1' + f_1''(x_0 - x_1) + \frac{1}{2} f_1'''(x_0 - x_1)^2 + \frac{1}{6} f_1^{(iv)}(x_0 - x_1)^3 \tag{A.22}$$

$$f_0'' = f_1'' + f_1'''(x_0 - x_1) + \frac{1}{2} f_1^{(iv)}(x_0 - x_1)^2 \tag{A.23}$$

Obtaining the first and second order derivatives at $x_0$ requires the third and fourth order derivatives at $x_1$. A three point forward difference method, using the first and second order derivatives at $x_1$, $x_2$, and $x_3$ can estimate these higher order terms.

For the data reduction, only the derivatives of the bottom point are predicted in this way. Using this algorithm for two consecutive points only compounds the error. The derivatives of the second point from the wall are determined by the same least squares fits used in either methods 1 or 2. The Taylor series extrapolation coupled with method 2 is referred to as method 4 in the graphs. Method 3 is the Taylor prediction scheme that utilizes method 1.

The graphs (Figures 75-77) show that these numerical methods do not agree on the value of the derivatives nearest the wall. The distance between points may be too large to properly construct derivatives here. Validating this conclusion would require testing each method against itself using a set of more closely spaced points. Unfortunately, this need was not foreseen; a profile with a higher density of points near the wall was not taken. The methods that use the wall as a data point predict much larger derivatives than their counterparts which use only measured points. The wall must be too distant from the initial measured point to be helpful; the large uncertainty in its actual position (section A.5 & A.7) makes its use unwise.

In every plot, at least one pair of methods agree closely. Method 4 frequently belongs to these pairs and exhibits the smoothest behavior. Therefore, this method was chosen for the final data reduction. One encouraging sign is the agreement between the central difference scheme (method 5) and the four point quadratic fit (Methods 2 & 4) on most of the gradients at $r_2$. However, the general lack of agreement on the derivatives decreases confidence in the values of derived flow quantities near the wall that incorporate gradients. The gradients at $r_2$ are reasonably correct; the second order derivatives and all derivatives at $r_1$ are unreliable.

The most disturbing effect of derivative uncertainty is the gradient broadening correction of the velocity statistics; the error of the velocity statistics could worsen considerably. The correction was applied to the velocity statistics of one profile ($\phi$= 123°, x/L= 0.7622) using the derivatives gathered from the different methods describe earlier. Figures 78 and 79 display the results for the

means and Reynolds stress. The small diameter of the measurement volume, 55μm, kept the correction tiny for these velocity statistics. Thus, the means and Reynolds stresses show an immunity to the difference between the derivative calculations. The triple products, on the other hand, exhibited discernible changes near the wall and, thus, lose reliability. (These results are not shown because this paper does not examine the triple products.)

Next, the gradient broadening correction for all the profiles was examined using method 4. Table B-1 shows the correction for the bottom point where derivative uncertainty is high. Table B-2 shows the correction for the third profile point (the last able to use the quadratic fit with five data points). The correction for the means and Reynolds stresses at the third point remain within the uncertainty of those statistical quantities with a few exceptions (See Appendix C). Also, these corrections remain within the same order of magnitude across all profiles. In comparison with the corrections at the third point, the majority of the corrections do not appear unreasonable. But, a few are clearly incorrect.

**Table A-1: Percentage Change Performed By Gradient Broadening At The Bottom Point Of The Profile**

| Position | U | V | W | u'u' | v'v' | w'w' | u'v' | u'w' | v'w' |
|---|---|---|---|---|---|---|---|---|---|
| 105a | 0.35% | -1.06% | 0.30% | -7.15% | -0.50% | -0.71% | -1.00% | 8.34% | -0.76% |
| 110a | 0.30% | 23.03% | 0.30% | -4.35% | 0.79% | -0.15% | -1.65% | 6.08% | -1.16% |
| 115a | 0.26% | -3.10% | -0.57% | -4.46% | -2.15% | 0.39% | 0.31% | 4.65% | -1.00% |
| 120a | 0.06% | 25.63% | -4.46% | -2.45% | -4.08% | -0.04% | 2.55% | -51.11% | -0.48% |
| 123a | 0.29% | 3.69% | 0.74% | -3.69% | -0.03% | 0.28% | 0.40% | 9.17% | -0.88% |
| 125a | 0.32% | 143.50% | 0.15% | -5.89% | -7.44% | 0.12% | 11.03% | 5.18% | -1.81% |
| 130a | -0.49% | 1.21% | -0.67% | -0.41% | -6.05% | -0.94% | 3.83% | -0.94% | -0.09% |
| 120b | 0.52% | -50.26% | 3.21% | -7.13% | -0.20% | 0.69% | 1.14% | 38.21% | -0.22% |
| 123b | 0.57% | -5.50% | 3.42% | -8.27% | -0.72% | 0.85% | 0.51% | 21.30% | -2.87% |
| 125b | 0.15% | 2.90% | 0.39% | -3.69% | -1.31% | 0.04% | -0.26% | 5.95% | -3.71% |
| 120c | 0.29% | 4.80% | 0.66% | -3.81% | 0.10% | 0.37% | -0.59% | 8.23% | 0.09% |
| 123c | 0.09% | 14.64% | -3.60% | -2.31% | -0.55% | 0.36% | -2.65% | 63.48% | -0.29% |
| 125c | 0.10% | 0.56% | -0.00% | -1.21% | 0.21% | 0.12% | -0.06% | 4.96% | 2.72% |

** The numbers in 'Position' give the ϕ location. The letter indicates x/L (a= 0.80, b= 0.79, c=0.78).

| Table A-2: Percentage Change Performed By Gradient Broadening At The Third Point Of The Profile | | | | | | | | | |
|---|---|---|---|---|---|---|---|---|---|
| Position | U | V | W | u'u' | v'v' | w'w' | u'v' | u'w' | v'w' |
| 105a | 0.13% | 0.06% | 0.11% | -1.88% | 0.24% | -0.11% | -0.19% | 2.58% | -0.25% |
| 110a | 0.04% | -0.18% | 0.03% | -0.92% | 0.08% | -0.03% | -0.07% | 1.52% | -0.06% |
| 115a | 0.13% | 0.43% | 0.21% | -1.79% | 0.25% | 0.08% | -0.37% | 3.23% | -0.26% |
| 120a | 0.09% | 0.10% | -0.42% | -1.57% | 0.12% | 0.14% | -0.38% | 1.07% | -0.04% |
| 123a | 0.08% | 0.55% | 0.18% | -1.03% | 0.13% | 0.09% | -0.24% | -2.23% | 0.01% |
| 125a | 0.05% | 0.04% | 0.07% | -1.36% | 0.08% | 0.06% | -0.22% | -3.95% | -0.00% |
| 130a | 0.05% | -0.14% | 0.09% | -1.48% | -0.33% | -0.02% | -0.39% | 1.73% | 0.64% |
| 120b | 0.10% | -1.11% | -0.15% | -1.69% | 0.08% | 0.07% | -0.33% | 3.09% | -0.05% |
| 123b | 0.14% | 0.87% | 0.21% | -1.80% | 0.14% | 0.17% | -0.27% | 3.36% | 0.14% |
| 125b | 0.11% | -8.23% | 0.18% | -1.46% | 0.13% | 0.15% | -0.31% | 4.92% | 0.09% |
| 120c | 0.08% | 2.09% | -0.07% | -1.06% | 0.14% | 0.04% | -0.26% | 1.93% | -0.20% |
| 123c | 0.09% | 0.16% | -0.19% | -1.26% | 0.03% | 0.12% | -0.10% | 1.97% | 0.18% |
| 125c | 0.04% | -0.10% | 0.04% | -0.56% | 0.10% | 0.06% | -0.07% | -0.13% | -0.14% |
| ** The numbers in 'Position' give the $\phi$ location. The letter indicates x/L (a= 0.80, b= 0.79, c=0.78). | | | | | | | | | |

Judging from the graphs and the tables, the gradient broadening corrections for the bottom point maintains only an order of magnitude accuracy. These corrections also occasionally balloon in size. The overall effect increases the uncertainty of velocity statistics near the wall to approximately the size of the correction. For the means and Reynolds stresses, the added uncertainty remains the same size as the statistical uncertainty or smaller. However, the triple products lose all practical value. All of this emphasizes the need to obtain a greater density of points near the wall. Any future work must include such a profile. This profile can validate or reject the methods presented here. Otherwise, the problem of derivative uncertainty near the wall will persist.

## A.7 Skin Friction Coefficient And Wall Location Refinement

The following relation defines the skin friction, $\vec{\tau}$ ,and skin friction coefficient, $C_f$ (Shetz, 1992):

$$\vec{\tau} = \mu \left( \frac{\partial \vec{V}}{\partial y} \right)_w \qquad C_f = \frac{\left| \vec{\tau} \right|}{\frac{1}{2} \rho U_e^2} \qquad \text{(A.24, 25)}$$

The viscosity, $\mu$, and the density, $\rho$, are assumed equal to their free-stream values. This leaves the velocity gradient at the wall as the only unknown. The previous section demonstrated that obtaining velocity gradients near the wall was wrought with uncertainty. Direct calculation of the

velocity gradient at the wall is not possible. Instead, assumptions will be made about the laws which govern the flow.

The LDV device has allowed flow measurements very close to the model surface. In the near wall region, the flow angle turns very slowly (see Figures 49 & 50). A coordinate system can be defined where the local flow becomes nearly two dimensional in the mean. It is called the wall collateral coordinate system and is explained in Appendix A.2.5. In this system, relationships developed for the 2D turbulent boundary layer may still hold some value. Two formulas present themselves as candidates which may be used to derive the skin friction coefficient. The first, eqn. A.26, represents the reduction of the Navier-Stokes equation in the laminar sublayer, $y^+ < 7\text{-}10$.

$$u^+ = y^+ - A(y^+)^4 \qquad \text{(A.26)}$$

$$u^+ \equiv \sqrt{\frac{2}{C_f}}\frac{U}{U_e} \quad y^+ \equiv \sqrt{\frac{C_f}{2}}\frac{yU_e}{\nu} \qquad \text{(A.27,28)}$$

The Spalding Continuous Wall law, eqn A.30, is the second; it is valid from the wall to the log region in 2D flows, $\sim 7\text{-}10 < y^+ < \sim 100$.

$$y^+ = u^+ + \frac{1}{E}\left[ e^{ku^+} - 1 - ku^+ - \frac{(ku^+)^2}{2!} - \frac{(ku^+)^3}{3!} \right] \qquad \text{(A.29)}$$

Equation A.26 contains only two unknowns, A and $C_f$. (The kinematic viscosity, $\nu$, is assumed to be constant throughout the boundary layer.) A least squares fit of this equation using the first few points of the profile can estimate the skin friction coefficient. As mentioned in section 3.1, the error of the wall's position is a good percentage of the radial positions of the first few points. Section 5.2 discusses evidence that human error during the wall-position calibration has increased this uncertainty. This uncertainty jeopardize the accuracy of the least squares fit. By introducing another unknown, $\Delta y$, the position of the wall becomes another quantity to solve (i.e., $y = r + \Delta y$, where r is the 'calibrated' radial position. For the first point of the profile, r = 0.01 cm.) This provides a theoretical refinement of the wall's position.

The same can be done with the Spalding continuous wall law. The formula can be rearranged so that the only unknowns are $C_f$, k, E, and $\Delta y$ (if refining the wall position is desired). This introduces more unknowns than equation A.26; this is undesirable since precious few points lie in the quasi-collateral region. However, Coles observed that, for a majority of 2D turbulent boundary layers, $u^+ = 16.23$ at $y^+ = 100$; this led to discovery of Coles constants, k= 0.41 and E= 5.0 (Stanford Conference, 1968). Use of Coles constants reduces the number of unknowns to two (one, if wall refinement is not used).

The least squares fit of eqn. A.26 needs two points; adding the wall position as an unknown requires three. The fit of the Spalding continuous wall law with Coles constants requires one fewer. Equation A.26 requires that all the points used in the fit lie within the viscous sublayer for accuracy; this is unlikely. The flow angles of the lowest points on the profile do turn slowly. Although the difference between flow angles does remain within error, these points likely lie in the

buffer region (7-10 < $y^+$ < 30-40) or the log layer (30-40 < $y^+$ < 100). The Spalding continuous wall law allows the points to lie within a much broader range. However, using Coles constants may impose an artificial constraint on the problem which contradicts the flow physics. Therefore, both equations were thoroughly tested.

The only tested variation on Eqn. A.26 assumed that the position of the wall was correct. Eqn. A.29 was examined with and without the wall as an unknown. Table B-3 displays the results. No direct skin friction measurements have been performed on the 6:1 prolate spheroid at the Reynolds number of this experiment (4.2E+06). However, skin friction of a 6:1 prolate spheroid has been measured at Göttingen with a Reynolds number of 7.7E+06 (Kreplin, Vollmers, and Meier, 1985). The skin friction coefficients derived from the curve fits were loosely compared to the Göttingen data. The skin friction coefficient values from eqn. A.26 are not unreasonable; but, they are low. $C_f$ grows increasingly smaller with the number of points fit to the curve. Using the Göttingen data to define $y^+$ would reveal that the bottom point of all profiles would not fall within $y^+$ of 10; the points lie outside the viscous sublayer. Thus, eqn. A.26 is being applied to a region where it is not valid; thus, it performs poorly. Since the form of eqn. A.26 which adds the wall position as an unknown requires an extra data point, examining it becomes a useless exercise.

The $C_f$ values derived from eqn. A.29 are close in value and behavior to the data from Göttingen. These values demonstrated little dependence on the number of points used in the curve fit beyond the third or fourth point. The differences fall within 6% of each other when no wall refinement is used. With wall refinement, the largest discrepancy jumps to 13% at x/L= 0.7522 & $\phi$= 125°. The wall refinement itself ($\Delta y$) heavily depends on the number of points used in the curve fit. Wall refinement suffers from the same problem as the methods for extracting derivatives. There are too few points near the wall; not enough points can be utilized to sufficiently suppress the influence of data uncertainty on the results. Nevertheless, the impact of the data shortage is not as devastating as it was for the derivatives. The wall refinement does level out for profiles that have four points within the wall collateral region and the buffer layer. A minimum of five points in the buffer layer should produce optimal results. Although none of the profiles meet this ideal, the resulting uncertainty in $\Delta y$ averages to $\pm$ 6 μm and could be as high as $\pm$18 μm (at x/L= 0.7522 & $\phi$= 125°). This is superior to the original uncertainty of the wall position.

Section five discusses the merits of using the Spalding continuous wall law. That analysis shows that the data appears to greatly benefit from inclusion of the wall refinement technique. The final data analysis incorporated this refinement. For the final data analysis, two criteria determined the number of points used in the final evaluation of the methods based on the Spalding relation. All points had to lie in the wall collateral region. The Johnston hodographs (Figures 43-44) became the visual tool for this determination. The points that rest to the left of maximum crossflow and lie along a line connecting the first and third point of the plot occupy the wall collateral region. The points also had to lie within $y^+$ < 40. This requirement is consistent with the work of Flack and Johnston (1993). They examined a pressure driven 3D turbulent boundary layer generated by a sharp edged step swept at 45°. They demonstrated that the Spalding continuous wall law (using

direct skin friction measurements) described the velocity profile to $y^+ < 30$ (the buffer region) and significantly deviated from the flow at $y^+ > 40$. A listing of the number of points is displayed in Table B-4 in Appendix A.11 which discusses the flow angle.

# TABLE D-3: Data Generated in Evaluation of Methods for Finding Cf

Cf-DLR: The skin friction coefficient obtained from linearly interpolating direct skin friction measurements performed at Göttingen. NOTE: This data was taken at 7.7E+6 Reynolds Number

Cf-1: Cf generated using u+= y+ - A y+**4

Cf-2: Cf estimated by Spalding continous law of the wall.

Cf-3: Same as Cf-3 except it includes wall refinement.

A: The constant in the equation u+= y+ - A y+**4

y1: The relative position of the wall to the assumed position as calculated by the method for obtaining Cf-3. This quantity has units of micrometers.

Numbers surrounded by asterisks represent the edge of the Quasi-Collateral region.

| x/L= 0.7722 |
|---|

| Phi= 105° Cf-DLR= 0.00290 | number of points used in LS fit | | | | |
|---|---|---|---|---|---|
| | 2 | 3 | *4* | 5 | 6 |
| Cf-1 | 0.00195 | 0.00178 | 0.00162 | 0.00145 | 0.00110 |
| Cf-2 | 0.00233 | 0.00260 | 0.00268 | 0.00268 | 0.00263 |
| Cf-3 | 0.00250 | 0.00289 | 0.00286 | 0.00277 | 0.00263 |
| A | 0.000067 | 0.000035 | 0.000019 | 0.000012 | 3.3E-06 |
| y1 | -14 | -34 | -32 | -25 | -2 |

| Phi= 110° Cf-DLR= 0.00259 | number of points used in LS fit | | | | |
|---|---|---|---|---|---|
| | 2 | *3* | 4 | 5 | 6 |
| Cf-1 | 0.00194 | 0.00160 | 0.00136 | 0.00102 | 0.00068 |
| Cf-2 | 0.00250 | 0.00250 | 0.00248 | 0.00243 | 0.00253 |
| Cf-3 | 0.00260 | 0.00255 | 0.00250 | 0.00240 | 0.00255 |
| A | 0.000042 | 0.000021 | 0.000013 | 3.6E-06 | 9.3E-07 |
| y1 | -15 | -11 | -5 | 16 | -38 |

| Phi= 115° Cf-DLR= 0.00232 | number of points used in LS fit | | | | |
|---|---|---|---|---|---|
| | 2 | *3* | 4 | 5 | 6 |
| Cf-1 | 0.00173 | 0.00167 | 0.00146 | 0.00131 | 0.00099 |
| Cf-2 | 0.00212 | 0.00214 | 0.00229 | 0.00225 | 0.00222 |
| Cf-3 | 0.00236 | 0.00225 | 0.00240 | 0.00231 | 0.00222 |
| A | 0.000064 | 0.000047 | 0.000022 | 0.000014 | 3.9E-06 |
| y1 | -21 | -14 | -27 | -18 | -2 |

| Phi= 120° Cf-DLR= 0.00206 | number of points used in LS fit | | | | |
|---|---|---|---|---|---|
| | 2 | 3 | *4* | 5 | 6 |
| Cf-1 | 0.00166 | 0.00142 | 0.00127 | 0.00115 | 0.00090 |
| Cf-2 | 0.00165 | 0.00184 | 0.00194 | 0.00198 | 0.00191 |
| Cf-3 | 0.00143 | 0.00203 | 0.00207 | 0.00207 | 0.00192 |
| A | 0.000106 | 0.000052 | 0.000025 | 0.000016 | 4.5E-06 |
| y1 | 35 | -29 | -32 | -32 | -5 |

| Phi= 123° Cf-DLR= 0.00191 | number of points used in LS fit | | | | |
|---|---|---|---|---|---|
| | 2 | 3 | 4 | *5* | 6 |
| Cf-1 | 0.00182 | 0.00168 | 0.00142 | 0.00122 | 0.00091 |
| Cf-2 | 0.00201 | 0.00194 | 0.00191 | 0.00187 | 0.00186 |
| Cf-3 | 0.00201 | 0.00186 | 0.00183 | 0.00183 | 0.00184 |
| A | 0.000086 | 0.000059 | 0.000028 | 0.000017 | 4.6E-06 |
| y1 | 0 | 15 | 20 | 19 | 14 |

| Phi= 125° Cf-DLR= 0.00178 | number of points used in LS fit | | | | |
|---|---|---|---|---|---|
| | 2 | 3 | *4* | 5 | 6 |
| Cf-1 | 0.00108 | 0.00114 | 0.00099 | 0.00076 | 0.00053 |
| Cf-2 | 0.00146 | 0.0016 | 0.00164 | 0.00171 | 0.00169 |
| Cf-3 | 0.00183 | 0.00169 | 0.00171 | 0.00175 | 0.00169 |
| A | -2.2E-05 | 0.000031 | 0.000018 | 5.3E-06 | 1.4E-06 |
| y1 | -38 | -29 | -30 | -41 | -16 |

| Phi= 130° Cf-DLR= 0.00154 | number of points used in LS fit | | | | |
|---|---|---|---|---|---|
| | 2 | 3 | 4 | *5* | 6 |
| Cf-1 | 0.00119 | 0.001 | 0.00088 | 0.00083 | 0.0007 |
| Cf-2 | 0.00105 | 0.00111 | 0.00133 | 0.00143 | 0.0015 |
| Cf-3 | 0.00078 | 0.00116 | 0.00149 | 0.00155 | 0.00155 |
| A | 0.000187 | 0.000091 | 0.000031 | 0.00002 | 6.0E-06 |
| y1 | 73 | -11 | -51 | -57 | -57 |

x/L= 0.7622

| Phi= 120° Cf-DLR= 0.00215 | number of points used in LS fit | | | | |
|---|---|---|---|---|---|
| | 2 | 3 | *4* | 5 | 6 |
| Cf-1 | 0.00154 | 0.00149 | 0.00134 | 0.00118 | 0.00093 |
| Cf-2 | 0.00186 | 0.00191 | 0.00198 | 0.00209 | 0.00203 |
| Cf-3 | 0.00207 | 0.00205 | 0.00205 | 0.00218 | 0.00203 |
| A | 0.000067 | 0.00005 | 0.000025 | 0.000015 | 4.3E-06 |
| y1 | -21 | -20 | -19 | -35 | -7 |

| Phi= 123° Cf-DLR= 0.00201 | number of points used in LS fit | | | | |
|---|---|---|---|---|---|
| | 2 | 3 | 4 | *5* | 6 |
| Cf-1 | 0.00135 | 0.00133 | 0.00123 | 0.00110 | 0.00086 |
| Cf-2 | 0.00164 | 0.00174 | 0.00181 | 0.00184 | 0.00186 |
| Cf-3 | 0.00187 | 0.00192 | 0.00191 | 0.00191 | 0.00187 |
| A | 0.000059 | 0.000049 | 0.000027 | 0.000016 | 4.7E-06 |
| y1 | -24 | -28 | -26 | -26 | -20 |

| Phi= 125° Cf-DLR= 0.00188 | number of points used in LS fit | | | | |
|---|---|---|---|---|---|
| | 2 | 3 | *4* | 5 | 6 |
| Cf-1 | 0.00152 | 0.00135 | 0.00120 | 0.00108 | 0.00084 |
| Cf-2 | 0.00156 | 0.00165 | 0.00175 | 0.00175 | 0.00172 |
| Cf-3 | 0.00147 | 0.00174 | 0.00184 | 0.00180 | 0.00174 |
| A | 0.000113 | 0.000059 | 0.000029 | 0.000017 | 4.9E-06 |
| y1 | 13 | -15 | -26 | -19 | -7 |

x/L= 0.7522

| Phi= 120° Cf-DLR= 0.00225 | number of points used in LS fit | | | | |
|---|---|---|---|---|---|
| | 2 | 3 | *4* | 5 | 6 |
| Cf-1 | 0.00198 | 0.00181 | 0.00153 | 0.00132 | 0.00098 |
| Cf-2 | 0.00225 | 0.00220 | 0.00216 | 0.00214 | 0.00207 |
| Cf-3 | 0.00225 | 0.00214 | 0.00210 | 0.00210 | 0.00201 |
| A | 0.000077 | 0.00005 | 0.000024 | 0.000015 | 4.1E-06 |
| y1 | 0 | 8 | 13 | 13 | 38 |

| Phi= 123° Cf-DLR= 0.00211 | number of points used in LS fit | | | | |
|---|---|---|---|---|---|
| | 2 | 3 | 4 | *5* | 6 |
| Cf-1 | 0.0017 | 0.00153 | 0.00131 | 0.00116 | 0.00089 |
| Cf-2 | 0.0018 | 0.0018 | 0.00189 | 0.00191 | 0.00187 |
| Cf-3 | 0.00171 | 0.00178 | 0.00196 | 0.00196 | 0.00187 |
| A | 0.000101 | 0.00006 | 0.000027 | 0.000016 | 4.6E-06 |
| y1 | 11 | 3 | -18 | -19 | -1 |

| Phi= 125° Cf-DLR= 0.00197 | number of points used in LS fit | | | | |
|---|---|---|---|---|---|
| | 2 | 3 | *4* | 5 | 6 |
| Cf-1 | 0.00229 | 0.00193 | 0.00157 | 0.00132 | 0.00095 |
| Cf-2 | 0.00233 | 0.00222 | 0.00209 | 0.00201 | 0.00187 |
| Cf-3 | 0.00171 | 0.00192 | 0.00184 | 0.00181 | 0.00177 |
| A | 0.000087 | 0.000052 | 0.000025 | 0.000015 | 4.3E-06 |
| y1 | 100 | 54 | 72 | 81 | 97 |

## A.8 The Boundary Layer Thickness

The boundary layer thickness, $\delta$, was determined using the classical relation, $U_\delta = 0.99\ U_e$ (Shetz, 1993). ($U_e$ is the profile edge velocity; See section A.4.) Since the $U_e$ is different for every profile point, the program searches for the point where $|V|/U_e < 0.99$, where $|V|$ is the magnitude of the mean velocity vector. A quadratic equation is fit to that point and the one above; then, it is solved for the position where $|V|/U_e = 0.99$. Figure 66 plots $\delta$.

## A.9 Displacement And Momentum Thicknesses

Two displacement and four momentum thicknesses exist for the 3D flow (Cooke and Hall, 1962):

$$\delta_1 = \int_0^\delta \left(1 - \frac{\overline{U}}{U_e}\right) dy \qquad \delta_2 = -\int_0^\delta \frac{\overline{W}}{U_e}\, dy \qquad \text{(A.30, 31)}$$

$$\theta_{11} = \int_0^\delta \left(1 - \frac{\overline{U}}{U_e}\right)\frac{\overline{U}}{U_e}\, dy \qquad \theta_{12} = \int_0^\delta \left(1 - \frac{\overline{U}}{U_e}\right)\frac{\overline{W}}{U_e}\, dy \qquad \text{(A.32, 33)}$$

$$\theta_{21} = -\int_0^\delta \frac{\overline{U}\,\overline{W}}{U_e^2}\, dy \qquad \theta_{22} = -\int_0^\delta \frac{\overline{W}^2}{U_e^2}\, dy \qquad \text{(A.34, 35)}$$

In the actual implementation, the integral is carried out to the data point, $\delta_p$, closest to but higher than $\delta$. The integral is evaluated using the trapezoidal rule in the free-stream coordinate system.

## A.10 Flow, Gradient, Stress, And Intensity Angles

The mean flow angle (eqn. A.36), the mean velocity gradient angle (eqn. A.37), the Reynolds shear stress angle (eqn. A.38), and intensity angle (eqn. A.39) were calculated in two axis systems, body surface coordinates (Section A.3.3) and free-stream coordinates (Section A.3.4).

$$\alpha_f = \arctan\left(\frac{\overline{W}}{\overline{U}}\right) \qquad \text{(A.36)}$$

$$\alpha_g = \arctan\left(\frac{\partial\overline{W}/\partial y}{\partial\overline{U}/\partial y}\right) \qquad \text{(A.37)}$$

$$\alpha_s = \arctan\left(\frac{\overline{v'w'}}{\overline{u'v'}}\right) \qquad \text{(A.38)}$$

$$\alpha_i = 0.5 \arctan\left(\frac{2\overline{u'w'}}{\overline{u'^2} - \overline{w'^2}}\right) \qquad \text{(A.39)}$$

Flow angles define the free-stream (Section A.3.4) and wall collateral coordinate systems (Section A.3.5). The uncertainty in $\alpha_f$ is approximately $\pm$ 0.4° for the range of values exhibited by the profiles. The flow angle, in free-stream coordinates, indicates the level of three dimensionality in the flow. The largest $\alpha_f$ encountered is about 20°; the flow experiences a moderate 3D effect. This explains the success of the Spalding continuous wall law (Section A.9) in describing the buffer region of this flow. The flow slowly develops a moderate change in its direction within the profile.

The flow angle hits a maximum at $y^+ < 50$ and remains constant to the wall. This nearly 2D region is the wall collateral region. Table A.4 shows the extent of the wall collateral region for each profile. The flow angle profiles are plotted in Figures 49 and 50 using the wall-collateral coordinate system.

| Table A-4: Extent Of Wall Collateral Region | | | |
|---|---|---|---|
| $\phi$ Location | Number of Points in Region | | |
| | 3 | 4 | 5 |
| 105a | | x | |
| 110a | x | | |
| 115a | x | | |
| 120a | | x | |
| 123a | | | x |
| 125a | | x | |
| 130a | | | x |
| 120b | | x | |
| 123b | | | x |
| 125b | | | x |
| 120c | | x | |
| 123c | | | x |
| 125c | | | x |
| x/L location: a=0.7722 b=0.7622 c=0.7522 | | | |

The physical significance of $\alpha_g$ and $\alpha_s$ lies in their difference which signifies the level of isotropy. The uncertainties of $\alpha_g$ and $\alpha_s$ are $\pm 0.9°$ and $\pm 3.7°$, respectively. Therefore, their difference is uncertain to $\pm 4.6°$. In the outer layer, the shear stress angle lags behind the gradient angle. According to Flack and Johnston (1993), these angles become nearly coincident near the wall and this would justify the use of the eddy viscosity model near the wall. However, the prolate spheroid data indicates that the shear stress angle approaches and then leads the velocity gradient angle at $y^+ < 50$. (Although data exists at $y^+ < 20$, the uncertainty in the gradients makes any attempt at interpretation of the gradient angle suspect.) The difference between the gradient and shear stress angles are plotted by x/L station in Figures 45 and 46. The gradient and stress angles are plotted under wall collateral coordinates in Figures 51-54. The intensity angle ($\alpha_i$) is the direction in which $u'^2$ is largest and, consequently, u'w' is zero. This angle is plotted in Figures 55 and 56 under wall-collateral coordinates.

## A.11 TKE, $a_1$ Structural Parameter, And S Parameter

The TKE, $a_1$ structural parameter, and S parameter are all invariant to coordinate rotation. Since 3DTBL research still struggles with the question of the appropriate coordinate system in which to examine data, these quantities garner attention. They appear in closure models and are used to compare 3D and 2D TBLs. Each of the turbulent fluctuations (u', v', and w') carries part of the kinetic energy (per unit mass) of the flow. The average of this turbulent kinetic energy (or TKE) can indicate the level of turbulence in a region of flow:

$$K = \frac{1}{2}\overline{q'^2} = \frac{1}{2}\left(\overline{u'^2} + \overline{v'^2} + \overline{w'^2}\right) \tag{A.40}$$

Because the TKE represents a characteristic of the fluctuating flow and is independent of coordinate system, the TKE appears in many turbulence models such as the K-ε model and its derivatives. Plots of the TKE profiles normalized by the square of $U_e$ are found in Figures 41 and 42. The structural parameter, $a_1$, is the ratio of turbulent shear stress to twice the turbulent kinetic energy (TKE):

$$a_1 = \frac{\left[\overline{u'v'}^2 + \overline{v'w'}^2\right]^{\frac{1}{2}}}{\overline{q'^2}} \tag{A.41}$$

The $a_1$ parameter is invariant with respect to coordinate rotations about the Y-axis of a body surface axis system. It, therefore, gathers alot of attention in flow studies. It has mainly been the focus of comparisons between similar 2D and 3D turbulent boundary layers because its value drops in the 3D case. This has been shown in the channel flow experiments of Schwarz & Bradshaw (1993) and Flack & Johnston (1993). Senstad & Moin (1992) have also shown similar behavior in the numerical simulation of a channel flow experiencing a spanwise pressure gradient. However, there is no companion 2D boundary layer in the current experiment. Here, the $a_1$ parameter has shown its worth as a test of the wall refinement method. Flack and Johnston (1993) showed that profiles of the $a_1$ parameter collapsed on a $y^+$ plot for their moderate 3DTBL. The $a_1$ parameter exhibits a similar behavior in this flow, which is enhanced when wall refinement is used. (A more in depth discussion appears in Chapter three.) Plots of the $a_1$ profiles appear in Figures 37-40.

The flow structure parameter, S (Eqn. 42), is a lesser known and rarely referenced quantity in 3DTBL research. But it is gathering more attention in recent studies: McEgliot and Eckelmann (1993), Olcmen and Simpson (1995), and Fleming, Simpson, and Sinpaugh (1995). In 2D flows, the S parameter actually represents the ratio of -v'w' production to -u'w' production (Olcmen and Simpson, 1995). In 3D flows, S is a close approximation of this ratio.

$$S = \frac{\overline{v'^2}}{\left[\left(\overline{u'v'}\right)^2 + \left(\overline{v'w'}\right)^2\right]^{\frac{1}{2}}} \tag{A.42}$$

S and 1/S are plotted in Figures 57-60.

# Appendix B: Uncertainty Analysis

## B.1 Sources Of Uncertainty

The instrumentation accuracy and the sample size at each location in the profile contribute to the uncertainty of the time-averaged velocity statistics. Instrumentation accuracy is based on the physical properties of the experimental apparatus. Its affect on data uncertainty is direct and propagates through successive calculations. Sample size is the major determinant of statistical uncertainty. This uncertainty affects calculations containing the time-averaged velocity statistics. The instrument accuracies and statistical uncertainties combine to form the base of uncertainties used in the analysis of successive computations. This section details the origins and utilization of these uncertainties.

### B.1.1 Instrumentation Accuracy

All the instruments described in Appendix B have finite accuracies; those with significant impact on the data originate from the LDV system, the probe traverse, the initial placement of the measurement volume at the wall, and the rigidity of the probe within the model.

When possible, instrumentation accuracies were measured during calibration. The LDV probe used in these experiments was calibrated against a spinning wheel of know diameter and rotational rate; repeated velocity readings of the wheel determined that the uncertainty in the LDV system was $\pm 0.5\%$ (Chesnakas and Simpson, 1993). Likewise, the probe traverse was observed to have a positioning accuracy of $\pm 8$ μm (Chesnakas and Simpson, 1993).

Some instrumentation accuracies are dependent on human error or unforeseen circumstances; these are quantified guesses based on expected behavior of the data. Initial placement of the measurement volume at the wall was performed for each profile visually with the use of a magnifying lens. The uncertainty of this procedure depends on the acuity of the individual that performed the positioning. The uncertainty was ultimately derived from application of the Spalding continuous wall law on the data. As explained in chapter three, a least squares fit was used to refine the location of the wall. The uncertainty of the refinement was determined to be the rms average of the difference obtained when using one more or one less data point in the curve fit. (The number of data points used in the curve fit is the dominating influence over the wall correction.) For the set of thirteen profiles, the error came to $\pm 8$ μm.

As explained in Section A.1.3.2, a compromise in the rigidity of the probe was discovered after the wind tunnel experiment was complete. The clue was a sudden jump in the v component of velocity from the profiles at x/L=0.7722 to those at x/L=0.7622. Based on the assumption that the v component of velocity should be near zero at the wall, the coordinate rotations were redefined. Furthermore, an uncertainty also exists for the orthogonality of the three laser beams. These two factors combine into an estimated 0.5° uncertainty in the coordinate rotation to body surface coordinates.

| Table B-1: Instrumentation Error | |
|---|---|
| Source | Uncertainty |
| LDV Optic Probe | ±0.5% (Velocity) |
| Probe Traverse | ±8 μm |
| Initial Measurement Volume Placement | ±8 μm |
| Probe Orientation and Orthogonality of Beams | ±0.5° |

### B.1.2 Statistical Uncertainty

Uncertainties in estimating a statistical quantity based on a finite sample size are mathematically defined. It is the largest contributor to the overall uncertainty of time-averaged statistics more complicated than the mean. Unfortunately, texts on statistics only cover confidence intervals for means and variances. A few authors have presented formulae for estimating the error of the covariances due to finite sample size. However, no reference can be found for higher order statistics like the triple products presented here. Deriving such relations would be a thesis in itself and is beyond the scope of this work. One can only qualitatively say that the error would be higher than that of the variances or covariances; this error would make them greater than ten percent. Thus, the numbers for these higher order terms hold questionable value; thus, this paper does not evaluate the triple products. Plots and tables of their values are provided as an addendum to this thesis. The following relations define the statistical uncertainties:

**Mean**

$$E\left(\overline{U}\right) \cong \pm z_{\alpha/2}\sqrt{\frac{\overline{u'^2}}{n}} \tag{B.1}$$

**Variance (Reynolds Normal Stress)**

$$E\left(\overline{u'^2}\right) \cong \sigma - \frac{(n-1)s^2}{\chi^2_{0.025}} \tag{B.2}$$

### B.1.3 Total Uncertainty

Assuming that each of the uncertainties represents a 95% confidence interval. The combined influence of all the listed uncertainties can be found using:

$$E\left(\overline{u'^2}\right)\Big|_{tot} = \left\{\sum_{i=1}^{n}\left[\frac{\partial \overline{u'^2}}{\partial x_i} E\left(\overline{u'^2}\right)\Big|_{x_i}\right]^2\right\} \tag{B.3}$$

where $u'^2$ is a function of $x_{1..n}$. The partial derivative was obtained numerically using a central

difference scheme. Uncertainties were calculated for each point in each profile. For a given velocity statistic, an uncertainty percentage was obtained for each profile by dividing the largest uncertainty by the largest value. This method gives a reasonable overall percentage, particularly for quantities that change sign. This method, however, can obscure the true reliability of the data when the disparity between the minimum and maximum values of the velocity statistic are large; however, there was very little evidence of this problem in the current statistics. A velocity statistic's overall uncertainty percentage for the experiment was taken by averaging the percentages generated for each profile. This treats the profiles as single environments that equally contribute to the uncertainty. The fact that each profile was measured under similar but not exact conditions makes this separation necessary. Table B-2 contains the results:

**Table B-2:Uncertainty Analysis For Velocity Statistics**

| $\overline{U}$ | $\overline{V}$ | $\overline{W}$ | $\overline{u'^2}$ | $\overline{v'^2}$ | $\overline{w'^2}$ | $\overline{u'v'}$ | $\overline{u'w'}$ | $\overline{v'w'}$ |
|---|---|---|---|---|---|---|---|---|
| 0.5% | 1.1% | 1.0% | 1.8% | 7.8% | 2.2% | 11.0% | 12.0% | 11.0% |
| $\overline{u'^3}$ | $\overline{v'^3}$ | $\overline{w'^3}$ | $\overline{u'^2v'}$ | $\overline{u'^2w'}$ | $\overline{v'^2u'}$ | $\overline{v'^2w'}$ | $\overline{w'^2u'}$ | $\overline{w'^2v'}$ |
| 1.5% | 36.0% | 5.0% | 10.0% | 9.8% | 19.0% | 4.5% | 1.5% | 11.0% |

Percentage applies to the largest value of the velocity statistic for a given profile.

The method described in the previous paragraph was not used for gradients of the velocity statistics or the anisotropy constant derived from them. The gradients exhibit diverging uncertainties near the wall that would have skewed the results. This divergence arises from two factors. The combination of the wall location and probe position uncertainties is large in comparison to the distance from the wall for the lowest points. Furthermore, the two lowest points cannot benefit from the more stable five point central difference scheme; they must use a smaller number of points in their finite difference algorithm (see section A.6). Uncertainty percentages were generated for each data point; these percentages divided the uncertainty at the given point by the largest value of the gradient in the profile. These percentages were averaged over all profiles discarding the largest and smallest percentages at each position; this prevents aberrant percentages from influencing results (see Table B-3).

| Table B-3: Gradient Uncertainties* By Profile Position** | | | | | | | | | |
|---|---|---|---|---|---|---|---|---|---|
| Position | $\frac{\partial \overline{U}}{\partial y}$ | $\frac{\partial \overline{V}}{\partial y}$ | $\frac{\partial \overline{W}}{\partial y}$ | $\frac{\partial \overline{u'^2}}{\partial y}$ | $\frac{\partial \overline{v'^2}}{\partial y}$ | $\frac{\partial \overline{w'^2}}{\partial y}$ | $\frac{\partial \overline{u'v'}}{\partial y}$ | $\frac{\partial \overline{u'w'}}{\partial y}$ | $\frac{\partial \overline{v'w'}}{\partial y}$ |
| 1 | 11.0% | 1265% | 46.0% | 25.0% | 105% | 19.0% | 65.0% | 93.0% | 175.0% |
| 2 | 6.87% | 756% | 24.0% | 12.0% | 55.0% | 12.0% | 34.0% | 49.0% | 93.0% |
| 3 | 3.21% | 356% | 15.0% | 5.20% | 24.0% | 5.80% | 16.0% | 23.0% | 42.0% |
| 4 | 1.31% | 155% | 9.20% | 3.00% | 14.0% | 3.10% | 8.00% | 17.0% | 28.0% |
| 5 | 0.43% | 55.0% | 5.20% | 1.20% | 5.50% | 1.80% | 4.00% | 9.70% | 16.0% |
| 6 | 0.19% | 24.0% | 2.50% | 0.46% | 1.90% | 0.83% | 1.50% | 4.00% | 7.30% |
| 7 | 0.09% | 13.0% | 1.40% | 0.21% | 0.85% | 0.41% | 0.69% | 1.80% | 3.50% |
| 8 | 0.06% | 8.80% | 0.95% | 0.12% | 0.52% | 0.27% | 0.39% | 1.20% | 2.30% |
| 9 | 0.04% | 5.40% | 0.66% | 0.05% | 0.22% | 0.12% | 0.18% | 0.51% | 0.99% |
| 10 | 0.03% | 4.50% | 0.55% | 0.03% | 0.14% | 0.08% | 0.12% | 0.34% | 0.67% |
| 11 | 0.03% | 4.40% | 0.47% | 0.02% | 0.10% | 0.06% | 0.09% | 0.24% | 0.51% |
| 12 | 0.02% | 2.90% | 0.28% | 0.01% | 0.03% | 0.01% | 0.03% | 0.06% | 0.17% |

* - Percentage applies to largest gradient in the profile.
** - The position ascends from the location closest to wall, i.e. 1 = position closest to wall.

Table B-4 displays the error for select quantities derived from the velocity statistics and gradients.

**Table B-4: Miscellaneous Uncertainties**

| Position | Anisotropy Constant | Flow Angle Degrees | Gradient Angle (deg.) | Stress Angle Degrees | Stress-Gradient Angle Difference |
|---|---|---|---|---|---|
| 1 | 35.6% | 0.53 | 1.64 | 6.76 | 7.02 |
| 2 | 77.4% | 0.52 | 0.99 | 4.21 | 4.35 |
| 3 | 20.7% | 0.51 | 0.76 | 3.42 | 3.52 |
| 4 | 8.8% | 0.51 | 0.76 | 2.40 | 2.53 |
| 5 | 3.2% | 0.51 | 0.75 | 2.37 | 2.49 |
| 6 | 1.4% | 0.51 | 0.71 | 2.27 | 2.38 |
| 7 | 1.0% | 0.51 | 0.64 | 2.31 | 2.40 |
| 8 | 0.8% | 0.50 | 0.60 | 2.37 | 2.45 |
| 9 | 0.7% | 0.50 | 0.51 | 2.54 | 2.59 |
| 10 | 0.8% | 0.48 | 0.54 | 2.76 | 2.82 |
| 11 | 1.7% | 0.48 | 0.66 | 2.97 | 3.06 |
| 12 | 5.2% | 0.48 | 2.26 | 2.68 | 4.04 |
| A1 Parameter 5.0% | | | | | |

# Appendix C The Governing Equations

The myriad of closure models and algebraic terms (e.g. the $a_1$ parameter) can distract the mind from the root physics of aerodynamics. Every paper should have a central location which emphasizes the basic laws of fluid mechanics. Both the reader and writer need this section when their thoughts stray from the actual problem of simplifying the solution for general 3D TBLs. This section first focuses on the mathematical expression of the three laws of conservation: mass, momentum, and energy. It then outlines the two other equations derived from the Navier-Stokes equations: the Reynolds transport equation and the dissipation equation. All equations are presented in their steady, ensemble-averaged form.

## C.1 Conservation Of Mass: The Continuity Equation

The continuity equation demonstrates that the net mass flow of any point in the fluid is zero, i.e. inflows equal outflows; the form below assumes that the fluid maintains a constant density through out the flow.

$$\frac{\partial \overline{U}}{\partial x}+\frac{\partial \overline{V}}{\partial y}+\frac{\partial \overline{W}}{\partial z}=0 \qquad \text{(C.1)}$$

## C.2 Momentum Principle: The Navier-Stokes Equations

The left side of the Navier-Stokes equations represent the change in momentum of the fluid; the right side of the equations symbolizes the external forces acting on the fluid. Three external forces are the mean pressure gradient, the mean shear stress, and the turbulent shear stress (a.k.a. the Reynolds stress). (Body forces such as gravity or buoyancy are considered negligible). The Reynolds stresses are not truly external forces; they actually are part of the momentum change in the fluid. However, their mathematical representation resembles shearing and normal stresses.

$$\overline{U}\frac{\partial \overline{U}}{\partial x}+\overline{V}\frac{\partial \overline{U}}{\partial y}+\overline{W}\frac{\partial \overline{U}}{\partial z}=-\frac{1}{\rho}\frac{\partial \overline{p}}{\partial x}+\nu\left(\frac{\partial^2 \overline{U}}{\partial x^2}+\frac{\partial^2 \overline{U}}{\partial y^2}+\frac{\partial^2 \overline{U}}{\partial z^2}\right)-\frac{\partial \overline{u'^2}}{\partial x}-\frac{\partial \overline{u'v'}}{\partial y}-\frac{\partial \overline{u'w'}}{\partial z} \qquad \text{(C.2)}$$

$$\overline{U}\frac{\partial \overline{V}}{\partial x}+\overline{V}\frac{\partial \overline{V}}{\partial y}+\overline{W}\frac{\partial \overline{V}}{\partial z}=-\frac{1}{\rho}\frac{\partial \overline{p}}{\partial y}+\nu\left(\frac{\partial^2 \overline{V}}{\partial x^2}+\frac{\partial^2 \overline{V}}{\partial y^2}+\frac{\partial^2 \overline{V}}{\partial z^2}\right)-\frac{\partial \overline{u'v'}}{\partial x}-\frac{\partial \overline{v'^2}}{\partial y}-\frac{\partial \overline{v'w'}}{\partial z} \qquad \text{(C.3)}$$

$$\overline{U}\frac{\partial \overline{W}}{\partial x}+\overline{V}\frac{\partial \overline{W}}{\partial y}+\overline{W}\frac{\partial \overline{W}}{\partial z}=-\frac{1}{\rho}\frac{\partial \overline{p}}{\partial z}+\nu\left(\frac{\partial^2 \overline{W}}{\partial x^2}+\frac{\partial^2 \overline{W}}{\partial y^2}+\frac{\partial^2 \overline{W}}{\partial z^2}\right)-\frac{\partial \overline{u'w'}}{\partial x}-\frac{\partial \overline{v'w'}}{\partial y}-\frac{\partial \overline{w'^2}}{\partial z} \qquad \text{(C.4)}$$

## C.3 Conservation Of Energy: The Energy Equation

Most flows of general interest in the study of turbulent boundary layers are adiabatic (propulsion, heating, and cooling systems being the major exceptions). Therefore, only the kinetic energy needs attention. A formula for the kinetic energy can be attained by multiplying the instantaneous Nevier-Stokes equations by their respective component velocity and then taking the ensemble

average. Once again, the effects of buoyancy are assumed negligible. Equation C.5 gives the total kinetic energy equation for steady flow using a condensed notation. In the condensed notation, 'U' is a mean velocity, 'u' is a velocity fluctuation, and 'x' is a Cartesian coordinate. The subscript 'i' represents the component (x, y, or z) for a individual instance of the equation; substituting 'x' for 'i' would produce the X-component instance of the equation. The subscript 'l' indicates a summation of the term containing the subscript for each Cartesian coordinate; the term $x_l$ expands to 'x+y+z'. (Townsend, 1976)

$$U_l\frac{\partial}{\partial x_l}\left[K+\frac{1}{2}U_i^2\right]+\frac{\partial}{\partial x_l}\left(\frac{1}{2}\overline{Ku_l}+\overline{u_iu_i}U_l+\overline{P}U_l+\overline{p'u_l}\right)=\nu\left[U_i\frac{\partial^2 U_i}{\partial x_l^2}+\overline{u_i\frac{\partial^2 u_i}{\partial x_l^2}}\right] \qquad \text{(C.5)}$$

The quantity, $K$, is the turbulent kinetic energy (TKE) as described in section A.12. The TKE receives special attention in the study of 3D TBL's; understanding the physical nature of the fluctuations is necessary to finding a closure model. One can create a formula for the TKE by multiplying the instantaneous Navier-Stokes equations by the corresponding velocity fluctuation and then take the ensemble average. Equation C.6 shows the result using the same condensed notation as for equation C.5. One should immediately notice that equation C.6 is a subset of equation C.5.

$$U_l\frac{\partial K}{\partial x_l}+\frac{\partial}{\partial x_l}\left(\overline{pu_l}+\overline{Ku_l}\right)+\overline{u_iu_l}\frac{\partial U_i}{\partial x_l}=\nu\overline{u_i\frac{\partial^2 u_i}{\partial x_l^2}} \qquad \text{(C.6)}$$

# References


AGARD, "Calculation of 3D Separated Turbulent Flows in Boundary Layer Limit", AGARD-AR-255, Neuilly sur Seine, France, 1990.

Ahn, S. and Simpson, R. L., "Cross-Flow Separation on a Prolate Spheroid at Angles of Attack", AIAA-92-0428, 30th Aerospace Sciences Meeting & Exhibit, Reno, January 1992.

Barber, K. M., "Mean Velocity and Turbulence Measurements of Flow Around a 6:1 Prolate Spheroid", VPI-AOE-174, Master's Thesis, Virginia Tech, 1990.

Barber, K. M. and Simpson, R. L., "Mean Velocity and Turbulence Measurements of Flow Around a 6:1 Prolate Spheriod.", AIAA-91-0255, 29th Aerospace Sciences Meeting, Reno, 1991.

Bates, C. J. and Hughes, T. D., "Reat-Time Statistical LDV System for the Study of a High Reynolds Number, Low Turbulence Intensity Flow", *Journal Of Physics*, Vol. 9, pp. 955-959, 1976.

Bogard, D. G., and Tiederman, W. G., "Burst Detection with Single-Point Velocity Measurments", Journal of Fluid Mechanics, Vol. 162, pp. 389-413, 1986.

Bradshaw, P., "Turbulent Secondary Flows", *Ann. Rev. Fluid Mech.*, Vol. 19, pp. 53-74, 1987.

Bütefish, K. A., "Three Component Laser Doppler Anemometry in Large Wind Tunnels", *Prog. Aerospace Sci.*, Vol. 26, pp. 79-113, 1989.

Chesnakus, C. J., and Simpson, R. L., "Three-Dimensional Turbulence Structure in the Vicinity of a 3-D Separation.", Forum on Turbulence in Complex Flows, Chicago, 1994.

Chesnakus, C. J., and Simpson, R. L., "Full Three-Dimensional Measurements of the Cross-Flow Separation Region of a 6:1 Prolate Spheroid", *Experiments in Fluids*, Vol. 17, pp. 68-74, 1994.

Chesnakus, C. J., Simpson, R. L., and Madden, M. M., "Three-Dimensional Velocity Measurements on a 6:1 Prolate Spheroid at 10° Angle of Attack.", VPI-AOE-202, AOE Department, Virginia Tech, 1994.

Chesnakus, C. J., and Simpson, R. L., "An Investigation of the Three-Dimensional Turbulent Flow in the Cross-Flow Separation Region of a 6:1 Prolate Spheriod", *Transactions of the ASME*, Vol. 118, pp. 268-274, June 1996.

Chesnakus, C. J. and Simpson, R. L., "A Detailed Investigation of the 3-D Separation About a 6:1 Prolate Spheroid at Angle of Attack", AIAA-96-0320, 34th Aerospace Sciences Meeting and Exhibit, Reno, January 1996.

Chiang, C. and Eaton, J. K., "An Experimental Investigation of Corotating Disks and Single Disk Flow Structures", Report MD-62, Thermosciences Division, Stanford University, June 1993.

Ciochetto, D. S. and Simpson, R. L., "An Investigation of Three-Dimensional Turbulent Shear Flow Experiments and New Modeling Parameters", Tenth Symposium on Turbulent Shear Flows, Paper 10-214, University Park, August 1995.

Coleman, G. N., Kim, J., and Spalart, P. R., "Direct Numerical Simulation of Strained Three-Dimensional Wall-Bounded Flows", AIAA-96-0655, 34th Aerospace Sciences Meeting and Exhibit, Reno, January 1996.

Cook, J. C., and Hall, M. G., "Boundary Layers in Three Dimensions", In: Progress in Aeronautical Sciences, (ed. Ferri, A., Kuchemann, D., amd Sterne, L. H. G.), Vol. 2, pp. 221-282, The MacMillan Company, New York, 1962.

Degani, A. T., Smith, F. T., and Walker, J. D. A., "The Three-Dimensional Turbulent Boundary Layer Near a Plane of Symmetry", *Journal of Fluid Mechanics*, Vol. 234, pp. 329-360, 1992.

Degani, A. T., Smith, F. T., and Walker, J. D. A., "The Structure of a Three-Dimensional Turbulent Boundary Layer", *Journal of Fluid Mechanics*, Vol. 250, pp. 43-68, 1993.

DeOtte, R. E., Morrison, G. L., and Wiedner, B. G., "Considerations on the Velocity Bias in Laser Doppler Velocimetry", Sixth International Symposium on Applications of Laser Techniques to Fluid Mechanics, Instituto Superior Tecnico, Portugal, July 1992.

Durst, F., Jocanovic, J., and Sender, J., "Detailed Measurments of the Near Wall Region of Turbulent Pipe Flows", Ninth Simposium on Turbulent Shear Flows, Kyoto, pp. 2.2.1-2.2.6, August 1993.

Durst, F., Martinuzzi, R., Sender, J., and Thevenin, D., "LDA-Measurements of Mean Velocity, RMS-Values and Higher Order Moments of Turbulence Intensity Fluctuations in Flow Fields with Strong Velocity Gradients", Sixth International Symposium on Applications of Laser Techniques to Fluid Mechanics, Instituto Superior Tecnico, Portugal, pp. 5.1.1-5.1.6, July 1992.

Eaton, J. K., "The Effects of Mean Flow Three Dimensionality on the Turbulent Boundary Layer Structure", AIAA-94-2225, 25th AIAA Fluid Dynamics Conference, Colorado, June 1994.

Flack, K. A., and Johnston, J. P., "Experiments on near-wall structure of three-dimensional boundary layers", Center for Turbulence Research Annual Research Briefs, pp. 317-324, 1992.

Flack, K. A., and Johnston, J. P., "Experimental Study of a Detaching Three-Dimensional Turbulent Boundary Layer", Near-Wall Turbulent Flows, Elsevier Science Publishers B. V., pp. 977-986, 1993.

Flack, K. A., and Johnston, J. P., "Near-Wall Investigation of Three-Dimensional Turbulent Boundary Layers", Report MD-63, Thermosciences Division, Stanford University, July 1993.

Flack, K. A., and Johnston, J. P., "Advances in Three-Dimensional Turbulent Boundary Layers with Emphasis on the Wall-Layer Regions", Draft of paper for Symposium on Boundary Layer and Free Shear Flows, Lake Tahoe, June 1994.

Flack, K. A., and Johnston, J. P., "Near-Wall Flow in a Three-Dimensional Turbulent Boundary Layer on the Endwall of a Rectangular Bend.", AIAA-94-0405, 32nd Aerospace Sciences Meeting & Exhibit, Reno, January 1994.

Flack, K. A., and Johnston, J. P., "Near-Wall Structure of Three-Dimensional Turbulent Boundary Layers", ???.

Fleming, J. and Simpson, R., "Experimental Investigationn of the Near Wall Flow Structure of a Low Reynolds Number 3-D Turbulent Boundary Layer", AIAA-94-0649, 32nd Aerospace Sciences Meeting & Exhibit, Reno, January 1994.

Fleming, J. L., Simpson, R. L., and Shinpaugh, K. A., "Further Investigation of the Near Wall Flow Structure of a Low Reynolds Number 3-D Turbulent Boundary Layer", 33rd Aerospace Sciences Meeting & Exhibit, Reno, January 1995.

Fu, T. C., Shekarriz, A., Katz, J., and Huang, T. T., "The Flow Structure in the Lee Side of an Inclined Prolate Spheroid", Nineteenth Symposium on Naval Hydrodynamics, Seoul, August 1992.

Fuchs, W., Albrecht, H., Nobach, H., Tropea, C., and Graham, L. J. W., "Simulation and Experimental Verification of Statistical Bias in Laser Doppler Anemometry including Non-Homogenous Particle Density", Sixth International Symposium on Applications of Laser Techniques to Fluid Mechanics, Instituto Superior Tecnico, Portugal, pp. 8.2.1-8.2.6, July 1992.

Fuchs, W., Nobach, H., and Tropea, C., "Laser Doppler Anemometry Data Simulation: Application to Investigate the Accuracy of Statistical Estimators", *AIAA JOURNAL*, Vol. 32, pp. 1883-1889, 1994.

Gee, K. and Cummings, R. M., "Turbulence Effects on Separated Flow about a Prolate Spheriod", *AIAA Journal*, Vol. 30, No. 3, pp. 655-664, March 1992.

Hepner, T. E., "State-of-the-Art Laser Doppler Velocimetry Signal Processors: Calibration and Evaluation", AIAA-94-0042, 32nd Aerospace Sciences Meeting & Exhibit, Reno, 1994.

Huang, T. T., Liu, H.-L., Groves, N. C., Forlini, T. J., Blanton, J. N., and Gowing, S., "Measurements of Flows Over an Axisymmetric Body with Various Appendages ( DARPA SUBOFF Experiments )", Draft Paper for Nineteenth Symposium on Naval Hydrodynamics, Seoul, August 1992.

Iuso, G., Onorato, M., Oggiano, M. S., De Ponte, S., Yuzhong, B., Xiaodi, Z., "Experimental Investigation of the Complex 3-D Flow Around a Body of Revolution at Incidence. A Sino-Italian Cooperative Research Program.", ICAS-88-4.9.1, pp. 1382-1391, 1988.

Karp, W. M., Convective Heat and Mass Transfer, McGraw-Hill, New York, 1968.

Kline, S. J., "Boundary Layer Structure - A Summary", Unpublished, May 1992.

Krahulec, J. L., "Experimental Investigation of Seperation on an Inclined Prolate Spheroid", Unpublished, AOE Department, Virginia Tech, March 1992.

Kreplin, H-P., and Eckelmann, H., "Behavoir of the three Fluctuating Velocity Components in the Wall Region of a Turbulent Channel Flow", *Physics of Fluids*, Vol. 22, No. 7, July 1979.

Kreplin, H.-P., Vollmers, H., and Meier, H. U., "Measurements of the Wall Shear Stress on an Inclined Prolate Spheroid", *Z. Flugwiss Weltraumforsch*, Vol. 4, No. 6, pp. 248-252, 1982.

Kreplin, H.-P., Vollmers, H., and Meier, H.U., "Wall Shear Stress Measurements on an Inclined Prolate Spheroid in the DFVLR 3M x 3M Low Speed Wind Tunnel, Gottingen", Report IB 222-84-A-33, DFVLR, Gottingen, 1985.

Kreplin, H.-P. and Stager, R., "Measurments of the Reynolds Stress Tensor in the Three-Dimensional Boundary Layer of an Inclined Body of Revolution", Ninth Simposium on Turbulent Shear Flows, pp. 2.4.1-2.4.6, Kyoto, 1993.

McEgilot, D. M., and Eckelmann, H., "Turbulence Structure in the Viscous Layer of Converging Flow", Ninth Simposium on Turbulent Shear Flows, Kyoto, pp. 8.5.1-8.5.6, August 1993.

Meier, H. U. and Kreplin, H.-P., "Experimental Investigation of the Boundary Layer Transition and Separation on a Body of Revolution.", *Z. Flugwiss Weltraumforsch*, Vol. 4, No. 2, pp. 65-71, 1980.

Meyers, J. F., Kjelgaard, S. O., and Hepner, T. E. "Investigation of Particle Sampling Bias in the Shear Flow Field Downstream of a Backward Facing Step", Fifth International

Symposium on Applications of Laser Techniques to Fluid Mechanics, Instituto Superior Tecnico, Portugal, pp. 29.1.1-29.1.6, July 1990.

Moin, P., Shih, T.-H., Drive, D., and Mansour, N. N., "Direct Numerical Simulation of a Three-Dimensional Turbulent Boundary Layer", *Physics of Fluids*, Vol. 2, No. 10, pp. 1846-1853.

Olcmen, M. S., "Study of Three-Dimensional Pressure-Driven Turbulent Boundary Layer", VPI-AOE-178, Phd Dissertation, Virginia Tech, 1990.

Olcmen, M. S. and Simpson, R. L., "Perspective: On the Near Wall Similarity of Three-Dimensional Turbulent Boundary Layers", *Transactions of the ASME*, 1992.

Robinson, S. K., Kline, S. J., and Sparlart, P. R., "A Review of Quasi-Coherent Structures in a Numerically Simulated Turbulent Boundary Layer", NASA-TM-102191, Moffet Field, May 1989.

Robinson, S. K., "A Perspective on Coherent Structures and Conceptual Models for Turbulent Boundary Layer Physics", AIAA-90-1638, AIAA 21st Fluid Dynamics, Plasma Dynamics and Lasers Conference, Seattle, June 1990.

Robinson, S. K., "Coherent Motions in the Turbulent Boundary Layer", *Annu. Rev. Fluid Mech.*, Vol. 23, pp. 601-639, 1991

Rotta, J. C., "Turbulent Boundary Layers in Incompressible Flow", In: Progress in Aeronautical Sciences, (ed. Ferri, A., Kuchemann, D., amd Sterne, L. H. G.), Vol. 2, pp. 1-220, The MacMillan Company, New York, 1962.

Schetz, J. A., Boundary Layer Analysis, Prentice Hall, Englewood Cliffs, N.J., 1993.

Schuman, U., "Realizability of Reynolds-stress Turbulence Models", *Physics of Fluid*, Vol. 20, No. 5, pp. 721-725, May 1977.

Schwarz, W. R. and Bradshaw, P., "Measurements in a Pressure-Driven Three-Dimensional Turbulent Boundary Layer During Development and Decay", AIAA-93-0543, 31st Aerospace Sciences Meeting & Exhibit, Reno, January 1993.

Sendstad, O. and Moin, P., "On the Mechanics of 3-D Turbulent Boundary Layers", Report No. TF-57, Thermosciences Devision, Standford University, December 1992.

Sendstad, O. and Moin, P., "The Near Wall Mechanics of Three-Dimensional Turbulent Boundary Layers", Eighth Simposium on Turbulent Shear Flows, Munich, pg. 5.4.1 - 5.4.5, September, 1991.

Shinpaugh, K. A., Simpson, R.L., Wicks, A. L., Ha, S. M., and Fleming, J. L., "Signal-Processing Techniques for Low Singal-to-Noise Ration Laser Doppler Velocimetry Signals", *Experiments in Fluids*, Vol. 12, pp. 319-328, 1992.

Simpson, R. L. and Devenport, W. J., "A Conceptual Model for the Near Wall Region of Three-Dimensional Turbulent Boundary Layers", Boundary-Layer Structure Workshop, Langley Research Center, Hampton, Virginia, 1990.

Simpson, R. L., "Three-Dimensional Turbulent Boundary Layers and Separation", AIAA-95-0226, 33rd Aerospace Sciences Meeting & Exhibit, Reno, January 1995.

Simpson, R. L., "Aspects of Turbulent Boundary-Layer Separation", *Prog. Aerospace Sci.*, Vol. 32, pp. 457-521, 1996.

Subramanian, C. S., Rajagopalan, S., Antonia, R. A., and Chambers, A. J., "Comparison of Conditional Sampling and Averaging Techniques in a Turbulent Boundary Layer", *Journal of Fluid Mechanics*, Vol. 123, pp. 335-362, 1982.

Tiederman, W. G. and Luchik, T. S., "Timescale and Structure of Ejections and Bursts in Turbulent Channel Flows", *Journal of Fluid Mechanics*, Vol. 174, pp. 529-552, 1987.

Wetzel, T. G., Simpson, R. L., and Chesnakus, C. J., "The Measurement of Three Dimensional Crossflow Separation", Unpublished, 1997.

Wallace, J. M., Eckelmann, H., and Brodkey, R. S., "The Wall Region in Turbulent Shear Flow", Journal of Fluid Mechanics, Vol. 54, pp. 39-48, 1972.

Willmarth, W. W. and Lu, S. S., "Sturcture of the Reynolds Stress Near the Wall", Journal of Fluid Mechanics, Vol. 55, pp. 65-92, 1972.

Winter, A. R., Graham, L. J., and Bremhorst, K., "Effects of time scales on velocity bias in LDA measurements using sample and hold processing", *Experiment in Fuilds*, Vol. 11, pp. 147-152, 1991.

Winter, A. R., Graham, L. J., and Bremhorst, K., "Velocity Bias Associated with Laser Doppler Anemometer Controlled Processors", *Transactions of the ASME*, Vol. 113, pp. 250-255, 1991.

Walpole, R. E., and Myers, R. H., Probability and Statistics for Engineers and Scientists, MacMillan Publishing, New York, 1978.